



Improving performance and reliability of M&NEMS accelerometers based on resonant detection

Théo Miani

► To cite this version:

Théo Miani. Improving performance and reliability of M&NEMS accelerometers based on resonant detection. Micro and nanotechnologies/Microelectronics. Université Grenoble Alpes [2020-..], 2022. English. NNT : 2022GRALT022 . tel-03710506

HAL Id: tel-03710506

<https://theses.hal.science/tel-03710506>

Submitted on 30 Jun 2022

HAL is a multi-disciplinary open access archive for the deposit and dissemination of scientific research documents, whether they are published or not. The documents may come from teaching and research institutions in France or abroad, or from public or private research centers.

L'archive ouverte pluridisciplinaire **HAL**, est destinée au dépôt et à la diffusion de documents scientifiques de niveau recherche, publiés ou non, émanant des établissements d'enseignement et de recherche français ou étrangers, des laboratoires publics ou privés.

THÈSE

Pour obtenir le grade de

DOCTEUR DE L'UNIVERSITÉ GRENOBLE ALPES

Spécialité : NANO ELECTRONIQUE ET NANO TECHNOLOGIES

Arrêté ministériel : 25 mai 2016

Présentée par

Théo MIANI

Thèse dirigée par **Julien ARCAMONE**, Chef du Service des Composants pour le Calcul et la Connectivité, Université Grenoble Alpes

et co-encadrée par **Marc SANSA**
et **Thierry VERDOT**

préparée au sein du **Laboratoire CEA/LETI**
dans l'**École Doctorale Electronique, Electrotechnique, Automatique, Traitement du Signal (EEATS)**

Amélioration des performances et de la fiabilité d'accéléromètres à détection résonante en technologie M&NEMS

Improving performance and reliability of M&NEMS accelerometers based on resonant detection

Thèse soutenue publiquement le **25 mars 2022**,
devant le jury composé de :

Monsieur Julien ARCAMONE

DIRECTEUR DE RECHERCHE, CEA, Directeur de thèse

Monsieur Raphaël LEVY

INGENIEUR DE RECHERCHE, ONERA, Examineur

Madame Panagiota MORFOULI

PROFESSEUR DES UNIVERSITES, Grenoble INP, Examinatrice,
Présidente

Monsieur Ashwin SESHIA

PROFESSEUR DES UNIVERSITES, University of Cambridge,
Rapporteur

Madame Nuria BARNIOL

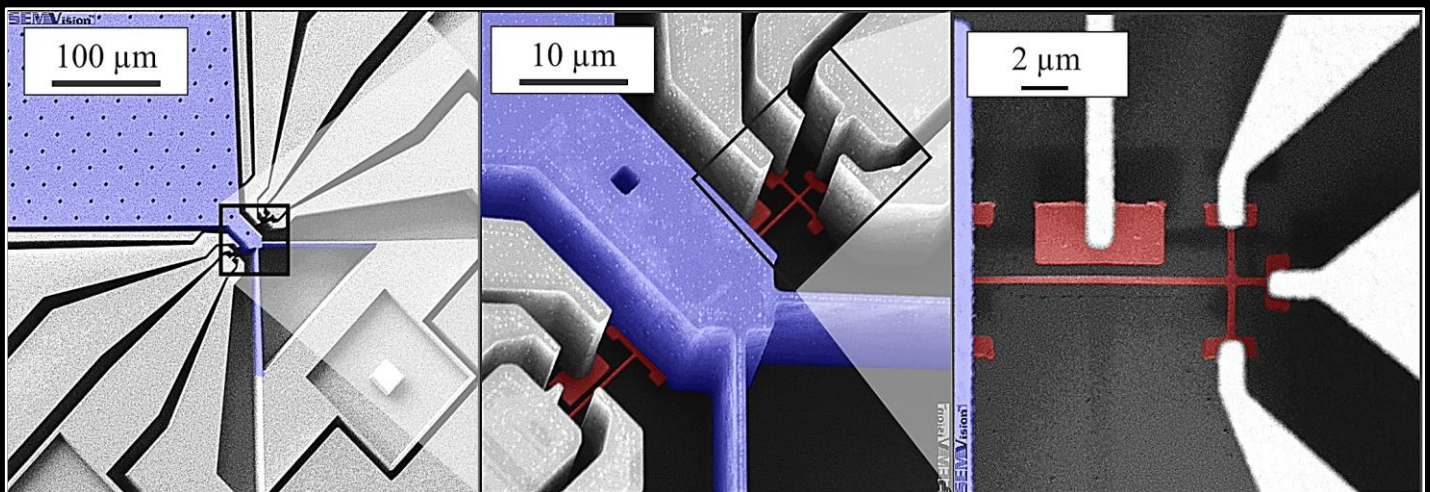
PROFESSEUR DES UNIVERSITES, Universitat Autònoma de
Barcelona , Rapporteure



Improving performance and reliability of M&NEMS accelerometers based on resonant detection

Thesis by:

Théo Miani



Supervised by:

Marc Sansa Perna



Contents

Remerciements.....	4
Résumé.....	5
Abstract.....	6
1 Introduction.....	7
1.1 General approach	7
1.2 Accelerometer applications	8
1.2.1 Accelerometer specifications	9
1.2.2 Accelerometer architectures	12
1.3 Resonant detection	14
1.3.1 Resonators at the nanoscale	15
1.3.2 Resonant beam accelerometer	16
1.3.3 Single-layer trade-offs	18
1.4 <i>M&NEMS</i> technology	22
2 Electromechanical modelling	24
2.1 Transduction chain of the accelerometer	25
2.2 Nanoresonator used as force sensor	27
2.2.1 Formulation of the equation of motion	29
2.2.2 Modal analysis	32
2.3 Transduction chain of the nanoresonator	36
2.3.1 Electrostatic actuation.....	37
2.3.2 Piezoresistive transduction	40
2.4 Frequency measurement.....	43
2.4.1 Phase noise.....	46
2.4.2 Frequency noises.....	48
2.5 Voltage readout	50
3 Electromechanical design of resonant accelerometers	53
3.1 Design of the MEMS structure	54
3.1.1 <i>M&NEMS</i> fabrication process	55
3.1.2 Nanoresonator design	58
3.1.3 Accelerometer design	63
3.1.4 Design strategy	68

3.2	Design of the electronic readout	74
3.2.1	Adapted readout	75
3.2.2	Oscillator architecture	79
3.2.3	Feedthrough correction	82
3.2.4	Implementation of the oscillator	85
4	Experimental characterization	88
4.1	Isolated nanoresonators	90
4.1.1	Frequency response	92
4.1.2	Noise analysis	93
4.1.3	Non linearity	99
4.2	Accelerometer	100
4.2.1	Frequency response	101
4.2.2	Noise analysis	105
4.2.3	Non linearities	110
4.2.4	Closed loop operation	112
4.3	Self-oscillating circuit	123
4.3.1	Adapted readout analysis	126
4.3.2	Feedthrough correction	128
5	Towards next generations of resonant accelerometers	130
5.1	Mode-decoupling solution	131
5.1.1	Presentation and modelling of the decoupling mechanism	132
5.1.2	Implementation	134
5.1.3	FEM simulations method	138
5.2	Design of the second generation of resonant accelerometers	140
5.2.1	Second generation of nanoresonators	141
5.2.2	Second generation of accelerometers	144
	Conclusions	152
6	Appendix	153
	Appendix A	153
	Appendix B	157
	Appendix C	159
	Coupling modelling	160
	FEM-simulation identification method	162
	Decoupling modelling	168

Appendix D.....	169
Pendulum accelerometer generation 1	170
Pendulum accelerometer generation 2	173
Translation accelerometer	177
Lever arm accelerometer	181
Bibliography	185
Additional work	194

Remerciements

Je tiens à remercier Marc, mon superviseur, pour m'avoir accompagné tout au long de mes recherches. C'était vraiment une aventure que je n'oublierai pas ! Merci pour ton soutien, tes conseils et ta pédagogie ! Et surtout, je te remercie de m'avoir assumé pendant la fameuse « avion wheel », quelle sombre époque...

Je tiens également à remercier Julien, mon directeur de thèse, pour m'avoir guidé jusqu'au bout de mon travail. Merci pour ton soutien qui est allé bien au-delà de celui d'un directeur de thèse ! Et surtout, merci de m'avoir fait passer du statut de « kid » à celui de « docteur » !

Enfin, je tiens à remercier Thierry, mon co-superviseur, pour sa patience à mon égard ! Bien que mon nez ait saigné plusieurs fois pendant tes explications, je récolte déjà les fruits de ce travail ! Un grand merci de m'avoir accompagné avec cette bouteille de porto... et les autres...

In addition, I would like to thank our partner from polimi for their support in this work. Federico Maspero, thank you for the time you spent sharing your knowledge with me! Giacomo Langfelder, thank you for your support and your welcome in your lab! Both of you, many thanks for the discovery of the "focaccia recco"!

Bien entendu, cette aventure n'est pas seulement le fruit de mes proches encadrants (bien qu'ils en soient le noyau). C'est pourquoi je tiens également à remercier les principaux acteurs de cette recherche ! Merci à Audrey d'avoir fabriqué ces magnifiques puces que j'ai tant chéries ! Merci à Alexandra de m'avoir formé sur toutes ces belles machines ! Merci Auuuuuude d'avoir été le meilleur co-bureau de tous les temps ! Merci à Loïc pour tous tes conseils utiles ! Merci à François et Christophe de m'avoir prêté leur matériel pendant mes mesures ! Merci à Antoine de m'avoir montré que l'impossible était possible ! Je tiens également à remercier Philippe, Mickael et Caroline pour avoir soutenu notre projet !

Moins sérieusement, merci à mon crush fafa, qui est parti trop tôt... Un brave homme avec qui je pouvais travailler jusqu'à tard dans la nuit... Mes mesures n'avaient plus le même goût après ton départ ! Heureusement, il y avait aussi mon crush numéro 2 : Romain l'acousticien ! Je sais que j'ai été un mentor pour toi, mais tu t'en sortiras sans moi je n'en doute pas ! Rappelle-toi, la thèse, « c'est pas ce qu'on croit » !

Thank you Thijs for accepting my very grammatical sentences in our discussion ! Sam I put you here because as a Golden Boy you speak a lot of language! Thank you for making me write my manuscript in Word, only the jealous will say it's latec!

Merci à Lucas, Louise et tous les autres ! Ce fut une super expérience !

Résumé

Les accéléromètres à poutre vibrante ont démontré leur capacité à atteindre un niveau de bruit inférieur au μg , auparavant réservé aux accéléromètres macroscopiques. Ces systèmes microélectromécaniques (dits MEMS, leur acronyme en anglais) sont des candidats prometteurs pour les applications commerciales de haute précision en raison de leur faible coût, de leur petite taille et de leur possibilité de fabrication en série. Dans la grande majorité des capteurs inertiels commerciaux, la masse sismique et les éléments de détection sont gravés dans la même couche de silicium. Dans le cas particulier où l'élément de détection est une poutre résonante, l'utilisation d'une seule couche de silicium implique un compromis entre la sensibilité et la bande passante de l'accéléromètre. Pour contourner ce compromis nous proposons ici d'utiliser une technologie bicouche, dite *M&NEMS*, qui permet de concevoir des capteurs beaucoup plus sensibles, et ouvre le champ à de nouvelles applications nécessitant des capteurs intégrés de haute performance. L'accéléromètre proposé combine ainsi une masse d'épreuve micrométrique avec des poutres vibrantes de taille nanométrique pour une détection de haute sensibilité. De plus, une détection piézorésistive des nanorésonateurs est proposée, permettant de mesurer leur fonctionnement à haute fréquence dans des conditions plus optimales qu'avec une détection classique capacitive.

Ce travail est la première preuve de concept d'un accéléromètre résonant basé sur la détection d'un nanorésonateur piézorésistif. D'abord, la modélisation, la conception et la fabrication de la première génération de capteur sont présentées. Comme le nanorésonateur conçu fonctionne au-delà du MHz, une électronique de lecture dédiée a été conçue en partenariat avec le laboratoire du Prof. Langfelder du Politecnico di Milano. La deuxième partie de ce travail se concentre sur la caractérisation des accéléromètres. L'utilisation du procédé multicouche *M&NEMS* permet d'atteindre la plus haute sensibilité de l'état de l'art pour une empreinte de masse de $0,18 \text{ mm}^2$: $100\,000 \text{ ppm/g}$ avec $<1\%$ de non-linéarité sur la gamme $\pm 1 \text{ g}$. L'analyse du bruit montre que la limite de détection du nanorésonateur est de $1,75 \mu\text{g}/\sqrt{\text{Hz}}$ de bruit de fond, sur une bande passante de 1 kHz . La dernière partie propose des améliorations de l'architecture de l'accéléromètre et des nanorésonateurs afin de surmonter les limites de fonctionnement mises en évidence par les premiers résultats expérimentaux. Le processus de fabrication étant compatible avec des capteurs gyroscopiques et des accéléromètres hors plan, la détection par nanorésonateurs proposée représente une alternative de haute sensibilité pour les unités de mesure inertielle (IMU) à 6 axes, ainsi que pour d'autres dispositifs comme des capteurs de pression ou des magnétomètres.

Abstract

Resonant beam accelerometers have demonstrated their ability to achieve sub- μg resolutions previously reserved for macroscopic accelerometers. These microelectromechanical systems (MEMS) are promising candidates for high-precision commercial applications due to their low cost, small size, and batch manufacturability. In the vast majority of commercial MEMS inertial sensors, the proof mass and sensing elements are defined in the same silicon layer. When the sensing element is a resonant beam, the use of a single layer of silicon imposes a trade-off between the sensitivity and the bandwidth of the accelerometer. In order to circumvent this trade-off, we propose here to use a bi-layer technology, so-called *M&NEMS*, which results in sensors that are more sensitive and would open the field to new applications requiring high-performance integrated sensors. The proposed accelerometer combines a micrometric proof mass with the high detection sensitivity of a nanoresonator. In addition, we propose to employ a piezoresistive detection that provides a performance transduction at high frequency, unlike capacitive detection.

This work represents the first proof of concept of a resonant accelerometer based on a piezoresistive nanoresonator detection. First, the modelling, design and fabrication of the first generation of sensors is presented. Because the designed nanoresonator operates at several MHz, a dedicated readout electronics was designed in partnership with the group of Prof. Langfelder from the Politecnico di Milano. The second part of this work focuses on the characterization of the accelerometers. The use of the *M&NEMS* multi-layer process allows reaching the highest sensitivity of the state of the art for a 0.18 mm^2 mass footprint, i.e. $100,000\text{ ppm/g}$ with $<1\%$ nonlinearity over the $\pm 1\text{g}$ range. The noise analysis shows a noise floor of $1.75\mu\text{g}/\sqrt{\text{Hz}}$ over a 1-kHz bandwidth. The last part deals with the improvement of the accelerometer and nanoresonator architecture in order to overcome the operating limitations highlighted by the first experimental results. Because the manufacturing process is compatible with gyros and out-of-plane accelerometers, the proposed nanoresonator-based detection represents a high-sensitivity alternative for 6-axis inertial measurement units (IMU), as well as other devices such as pressure sensors or magnetometers.

1 Introduction

1.1 General approach

An accelerometer is a sensing device that measures acceleration in one, two or three orthogonal axes. The device consists of a proof body that translates acceleration into a variation of a physical quantity, and of a sensing element that measures this variation. The first accelerometer in the modern sense of the term was developed in the early 1920s [1] and consisted of a macroscopic proof mass that produced a stress variation on the sensing elements. Because of the piezoresistive nature of these sensing elements, the stress variation could then be measured by a voltage variation across a Wheatstone bridge. This was the first acceleration measurement that was exploited for specific applications. However, the size of these devices, presented in Figure 1-1 (a), posed a problem for integration in embedded applications. The development of the bonded resistance strain gauge (Figure 1-1 (b)) around 1938 [2] made it possible to reduce the size of the sensing elements considerably, which facilitated the integration of the accelerometers in many applications. As a result, the volume and price of the device decreased and the commercialization of accelerometers increased dramatically. It was in 1979 that the first micromachined accelerometer (Figure 1-1 (c)) based on piezoresistive properties was produced [3]. The large commercial diffusion of MEMS started ten years later with the introduction of accelerometers in airbags for automotive applications. Since then, the market for inertial MEMS has continued to grow, constantly encompassing new applications and encouraging the development of more powerful and compact sensors.

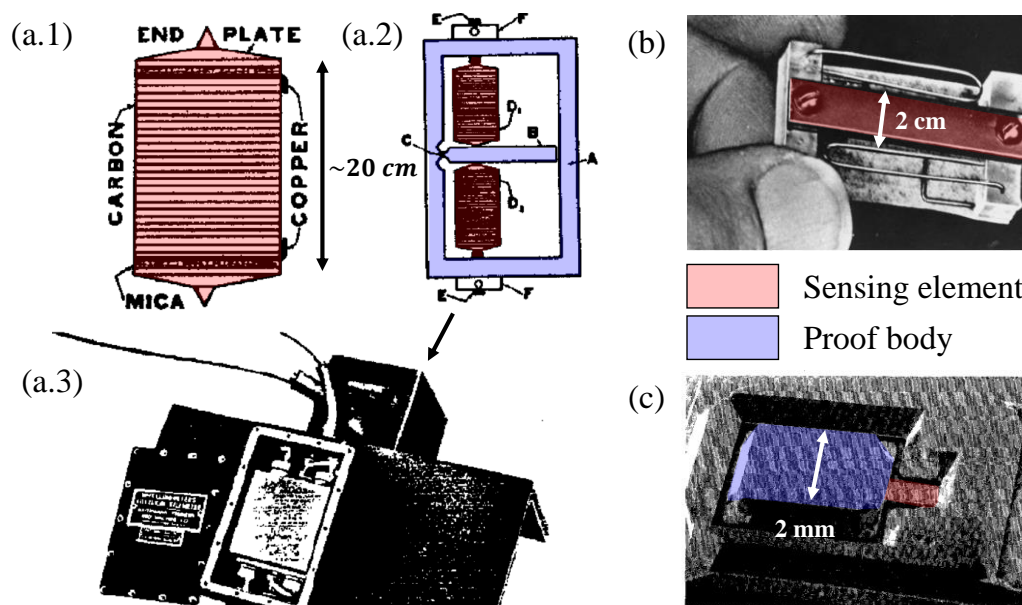


Figure 1-1 History of the first accelerometers: (a) is the first commercialized accelerometer (a.1) its sensing element based on a piezoresistive carbon ring, (a.2) its working principle architecture and (a.3) the integration of the accelerometer in a system. (b) Is the first bonded resistance strain gauge and (c) is the first produced micro-machined accelerometer.

1.2 Accelerometer applications

The MEMS market continues to grow due to the increasing number of electronic devices, but also due to new applications. According to Yole Development [4], inertial MEMS production is expected to grow from \$3.4 billion in 2020 to \$4 billion in 2026. This growth is mainly due to the increasing demand for inertial measurement units and the advancement of co-integration of MEMS sensors in their specific integrated circuit (ASIC), which represents a new step of integration of the sensor in an embedded system. Besides, the automotive market is making ever more intensive use of accelerometers with the advent of autonomous cars. The consumer market has taken a significant share of total revenues with the introduction of inertial sensors in smartphones and game consoles. Moreover, with the emergence of new consumer applications such as augmented reality and the Internet of Things (IoT), this field is expected to grow in the coming years. Although the defence market represents only a small portion of the MEMS market, the increasing reliance on high technology of warfare is driving the development of the latest disruptive technologies in accelerometers, which is improving performance in the aeronautics and industrial markets.

Whatever the market, the applications of accelerometers can be grouped into three main families. From missile guidance systems to directional drilling and smartphone tracking, navigation is the most widespread application of the measurement of acceleration, where it is exploited to calculate the position in real time. Acceleration can also be used to measure vibrations. This allows for geological studies, such as seismometers, which detect earthquakes, and the gravimeter, which measures fluctuations in gravity. In addition, vibration measurement is used to control the operation of industrial machinery, but also has medical applications such as monitoring heart rate for pacemakers. More commonly, the accelerometer is used to measure shock, such as for airbag deployment, crash testing, or smart munitions. The use of acceleration measurement varies widely across markets and need different specifications. Table 1 shows the diversity of the three applications across major markets.

Markets	Applications
Consumer	Remote control / camera stabilization / drop protection
Automotive	Integrated GPS / active suspension / airbag sensor
Medical	Motion study and rehabilitation / ballistocardiology
Industrial	Directional drilling / seismometer / shock monitoring for safety
Aeronautics	Inertial navigation / vibration monitoring
Defense	Missile guidance / defence stabilization system / smart munitions

Table 1 Examples of accelerometer applications in different markets. In blue: inertial navigation, where position is deduced from the acceleration. In black: vibration monitoring. In red: shock monitoring.

1.2.1 Accelerometer specifications

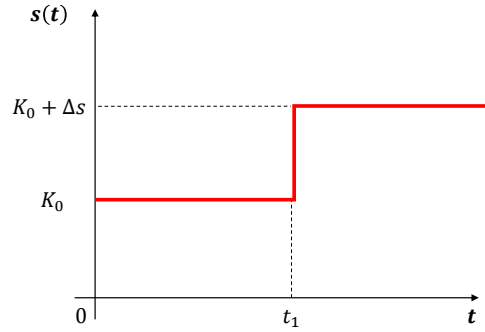


Figure 1-2 Accelerometer signal variation due to an acceleration step.

A sensor is a device that measures an input physical phenomenon by generating a change in an output quantity, usually in the form of an electrical signal. Accelerometers are sensors that generate a temporal signal $s(t)$ in order to measure an acceleration a in real time. In practice, the accelerometer generates initial signal of magnitude K_0 and the acceleration is deduced from the variation of this signal Δs . Figure 1-2 represents the accelerometer signal $s(t)$ when an acceleration step of magnitude Δa is applied at $t = t_1$. The initial signal K_0 is shifted to $K_0 + \Delta s$. The scale factor of the accelerometer is the ratio of the applied acceleration to the signal variation $K_1 = \Delta s / \Delta a$. In practice, the scale factor is determined within a range to ensure linearity of the signal variation as a function of the applied acceleration. Then, the acceleration is deduced from the accelerometer signal measurement.

$$s(t) = K_0 + K_1 a(t) \quad 1-1$$

The main specifications of an accelerometer are the dynamic range, which represents the ratio of maximum to minimum measurable acceleration, and the bandwidth that represents the maximum measurable acceleration frequency. Figure 1-3 represents the operation ranges, both in amplitude and frequency, of the acceleration measurement.

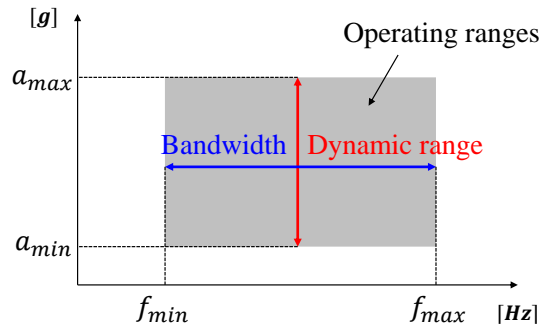


Figure 1-3 Representation of the operating ranges of an accelerometer. In blue, the bandwidth bounded by a minimum and maximum measurable frequency. In red, the dynamic range bounded by a minimum and a maximum measurable acceleration magnitude.

In practice, the bandwidth is the frequency at which the output signal is reduced by 3dB with regards to the in-band signal. The bandwidth is related to both the resonance frequency of the mechanical structure, the accelerometer, and the sensing element operation, response time and electronics readout. High bandwidth requires high output data rate, which increases the power consumption of the system. The dynamic range is usually limited by the maximum acceleration signal that can be detected with a linearity error smaller than the limit set by the application: the Full Scale Range (FSR). The dynamic range is also limited by the minimum measurable acceleration: the resolution. Again, the resolution is determined by the intrinsic limits of the accelerometer set by the integrated noise density over the desired bandwidth. It is often expressed in μg . By definition, $1 \mu\text{g}$ represents $9.81e^{-6} \text{ m/s}^2$. The noise density is the noise spectral density expressed in terms of acceleration. The noise can have a mechanical origin, such as the thermomechanical noise of the mechanical structure, or an electrical origin, such as the noise added by the sensing element and by the electronics readout. The noise density is usually expressed in $\mu\text{g}/\sqrt{\text{Hz}}$ that is an ideal representation for a system dominated by white noise. However, depending on the noise source, which may differ from white noise, the noise spectral density can be expressed over a 1Hz-bandwidth to compare its rms value. In this way, the noise deviation is expressed in $\mu\text{g rms}$. In the field of accelerometers, it is common to express the smallest resolution that the sensor can achieve: the bias stability. Bias stability is used to compare the resolution of accelerometers in different applications and it is expressed from the variance in terms of μg .

One might think that dynamic range and bandwidth are sufficient specifications to address an application. In other words that the intrinsic parameters of the accelerometer are the only considerations. In practice, this is insufficient. One must also consider its operating environment, and thus how the acceleration measurement is affected by extrinsic parameters. The stability of the measurement is one indicator of the performance of the accelerometer. Stability represents the sensitivity to extrinsic parameters and can be characterized by three sources of measurement error: the bias error δK_0 , the scale factor error δK_1 and the linearity error K_2 represented in Figure 1-4.

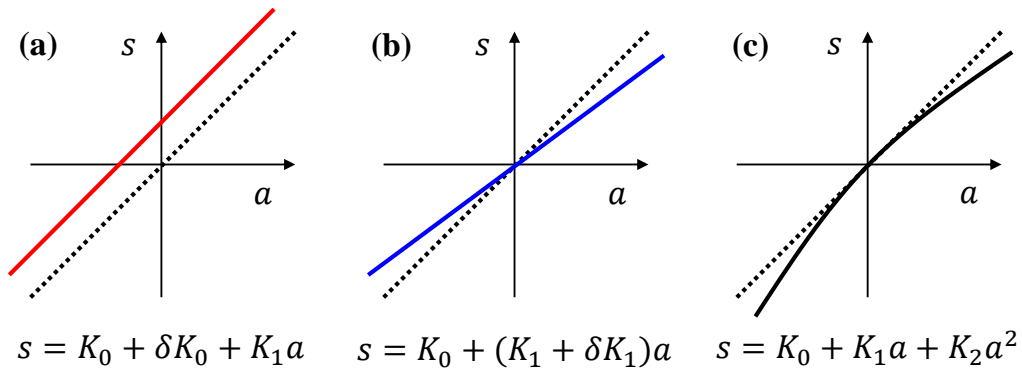


Figure 1-4 Comparison of the ideal scale factor (dotted line) with the different errors (color lines) : (a) Bias error; (b) scale factor error, (c) linearity error.

In practice, sensors are calibrated in order to minimize the initial bias offset K_0 . The bias error δK_0 is then the measured signal variation in absence of acceleration. The origins of bias error are mainly due to temperature drifts and aging of the sensor. In this way, the bias error can be expressed respectively by a temperature coefficient, usually expressed in $\text{mg}/^\circ\text{C}$ and by long-term repeatability, usually expressed in mg . The scale factor error δK_1 represents a measurement error proportional to the input acceleration. Here too, the origins of scale factor error are mainly due to temperature and aging. In practice the scale factor error is expressed as ratio of the scale factor. In this way, the scale factor error can be expressed by a temperature coefficient, usually in $\text{ppm}/^\circ\text{C}$, and long-term repeatability, usually expressed in ppm . Moreover, bias and scale factor errors can also be induced by cross-axis acceleration or shock. The linearity error K_2 , expressed usually in $\mu\text{g}/\text{g}^2$, represents a measurement error proportional to the square of acceleration that can be induced by environmental vibrations. It is important not to confuse the linearity error induced by extrinsic parameters with the sensor nonlinearity induced by intrinsic parameters, which is induced by a physical phenomenon that links the change in physical quantity to the acceleration. The nonlinearity corresponds to the relative error of the scale factor for the full scale. Typically, accelerometers are designed to operate in a linear range and have a nonlinearity of less than 1%.

In conclusion, the main specifications of the accelerometer depend both on the application and the market, i.e. the specific conditions under which the application will be performed. Table 2 highlights these requirements: navigation is an application that requires a relatively high resolution in order to provide a good accuracy on the position measurement, but it does not generally require a bandwidth larger than 400 Hz and a dynamic range larger than 140 dB. However, the stability of the measurement is a key parameter for this application. In the case of smartphone navigation (Consumer Grade), high stability measurements are not required due to GPS recalibration. However, in the military market, submarine navigation (Strategic Grade) requires long-term high stability to cover long immersions. On the contrary, the guidance of a missile (Tactical Grade), because of its very short flight time, does not require long-term stability. Here the conditions under which the application is performed impose different stability requirements for the same application. In general, accelerometers can be classified into four families: high-resolution for accuracy needs, high-g for high FSR and shock resistance needs, high-bandwidth for large frequency range needs such as vibration control, and high stability for slow measurement, long-term durability needs

	High-res	High-g	High-BW	High-stability*
Smartphone navigation	$\sim 1 \mu\text{g}$	$\sim 10 \text{ g}$	$< 400 \text{ Hz}$	$> \text{mg}$
Submarine navigation	$< 1 \mu\text{g}$	$\sim 1 \text{ g}$	$< 400 \text{ Hz}$	$< \mu\text{g}$
Missile guidance	$\sim 1 \mu\text{g}$	$\sim 10 \text{ g}$	$< 400 \text{ Hz}$	$< \text{mg}$

Table 2 Comparison of the specifications required for navigation applications as a function of the the conditions under which the application is performed. * Here High-stability represents long-term bias stability (δK_0) but can be also due to thermal environment [5],[6].

1.2.2 Accelerometer architectures

The main accelerometer architectures are discussed in terms of advantages and drawbacks. The majority of accelerometers transform acceleration into a physical quantity using a proof mass, except for thermal accelerometers where the proof body is a volume of gas [7]. For proof mass-based accelerometers, the sensors can be classified according to the measured physical quantity. On one hand, motion-measuring accelerometers measure the movement of the proof mass due to acceleration. On the other hand, force-measuring accelerometers measure mechanical stress resulting from the acceleration's inertial force.

The most common motion-measuring accelerometers are capacitive accelerometers. The principle is to take advantage of the modification of the capacitive coupling between a movable mass and fixed electrodes (Figure 1-5 (a)). The vast majority of MEMS accelerometers on the market use capacitive sensing [8], [9], [10], [11] because it can be implemented using a relatively simple process. In addition, the ability to integrate signal conditioning circuitry near the sensor allows for highly sensitive and compensated devices [12]–[14]. The main drawback is that capacitive sensors are sensitive to electromagnetic fields in their environment, so they must be carefully shielded. An alternative to current motion-measuring accelerometers are optomechanical accelerometers. The principle is to take advantage of the proof mass motion to modify the optical properties of an optical resonator (Figure 1-5 (b)). The optomechanical transduction method offers superior displacement resolution and shows promising performance [15], [16], in terms of resolution and bandwidth. However, optical sensing does not yet allow for chip-scale integration, but some devices are already fabricated with large VLSI process [17] and could lead to a new generation of sensors. There are other, less conventional, motion-measuring accelerometers such as electrostatic levitation [18] or tunneling [19] accelerometers, but they are not discussed here.

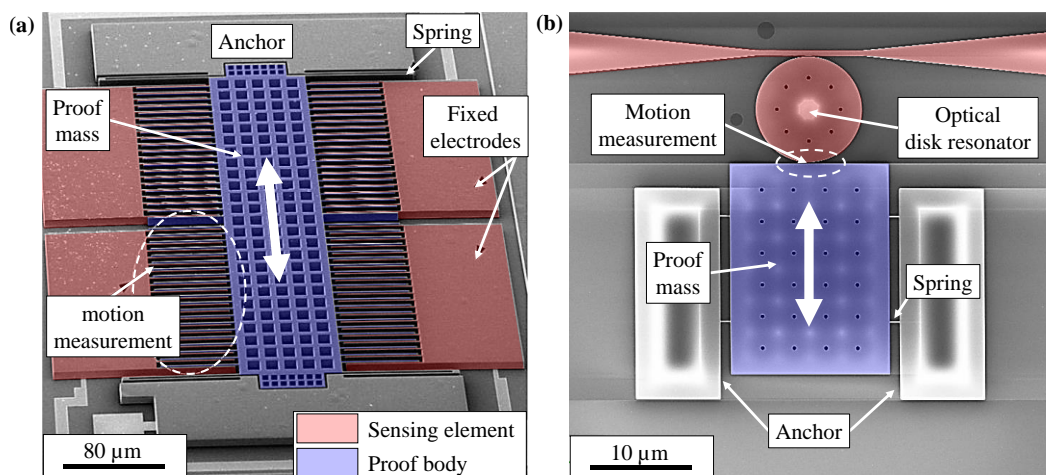


Figure 1-5 Presentation of (a) in-plane capacitive accelerometer [9] and (b) in-plane optomechanical accelerometer [14], both based on motion measurement.

An example of force-measuring accelerometers are piezoresistive accelerometers. The principle is to take advantage of the resistance variation of one or more piezoresistive elements loaded by the suspended proof mass (Figure 1-6 (a)). This reading technique allows reducing size of the sensing elements, which can be small piezoresistive layers [20],[21] or piezoresistive gauges [22]. This technology offers a large dynamic range but suffers from Johnson noise and $1/f$ noise, which limit its achievable resolution. Thus, piezoresistive accelerometers are mostly used for high-g applications [23]. A second family of force-measuring accelerometers are piezoelectric accelerometers, where the stress induces a charge variation on the piezoelectric material [24], [25]. The advantage of this approach is its low power consumption due to intrinsic charge generation. However, charge losses due to the dielectric layer limit the use of these devices for low frequency signals. Therefore, piezoelectric accelerometers are better suited for high-bandwidth measurements. Because of the complexity of depositing piezoelectric materials on micromachined accelerometers, the use of this technology is limited for the MEMS market and most available piezoelectric accelerometers are macroscopic [26]. Resonant accelerometers are another class of force-measuring accelerometers. The principle is to take advantage of the stiffness modulation of an oscillating structure, caused by acceleration, to measure the induced frequency shift. The oscillating structure consists in a beam [27]–[29] or the vibrating proof mass itself, usually kept in oscillation by an electrostatic drive. The proof mass motion causes either a stress on the vibrating beam or a change in the distance to fixed electrodes. In both cases, this results in a change in the frequency of the oscillating structure, respectively due to the modulation of the beam stiffness by axial stress (Figure 1-6 (b)) or a change in electrostatic stiffness [30]–[33]. The detection of a frequency shift is advantageous because the output is less sensitive to spurious or parasitic effects than static capacitive or piezoresistive sensing methods [34]. The relatively high complexity of the electronic systems required to maintain the structure oscillating represents the main drawback of this type of sensor, but the design of low-power oscillators and accurate frequency-to-digital converters makes it an interesting alternative to existing commercial devices. In the next section, the resonant accelerometer based on vibrating beams are discussed.

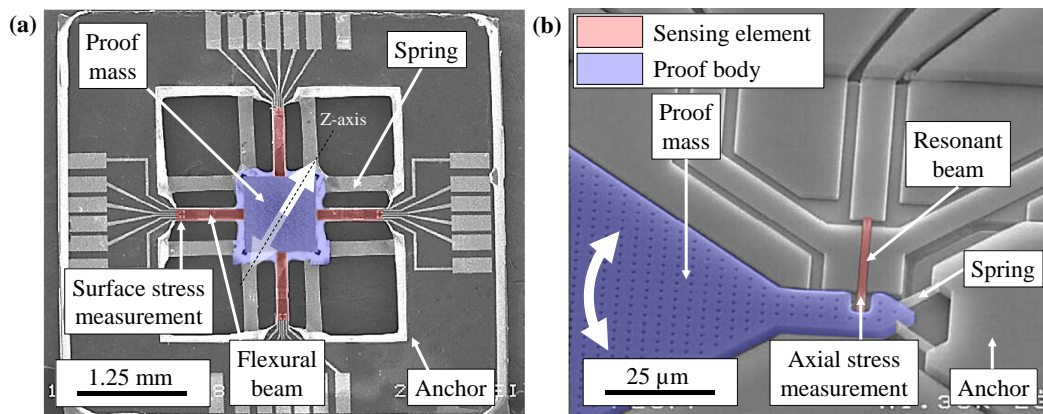


Figure 1-6 Presentation of resonant accelerometers based on force measurements. (a) Out-of-plane piezoresistive accelerometer [20]. (b) In-plane vibrating beam accelerometer [29].

1.3 Resonant detection

In the past, the development of analog control systems was accompanied by the development of electrical sensors that detect the measurand with an analog voltage or current. However, these sensors are less suitable for digital control due to the added penalty in terms of reliability, cost and speed induced by an analog-to-digital conversion step between the sensor and the control circuit. Therefore, the development of sensors that provide an inherently digital output has an advantage for their integration into systems. Figure 1-7 compares static detection with resonant detection. Temporal sensors, whose outputs are based on frequency or phase, can be measured directly in digital systems by pulse counting and thus have a natural advantage. The most common resonant sensing techniques involve modulating either the spring constant, typically for force sensing [35], or the mass of the resonant element, typically for mass sensing [36]. In addition to the resonance frequency, other parameters depending on the temporal properties of mechanical resonators can be used: for example, by selecting an appropriate oscillating structure, a viscosity sensor can be constructed due to the dependence of the decay time of a mechanical resonator on viscosity [37]. When a mechanical resonator is immersed in a moving fluid, the flow of the fluid causes phase differences in the motion of the resonator between one point and another. Therefore, the flow velocity can be measured with the time difference between the signals of displacement sensors fixed at different points [38].

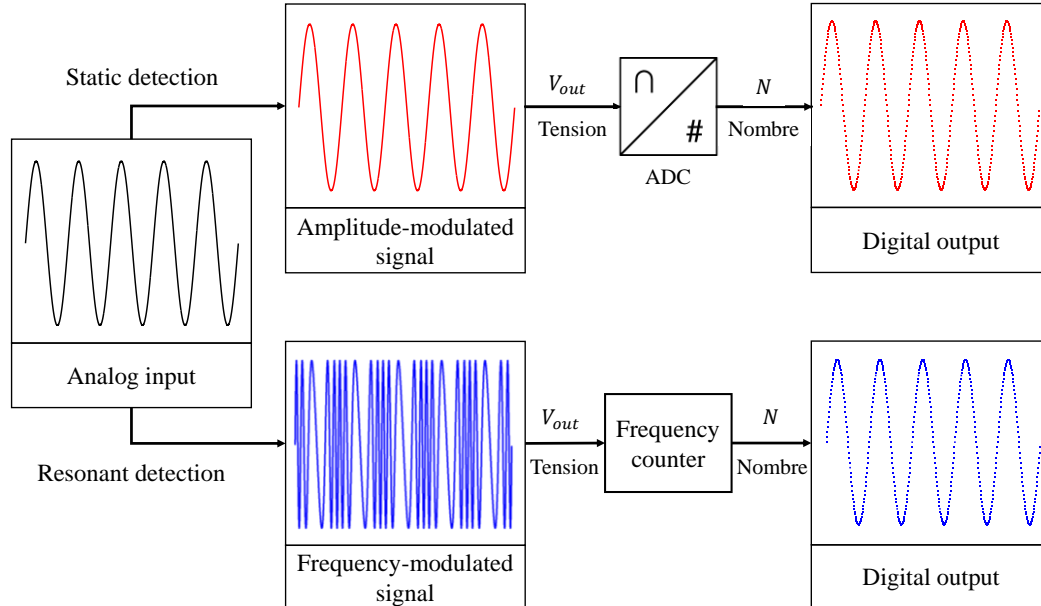


Figure 1-7 Comparison between static detection and resonant detection. For static detection, the analog input signal coming from the measurand is transduced as an amplitude-modulated signal by the sensor. An Analog-to-Digital-Converter allows sampling the signal and transferring it as digital output signal. For a resonant detection, the analog input signal coming from the measurand is transduced as frequency-modulated signal by the sensor. A frequency counter allows generating a digital output signal based on the counting frequency.

1.3.1 Resonators at the nanoscale

Over the last three decades, the evolution of microelectronic technologies has made it possible to fabricate mechanical structures of increasingly smaller dimensions. Manufacturing technology has finally allowed the fabrication of sub-micrometer size structures, thus opening the field of Nanoelectromechanical Systems (NEMS). This miniaturization offers mechanical advantages such as high surface-to-volume ratios, lower masses, and higher resonant frequencies. Nanobeam resonators are specific NEMS structures based on a beam with at least two dimensions smaller than a micrometer. The frequency response of nanobeams is well-known as it is described by the standard theory of elasticity. Nanobeams resonators can be implemented with graphene [39] or carbon nanowires [40], but silicon nanowires (NWs) are the most widely used technology because some of them are compatible with large VLSI processes [41]. Nano beam resonators, named nanoresonators afterwards, consist of a mechanical element and transducers that interact with it. The actuation transducer is in charge of transforming an input signal into mechanical stimuli to drive the mechanical element. Then, the sensing transducer measures its mechanical response and converts it into signals. One of the most commonly used actuators is the capacitive actuation (Figure 1-8), but there are also other alternatives such as the piezoelectric actuation [42]. Capacitive transduction is very inefficient at the nanoscale because the coupling area of the electrodes is proportional to the size of the device. Other detection methods, such as optomechanical transduction [43] or piezoresistive detection [44], have demonstrated high performance by routinely measuring the detection limit of the nanoresonator: its thermomechanical noise. Due to their exceptionally low masses and high resonance frequencies, nanoresonators have exceptional qualities as mass sensors [45]. The inertial mass of molecules landing on a nanoresonator can be deduced from the variation of its resonance frequency. This variation of the resonance can be due to either a change in the effective mass or the effective stiffness depending on the location of the deposit. Moreover, nanoresonators have been used as force sensors [46] due to their high sensitivity to force which modulates their effective stiffness and thus their resonance frequency.

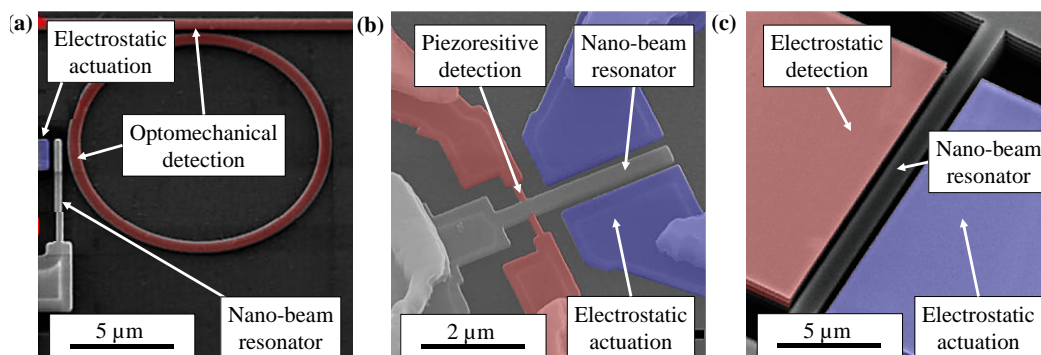


Figure 1-8 Examples of nanoresonator using (a) capacitive actuation and optomechanical detection [43], (b) capacitive actuation and piezoresistive detection [44] and (c) capacitive actuation and detection.

1.3.2 Resonant beam accelerometer

Resonant beam accelerometers (RBAs) are accelerometers based on the frequency modulation of their sensing element. Historically, it was the use of single-crystal quartz that made it possible to produce the first resonant beam accelerometer [27] because of the stable properties of this material. In the late 1980s, ONERA decided to produce the first resonant beam accelerometer from the same quartz substrate in order to avoid performance-limiting assemblies and to allow easier miniaturization [47]. Subsequently, the emergence of MEMS technologies in the 1990s enabled the fabrication of micromachined resonant accelerometers from a single-crystal silicon structure [48], opening up the possibility of larger-scale fabrication processes. However, resonant MEMS accelerometers suffer from effects such as temperature sensitivity, the need for vacuum packaging, as well as the complexity of closed-loop readout interfaces. Today, many significant improvements have been made on these topics: improved on-chip vacuum packaging allows for high quality factor resonators, which are needed for sub- μg resolution [49], and open the possibility of gravimetric or seismic applications previously reserved for macroscopic sensors. In addition, specialized high-performance circuits have been developed to realize resonance detection with an integrated readout architecture [50], which allows for reduced power consumption and system size for integration into embedded systems. While the ONERA accelerometer architecture has an isolation system that insulates the vibrating beam from thermal stresses, the impact of temperature is a critical issue in conventional resonant beam accelerometers. However, many accelerometer architectures have demonstrated resistance to thermal stress [51]–[53] by optimizing the position of the anchors and using a specially-shaped substrate.

The classical architecture of a resonant beam accelerometer is shown in Figure 1-9. The resonant beam accelerometer consists in a moving mass guided in one direction, a lever arm and one or several resonant beams. The lever arm, consisting of one (Figure 1-9 (a)) or two stages (Figure 1-10 (b)), receives the acceleration force of the proof mass as an input and transmits it as an axial stress into the resonant beam. Under the effect of this stress, the resonance frequency of the resonant beam changes. The performance of the accelerometer is directly related to the intrinsic stability of the frequency of the resonant beam, since any variation in frequency is considered as a measurement of acceleration. In general, a differential configuration with two resonant beams, identical but subject to opposite axial forces, is used. In the literature, there are mainly two ways to design resonant beams. The most classical is to use a simple beam in its first bending mode [54], or its second mode [55], but this architecture has the disadvantage of having a low quality factor due to thermoelastic damping at the anchors. Thus, another common approach is the use of Double Ended-Tuning Fork (DETFs), i.e., two parallel vibrating beams, for which the angular moments of the two beams cancel each other out and thus no energy is lost in the support, which implies a higher quality factor.

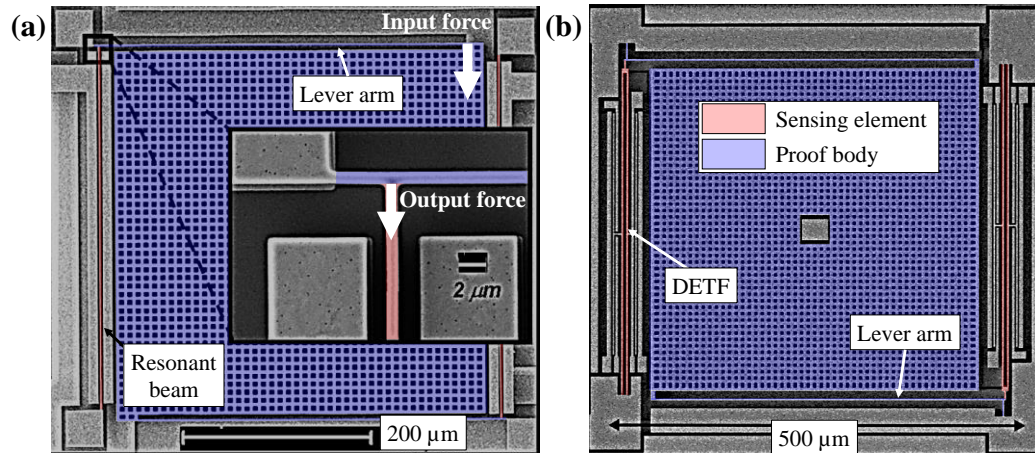


Figure 1-9 Resonant beam accelerometers with capacitive transduction. (a) The resonant beam is a simple beam [56]. The acceleration force of the proof mass is transmitted as an input force in the lever arm. The resonant beam receives the amplified output at the end of the lever arm. (b) The resonant beam is a DETF [57], and the amplification mechanism is similar.

In general, there are two ways to transduce the resonant micro-beam motion. The first is to use conventional capacitive sensing, as shown in Figure 1-9, to measure the resonance frequency of the vibrating beam. This transduction has the advantage of being easily implemented in industrial manufacturing processes. However, it suffers from parasitic capacitances that can be problematic at the working frequencies of resonant beams and require suitable readout electronics. Another less common method is the piezoelectric transduction presented in Figure 1-10. The piezoelectric material make it easy to actuate/detect useful vibrations at high working frequencies. However, this technology is still largely incompatible with large-scale manufacturing processes. In conclusion, the resonant beam accelerometer has the advantage of presenting a very good scale factor, but they require materials with excellent mechanical quality and the control of the resonant beam size by micromechanical fabrication.

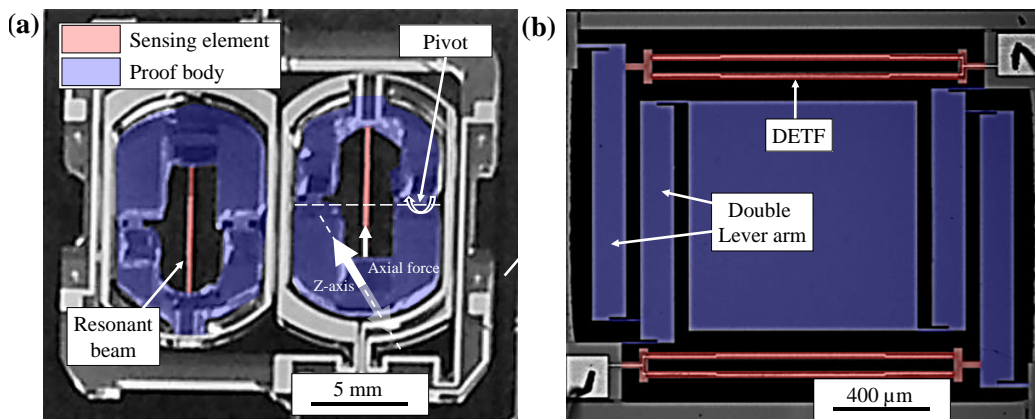


Figure 1-10 Resonant beam accelerometer with piezoresistive transduction. (a) The resonant beam is a simple beam. The ONERA architecture acts out-of-plane. A thickness reduction of its mass in its center gives it a pivot characteristic that allows to axially stress the resonant beam under the effect of an acceleration [47]. (b) The resonant beam is a DETF and the accelerometer is based on double lever arm mechanism [58].

1.3.3 Single-layer trade-offs

To illustrate the single layer trade-offs of resonant beam accelerometers, a comparison with capacitive accelerometers is presented. In the simplest representation, an accelerometer consists of a suspended mass M guided by bending elements represented by a stiffness K_{eq} and associated with the damping coefficient b_m (Table 3). In this configuration, the accelerometer can be associated with a resonance frequency ω_{0m} and an intrinsic acceleration resolution imposed by the thermomechanical noise of the system $a_{min,m}$. Already, the accelerometer suffers from a trade-off between resolution and bandwidth imposed by these accelerometer characteristics. If the bandwidth of the accelerometer is increased, its thermomechanical noise is also augmented (section 2.4.2). On the other hand, the increase of the proof mass allows reducing the thermomechanical noise at the cost of the bandwidth and the footprint. However, in recent years, sub- μg accelerometers have been developed [59] thanks to improved wafer-level packaging and a closed-loop control system that guarantee high quality factors and stability, respectively. In this way, the thermomechanical noise of the accelerometer $a_{min,m}$ is reduced and the resolution of the accelerometer is fixed by its transduction method. However, the sensitivity of the displacement (or, equivalently, force) to an acceleration S_a is the ratio of the effective proof mass M to the effective stiffness K_{eq} . Thus, there is a trade-off here between the displacement (force) sensitivity and the bandwidth of the accelerometer.

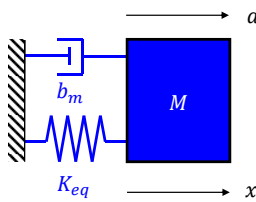
Architecture	General
Schematic	
Accelerometer resonance	$\omega_{0m} = \sqrt{\frac{K_{eq}}{M}}$
Thermomechanical resolution	$a_{min,m} \propto \sqrt{\frac{\omega_{0m}}{M}}$
Accelerometer sensitivity	$S_a = \frac{\partial x}{\partial a} = \frac{M}{K_{eq}}$

Table 3. General characteristics of an accelerometer. The accelerometer can be represented as a damped spring-mass system where the effective stiffness depends on the suspension stiffness and stiffness added by transduction method. The proof mass is guided on the x axis when an axial acceleration a is applied. The natural resonance frequency ω_{0m} , the thermomechanical resolution $a_{min,m}$ and the accelerometer sensitivity S_a depend on the effective stiffness K_{eq} and effective proof mass M .

The transduction method consists in using a sensitive element to transform the displacement of the standard mass into a physical quantity. The sensitivity of the physical quantity to the displacement S_s as well as the minimum measurable physical quantity, i.e. the detection limit, are characteristics of the method. The detection limit of the sensing element can be related to the acceleration resolution $a_{min,s}$ by the two system sensitivities S_a and S_s . In addition, the transduction method has an impact on the mechanical system, including its stiffness. The equivalent stiffness of the accelerometer is then expressed as a function of the stiffness of the suspension element k_{ff} and the stiffness added by the sensing element. In Table 4 and Table 5, the impact of two different transduction methods is discussed.

The capacitive transduction method consists in measuring the capacitance change ∂C due to the displacement change ∂x , i.e. $S_s = \partial C / \partial x$. The capacitive sensitivity depends on the coupling area S_e and the electrode gap g_e . In addition, the capacitive coupling adds a negative stiffness k_e to the system. In this case, the equivalent stiffness consists of the bending stiffness of the suspension element k_{ff} reduced by k_e . In general, the ratio of k_e to k_{ff} is negligible and thus the equivalent stiffness K_{eq} is proportional to k_{ff} . The equivalent resolution of the acceleration imposed by the sensitive element $a_{min,s}$ is due to the minimum measurable capacitance C_{min} and the sensitivities S_a and S_s . In this configuration, the bandwidth and resolution of the accelerometer are proportional to the ratio of k_{ff} to M (Table 5). In theory, the resolution can be improved independently of the bandwidth through the capacitive transduction parameters S_e and g_e . However, the minimum gap is usually imposed by the technological process and maximizing the coupling area is usually at the expense of the footprint. In this way, the single-layer capacitive accelerometer suffers from a trade-off between footprint and resolution.

Architecture	Capacitive accelerometer	Resonant beam accelerometer
Schematics		
Effective stiffness	$K_{eq} \propto k_{ff} \left(1 - \frac{k_e}{k_{ff}} \right)$	$K_{eq} \propto k_{ff} \left(1 + \frac{k_{rc}}{k_{ff} LA^2} \right)$
Sensing sensitivity	$S_s = \frac{\partial C}{\partial x} \propto \frac{S_e}{g_e^2}$	$S_s = \frac{\partial \sigma}{\partial x} \propto \frac{1}{S_r LA}$
Sensing resolution	$a_{min,s} = \frac{C_{min}}{S_a S_s}$	$a_{min,s} = \frac{\sigma_{min}}{S_a S_s}$

Table 4. Comparison between capacitive and resonant beam accelerometers. The capacitive transduction induces a small negative stiffness ($k_e \ll k_{ff}$) and presents a minimum measurable capacitance C_{min} due to electronic noises. Resonant beam detection induces a high compressive stiffness, which is generally balanced by the leverage effect $k_{rc}/LA^2 \ll k_{ff}$. It presents a minimum measurable stress σ_{min} due to electronic and mechanical noises.

Architecture	Capacitive accelerometer	Resonant beam accelerometer
Accelerometer resonance	$\omega_{0m} = \sqrt{\frac{k_{ff}}{M}}$	$\omega_{0m} \propto \sqrt{\frac{k_{ff}}{M}}$
Sensing resolution	$a_{min,s} \propto \frac{k_{ff}}{M} \left[\frac{g_e^2}{S_e} \right]$	$a_{min,s} \propto \frac{k_{ff}}{M} [S_r LA]$

Table 5. Comparison of capacitive accelerometers and resonant beam accelerometers neglecting the noise contribution of the proof mass. For the capacitance accelerometer the resonance frequency and sensing resolution depend both on the suspension stiffness k_{ff} and the effective proof mass M . But sensing resolution can be set by the capacitive transduction parameters g and S_e . Similarly, for a resonant beam accelerometer the accelerometer resonance and sensing resolution depend both on the suspension stiffness k_{ff} and the effective proof mass M . But sensing resolution can be set by the lever arm mechanism LA and the resonant beam cross-section S_r .

Alternatively, the resonant beam transduction method consists in measuring the stress variation $\partial\sigma$ due to the displacement variation ∂x , i.e. $S_s = \partial\sigma/\partial x$. The stress sensitivity depends on the sensing element's cross-section S_r and the lever arm mechanism LA . In addition, the sensing element adds its compressive stiffness balanced by the lever arm effect in parallel to the stiffness of the suspended element k_{ff} . In general, the ratio of k_{rc}/LA^2 to k_{ff} is negligible thus the equivalent stiffness K_{eq} is proportional to k_{ff} . The equivalent acceleration resolution imposed by the sensing element $a_{min,s}$ is limited by the minimum measurable stress σ_{min} and the sensitivities S_a and S_s . In this configuration, the bandwidth and resolution of the accelerometer are proportional to the ratio of k_{ff} to M (Table 5). In theory, the resolution can be improved independently of the bandwidth through the mechanical transduction parameters S_r and LA . However, the minimum cross section S_r is usually imposed by the technological process and maximizing the lever arm mechanism is usually at the expense of the footprint. In this way, the single-layer resonant beam accelerometer also suffers from a trade-off between footprint and resolution.

In conclusion, Single-layer accelerometers suffer from fabrication limitations imposed by critical dimensions (CD), which limit the sensitivity of sensing element (electrode gap and resonant beam cross-section). Thus, sub- μg accelerometers achieve high resolution by increasing their mass or softening their structure at the cost of their bandwidth. This is the first trade-off of single layer accelerometers. However, there are mechanisms to overcome this, such as multiple electrode combs or lever arm mechanisms. However, these mechanisms are costly in terms of space and impose a second compromise between resolution and footprint.

Sub- μg resonant beam accelerometers are mainly based on a single-layer fabrication process. Figure 1-11 (a) and (b) represent respectively the resolution-bandwidth and resolution footprint trade-off for 8 recent sub- μg resonant beam accelerometers based on a single-layer fabrication process.

The ability to measure acceleration is highlighted by the Bandwidth / Noise density ratio, while integrability is defined by the sensor footprint. The performance of these sub- μg resonant beam accelerometers are detailed in Table 6 and can be highlighted by the figure of merit (FOM_{tot}) :

$$FOM_{tot} = \frac{\text{Bandwidth}}{\text{Noise density} \times \text{Footprint}} \left[\frac{\text{Hz}}{\mu\text{g}/\sqrt{\text{Hz}} \times \text{mm}^2} \right] \quad 1-2$$

The resonant beam architecture is a promising candidate for a high performance integrated sensor. Because the scale factor depends on the cross section of the resonator, a reasonable mass can be used to achieve high performance. Currently, sub- μg resonant beam accelerometers are mainly made of millimetric masses ($>1 \text{ mm}^2$) and low bandwidth ($<1 \text{ kHz}$) which makes them promising candidates for gravimetry in particular. However, high-frequency applications, such as condition monitoring, or small footprints for consumer applications are excluded. Sub- μg resonant beam accelerometers are therefore reserved for a very limited range of applications. Our objective here is to extend the use of these accelerometers by proposing more sensitive structures using a multi-layer manufacturing process.

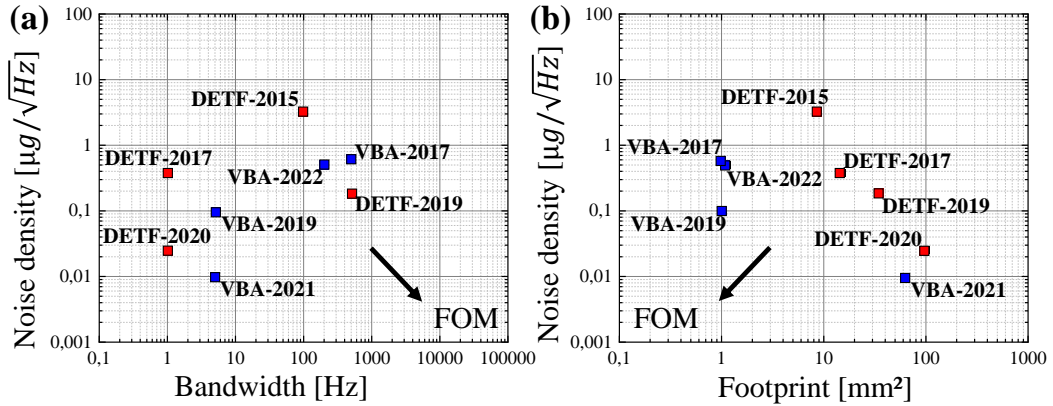


Figure 1-11. Representation of the trade-offs of sub- μg resonant beam accelerometers based on a single-layer fabrication process. (a) Resolution-bandwidth trade-off. (b) Footprint-resolution trade-off. VBA accelerometers (blue) are based on a single resonant beam while DETF accelerometers (red) are based on a double-ended tuning fork. Both FOMs are improved for low resolution, high bandwidth and small footprint.

Ref & Type	Noise [$\mu\text{g}/\sqrt{\text{Hz}}$]	Bandwidth [Hz]	Footprint [mm^2]	FOM_{tot}
[54] <i>Kenny at al.</i> VBA-2017	0.6	500	1	833
[60] <i>SMG-gen2</i> VBA-2022	0.5	200	~ 1.13	353
[52] <i>Han at al.</i> DETF-2019	0.18	500	35	79
[55] <i>Zaho at al.</i> VBA-2019	0.098	5	>1	51
[49] <i>Seshia at al.</i> VBA-2021	0.01	5	64	7.81
[61] <i>Seshia at al.</i> DETF-2015	3.22	100	8.68	3.57
[62] <i>Seshia at al.</i> DETF-2020	0.025	1	<100	0.4

Table 6. Comparison of the state of the art of sub- μg resonant beam accelerometers based on single-layer fabrication process.

1.4 *M&NEMS* technology

All the sensors designed in this thesis are based on the so-called '*M&NEMS* technology'. Based on a multi-layer fabrication process, the concept is to create a sensor with mechanical parts of very different dimensions using two different silicon thicknesses: a thin layer allows defining nanogauges with piezoresistive properties, and a thick layer that constitutes the proof mass and the flexible elements. This approach has been presented as new solution for low-cost inertial sensors in 2009 [22] and has allowed to overcome single-layer trade-offs for capacitive accelerometers [63].

The use of nanogauges allows for a high stress concentration, which in this case transforms the stress into resistance changes due to the piezoresistive properties. The use of high stress concentration is also a particular advantage for the use of the resonant beam as a force sensor. Indeed, the sensitivity of the resonant sensing S_s increases with decreasing resonant beam cross-section, as shown in Table 4. This concept thus enables high-sensitivity sensors with a small mechanical footprint. In addition, it is compatible with large-scale VLSI processes, which could extend the applications of resonant beam accelerometers to industrial needs for low-cost inertial sensors.

Moreover, the uncentred position of the thin layer relative to the thick layer allows the development of out-of-plane accelerometers as well as pressure sensors [64]. In addition, the compatibility of the technology with gyroscopes [65] and magnetometers [66] makes this technology a promising solution towards compact inertial units

The development of the first generation of resonant nano-beam accelerometer aims at proposing a sub- μg accelerometer with high bandwidth and small footprint. On one hand, the high sensitivity of the nanogauge-based accelerometer coupled with a pendular architecture allows to address structures smaller than mm^2 and with high bandwidth [67]. On the other hand, the piezoresistive properties of the thin film allow to build high-performance nanoresonators, as presented in section 1.3.1, which ensures a high-performance accelerometer. Indeed, nanoresonators work at high frequencies and have small surfaces that make capacitive detection difficult. Piezoresistive nanogauges take advantage of the small cross-sectional and are therefore the ideal transducer for this type of application.

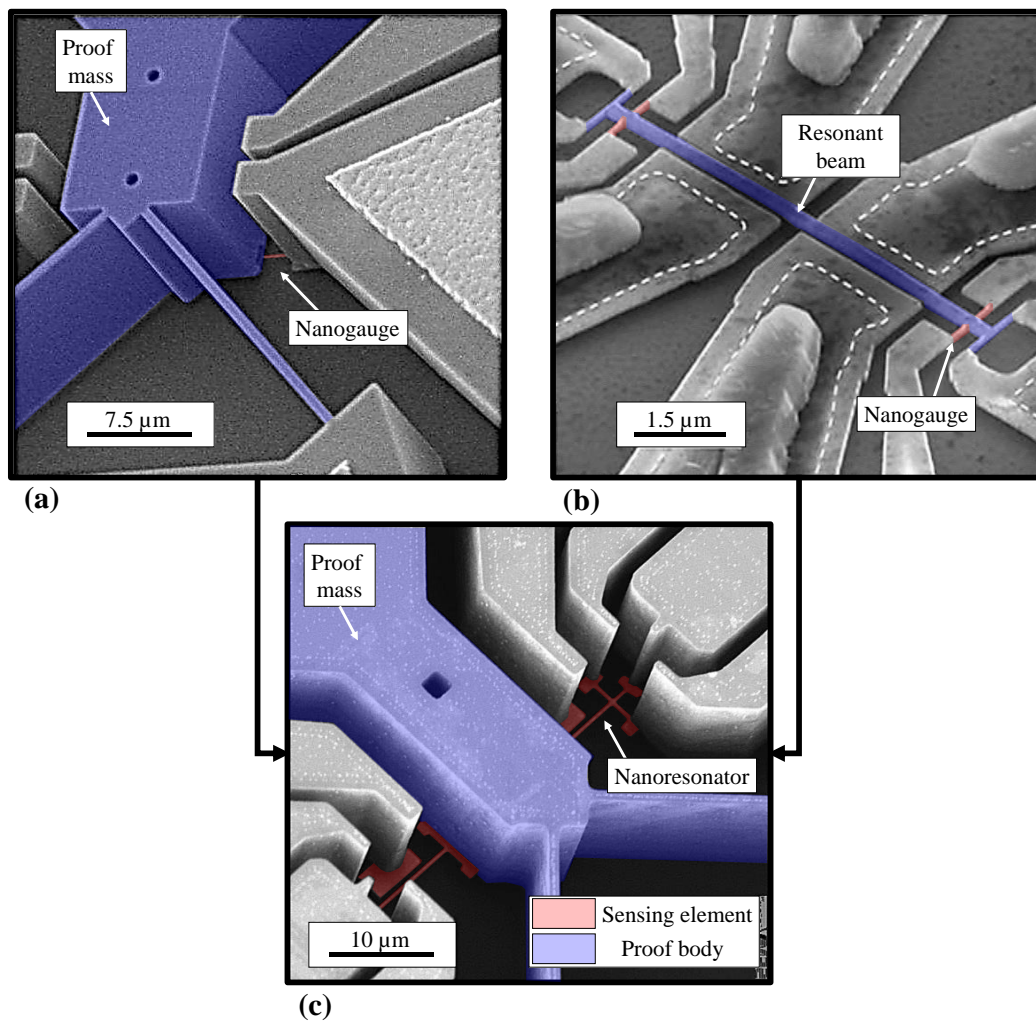


Figure 1-12. Representation of the capabilities of the M&NEMS technology. (a) Static accelerometer realized with M&NEMS technology is composed of a micrometric proof mass and a nanogauge sensing element. (b) A nanoresonator-based mass sensor consists of a resonant beam and nanogauges. Here, both are etched on the nanometric layer. (c) combination of M&NEMS proof mass with piezoresistive nanoresonators.

2 Electromechanical modelling

Resonant accelerometers detect the acceleration through variations of resonance frequency. This chapter presents the theoretical principles of accelerometers using a resonant beam as force sensor. In this configuration, the resonant beam is the sensing element that transduces the acceleration into a variation of resonance frequency. This resonant accelerometer architecture is called resonant beam accelerometer. In this work resonant beams are of nanometric dimensions, and therefore they are called nanoresonators.

Figure 2-1 represents the operation of this inertial sensor. The resonant beam is the hub of the acceleration detection. On one hand, an actuation force F_{act} maintains the resonant beam oscillation at its first bending mode frequency ω_r , and its motion is transduced into an output voltage V_{out} . On the other hand, the accelerometer modulates the beam resonance frequency through an axial stress σ_r induced by an acceleration a . The measurement of the output voltage allows detecting resonance frequency variations, thus measuring the acceleration.

The accelerometer transforms an acceleration into an axial stress on the nanoresonator.

The nanoresonator used as force sensor undergoes a variation of resonance frequency caused by that axial stress (see above).

In our particular case, **the nanoresonator** is electrostatically actuated and its resulting mechanical motion is piezoresistively detected. A resonance frequency **measurement** is performed in real time to track its variations, in particular the ones induced by the acceleration-related axial stress (goal / principle of the sensor).

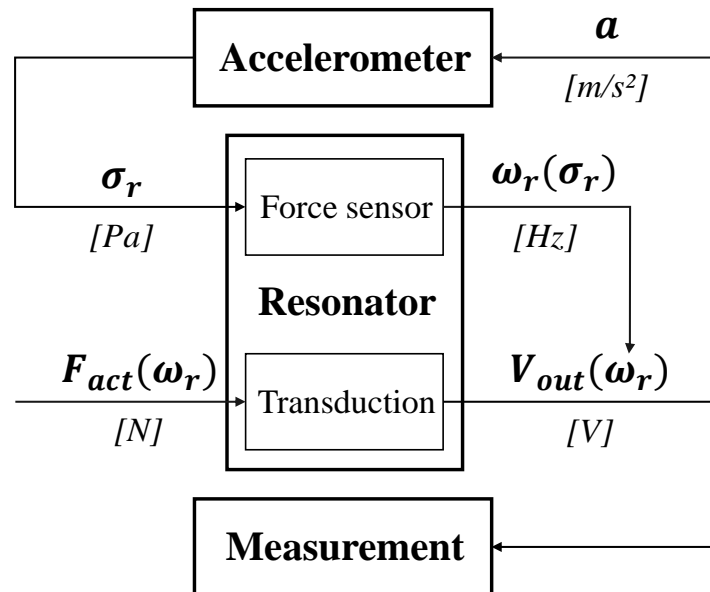


Figure 2-1 Principle of resonant beam accelerometers using nanoresonators as force sensors.

2.1 Transduction chain of the accelerometer

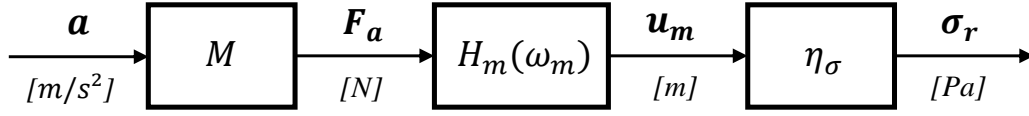


Figure 2-2 Principle of the accelerometer transduction chain: the acceleration generates a force, which is transduced into a stress on the nanoresonator.

This section provides the theoretical notions of the accelerometer's transduction chain. It aims at understanding the transduction of the acceleration into stress on the nanoresonator. Figure 2-2 shows the block diagram of the accelerometer transduction. The proof mass M , put into motion by an acceleration a , generates a force F_a . The mechanical response of the accelerometer is represented by the transfer function H_M dependent on the acceleration pulsation ω_m . The input force applied on the system is transformed into a proof mass displacement u_m . The mechanical gain η_σ represents the transduction of the proof mass displacement to an axial stress applied on the nanoresonator.

An example of a simplified accelerometer architecture is described on Figure 2-3 (a). A proof mass is suspended by flexible springs and connected to a nanoresonator. Here the flexible springs consist of bending beams to allow movement in the desired direction (x) and block unwanted movement in the orthogonal directions (y, z). The nanoresonator consists of a beam used in compression / tension, and is used to detect the proof mass movement.

The accelerometer can be represented by a damped spring-mass system. Because the mechanical response of the system is studied before its first resonance mode, the strain energy is concentrated in the flexible elements while the kinetic energy is concentrated in the proof mass. On this configuration, Figure 2-3 (b) reduces the system stiffness to the flexural stiffness of the flexible springs k_{ff} , and the compressive stiffness of the nanoresonator k_{rc} . The effective mass M represents the proof mass and the damping coefficient b_m represents the losses associated to the accelerometer environment.

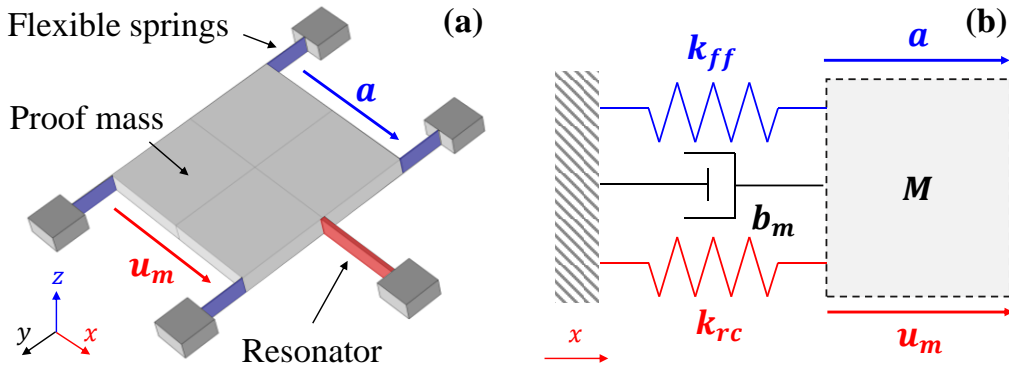


Figure 2-3 (a) Architecture of the accelerometer. (b) Schematic representation of the accelerometer as a damped spring-mass system.

The dynamics of the equivalent damped spring-mass model can be expressed by the Newton Principle:

$$M\ddot{u}_m + b_m\dot{u}_m + (k_{rc} + k_{ff})u_m = F_a \quad 2-1$$

From the equation of motion of the accelerometer, the transfer function of the accelerometer can be expressed as a function of the acceleration pulsation:

$$H_m(\omega_m) = \frac{1}{k_{ff} + k_{rc}} \frac{1}{1 + j \frac{\omega_m}{\omega_{0m} Q_m} + \left(j \frac{\omega_m}{\omega_{0m}}\right)^2} \left[\frac{m}{N} \right] \quad 2-2$$

where $\omega_{0m}^2 = (k_{ff} + k_{rc})/M$ is the fundamental pulsation of the system, called the resonance, and $Q_m = M\omega_{0m}/b_m$ represents the energy lost per cycle, called the quality factor. At resonance ($\omega_m = \omega_{0m}$) the output displacement is the static gain amplified by the quality factor $H_m = Q_m/(k_{ff} + k_{rc})$. The resonance of the accelerometer has interesting properties but is not used here as a detection mechanism, and it is considered to depend weakly on the acceleration. The frequency range higher than resonance ($\omega_m > \omega_{0m}$) is not efficient for performance transduction, due to the filtering of the output signal. Thus, the ideal frequency operation is the quasi-static regime ($\omega_m < \omega_{0m}$) where the output displacement is expressed by the static gain $H_m = 1/(k_{ff} + k_{rc})$. The resonance frequency of the system (ω_{0m}) is therefore defined as the bandwidth of the accelerometer.

The nanoresonator performs the measurement of the displacement of the proof mass. In fact, one of its extremities is fixed to the proof mass and the other one is clamped to the substrate, so that the sensing element is deformed by the displacement of the proof mass. Because the beam is oriented parallel to the direction of motion, the deformation causes an axial stress along the nanoresonator. The mechanical gain

$$\eta_\sigma = \frac{k_{rc}}{S_r} \left[\frac{N}{m^3} \right] \quad 2-3$$

describes this effect, where S_r is the section of the nanoresonator. The static gain between acceleration and axial stress on the nanoresonator is given by:

$$S_{\sigma a} = \rho t_m \left[\frac{S_m}{S_r} \right] \left[\frac{k_{rc}}{k_{ff} + k_{rc}} \right] \left[\frac{k_g}{m^2} \right] \quad 2-4$$

where t_m , S_m and ρ are respectively the proof mass thickness, footprint and density. Therefore the nanoresonator has several effects on the properties of the accelerometer: a large area ratio S_m/S_r improves the accelerometer's sensitivity at the detriment of its bandwidth ω_{0m} . The next part is focused on the internal dynamics of the sensing element, and especially how it is affected by the axial stress caused by the acceleration.

2.2 Nanoresonator used as force sensor

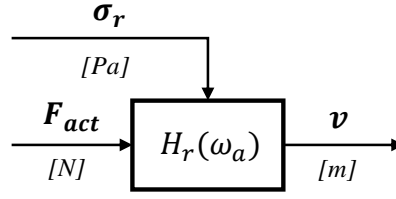


Figure 2-4 Principle of the nanoresonator used as force sensor. The driven nanoresonator undergoes an input axial stress.

This section describes the modelling of a doubly-clamped beam affected by an axial stress. Figure 2-4 schematizes the different parameters of the nanoresonator dynamics. The mechanical response H_r of a doubly-clamped beam transforms the actuation force F_{act} applied on the beam into a displacement at the central node of the beam v . The transfer function depends on the actuation frequency ω_a . The axial stress σ_r applied on the beam affects the mechanical response of the structure.

The nanoresonator is a passive system that requires an energy input. Once loaded, the nanoresonator cyclically transforms elastic energy into kinetic energy. Its effective stiffness and mass represent respectively the amount of kinetic energy and strain energy stored by the system. The duration of the cycle, characterised by the resonance frequency of the system, depends on its stiffness and mass. The principle of the nanoresonator used as a force sensor is to take advantage of the applied stress to modify the stiffness of the structure and therefore its resonance frequency. By monitoring the resonance frequency variations, the stress applied on the beam can be measured. Here the nanoresonator is an ideal double clamped beam. The force sensing mechanism is modelled with the damped spring-mass system of Figure 2-5 (a) where the spring $k_{rf}(\sigma_r)$ is the bending stiffness of the beam modulated by the axial stress σ_r and m_r its effective mass. In reality, the presence of losses dissipates the energy initially supplied to the nanoresonator that is represented by damping coefficient b_r .

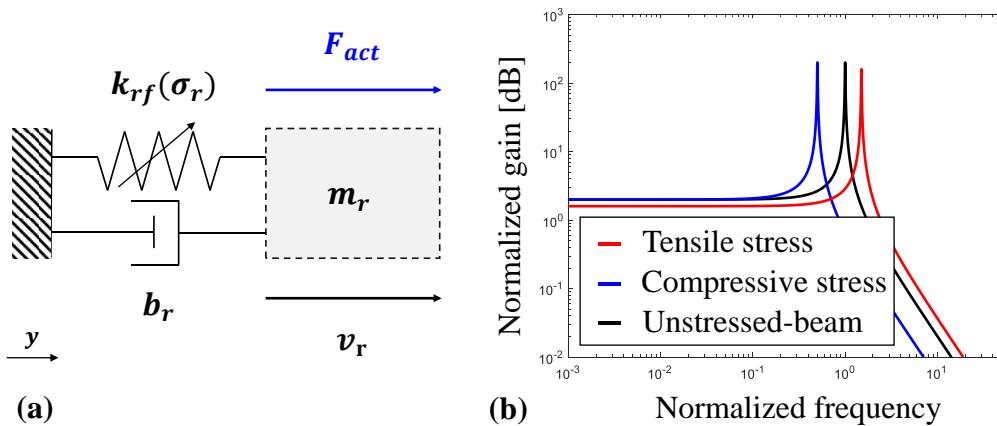


Figure 2-5 Modelling of a doubly clamped beam. (a) Equivalent damped spring-mass system. (b) Transfer function of a nanoresonator used as force sensor.

The transfer function of a doubly-clamped beam can be reduced to familiar harmonic resonator expressed as a function of the actuation frequency ω_a :

$$H_r(\omega_a) = \frac{1}{k_{rf}} \frac{1}{1 + j \frac{\omega_a}{\omega_r Q_r} + \left(j \frac{\omega_a}{\omega_r}\right)^2} \left[\frac{m}{N}\right] \quad 2-5$$

where $\omega_r^2 = k_{rf}/m_r$ is the fundamental pulsation of the system, called the resonance, and $Q_r = m_r \omega_r / b_r$ is the quality factor of the system that represents the energy lost per cycle. In a conceptual approach, Figure 2-5 (b) represents the operation of doubly-clamped beam used as force sensor. Because compressive stress reduces effective stiffness and tensile stress increases it, the resonance frequency follows the same behaviour.

The objective of using a nanoresonator as force sensor is to measure the axial stress applied on the beam. Similarly to the accelerometer system, the frequency range higher than resonance ($\omega_a > \omega_r$) is not efficient for performance measurement, due to the filtering of the frequency response. The frequency range lower than resonance ($\omega_a < \omega_r$) has interesting properties because the static gain $H_r = 1/k_{rf}(\omega_r)$ is modulated by the axial stress. In our case, the use of amplitude measurement as a detection mechanism is not considered efficient because the signal to noise ratio is not very high. However, the measurement of the resonance frequency ($\omega_a = \omega_r$) has interesting properties for the measurement. In addition to having an amplitude amplification $H_r = Q_r/k_{rf}(\omega_r)$ of the signal, the phase-frequency relationship can be linearized as $\delta\omega = [\omega_{0r}/2Q_r] \delta\varphi$ in a limited frequency range around the resonance. Around this operating point, resonance frequency variations can be directly deduced from phase variations when driving the nanoresonator with a fixed actuation frequency. Figure 2-6 shows the impact of axial stress on the phase. When the nanoresonator is driven at a fixed frequency close to resonance, axial stress induces a phase shift proportional to $\pm f_r/2Q_r$, where $\omega_r = 2\pi f_r$. Having pre-measured the quality factor of the system, the frequency measurement can be deduced from the phase measurement.

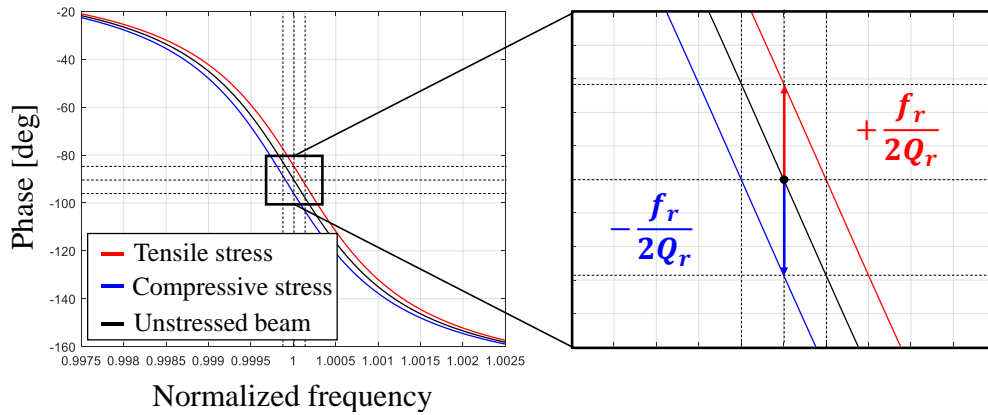


Figure 2-6 Phase response of a nanoresonator as a function of axial stress. Because the resonance frequency of the system shifts, phase measurements at a fixed actuation frequency can be processed to deduce the resonance frequency variations.

2.2.1 Formulation of the equation of motion

The equation of motion of a stressed beam is studied in this section. The variational approach considerably simplifies the analytical formulation of the equation of motion. It is appropriate to begin by a kinematic description of the bending motion in order to express the kinetic energy (1). Then, to express the strain energy of the system, the elasticity theory for small deformations is necessary (2). In order to illustrate the beam used as force sensor, the case of an initial stress is treated separately to complement the strain energies of the system (3). The actuation forces that maintain the oscillation of the system are considered as external forces (4). Finally, to complete the equation of motion, the boundary conditions are defined.

First, the description of the bending motion must be defined according to the beam theory: for negligible length-width ratios in the beam ($w_r/L_r \ll 1$), with w_r and L_r respectively the beam width and length, its cross-section is not deformable, so it remains orthogonal to the neutral axis. This assumption is equivalent to neglecting the shear deformation of the material. These assumptions, called the Bernoulli assumptions, are illustrated in Figure 2-7 by the kinematic description: the flexural motion $v_r(x)$ depends on the position along the neutral axis and has a maximum in the central node of the beam $v_r(L_r/2) = v$. This neutral axis is defined for a null orthogonal position $y = 0$. The rotation of the cross-section is the derivative of flexural motion $\theta_r(x) = \partial v_r / \partial x$. The axial displacement results from the rotation of the cross-section and the distance y from the neutral axis, $u_r(x, y) = -y \theta_r(x)$.

(1) In accordance with these assumptions, the rotational inertia of the cross-section is negligible. It is consistent that the kinetic energy for vertical translation describes the kinetic energy of the system:

$$\mathcal{T} = \frac{1}{2} \int_0^{L_r} \rho S_r \left(\frac{\partial v_r}{\partial t} \right)^2 dx \quad [J] \quad 2-6$$

where ρ is the density of the beam material.

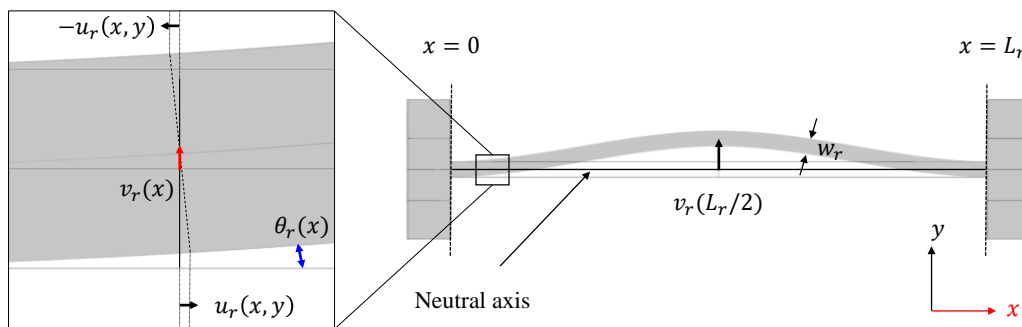


Figure 2-7 Kinematic description of the bending motion of a doubly clamped beam according to the Bernoulli's assumptions.

(2) In the small deformation regime, the linear term in the displacement is sufficient to define the axial strain $\epsilon_x = \partial u_r / \partial x$. In addition, the linear theory of elasticity completes the kinematic description. This theory assumes that the stress remains proportional to the strain. Thus, according to the elasticity coefficients of an anisotropic material, the elastic energy \mathcal{V}_{int} can be expressed as:

$$\mathcal{V}_{int} = \frac{1}{2} \int_0^{L_r} EI \left(\frac{\partial^2 v_r}{\partial x^2} \right)^2 dx \quad [\text{J}] \quad 2-7$$

where E is the Young modulus of the anisotropic material, and I is the quadratic moment of the beam section.

(3) In our case, the beam undergoes a stress, which has to be taken into account. In this configuration, the strain definition is supplemented by an initial strain ϵ_r , due to the initial stress, and therefore the small deformation regime no longer describes the movement. For large initial strain, it is necessary to take into account the nonlinear effects induced by the main quadratic term in the displacement: $\epsilon_x \cong \epsilon_r + \partial u_r / \partial x + (\partial v_r / \partial x)^2$. The Geradin's description [68] completes the elastic energy by an additional energy \mathcal{V}_g when the beam is submitted to initial axial stress σ_r

$$\mathcal{V}_g = \frac{1}{2} \int_0^{L_r} \sigma_r S_r \left(\frac{\partial v_r}{\partial x} \right)^2 dx \quad [\text{J}] \quad 2-8$$

(4) In order to compute the potential energy of the external force F_{act} , the beam is subjected to a distributed vertical load $\overline{F_{act}}$ per unit length. When the force operates on the whole beam, the potential energy of external load is

$$\mathcal{V}_{ext} = - \int_0^{L_r} \overline{F_{act}} v_r dx \quad [\text{J}] \quad 2-9$$

(5) The problem can now be discussed reduced to an in-plane description. The rotation and transverse motion are the degrees of freedom of the anchors. The reaction forces associated to the anchors are localized at both sides of the beam $x = 0$ and $x = L_r$. The work developed by the reaction forces associated to their degrees of freedom, respectively the moment M and transverse force T , are:

$$\delta W = [T(x)v_r(x)]_{x=0,L_r} + [M(x)\theta_r(x)]_{x=0,L_r} \quad [\text{J}] \quad 2-10$$

The problem of a pre-stressed beam can be described in its entirety by the previous potentials and works. The description of the dominant potential allows expressing the Lagrangian $L = \mathcal{T} + \mathcal{V}_{int} + \mathcal{V}_g + \mathcal{V}_{ext}$ of the system. The degrees of freedom allow expressing the work of the reaction force δW for generic boundary conditions. The description of the Lagrangian and works aims at implementing the variational principle. In the final part, this approach, called Hamilton's principle, is used to formulate the global equations of motion of the system.

The strength of Hamilton's principle is that it deals with all aspects of the system in a single equation. The derivative of the equilibrium equation is detailed in [68]. The resulting formulation allows discerning two physics of a beam in bending: on one hand, the internal dynamics of the element, on the other hand, the impact of the boundary conditions. The first one highlights the equation of motion of stressed beams. Here it is relevant to add a damping term to this equation, which comes from the losses represented by b_r introduced in the damped spring-mass system in Figure 2-5:

$$\rho S_r \frac{\partial^2 v_r(x, t)}{\partial t^2} + \frac{b_r}{L_r} \frac{\partial v_r(x, t)}{\partial t} + EI \frac{\partial^4 v_r(x, t)}{\partial x^4} + \sigma_r S_r \frac{\partial^2 v_r(x, t)}{\partial x^2} = \overline{F_{act}} \quad 2-11$$

This formulation allows observing the contributions of the different terms involved in the equation. The first term represents the kinetics of the system, the second term represent the losses of the system and the last two terms represents the elasticity of the system. Then, the modal analysis of the homogeneous equation, developed in section 2.2.2, allows identifying the modulated stiffness from the elasticity block and thus, to reduce the equation of motion to a characteristic equation of a damped spring-mass system.

Because the equation of motion has an infinite number of solutions, boundary conditions are necessary to solve the modal analysis. The Hamilton's principle allows expressing the equation of motion and the reaction to the boundaries. In other words, it considers at the same time how the degrees of freedom affect the bending motion or how the bending motion affects the associated reactions. From the same derivative of the equilibrium equation (detailed in [68]), the boundary conditions based on the kinematic description of the Eq. 2-10 are:

$$\begin{cases} v_r(x = 0, L_r) = v_{0,L_r} \\ \theta_r(x = 0, L_r) = \theta_{0,L_r} \end{cases} \text{ or } \begin{cases} EI \frac{\partial^3 v_r}{\partial x^3} + \sigma_r S_r \frac{\partial v_r}{\partial x} = \pm T_{0,L_r} \\ EI \frac{\partial^2 v_r}{\partial x^2} = \pm M_{0,L_r} \end{cases} \quad 2-12$$

These boundary equations allow determining a unique solution of the equation of motion for specific boundary conditions. The boundary conditions can be introduced in two ways. (i) The degrees of freedom can be associated to the boundary, v_{0,L_r} and θ_{0,L_r} . The beam is then free and it does not have reactions at its borders ($T_{0,L_r} = 0$ and $M_{0,L_r} = 0$), but it has a unique solution of its equation of motion. (ii) The boundaries are fixed, $v_{0,L_r} = 0$ and $\theta_{0,L_r} = 0$. Here the beam is clamped and reaction terms appear at its borders (T_{0,L_r} and M_{0,L_r}), setting a unique solution of its equation of motion.

With the global equations (equation of motion + boundary conditions), the modal analysis can be tackled in order to express the closed-form expression of the resonance frequency of a stressed-beam.

2.2.2 Modal analysis

The aim of this section is to determine a closed-form expression for the first in-plane bending mode as a function of stress. In this way, a closed-form expression of the bending stiffness can be deduced. This will allow introducing the stress-induced frequency and amplitude variations as a modulated stiffness in the model of Figure 2-5. The expression of the eigenfrequency as a function of the axial stress can be solved numerically using an eigenvector approach [69]. However, a closed-form expression of the frequencies can be expressed using an energy approach under certain assumptions. This closed-form expression is compared with the numerical approach in order to express the validity of these assumptions.

The eigenvector approach starts by separating the equation of motion into two equations: one temporal, the other spatial. The separation of variables allows defining v_r as the product of a normalized spatial function $\overline{W}_0(x)$ associated to the first bending mode and a temporal function $v(t)$. Substituting this equation in Eq. 2-11 gives an equality between two equation of the different function: $v(t)$ and $\overline{W}_0(x)$. It is usual for this technique to set each function equal to $-\omega_r^2$ [70] in order to express the two ordinary differential equations of the first in-plane mode

$$\begin{cases} \frac{d^2 v}{dt^2} + \left[\frac{b_r}{\rho S_r L_r} \right] \frac{dv}{dt} + [\omega_r^2] v = 0 & (A) \\ \frac{d^4 \overline{W}_0}{dx^4} - 2a \frac{d^2 \overline{W}_0}{dx^2} - k_0^4 \overline{W}_0 = 0 & (B) \end{cases} \quad 2-13$$

where $a = \sigma_r S_r L_r^2 / 2EI$ and $k_0^4 = \rho S_r \omega_r^2 L_r^4 / EI$ are respectively the eigenfunction and eigenvector associated to the eigenfrequency ω_r . The temporal equation (A) is the frequency response of the system associated to the eigenfrequency ω_r . The spatial equation (B) represents the normalized deformation of the beam associated with its eigenfrequency. Finding the solutions of the spatial equation for a specific set of boundary conditions allows deducing the associated eigenfrequency. The function $\overline{W}_0(x) = Ae^{i\lambda_0 x} + Be^{-i\lambda_0 x} + Ce^{\mu_0 x} + De^{-\mu_0 x}$, with $\mu_0 = [[a^2 + k_0^4]^{1/2} + a^{1/2}]$ and $\lambda_0 = [[a^2 + k_0^4]^{1/2} - a^{1/2}]$, is the general solution of the spatial equation. For doubly-clamped beams, the boundary condition $\overline{W}_0(0,1) = 0$ and $\overline{W}_0'(0,1) = 0$ allow expressing the characteristic equation as detailed in [71]. The solution of this characteristic equation is a specific set of eigenvectors as a function of the stress $k_0(\sigma_r)$. These eigenvectors allow the natural frequency to be approximated as a function of stress. Figure 2-8 (a) plots the characteristic equations as a function of different values of stress. The first intersection with zero represents the eigenvector associated to the first in-plane mode. Moreover, for these specific eigenvectors, non-trivial eigenfunctions, i.e. $(A, B, C, D) \neq (0, 0, 0, 0)$, are solutions of the spatial equation. In Figure 2-8 (b), the eigenfunction \overline{W}_0 is numerically estimated using the eigenvectors $k_0(\sigma_r)$. Thus, the eigenfunctions also depend on stress.

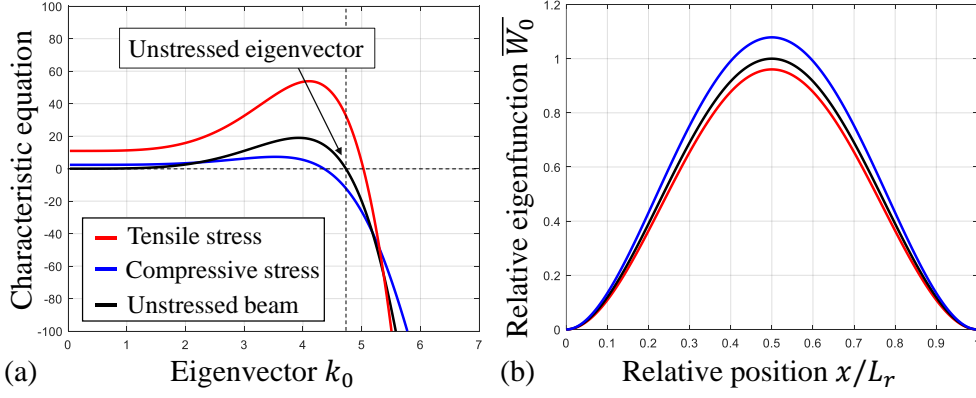


Figure 2-8. Representation of the characteristic equations and eigenfunctions for different axial stresses. (a) Characteristic equations as a function of the eigenvectors. The first zero of the equation is the eigenvector associated to the first in-plane mode. The Eigenvector is a unidimensional value. (b) Eigenfunctions as a function of relative position normalized by the unstressed eigenfunction.

By numerically solving the characteristic equations, the eigenvector and thus the natural frequency can be expressed as a function of the axial stress:

$$\omega_r^2(\sigma_r) = k_0^4(\sigma_r) \frac{EI}{\rho S_r L_r^4} [\text{Hz}] \quad 2-14$$

As detailed in the introduction, this numerical method is not efficient to provide a closed-form expression of the eigenfrequency as a function of the stress. That is why an approximate method, called the Rayleigh's method [70], is employed to express a closed-form of the natural frequency. This method is based on the assumption that the dynamic response of the beam of Eq. 2-13 (A) is not subject to damping ($b_r = 0$). Thus, the system vibrates sinusoidally at its natural frequency under the form $V(t) = |V| \sin(\omega_r t)$. In such an undamped spring-mass system, the conversion of mechanical energy takes place perfectly from elastic energy to kinetic energy. In other words, elastic energies are equal to kinetic energy $\mathcal{V}_g + \mathcal{V}_{int} = \mathcal{T}$. On the separation of variables approach, the beam motion v_r is the product of the eigenfunction $\overline{W}_0(x)$ and a temporal function $v(t)$. For an undamped system, substituting these terms in the energy equality allows expressing a closed form of the first in-plane eigenfrequency as a function of stress:

$$\omega_r^2(\sigma_r) = \alpha_0^4 \frac{EI}{\rho S_r L_r^4} \left(1 + \beta_0 \frac{S_r L_r^2}{EI} \sigma_r \right) [\text{Hz}] \quad 2-15$$

where α_0 and β_0 are coefficients depending on the eigenfunctions $\overline{W}_0(x)$:

$$\begin{cases} \alpha_0^4 = \left[\int_0^1 \left(\frac{\partial^2 \overline{W}_0(x)}{\partial x^2} \right)^2 dx \right] / \left[\int_0^1 \overline{W}_0^2(x) dx \right] [\mathbf{A} \cdot \mathbf{U}] \\ \beta_0 = \left[\int_0^1 \left(\frac{\partial \overline{W}_0(x)}{\partial x} \right)^2 dx \right] / \left[\int_0^1 \left(\frac{\partial^2 \overline{W}_0(x)}{\partial x^2} \right)^2 dx \right] [\mathbf{A} \cdot \mathbf{U}] \end{cases} \quad 2-16$$

This frequency expression is not a closed form neither. Indeed, the eigenfunction $\overline{W}_0(x)$ used to express the coefficients depends on the stress. Thus, coefficients themselves need a numerical approach to be expressed as a function of the stress. This energetic method is not effective neither to reach a closed-form of eigenfrequency.

However, supposing that the eigenfunction of a stressed beam is close to the eigenfunction of an unstressed beam solves the problem. In other words, it is assumed that the Duncan function is the general solution of the spatial equation. In this case, the coefficients do not depend on the stress and the closed-form expression of the eigenfrequency is reached. This approximate method raises a problem of validity: to what extent can it be assumed that a stress does not modify the beam function. Figure 2-9 compares the eigenfrequency as a function of stress for the three previous methods. The resonance frequency is normalized by the natural frequency $\omega_{0r} = \omega_r(\sigma_r = 0)$. The stress is normalized by the maximum allowable stress σ_{buck} defined in Eq. 2-18. As both the numerical method (1) and the Rayleigh's method (2) are based on the real spatial solution, they match perfectly and are considered to be the most realistic case. Because the Duncan's method (3) is based on an unstressed spatial solution, disparities appear for large values of stress. The inset quantifies the validity of Duncan's method (3) compared to the numerical method (1). The frequency vs stress function of Eq. 2-17, expressed from Eq. 2-15 and Duncan's method, is valid for a stress below $\pm 80\%$ of σ_{buck} because the approximation remains close to the most realistic case ($<5\%$).

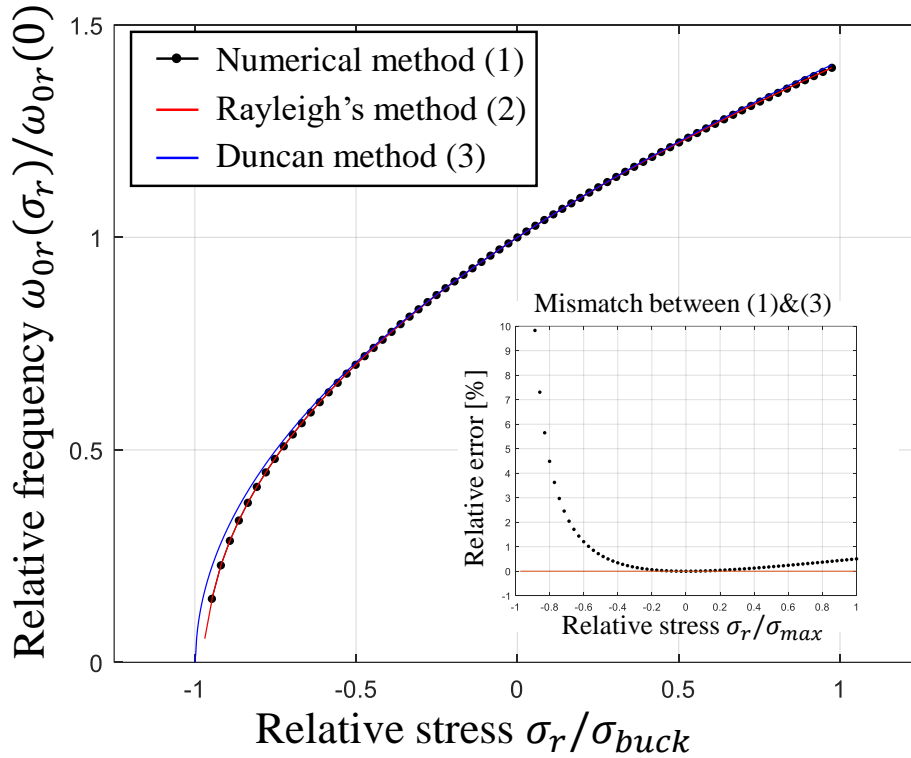


Figure 2-9. Relative frequency dependence upon relative axial stress, for a doubly-clamped beam. The inset shows the relative error between numerical method and Duncan's method.

Therefore, by using Duncan's method, the closed-form expression of the approximate eigenfrequency can be expressed as a function of the coefficient $\alpha_0^2 = 22.37$ and $\beta_0 = 0.0246$ calculated from the Equation 2-16. The resonance frequency can then be expressed as:

$$\omega_r(\sigma_r) = \omega_{0r} \sqrt{1 + \gamma \sigma_r} \quad [\text{Hz}] \quad 2-17$$

where $\omega_{0r} = \alpha_0^2 [EI / \rho S_r L_r^4]^{1/2}$ is the natural frequency in absence of stress and $\gamma = \beta_0 S_r L_r^2 / EI$ is the coefficient multiplying the stress σ_r . In order to provide tools for further analysis, this closed-form expression can be used to express the stress value that cancels the resonance frequency (i.e. the buckling limit):

$$\sigma_{buck} = -1/\gamma \quad [\text{Pa}] \quad 2-18$$

As well as the sensitivity to stress of the resonance frequency:

$$S_{\sigma\omega}(\sigma_r) = \frac{\partial \omega_r}{\partial \sigma_r} = \frac{1}{2} \frac{\omega_{0r} / \sigma_{buck}}{\sqrt{1 + \sigma_r / \sigma_{buck}}} \quad \left[\frac{\text{Pa}}{\text{Hz}} \right] \quad 2-19$$

which is dependant on the applied stress σ_r . It should be noted that, in the case of a nanoresonator, the square root term is not negligible because the input stress can be important with regards to σ_{buck} . In order to understand the origin of this maximum stress σ_{buck} , the closed-form of the eigenfrequency is decomposed from the definition given by the Rayleigh's method. The modulated stiffness $k_{rf}(\sigma_r)$ and the effective mass m_r can be respectively identified from the potential and kinetic energy:

$$\begin{cases} k_{rf}(\sigma_r) = \left[\int_0^1 \left(\frac{\partial^2 \overline{W}_0(x)}{\partial x^2} \right)^2 dx \right] \frac{EI}{L_r^3} (1 + \sigma_r / \sigma_{max}) \quad \left[\frac{\text{N}}{\text{m}} \right] \\ m_r = \left[\int_0^1 \overline{W}_0^2(x) dx \right] \rho S_r L_r \quad [\text{kg}] \end{cases} \quad 2-20$$

≈ 198
 ≈ 0.39

where the integrals, dependant on the eigenfunction, are calculated for the boundary conditions of a doubly-clamped beam. The flexural stiffness appears as the dominant effect of the frequency modulation. Thus, the stress for which the frequency is null is the stress for which the stiffness is cancelled, i.e. the buckling limit. Now, the mechanical transfer function of the pre-stressed doubly-clamped beam is completed. Amplitude and frequency variations are known and the acceptable stress range is defined. The next section defines how the movement of the beam is transduced into an electrical signal.

2.3 Transduction chain of the nanoresonator

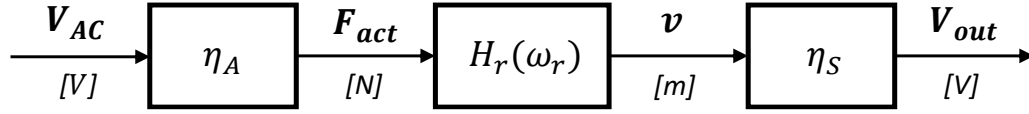


Figure 2-10 Block diagram of the nanoresonator's transduction: the actuation voltage generates a force to actuate the resonant element and its motion is transduced back into an output voltage.

This section aims at understanding the transduction of the beam motion. Figure 2-10 shows the block diagram of the nanoresonator transduction. The actuation gain η_A , powered by an input voltage V_{AC} , generates a force F_{act} . Because the nanoresonator operates at its resonance frequency, the mechanical response ($H_r(\omega_r) = Q_r/k_{rf}(\sigma_r)$) transforms the actuation force to a displacement v at the centre of the beam. The sensing gain η_S represents the transduction of the beam displacement into an output voltage V_{out} .

The nanoresonator architecture used in this work is described in Figure 2-11. The actuation is performed on the resonant beam by a fixed electrode. The resonant beam is fixed at one extremity to the accelerometer. Piezoresistive gauges are orthogonally placed at the other extremity of the resonant beam in order to transduce the beam motion. When the resonant beam vibrates, one gauge is elongated and the other one is compressed. As the gauges are piezoresistive, the mechanical strain induces a variation in resistance. The ends of the gauges are clamped to polarisation pins which are used to bias the system to take advantage of the change in resistance to induce a motional current. The beam-end is the continuity of the resonant beam, which measures the motional current from the gauges through the reading pin.

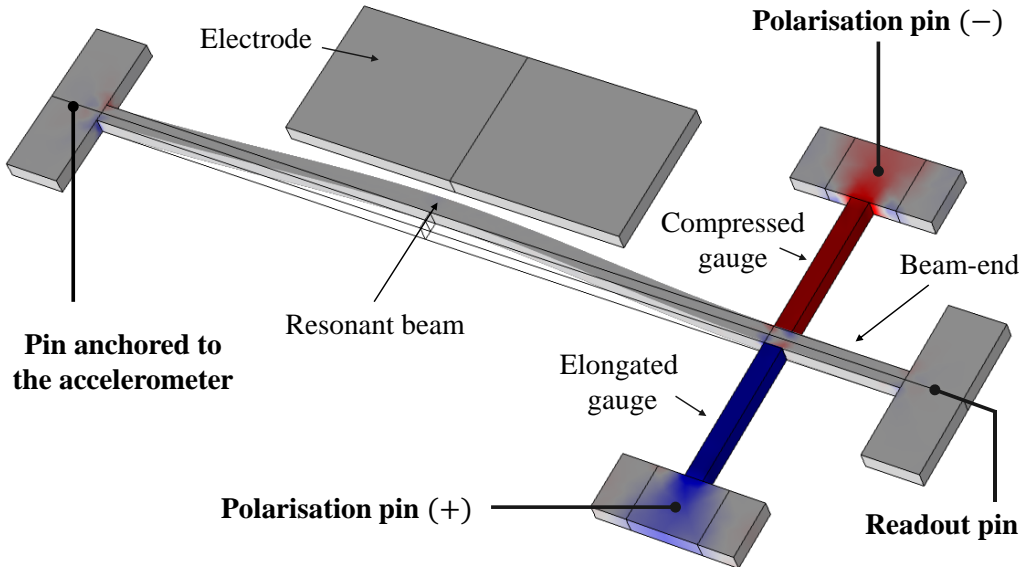


Figure 2-11 Architecture of a piezoresistive nanoresonator that consists of four parts: the actuation electrode, the resonant beam, the piezoresistive gauges and the beam end.

2.3.1 Electrostatic actuation

The actuation of resonant beam consists in using electrostatic forces to induce a mechanical motion. There are numerous transduction mechanisms, for instance the piezoelectric actuation [58] that induce mechanical motion. Here, the sub-section aims at expressing the actuation gain η_A of an electrostatic actuation and its domain of validity by assuming that the resonant beam is equivalent to a double-clamped beam. The description begins by the definition of the capacitive force applied on the resonant beam (1). The expression is projected on the first bending mode of the beam in order to determine the actuation gain (2). Finally, the linear limit of the actuation is defined (3).

(1) Figure 2-12 describes the operation of electrostatic actuation. The beam and its facing electrode, separated by an initial air gap $g(x, t)$ modulated by the beam motion $v_r(x, t)$, form a capacitance:

$$C_a = \frac{\epsilon_0 S_e}{g(x, t)} \quad [F] \quad 2-21$$

where S_e is the electrode area facing the beam, $g(x, t) = g - v_r(x, t)$ is the modulated gap and ϵ_0 the vacuum permittivity. The input voltage V_{act} applied from the fixed electrode to the movable beam is composed of an AC signal with a DC offset $V_{act}(t) = V_{DC} + V_{AC} \cos(\omega_a t)$, where ω_a is the actuation frequency. The actuation force can be derived from the stored energy on the capacitor $C_a V_{act}^2/2$,

$$F_{act}(x, t) = \frac{\epsilon_0 S_e}{2g(x, t)^2} \left[\frac{V_{AC}^2}{2} + V_{DC}^2 + 2V_{DC}V_{AC} \cos(\omega_a t) + \frac{V_{AC}^2}{2} \cos(2\omega_a t) \right] \quad 2-22$$

and it is distributed along the beam facing the electrode. The induced electrostatic force has three harmonics: the static harmonic, proportional to $V_{DC}^2 + V_{AC}^2/2$, the $2\omega_a$ harmonic, proportional to $V_{AC}^2/2$ and the ω_a harmonic, proportional to $2V_{AC}V_{DC}$. Here the nanoresonator is assumed to operate in its first bending mode at a frequency close to ω_a , so only this is considered in the analysis.

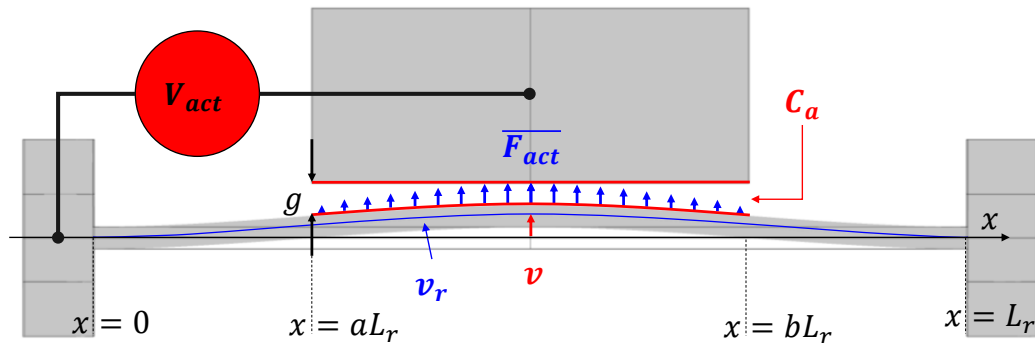


Figure 2-12. Description of the electrostatic actuation of a doubly-clamped beam. The electrostatic force is distributed on the length facing the beam $[a, b]L_r$.

(2) The capacitive force $F_{act}(x, t)$ depends on the beam displacement $v_r(x, t) = v(t)\overline{W}_0(x)$, which in our case is supposed to be far smaller than the air gap ($v_r \ll g$). Thus, it can be approximated by a Taylor series expansion:

$$F_{act}(x, t) = \frac{\epsilon_0 S_e V_{act}^2(t)}{2g^2} \left[1 + 2 \frac{v(t)\overline{W}_0(x)}{g} \right] [N] \quad 2-23$$

In the capacitive force distribution, the mode shape is correlated to the electrode position. Indeed, the capacitive force induced by an electrode centred at the central node of the beam is efficient to actuate the first bending mode but unable to operate the second mode. By projecting the actuation force onto the first bending mode, $F_{act}(x, t)$ can be expressed in terms of the normalized mode shape of the beam $\overline{W}_0(x)$, integrated along its relative length facing the electrode $[a, b]$.

$$F_{act}(t) = \frac{\epsilon_0 S_e V_{act}^2(t)}{2g^2} \int_a^b \overline{W}_0(x) \left[1 + v(t) \frac{2\overline{W}_0(x)}{g} \right] dx [N] \quad 2-24$$

where the first order of the limited development $\eta_0 = \int_a^b \overline{W}_0(x) dx$ is associated to the capacitive driving force $\overline{F}_0(t) = \eta_0 \epsilon_0 S_e V_{act}^2(t)/2g^2$ of the first bending mode, and the second order of the limited development $\eta_{02} = \int_a^b \overline{W}_0^2(x) dx$ is associated to the negative stiffness $k_e = \eta_{02} \epsilon_0 S_e V_{act}^2(t)/g^3$. Then, the temporal Equation 2-13 (A) is completed by the capacitive actuation:

$$m_r \frac{d^2 v}{dt^2} + b_r \frac{dv}{dt} + [k_{rf}(\sigma_r) - k_e]v(t) = \overline{F}_0(t) \quad 2-25$$

In conclusion, the capacitive actuation has two effects on the dynamics of the beam. First, the negative stiffness affects the global stiffness of the system, thus affecting its gain H_r at resonance. However, the stiffness modulation by capacitive actuation is proportional to the beam area facing the electrode: close to $0.001 N/m$ for the DC actuation used experimentally. The modulation of the stiffness by axial stress is inversely proportional to the beam section: more than $1 N/m$ for the axial stress applied experimentally. Because of the small sections of the nanoresonators, the negative stiffness is thus negligible in front of the modulation stiffness by axial stress. Then, the actuation gain of the first harmonic of 1ω actuation:

$$\eta_A = \eta_0 \frac{\epsilon_0 S_e V_{DC}}{g^2} \left[\frac{m}{V} \right], \quad 2-26$$

depends on the coefficient η_0 that is equal to 0.41 for an electrode centred at the middle of the beam and whose length is half the beam's one. The actuation gain shows the linearity of the beam displacement as a function of the applied voltage. Of course, the linearity comes from a limited development, and it is only valid for small displacements with regards to the initial air gap. That is why, in the last subsection, the non-linearity is defined in order to fix the system limit of displacement.

(3) As detailed in Figure 2-6, in the linear regime of a stressed doubly-clamped beam we can track its resonance frequency using the relation between phase and frequency. However, nonlinear spring forces on the nanoresonator induce a nonlinear regime that make it difficult to maintain a linear phase-frequency relationship at resonance. This part aims at determining the upper limit of the linear regime in terms of bending motion. In general, the nonlinear spring force can be written as:

$$F_k = -k_0 v - k_1 v^2 - k_2 v^3 + O(v^4) \text{ [N]} \quad 2-27$$

where k_0 is the linear spring constant, k_1 and k_2 are first and second order corrections. When the higher-order terms become important with regards to the linear spring constant, the system cannot be considered linear anymore. In doubly-clamped beams using capacitive actuation, there are mainly two origins for the nonlinear spring coefficients: the electrostatic stiffness modulation, and the dependence of the stiffness of the beam on its elongation. As detailed in Eq. 2-25, the linear spring constant depends on the modulated flexural stiffness and the negative electrostatic stiffness $k_0 = k_{rf}(\sigma_r) - k_e$. In practice, there are two main actors to the correction factors: the spring hardening due to large elongation of the beam that induces an increase of rigidity, and the spring softening due to the gradient of the electric field that induces decrease of its spring constant. When the rigidity in the beam is induced by bending and axial stress, as detailed in [72], the critical vibration amplitude before reaching the spring hardening, calculated from the method described in [73], can be expressed as a function of axial stress σ_r , the beam width w_r and its quality factor Q_r :

$$v_{max} = 0.745 \frac{2w_r}{\sqrt[4]{3}} \sqrt{\frac{(1 + \sigma_r/\sigma_{buck})}{3Q_r}} \text{ [m]} \quad 2-28$$

For a beam width of 250 nm and a quality factor close to 1000, the critical amplitude before the spring hardening effect is less than 10 nm. Moreover, as explained in [74], the spring softening effect appears for a beam movement up to 1/3 of the air gap, here for $v(t) > 500/3$ nm, thus after the spring hardening effect. As the nanoresonator must operate in linear regime, the spring hardening effect is considered in the following as the dominant effect.

In conclusion, the critical amplitude has two important dependences. The first one is on the axial stress: the larger the compressive stress imposed on the resonant beam, the smaller the critical amplitude. This implies that the maximum permissible stress must be set to define the minimum critical amplitude. The second one is that the quality factor of the system limits the linear regime for losses in low-damping regime. Thus, for a good vacuum environment, a very low driving power rapidly brings the nanoresonator into a non-linear regime. Therefore, it is important to efficiently transduce a signal from even a very low driving power. The next section presents an efficient scheme for the motion transduction of a nanoresonator based on piezoresistive nanogauges.

2.3.2 Piezoresistive transduction

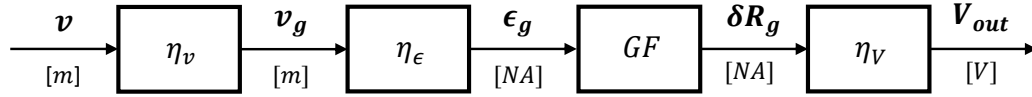


Figure 2-13 Description of the piezoresistive transduction of the nanoresonator of Figure 2-11.

The objective of this section is to present the transduction of the nanoresonator's motion. Microresonators make efficient use of electrostatic detection because of their relatively large area facing the electrode, thus benefiting from a long length and thickness [75]. In contrast, piezoresistive nanogauges take advantage of the small cross-sectional area due to their nanoscale size. This is an efficient transduction scheme for appropriately designed nanoresonators, as demonstrated in [44].

Figure 2-13 describes the principle of such piezoresistive transduction scheme. The displacement gain η_v represents the transduction from the motion of the resonant beam v to the gauges' strain ϵ_g . Due to the strain gain η_ϵ , the gauges motion induces a differential strain on the two gauges $\pm\epsilon_g$. As the gauges are piezoresistive, a linear gauge factor GF transduces the applied strain to a relative resistance variation δR_g . By polarising the gauges in voltage, the resistance variation generates a motional current. The readout pin is used to measure this current through an output voltage V_{out} . The readout gain η_V depends on the method used to measure the motional current. Figure 2-14 shows a schematic of piezoresistive transduction in the nanoresonators used in this work. The principle consists in a transduction of the resonant beam motion v to displacement at the central node of the gauge v_g . Because the gauge are clamped at their other sides, displacement v_g induces differential strain $\pm\epsilon_g$. From the piezoresistive properties of the gauges, the induced strain is transformed to resistance variation $R_g(1 \pm \delta R)$. At the end the motional current i_g , caused by gauges polarisation $\pm V_b$, is measured through the output voltage V_{out} .

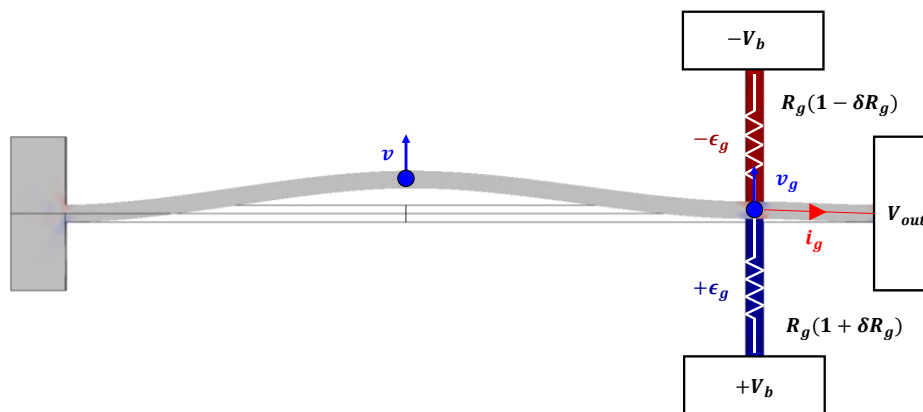


Figure 2-14 Illustration of the piezoresistive transduction scheme of the nanoresonators. The resonant beam displacement v induces displacement at the central node of the gauges v_g that causes differential axial strain $\pm\epsilon_g = v_g/L_g$ with L_g the gauges' length

This part covers the transduction of motion inside the nanoresonator. The objective is to express the displacement gain as a closed-form expression depending on of the nanoresonator's geometry. A 1D-assembly model is used to obtain a linear function of the displacement gain that depends only on the nanoresonator geometry. This methodology, based on a static approach, assumes that the dynamics of the intrinsic elements, mainly the gauges and the beam-end, do not influence the motion transduction. This assumption is based on the fact that the transducing elements are smaller than the resonant beam, so their dynamics appear at a higher frequency than those of the nanoresonator, i.e. the operation frequency of the system. Moreover, the motion transduction is assumed to be linear for a resonant beam motion limited by the critical amplitude of Eq. 2-27. This assumption is validated by 3D finite element method (COMSOL-FEM) simulations over the amplitude range of the system. Figure 2-15 illustrates the 1D model of the nanoresonator as an assembly of elementary flexible beams. The geometry of the transduction (gauges and beam-end) are expressed as form factor (α, β, γ) of the resonant beam geometry (w_r, L_r) . The discretization of the system allows expressing the mechanical equilibrium of an element according to its degrees of freedom. The degrees of freedom of several elements can be associated on a given node. Thus, the mechanical balance of the central element (the resonant beam) can be expressed as the equivalent mechanical balance of the whole system. In practice, this results in a stiffness matrix associating the degrees of freedom of the central element with an external load. The coefficients of this matrix are derived from the coefficients of each associated element. This methodology, detailed in Appendix A, gives a displacement gain between the displacement of the central node of the beam and the displacement of the central node of the gauges:

$$\eta_v = \frac{A}{B + \left(\frac{L_r}{w_r}\right)^2} [A \cdot U] \quad 2-29$$

where A and B depend on the form factor parameters α, β and γ . Appendix A shows that the displacement gain can be optimized, depending on the geometry of the resonant beam, with an ideal form factor. This optimization is used in Chapter 3 for the design of the nanoresonator.

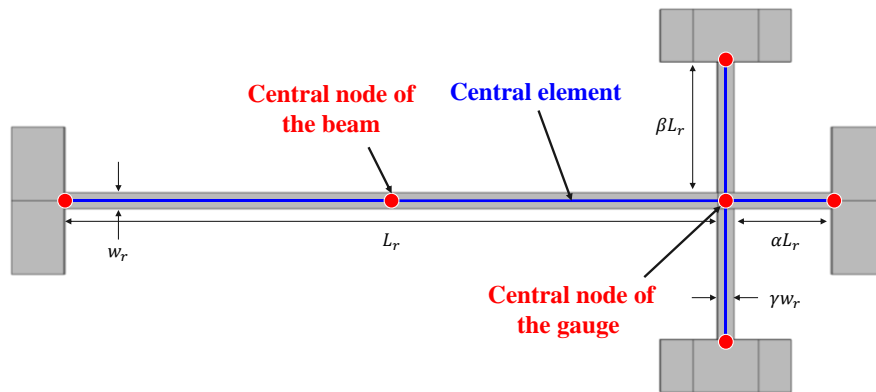


Figure 2-15 Decomposition of the nanoresonator in elementary beams. The model is reduced to the central element in order to express v_g/v from its stiffness matrix.

The resonant beam motion causes the displacement v_g and the rotation θ_g of the gauge. According to the small deformation regime, the axial strain of the gauge $\epsilon_{xx,g} = \partial v_g / \partial y + \partial \theta_g / 2 \partial y$ is affected by the cross-section rotation θ_g . But for a small length-to-width ratio of the gauges, it is confirmed by the 3D FEM simulations that the effect of the rotation is negligible, so we can consider that the strain depends only on the axial displacement v_g . Thus, the deformation gain is:

$$\eta_\epsilon = \frac{\eta_v}{\beta L_r} \left[\frac{1}{m} \right] \quad 2-30$$

(2) The resistance variation of the nanogauges caused by the axial strain results in two effects: the variation of the nanogauges' geometry (length and section), and the deformation of its atomic lattice. On piezoresistive conductors, the electrical carrier mobility modulation is the major contributor to the resistivity gauge factor GF . The relative resistance variation δR is proportional to its gauge factor and axial strain:

$$\delta R_g = GF \epsilon_g \text{ [A.U]} \quad 2-31$$

As shown in Figure 2-14, we place the nanogauges so that when one of them is in elongation, the other one is in compression. Their resistance variations are therefore of opposite sign, and the piezoresistive signal is differential.

(3) This last part presents how from the differential resistance variation, the piezoresistive transduction results in an output voltage. The gauges are equivalent to a resistor bridge where the output voltage node is in-between two gauges experiencing opposite resistance variations. Voltages of opposite sign applied to the two gauges bias the resistance bridge. The currents flowing through the gauges are modulated by the resistances' variations. A balance of the currents on the output voltage, detailed in section 2.5, shows that output voltage is proportional to the bias voltage and the resistance variation:

$$V_{out} \propto V_b \delta R_g \text{ [V]} \quad 2-32$$

The gain between the resonant beam motion and V_{out} is:

$$\eta_S \propto \eta_v \eta_\epsilon GF V_b \left[\frac{V}{m} \right] \quad 2-33$$

In conclusion, the piezoresistive gauges are a highly linear mechanism to read out the motion of the resonant beam. According to the nanoresonator transduction chain, the nanoresonator's signal is maintained at resonance by an electrostatic actuation and it is detected as an output voltage using piezoresistive transduction. The next section presents how the frequency measurement is performed from a modulated output voltage, but also how an output voltage limits the frequency measurement. In addition, the specific case of this nanoresonator's frequency measurement is presented taking into account the most important contributors of a real voltage readout.

2.4 Frequency measurement

The sensing element of resonant beam accelerometer is the nanoresonator, which traduces an applied acceleration to a resonance frequency shift. Thanks to the piezoresistive transduction, the bending motion of the nanoresonator is converted into an AC signal that can be detected to measure its frequency. However, the nanoresonator is a passive system. First, due to the losses associated with the damping of the system, the AC signal must be maintained at its resonance by an actuation. In addition, due to the frequency variations of the system, the actuation must follow the resonance so that the nanoresonator always operates at this frequency. In order to have a sensor application, i.e. to be able to measure the frequency variations in real time, the nanoresonator must be associated with an electronic circuit. Therefore the goal of the global system is to generating the periodic signal necessary to maintain the resonance frequency. Some electronic systems, such as PLLs or oscillators, maintain the operating frequency at the resonance frequency by correcting the phase shift measured in the system. Section 3.2 discusses the design of such electronic circuits adapted to the piezoresistive nanoresonators used here. In practice, the frequency of an AC signal $V_{out}(t) = |V_{out}| \cos(\omega_r t + \varphi_r)$ is measured by counting the number of zero crossings over a given time period. Figure 2-16 illustrates how the frequency measurement can be limited.

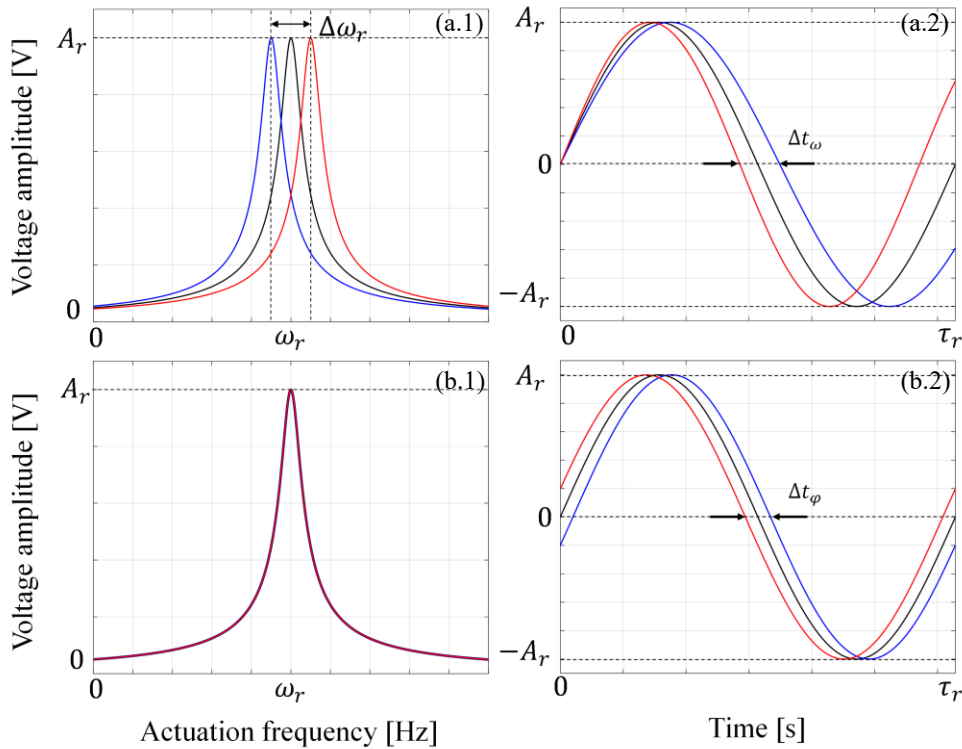


Figure 2-16 Representation of the impact of noise on the frequency measurement. A noise on the resonance frequency (a.1) is equivalent to a frequency modulation on the output signal of the nanoresonator (a.2). A noise in phase induces a measurement error on the frequency of the output signal of the nanoresonator (b.2). However, the phase noise does not affect the resonance frequency of the nanoresonator (b.1).

To illustrate how noises affect the frequency measurement, the signal is assumed to be modulated, as detailed in [76]. As the focus is on frequency, only the cases of frequency modulation (FM) and phase modulation (PM) are illustrated. On one hand, the resonance frequency can be modulated as $\omega_r(t) = \omega_r + \Delta\omega_r \cos(\omega_m t)$, where ω_m is the modulation frequency, as illustrated on Figure 2-16 (a). Thus, the frequency count can be affected by the induced delay $\Delta t_\omega \propto 1/\Delta\omega_r$. On the other hand, the phase can be modulated as $\varphi_r(t) = \varphi_r + \Delta\varphi_r \cos(\omega_m t)$. Figure 2-16 (b) shows that the PM does not affect the resonance frequency but induces a delay $\Delta t_\varphi \propto \Delta\varphi_r/\omega_r$. Both effects can degrade the stability of the frequency measurement: a modulation of the resonance frequency, equivalent to the frequency noise, or a measurement error of the resonance frequency, caused by a modulation of the phase (for example by electronic noise), equivalent to the phase noise. It is important however not to mix the frequency of the output signal of the system with the resonance frequency of the resonator: though both terms are linked, they can be considered equivalent only in specific closed-loop systems and under certain conditions.

The stability of the frequency measurement can be illustrated by the minimum measurable frequency deviation. This minimum depends on the integration time, i.e. the rate at which the frequency is measured. Depending on the integration time, several limiting phenomena can be observed. In this work we will define the long term stability, which is the minimum measurable frequency for a long acquisition time ($\tau > 1\text{s}$); the short term stability, which is the minimum measurable frequency for a short acquisition time ($\tau < 1\text{s}$); and the bias instability, which is the minimum measurable frequency arising from $1/f$ noise in the system, and which represents the detection floor for any integration time.

In practice, the Allan variance $\sigma_f(\tau)$ is used to characterize the stability of the frequency measurement. The Allan variance is a method of representing the root means square (RMS) random drift error as a function of averaging time τ [77]. This specific variance of a frequency signal is widely used in the field of sensors, as it makes it possible to highlight the different sources of noise affecting the signal and allows to plot the frequency stability (or resolution of the sensor) as a function of the measurement time. Figure 2-17 represents the colour of the main noise sources that can affect the frequency stability of a nanoresonator. White noises manifest in the Allan variance by a slope of $\tau^{-1/2}$. They are dominant for short integration times and fix the short term stability of the sensor. Flicker noise manifests as a plateau (τ^0) on the Allan variance and often fixes the bias stability of the measurement. Frequency drifts are long timescale variations of the resonance frequency caused by environmental fluctuations such as the temperature drifts. They generally appear at integration times above a few seconds and are represented by $\tau^{1/2}$ slope on the Allan variance. The Allan variance represents the stability of the frequency fluctuations measurement. I.e. the stability of the nanoresonator output signal: its frequency. Reducing the noise of the system (white noise and flicker noise) and limiting the drifts due to the environment is the first way to

improve the nanoresonator's limit of detection. However, the accelerometer signal is originated by the nanoresonator's signal transduced in acceleration by the sensitivity $S_{a\omega}$. In this way, the second improvement of the limit of detection of the accelerometer consists in increasing its sensitivity.

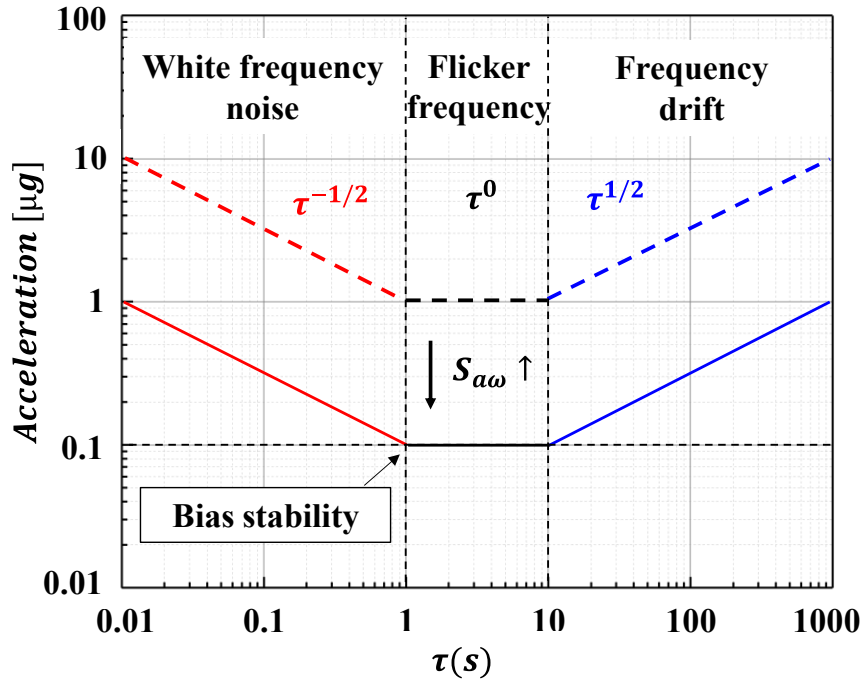


Figure 2-17 Allan variance expressed in terms of acceleration from the frequency measurement and the accelerometer scale factor. The dashed curves represent the type of noises highlighted by the Allan Deviation based on their integration on the measurement time τ . The solid line represents an improvement of the accelerometer's scale factor $S_{a\omega} = S_{a\sigma} S_{\sigma\omega}$. The bias stability can be identified as the minimum of Allan variance.

2.4.1 Phase noise

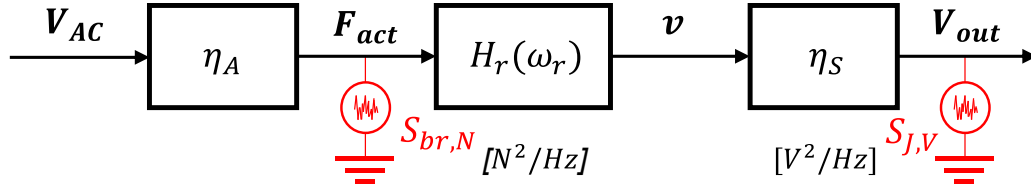


Figure 2-18 Block diagram of the nanoresonator transduction with additive noise sources: S_{br} is the power spectral density of the thermomechanical noise of the nanoresonator, S_J is the power spectral density of the Johnson noise of the nanogauges.

For piezoresistive nanoresonators, various noise sources can affect the frequency stability. Among them, $1/f$ noise generated by resistance fluctuations is the main noise source in a piezoresistor (Hooge noise). Yet, nanoresonators are weakly affected by it because they operate at relatively high frequency (>10 MHz). The extraction of Hooge's constant from similar nanogauges [44] yielded an estimated noise smaller than $1 \text{ nV}/\sqrt{\text{Hz}}$ at the operating frequency, negligible with respect to other sources of noise. The following analysis is focused on these other noise sources, especially additive white noises and their effects on frequency stability.

By definition, an additive white noise is a noise that is added to a signal. Figure 2-18 represents the block diagram of the nanoresonator transduction. V_{out} is the nanoresonator output signal where the frequency is counted. This signal is affected by additive white noises: the nanogauges of the nanoresonator add Johnson-Nyquist noise arising from the thermal agitation of electrical carriers in these resistors. For such piezoresistive nanogauges disposed in bridge configuration, the Johnson-Nyquist noise depends on the equivalent resistance at the output node of the nanoresonator $R_{out} = R_t + R_g/2$, where R_t is the beam-end resistance and R_g the gauge resistance. The Power Spectral Density (PSD) of this additive noise can be expressed as voltage noise on the nanoresonator output voltage:

$$S_{J,V} = 4k_B T R_{out} \left[\frac{\text{V}^2}{\text{Hz}} \right] \quad 2-34$$

where k_B is the Boltzmann's constant and T the temperature.

Thermomechanical noise comes from the coupling of the nanoresonator with its environment by a stochastic force accounting for its thermalization. It derives from the theorem of fluctuation-dissipation that states that any system dissipating energy is noisy. As shown on Figure 2-5 (a) the nanoresonator is represented by a damped spring-mass system where the dissipation is associated to its damping coefficient $b_r = m_r \omega_r / Q_r$. From [78] the definition of the force spectral density of thermomechanical noise is $S_{br,N} = 4k_B T b_r$. The transduction chain of nanoresonator ($H_r(\omega_r) = Q_r / m_r \omega_r^2$ & η_S) allows expressing the PSD of thermomechanical noise as white noise on the nanoresonator output voltage:

$$S_{br,V} = \eta_s^2 \frac{4k_B T Q_r}{\omega_r^3 m_r} \cdot \left[\frac{V^2}{Hz} \right] \quad 2-35$$

The thermomechanical noise is here considered as white noise on the output voltage because the mechanical response of the nanoresonator $\omega_r/2Q_r$ is larger than the measurement bandwidth, defined by the quasistatic regime of the accelerometer ω_{0m} . These noise sources originate from the nanoresonator itself. But the electronics used to maintain the nanoresonator at its resonance frequency add an additional external noise $S_{E,V}$. In practice, the components used for the readout of nanoresonator output signal add dominant noise sources. For instance Zurich Instrument's Lock In Amplifier (UHF) as well as the high-performance front-end amplifier (ADA4817) add $4nV/\sqrt{Hz}$ of noise, which is not negligible compared to the noise of nanoresonators. Because these noise sources are not correlated, the PSD of additive noises on the nanoresonator output is $S_V = S_{J,V} + S_{br,V} + S_{E,V}$. According to the phase noise theory [79], additive white noise is distributed both on the amplitude and the phase of the signal. The phase noise induced by the additive noise is proportional to the ratio between its PSD and the power carrier of the signal V_{out}

$$S_\phi = \frac{S_V}{|V_{out}|^2/2} \left[\frac{rad^2}{Hz} \right] \quad 2-36$$

For a system resonating at ω_r and dominated by additive white noises, the angular resonance frequency spectral density is given by 2-37 and the phase-to-frequency relationship of the resonator of Figure 2-6:

$$S_\omega = \left(\frac{\omega_r}{2Q_r} \right)^2 \frac{S_V}{P_0} \left[\frac{Hz^2}{Hz} \right] \quad 2-37$$

The effect of additive noises on the stability of the resonance frequency measurement can be quantified through $\omega_{min,\phi}$, the minimum measurable frequency shift, which depends on the measurement bandwidth BW , the output signal amplitude $|V_{out}|$ and the additive white noise S_V

$$\omega_{min,\phi} = \frac{\omega_r}{2Q_r} \frac{\sqrt{S_V BW}}{|V_{out}|} [Hz] \quad 2-38$$

In other words, $\omega_{min,\phi}$ is proportional to the inverse of the Signal-to-Noise-Ratio (SNR) with $SNR = |V_{out}|/\sqrt{S_V BW}$. Reducing the additive noise or increasing the output signal allow improving the effect of additive noise on the stability of the resonance frequency measurement.

2.4.2 Frequency noises

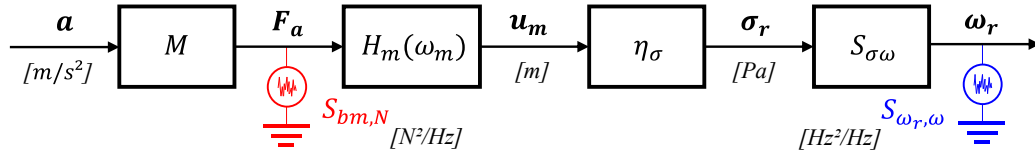


Figure 2-19 Block diagram of the accelerometer transduction including the noise sources affecting the resonance frequency: $S_{bm,N}$ is the force spectral density of the thermomechanical noise of the accelerometer, $S_{\omega_r,\omega}$ is the frequency spectral density of the intrinsic frequency fluctuations of the nanoresonator.

Figure 2-19 presents the accelerometer transduction chain from the input acceleration a to the resulting nanoresonator resonance frequency $\omega_r(a)$. Like the nanoresonator, the MEMS accelerometer can be modelled as a damped mass-spring system where the dissipation is associated to its damping coefficient $b_m = M\omega_{0m}/Q_m$. In this case the force spectral density of thermomechanical noise affecting the proof mass is $S_{bm,N} = 4k_B T b_m$ [80]. This force spectral density is filtered by the mechanical response of the accelerometer $H_m(\omega_m)$, transduced as an axial stress on the nanoresonator by the transduction gain η_σ , and then to a resonance frequency shift $\Delta\omega_r$ in the same way as an acceleration. In other words, the resonance frequency ω_r is affected by resonance frequency noise coming from the thermomechanical noise of the accelerometer. This frequency noise is not white noise such as its origin ($S_{bm,N}$) because the mechanical response of the accelerometer filters it. But, considering that the measurements are performed in the quasi-static regime of the accelerometer, i.e. $H_m(\omega_m < BW) = 1/M\omega_{0m}^2$, the thermomechanical noise of the accelerometer can be expressed as white noise on the resonance frequency ω_r with the frequency spectral density

$$S_{bm,\omega} = \frac{4k_b T}{M\omega_{0m}^3 Q_m} [\eta_\sigma S_{\sigma\omega}]^2 \left[\frac{\text{Hz}^2}{\text{Hz}} \right] \quad 2-39$$

This is a resonance frequency noise as presented on Figure 2-16 (a). Similarly to the phase noise, the frequency noise limits the achievable frequency stability. But in contrast to phase noise, this is not an uncertainty on the measurement of the resonance frequency, but fluctuations of the resonance frequency itself, which still affect the limit of detection of the sensor. Therefore, in this case, the stability of the resonance frequency $\omega_{bm,\omega}$ in a specific bandwidth BW does not depend on the measurement signal's SNR

$$\omega_{bm,\omega} = \sqrt{S_{bm,\omega} BW} [\text{Hz}] \quad 2-40$$

In practice, 1/f noise independent of SNR eventually limits the bias instability of the nanoresonator. Several teams, among them the Leti, have shown that nanoresonators suffer from intrinsic resonance frequency fluctuations [81] that represent a bias instability limit. These frequency fluctuations are represented on the Figure 2-19 as frequency spectral density $S_{\omega_r,\omega}$.

In conclusion, the resolution of the nanoresonator ω_{min} , i.e. the minimum frequency measurable for short integration time can be calculated from the frequency resolutions $\omega_{min,\phi}$ and $\omega_{min,\omega}$. Because these noises are not correlated, the resolution of the nanoresonator is

$$\omega_{min} = \sqrt{\omega_{min,\phi}^2 + \omega_{min,\omega_r}^2} \text{ [Hz]} \quad 2-41$$

In practice, for short integration time, the frequency stability is dominated by white noise, thus the resolution can be expressed as resonance frequency spectral density ($\text{Hz}/\sqrt{\text{Hz}}$) by dividing ω_{min} by the measurement instrument's integration bandwidth. The minimum measurable resonance frequency fluctuations are limited by the additive noises, which induce an uncertainty in the measurement $\omega_{min,\phi}$, and by resonance frequency noise, which induces an uncertainty affecting the sensing application ω_{min,ω_r} . Noise sources can be dissociated (1) by improving the SNR of the system, because only $\omega_{min,\phi}$ is improved, and (2) by integrating the output signal on large bandwidth $BW > \omega_{0m}$, because ω_{min,ω_r} is filtered by the accelerometer's resonance. In any case, both are dependant of the integration bandwidth. i.e. by reducing the bandwidth, the frequency stability can be improved, as both of them are white noises. Because the accelerometer sensitivity links the resonance frequency variation and the acceleration, the acceleration stability can be deduced from the frequency stability.

2.5 Voltage readout

In this section, the actuation and detection signals are studied by building an equivalent circuit of the nanoresonator. The physical analysis of section 2.3 assumes that the actuation voltage only causes a mechanical force on the beam. Thus, due to a static polarisation, the resistance variation generates a useful output voltage in the central node of the gauge bridge. However, electrostatic actuation also generates a feedthrough current through the resonant beam, which is added to the signal from the gauge variation. The challenge is to perform a voltage readout in the central node of the gauge bridge to measure only the useful signal without losses. This section presents the analysis of an equivalent circuit of the nanoresonator, which allows understanding the elements involved in the output voltage.

Figure 2-20 describes the equivalent circuit of the nanoresonator. The actuation voltage V_{AC} generates a feedthrough current I_a that flows through the actuation impedance Z_a . This impedance is composed of an actuation capacitance C_a in series with the resonant beam resistance R_a . The useful currents I_g that flows through the modulated resistances $R_{g\pm} = R_g(1 \pm \delta R_g)$ are due to the differential bias voltage $\pm V_b$. A load impedance Z_L is plugged at the beam-end in order to measure the output voltage V_0 . The current I_{out} flows through the beam-end resistor R_t before reaching the load impedance, thus the output voltage V_{out} is a fraction of V_0 . From a balance of currents on the V_0 node, and applying the Kirchhoff law to the voltage divider bridge, the output voltage of the nanoresonator is given by:

$$V_{out} = \frac{1}{\left(1 + \frac{R_t}{Z_L}\right)} \left[\frac{\delta R_g V_b}{\left(1 + \frac{R_g}{2} \left[\frac{1}{Z_L + R_t} + \frac{1}{Z_A} \right] \right)} + \frac{V_{AC}}{\left(1 + Z_A \left[\frac{1}{Z_L + R_t} + \frac{2}{R_g} \right] \right)} \right] [V] \quad 2-42$$

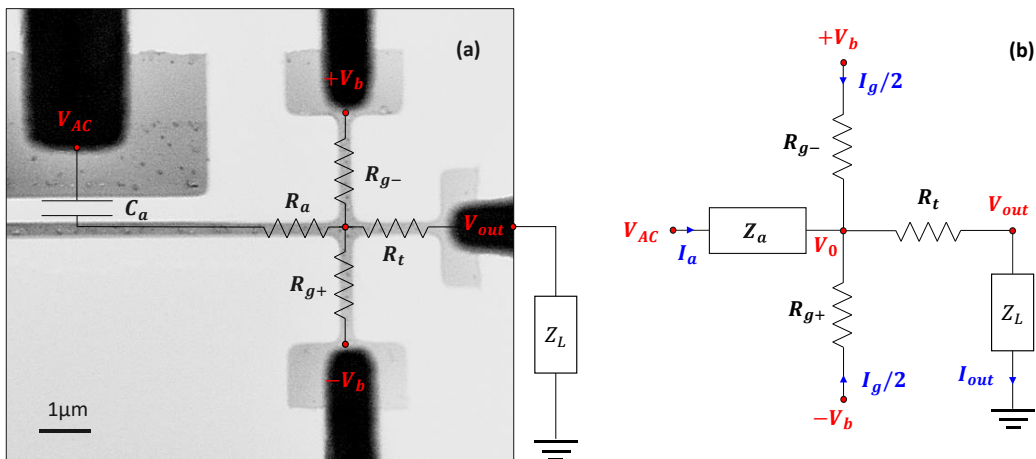


Figure 2-20. Equivalent circuit of the nanoresonator. (a) Scanning electron microscope (SEM) image of the nanoresonator and nanogauges, with the electrical equivalent circuit superposed. (b) Equivalent electrical model of the readout of the nanogauges.

The factorized term of Eq. 2-42 corresponds to the losses associated to voltage readout. The term proportional to $\delta R_g V_b = V_{AC} \eta_A H_r \eta_S$ corresponds to the useful (i.e. motionally-induced) part of the output voltage. The term proportional to V_{AC} corresponds to the part of the output voltage proportional to feedthrough current (i.e. from a purely electrical origin). The voltage transfer function of the system can be more clearly expressed as:

$$H(\omega_a) = \frac{V_{out}}{V_{AC}} = H_R(\omega_a)G_L(\omega_a) + H_A(\omega_a) \quad [A. U.] \quad 2-43$$

where $H_R = \eta_A H_r \eta_S$ is the ideal transfer function of the nanoresonator, $G_L^{-1} = [1 + R_t/Z_L][1 + R_g/2(Z_L + R_t)]$ is the loss associated to the voltage readout, which assumes $(Z_L + R_t)^{-1} \gg Z_A^{-1}$ because the actuation capacitance $C_a \sim fF$, the beam resistance $R_a \sim k\Omega$ and the operation frequency $\omega_r > 10 \text{ MHz}$. $H_A^{-1} = [1 + R_t/Z_L][1 + Z_A(1/[Z_L + R_t] + 2/R_g)]$ is the transfer function associated to the feedthrough current. The influence of these different phenomena is discussed for an output voltage operating at a frequency close to the MHz. The load impedance is usually a high-impedance resistor ($>1 \text{ M}\Omega$) in parallel with a capacitance, thus behaving similarly to a low-pass filter. Figure 2-21 (a) shows the impact of these different phenomena on the voltage transfer function of the system:

The reference transfer function (black) is an ideal case where the load impedance has no parasitic capacitances and the actuation capacitance does not affect the readout ($C_a = 0$). In this configuration, the losses and the background signal are negligible ($G_L = 1$ & $H_A = 0$).

The intermediate transfer function (blue) considers the parasitic capacitances of the load impedance but still neglects the background signal from the actuation. At the operation frequency close to the MHz, the load impedance has already started to cut off the nanoresonator signal, thus introducing losses $|G_L| < 1$ and a phase offset.

The real transfer function (red) considers the previous phenomena and the impact of the background signal. Although the reference transfer function is no more affected by output losses, the feedthrough current adds a background signal H_A on the useful signal $H_R^* = H_R G_L$. The background signal has an impact on the phase measurement that is discussed in Figure 2-21 (b).

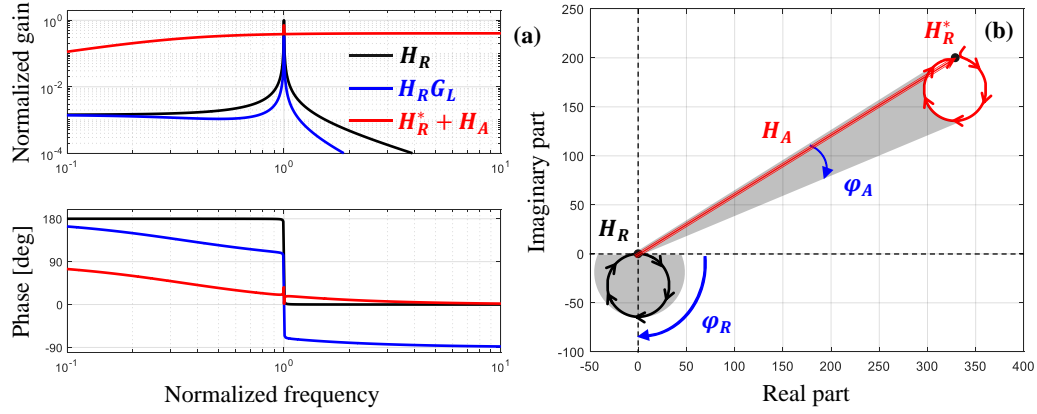


Figure 2-21 Representation of the nanoresonator's transfer functions in three different scenarios of parasitic coupling. (a) Bode diagrams, normalized to the actuation frequency, comparing the different effects that influence the transfer function. (b) Complex representation of the voltage transfer function comparing the influence of the background signal.

Figure 2-21 (b) shows the complex representation of the voltage transfer function $H_R^* + H_A$ for a ω sweep close to the resonance frequency. The transfer function of the background signal H_A is represented as constant vector because even though it comes from a capacitive source the frequency sweep is performed in a very small range around the resonance. However, the transfer function of the useful signal H_R^* makes a circle in the complex domain characteristic of the resonance of a second order system. For the ideal second order system H_R , the circle is centred to zero thus, at resonance the ideal phase shift $\varphi_R = 90^\circ$.

Without background signal, the circle is shifted by the vector H_A , thus at resonance the phase shift $\varphi_A < 90^\circ$. The higher the background (thus the vector H_A), the lower the phase shift at resonance. Due to this effect, the ratio between phase noise and phase shift at resonance is lower. In conclusion, the phase shift at resonance depends on the Signal-to-Background ratio (SBR), i.e. the ratio between H_A and H_R^* . In practice, a useful signal deteriorated by a background signal deteriorates the nanoresonator's measurement due to a lower phase shift at resonance. A PLL, such as that shown in Figure 4-22, can still be used to maintain the oscillation with the deteriorated signal.

Chapter 2 has described the tools to model force transduction accelerometers based on piezoresistive nanoresonators as force sensors. Using this knowledge, Chapter 3 exploits the analytical models in order to design these resonant accelerometers.

3 Electromechanical design of resonant accelerometers

This chapter aims at developing a design strategy of the MEMS structure and the electronics that keep the nanoresonator in resonance. The system consisting of a MEMS structure and dedicated electronics is called a sensor. The design of the MEMS structure is described in the first section. The discussion begins by presenting the fabrication process. Then, the MEMS design aims at optimizing the performance of the system in terms of resolution and bandwidth. The strategy is to translate the target specifications into the main geometrical parameters for a specific MEMS geometry (Figure 3-1 a). After proposing the implementation of the MEMS structure, an electronic readout dedicated to its operation is designed. The objective is to design an oscillator architecture that allows measuring the acceleration in real time and does not degrade the performance of the MEMS (Figure 3-1c).

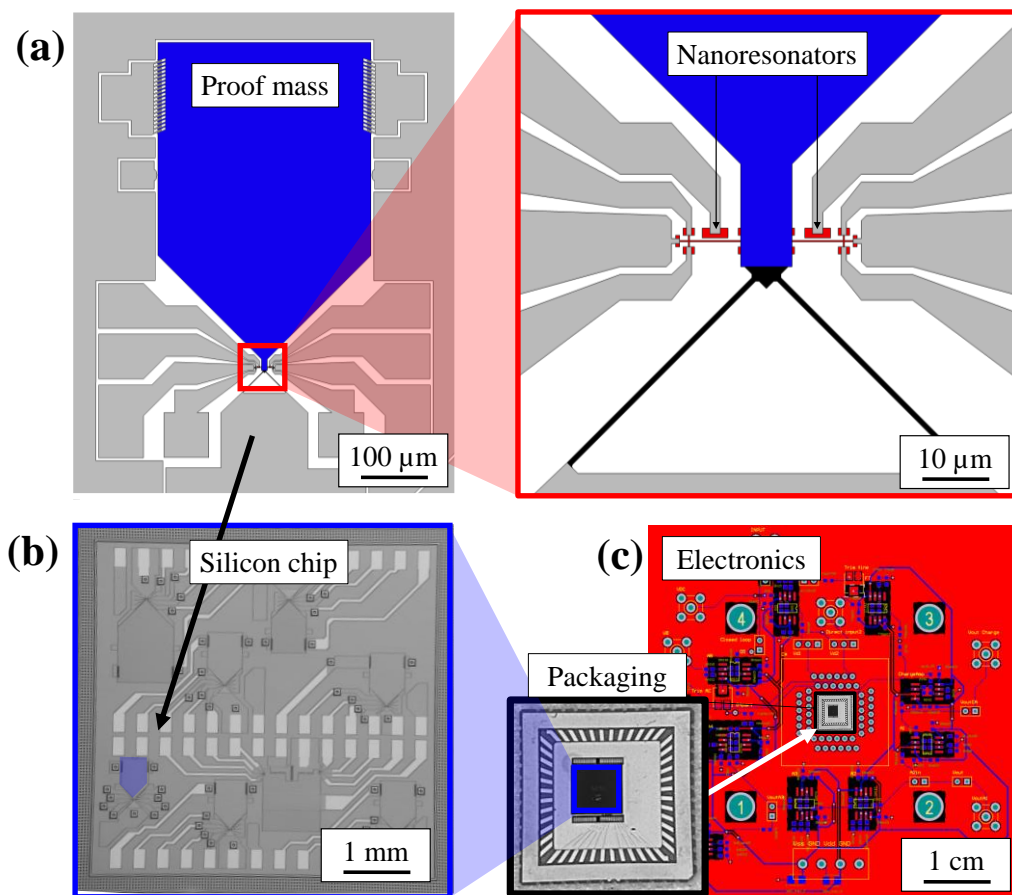


Figure 3-1 Overview of the elements of an acceleration sensor based on resonant detection.
(a) MEMS structure that translates the acceleration into a resonance frequency variation.
(b) Silicon chips regrouping several design of accelerometer and packaging in ceramic socket,
(c) Readout electronics compatible with the ceramic socket and comprising an oscillator in order to measure acceleration in real time.

3.1 Design of the MEMS structure

The objective of the design process is to optimize the performance in terms of both resolution and bandwidth: for this, a co-design of the nanoresonator and the accelerometer is necessary. On one hand, the overall stiffness of the accelerometer is determined by the compressive stiffness of the nanoresonator and the bending stiffness of the suspension elements, which determine its bandwidth together with the proof mass. On the other hand, the resolution is limited by the frequency resolution of the nanoresonator but also by the frequency noise generated by the accelerometer, thus by the design of the nanoresonator and the accelerometer.

Figure 3-2 presents the design strategy of the MEMS structure. The analysis begins by presenting the "*M&NEMS*" manufacturing technology that fixes certain technological parameters. The detection limit of the nanoresonator is generally limited by the piezoresistive transduction. However, by improving the transduction efficiency one can improve the signal-to-noise ratio (SNR) until reaching the detection limit set by the thermomechanical noise of the nanoresonator, which represents the ultimate nanoresonator resolution. Through the sensitivity of the accelerometer, the thermomechanical noise of the accelerometer is matched with the resolution of the nanoresonators. If the sensitivity is higher than this optimal value, the bandwidth is reduced (because of the larger proof mass), as is the thermomechanical noise of the proof mass, and the resolution of the nanoresonator becomes dominant.

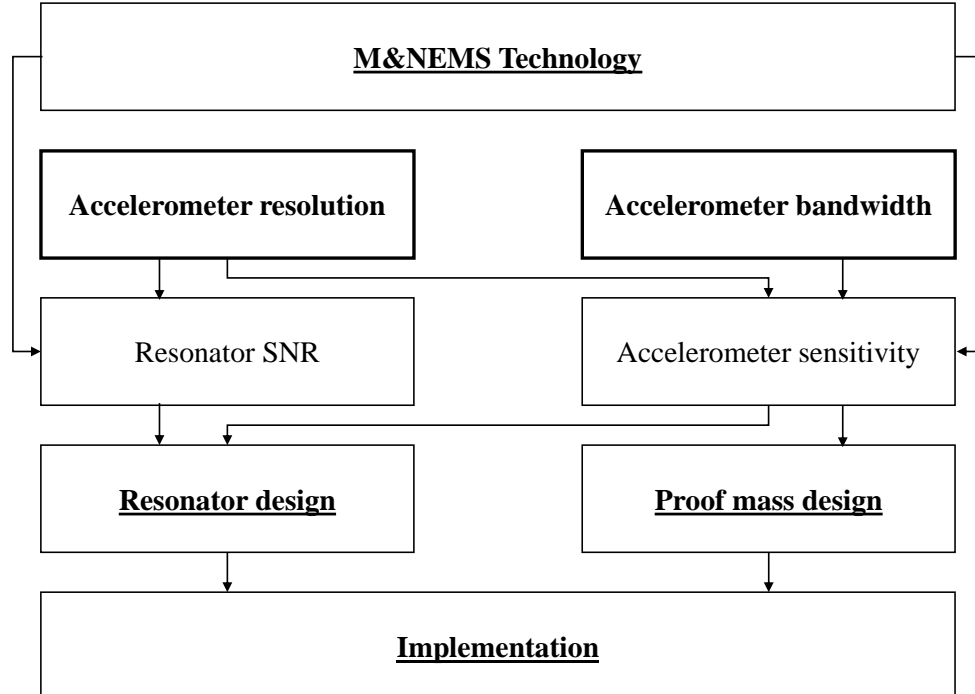


Figure 3-2 Design strategy used to optimise the resolution / bandwidth trade-off of the accelerometer. The sensitivity of the accelerometer and the SNR of the vibrating beams are central to the design process.

3.1.1 *M&NEMS fabrication process*

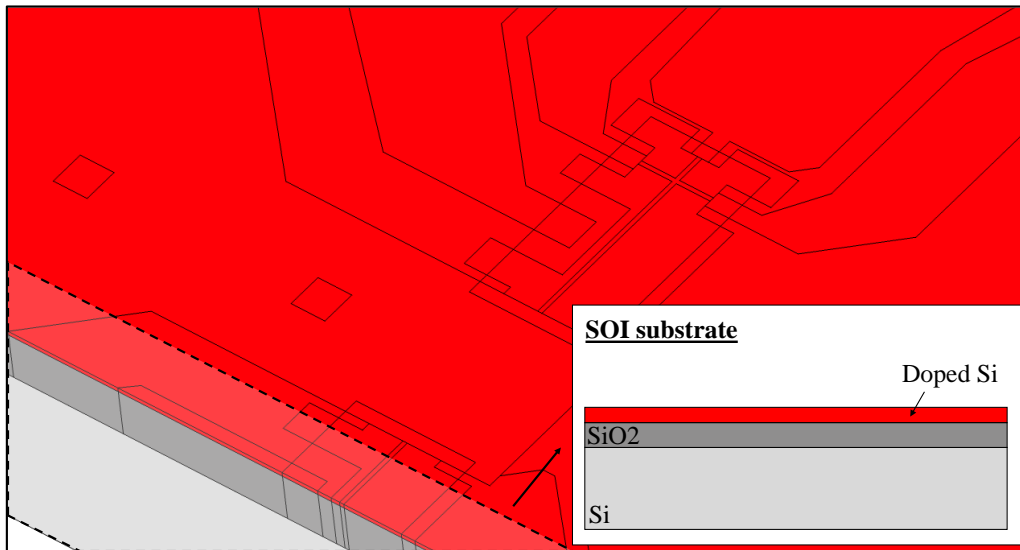


Figure 3-3 Composition of the initial wafer used in the fabrication of the nano-beam resonant accelerometer. A silicon (Si) substrate is separated from the nanoscale active layer by a sacrificial oxide (SiO₂). The active layer is then doped to give it piezoresistive properties.

M&NEMS technology is manufacturing process that allows combining a micrometric active layer with a nanometric active layer. The advantage of this technology is the association of two mobile mechanical objects of different sizes offering a high sensitivity and the possibility to integrate out-of-plane accelerometers. In addition, the *M&NEMS* technology has a wafer-level packaging step allowing the mechanical structures to operate in vacuum environment.

Figure 3-3 presents the initial steps of the *M&NEMS* technology, which define the nanometric active layer. The manufacturing process starts with a Silicon-on-Insulator (SOI) wafer. The Si device layer is doped to make it conductive and give it piezoresistive properties. It is then thinned to a thickness of 250 nm.

Figure 3-4 shows the etching and protection of the nanoscale patterns. First, the nanoresonator are patterned and etched (Figure 3-4-a). Then, an oxide layer is deposited to protect the nanoscale elements (Figure 3-4-b). This oxide layer is then partially etched away to leave only a localized protective layer on the nanoresonator (Figure 3-4-c).

Figure 3-5 shows the growth and etching of the micrometric active layer. First a micrometric epitaxy is performed (Figure 3-5-a), then the micrometric patterns are etched by reactive ion etching (DRIE) to the oxide layer (Figure 3-5-b). Finally the release of the micrometric and nanometric patterns is achieved by HF wet etching (Figure 3-5-c) of this oxide layer. In addition to have stress gradient on the device due to the SOI process, this release generates additional compressive pre-stress in the nanoresonator of about 150 MPa.

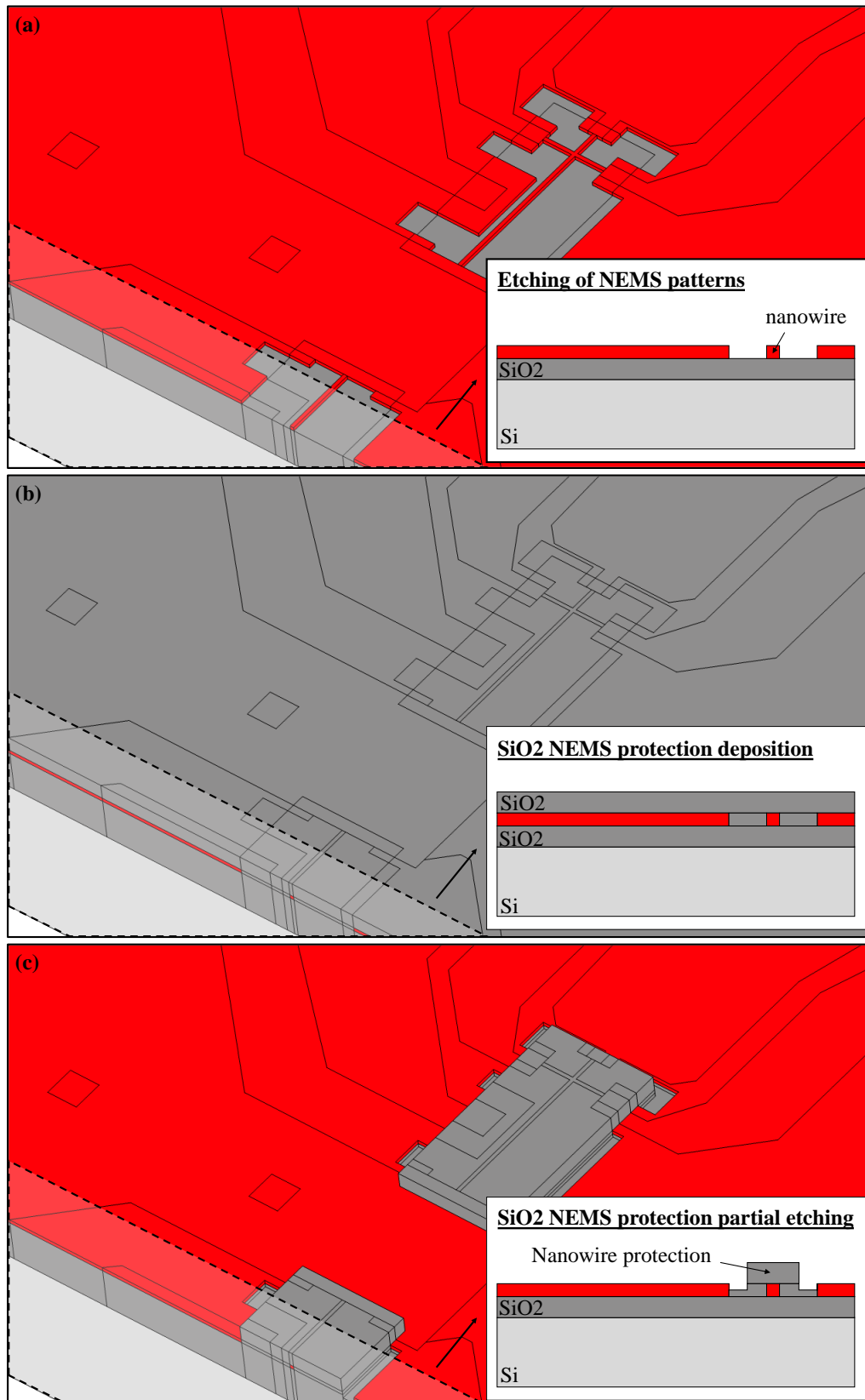


Figure 3-4 Fabrication of the nano-patterns. The resonant beams are first etched (a) and then covered by an oxide (b). The oxide is then partially etched to provide localised protection for the nano beams (c).

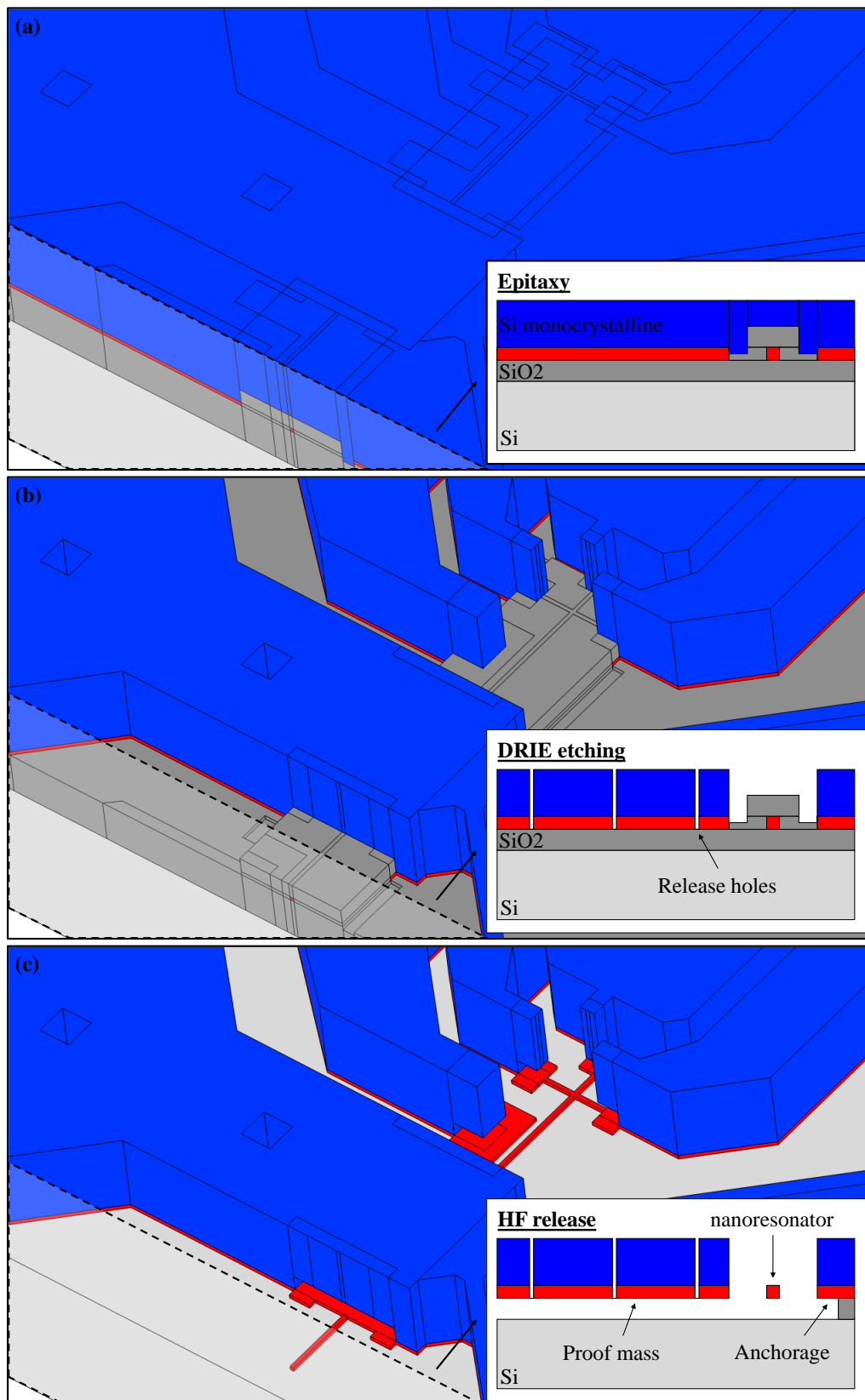


Figure 3-5 Fabrication of the micrometric patterns. The micrometric layer is epitaxially grown (a) and then the micrometric patterns are etched (b). The sacrificial oxide is then etched away by HF vapour to release the entire structure (c).

3.1.2 Nanoresonator design

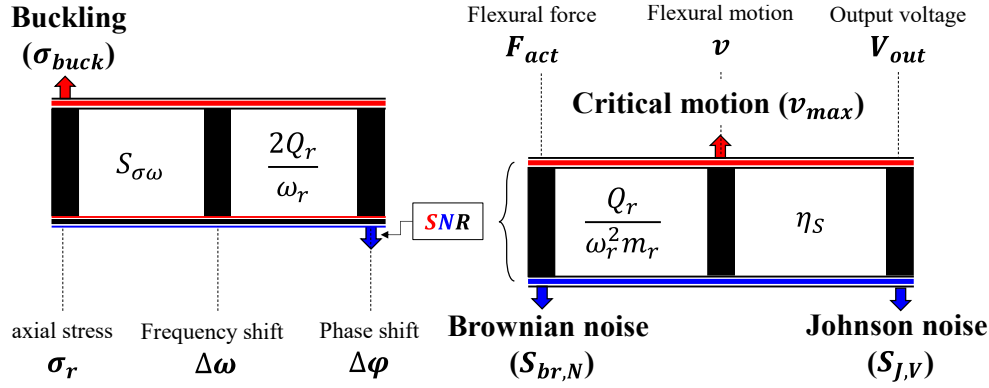


Figure 3-6 Block diagrams representing the dynamic range of a nanoresonator used as a force sensor. On the right the transduction of the bending motion, limited by the critical amplitude before non-linearity and by the Johnson and thermomechanical noises. On the left the force transduction, limited by the buckling stress and the SNR of the additive noises.

This subsection presents the design of a nanoresonator used as a force sensor. Because the nanoresonator measures axial stress by the variation of its resonance frequency, the minimum detectable frequency is equivalent to a minimum detectable stress $\sigma_{min,r}$. The objective of the nanoresonator design is to minimise $\sigma_{min,r}$ in order to optimise the resolution of the accelerometer.

Figure 3-6 presents the two transduction chains of a nanoresonator that allow expressing the minimum measurable stress $\sigma_{min,r}$. On the left, the frequency transduction chain, where the phase-frequency relationship and the sensitivity of the frequency to the stress $S_{\sigma\omega}$ allow expressing $\sigma_{min,r} = [\omega_r/2Q_r S_{\sigma\omega}] \Delta\phi_{min,r}$. On the right, the nanoresonator readout transduction chain where the inverse of Signal to Noise Ratio (SNR) sets the minimum measurable phase $\Delta\phi_{min,r} = 1/SNR$. The SNR is limited by the critical amplitude before nonlinearity v_{max} as well as by the additive noises of the system (the output voltage V_{out} suffers from Johnson noise $S_{J,V}$ and the actuation force F_{act} suffers from thermomechanical noise $S_{br,N}$). Considering the pre-stress σ_{PS} as an initial stress imposing an operating point ($S_{\sigma\omega} \propto \omega_{0r}/[2\sigma_{buck}\sqrt{1 + \sigma_{PS}/\sigma_{buck}}]$ and $\omega_r = \omega_{0r}\sqrt{1 + \sigma_{PS}/\sigma_{buck}}$), the minimum stress detectable by the nanoresonator is thus proportional to the inverse of the SNR

$$\sigma_{min,r} = \frac{\omega_r}{2Q_r S_{\sigma\omega}} \Delta\phi_{min} = \frac{\sigma_{buck} + \sigma_{PS}}{Q_r SNR} \left[\frac{Pa}{\sqrt{Hz}} \right] \quad 3-1$$

The buckling stress σ_{buck} is the maximum allowable stress on the nanoresonator which must be added the pre-stress σ_{PS} . Therefore the dynamic range is

$$DR \propto Q_r SNR \text{ [dB]} \quad 3-2$$

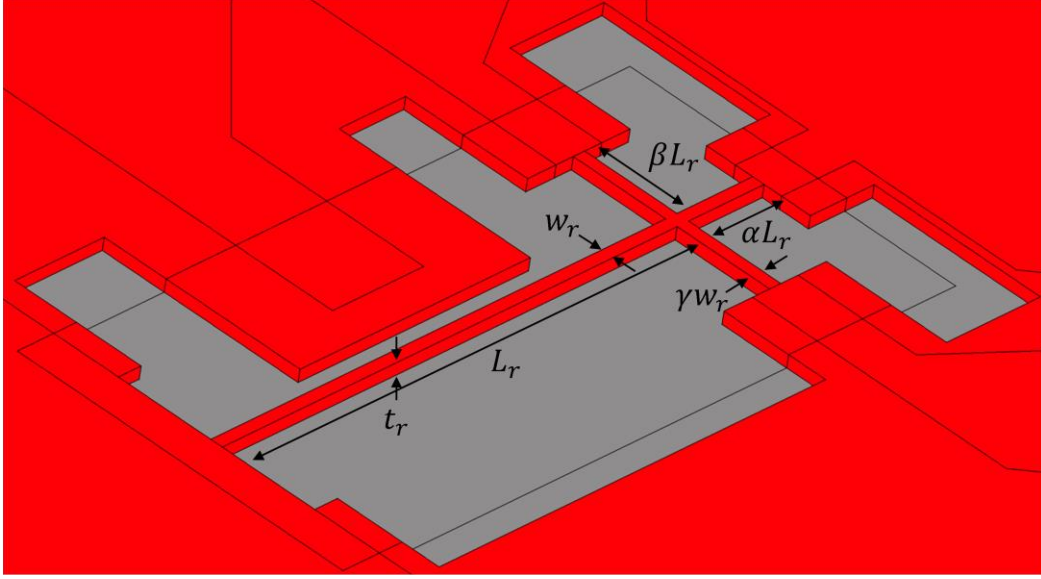


Figure 3-7 Geometrical description of the piezoresistive nanoresonator. The nanoresonator is composed of 3 parts: a resonant beam, two nanogauges orthogonal to the resonant beam and a beam-end, which is the extension of the resonant beam.

The improvement of the measurement of the nanoresonator in terms of SNR allows improving dynamic range and resolution of the accelerometer ($\sigma_{min,r}$). The nanoresonator design aims at improving the SNR due to the different additive noises. Figure 3-7 presents the nanoresonator geometry. In order to reduce the system parameters, the dimensions of the nanogauges providing the piezoresistive transduction are expressed as a function of the dimensions of the resonant beam. Each element of the nanoresonator has the same thickness t_r . The resonant beam has a length and width of L_r and w_r respectively. The beam-end has the same width as the resonant beam and a length αL_r . The gauges have length and width βL_r and γw_r respectively. The piezoresistive transduction parameters (α, β, γ) are called PTP afterwards.

The SNR is expressed between parameters of the same nature. The critical amplitude v_{max} is then expressed in terms of output voltage through the transduction gain η_s in order to be compared to the Johnson noise. Similarly, v_{max} is expressed in terms of force through the actuation gain to be compared to the thermomechanical noise:

$$\left\{ \begin{array}{l} SNR_j = \frac{\eta_s v_{max}}{\sqrt{S_{j,v} BW}} \text{ [rad}^{-1}\text{]} \\ SNR_{br} = \frac{v_{max} \left[\frac{\omega_r^2 m_r}{Q_r} \right]}{\sqrt{S_{br,N} BW}} \text{ [rad}^{-1}\text{]} \end{array} \right. \quad 3-3$$

The SNRs are expressed as a function of the integration bandwidth BW . In this case, the thermomechanical noise is equivalent to white noise defined to Eq. 2-35.

The mechanical limits (maximum linear amplitude of vibration and the thermomechanical noise) depend on both geometric parameters (w_r, L_r, t_r) and manufacturing process parameters (Q_r, σ_{PS})

$$\left\{ \begin{array}{l} v_{max} \propto \sqrt{\frac{w_r^2}{Q_r} \left(1 + \frac{\sigma_{PS}}{\sigma_{buck}}\right)} \quad [\mathbf{m}] \\ \sqrt{S_{br,N}} \left[\frac{Q_r}{\omega_r^2 m_r} \right] \propto \sqrt{\left[\frac{L_r^5}{w_r^4 t_r} \right] \left[\frac{Q_r}{\left(1 + \frac{\sigma_{PS}}{\sigma_{buck}}\right)^{\frac{3}{2}}} \right]} \quad \left[\frac{\mathbf{m}}{\sqrt{\mathbf{Hz}}} \right] \end{array} \right. \quad 3-4$$

The electrical limits depend on the geometrical parameters (w_r, L_r, t_r) but also on the PTP (α, β, γ). From its definition (Eq. 2-33), the transduction gain η_S is a function of resonant beam geometry and PTP. Moreover $S_{J,V}$ (Eq. 2-34) is a function of the nanoresonator output resistance R_{out} thus, (w_r, L_r, t_r) and (α, β, γ):

$$\left\{ \begin{array}{l} \eta_S \propto \frac{\eta_v}{\beta L_r} \quad \left[\frac{\mathbf{V}}{\mathbf{m}} \right] \\ \sqrt{S_{J,V}} \propto \sqrt{\left[\frac{L_r}{w_r t_r} \right] \left[\frac{\beta}{2\gamma} + \alpha \right]} \quad \left[\frac{\mathbf{V}}{\sqrt{\mathbf{Hz}}} \right] \end{array} \right. \quad 3-5$$

SNR optimization is first discussed for a fixed PTP deduced from previous nanoresonator designs: $(\alpha, \beta, \gamma) = (0.15, 0.2, 1)$. Only the design of the resonant beam (w_r, L_r, t_r) is optimised to maximise SNRs. In order to simplify the design process, some design rules are proposed. The designer must choose the working frequency of the nanoresonator ω_{0r} in order to fix the length of the nanoresonator according to its width: $L_r \propto \sqrt{w_r}$. The nanoresonator buckling is the minimum allowable stress before out-of-plane or in-plane buckling, respectively proportional to the nanoresonator thickness and width. To reduce resonant beam design parameters, the two dimensions of the beam are equalized by $w_r = t_r$. For the fixed the PTP and expected pre-stress ($\sigma_{PS} = -150 \text{ MPa}$) the SNRs depend only on the width of the beam, the vacuum level of the working environment (represented by Q_r) and the integration bandwidth:

$$\left\{ \begin{array}{l} SNR_{min,J} \propto w_r^{1.25} Q_r^{-0.5} \sqrt{BW} \quad [\mathbf{rad}^{-1}] \\ SNR_{min,br} \propto w_r^{2.25} Q_r^{-1} \sqrt{BW} \quad [\mathbf{rad}^{-1}] \end{array} \right. \quad 3-6$$

With the thickness-width equality design rule $\sigma_{buck} \propto w_r$ thus, from Eq. 3-1 and 3-6 the minimum detectable stress, in terms of stress spectral density, are

$$\left\{ \begin{array}{l} \sigma_{min,J} \propto w_r^{-0.75} Q_r^{-0.5} \quad [\mathbf{Pa}/\sqrt{\mathbf{Hz}}] \\ \sigma_{min,br} \propto w_r^{-1.25} \quad [\mathbf{Pa}/\sqrt{\mathbf{Hz}}] \end{array} \right. \quad 3-7$$

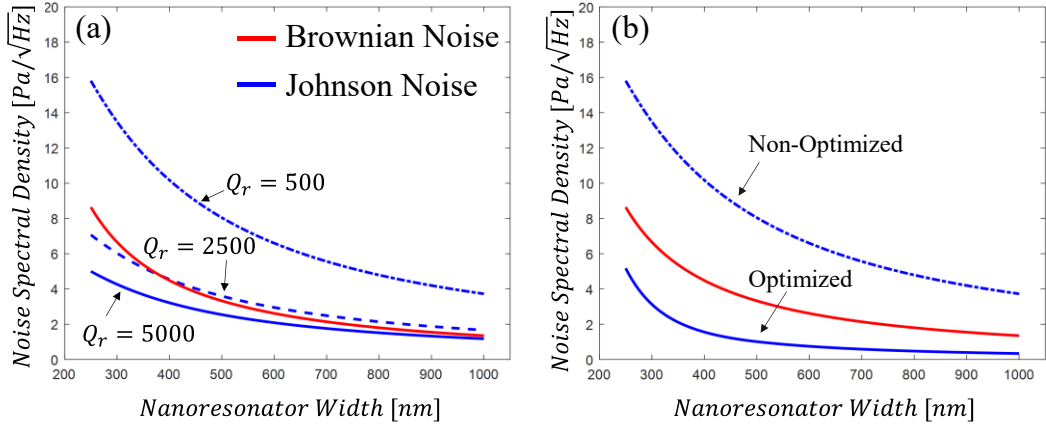


Figure 3-8 Power spectral density of stress fluctuations as a function of nanoresonator width for a pre-stress $\sigma_{ps} = -150 \text{ MPa}$, a working frequency $f_{or} = 20 \text{ MHz}$ and the initial PTP $(\alpha, \beta, \gamma) = (0.15, 0.2, 1)$. (a) In red the minimum stress imposed by Brownian noise, in blue the minimum stress imposed by Johnson noise as a function of different quality factors. (b) Improvement of the minimum detectable stress through the optimization of the Johnson noise. In red the minimum stress imposed by the Brownian noise, in blue the minimum stress imposed by the Johnson noise for a quality factor $Q_r = 500$. The solid line for the initial PTP, the other for an optimized PTP as a function of nanoresonator width w_r .

Figure 3-8 (a) shows that the minimum detectable stress for different noise sources is optimised for large nanoresonators. As expected from Eq. 3-7, the minimum stress set by the Johnson noise is inversely proportional to the vacuum level of the environment. For low quality factors, the Johnson noise limits the resolution of the nanoresonator. For high quality factors, it is the thermomechanical noise that limits the resolution of the nanoresonator. This mechanical limit represents the maximum achievable resolution for a given nanoresonator.

From the definition of SNR_J (Eq. 3-3), the definition of its terms (Eq. 3-5) and the reduction of resonant beam parameters $(w_r, t_r, L_t) \rightarrow (w_r)$, the improvement of the minimum stress set by the Johnson noise can be discussed through the SNR_J optimization

$$SNR_J \propto \frac{w_r^{1.25}}{\beta} \left(\sqrt{\frac{\beta}{2\gamma}} + \alpha \right)^{-1} \eta_v [\text{rad}^{-1}] \quad 3-8$$

Besides, we can observe that: (1) In addition to the dependence of SNR_J express in Eq. 3-6, the displacement gain η_v (Eq.2-29) is also improved by increasing w_r . (2) the deformation gain η_e can be improved by decreasing nanogauge length, i.e. β . (3) The Johnson noise $S_{J,V}$ can be reduced by increasing the nanogauge section, i.e. γ and decreasing the nanogauge length, i.e. β and α . (4) As detailed on the Appendix A, the displacement gain η_v can be improved by increasing the nanogauge length β and decreasing the nanogauge section γ . Moreover, for each resonant beam width, η_v has an optimum value for specific beam-end length, i.e. $\alpha = \alpha_{op}$.

In conclusion, the optimization of SNR_J starts with the choice of a beam width. Once w_r is fixed, two phenomena are in competition. On one hand the Johnson noise $S_{J,V}$ must be reduced ($\alpha \downarrow, \beta \downarrow, \gamma \uparrow$). On the other hand, the sensing gain must be maximized. For this purpose, the deformation gain η_ϵ must be improved ($\beta \downarrow$) as well as the displacement gain ($\beta \uparrow, \gamma \downarrow, \alpha = \alpha_{op}$). Thus, there is an optimum set of PTP ($\alpha_{op}, \beta_{op}, \gamma_{op}$) where the SNR_J is optimized. Thanks to an optimization algorithm, the best PTP are calculated for each value of resonant beam width. Figure 3-8 (b) shows the minimum detectable stress on the nanoresonator for the worst case ($Q_r = 500$). The dashed curve shows that for the initial PTP $(\alpha, \beta, \gamma) = (0.15, 0.2, 1)$ the Johnson noise dominated the resolution of the nanoresonator. The continuous curve shows that for an optimal PTP, calculated as a function of the nanoresonator width, Johnson noise is not limiting over the size range of the nanoresonator width.

In order to go on with the global design of the accelerometer, here is a summary of the important points of the nanoresonator design:

- The designer decides on a working frequency of the nanoresonator and estimates its quality factor. For a nanoresonator operating in vacuum $500 < Q_r < 5000$. The bandwidth of the nanoresonator must be higher than the bandwidth of the accelerometer, $\omega_r/2Q_r > \omega_{0m}$ in order to consider $S_{br,N}$ as white noise and avoid the problem related to the Leeson effect presented in section 3.2.2.
- The designer decides on a suitable nanoresonator width for the targeted application. Considering that the resolution of the nanoresonator ($\sigma_{min,r}$) is optimized with wide nanoresonators while the sensitivity of the accelerometer (Eq. 3-9) is optimized with thin nanoresonators.
- The designer optimizes the piezoresistive transduction of the nanoresonator according to the chosen width and taking into account the etching limits of the manufacturing process. In our specific case the gauge and beam-end lengths are limited to $\alpha_{min}L_r = \beta_{min}L_g = 500 \text{ nm}$ and the gauge width is limited to $\gamma_{min}w_r = 250 \text{ nm}$.

3.1.3 Accelerometer design

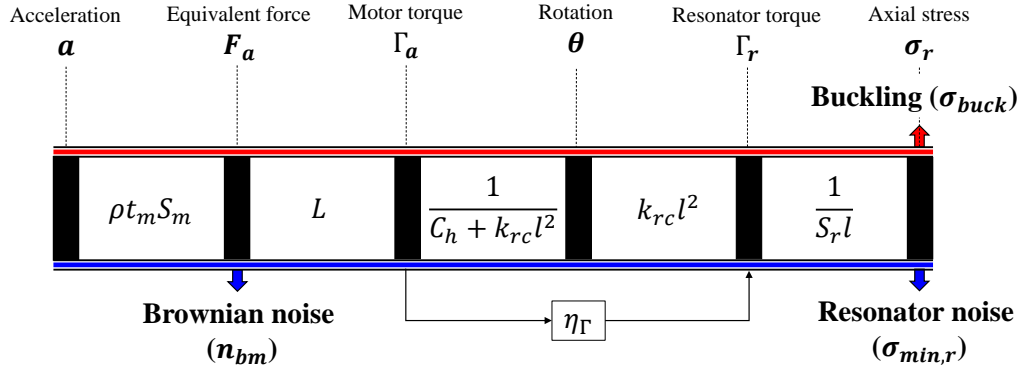


Figure 3-9 Block diagram of the transduction of a pendulum accelerometer. The dynamic range is limited by the maximum axial stress (red) and by the different noise sources (blue).

This subsection presents the design of an in-plane accelerometer. In order to benefit from increased sensitivity, a pendulum accelerometer architecture (Figure 3-10) is used. It takes advantage of a lever arm effect while reducing the sensor footprint by grouping the anchor points of the different elements in a reduced space. The first generation of nano-beam resonant accelerometers based on lever-arm architecture allows grouping 3-axis accelerometers on 12.5 mm²-chips. However, the pendulum architecture is not adapted to large mass-low bandwidth accelerometers.

Figure 3-9 describes the sensitivity $S_{\sigma a}$ of the axial stress on the nanoresonators to the input acceleration. The acceleration force F_a generated by the proof mass (characterized by a mass and density, $\rho t_m S_m$) is amplified by a lever arm of length L . The motor torque Γ_a is then transmitted into a torque on the nanoresonator Γ_r . Under the assumption of a small mass rotation θ , this input torque is proportional to the axial stress σ_r experienced by the nanoresonators. The gain η_Γ between the input torque and the torque experienced by the nanoresonators reflects the distribution of the deformation energies between the flexible elements: On one hand the hinges represented by a torque C_h and on the other hand the torque stiffness of the nanoresonators $k_{rc} l^2$ positioned at a distance l from the centre of thrust of the hinges. The sensitivity of a pendulum accelerometer is then proportional to the ratio between the mass area S_m and the cross-sectional area of the nanoresonators S_r , the lever arm effect and the deformation energy distribution:

$$S_{\sigma a} \propto \left[\frac{S_m}{S_r} \right] \left[\frac{L}{l} \right] [\eta_\Gamma] \left[\frac{Pa}{m \cdot s^{-2}} \right] \quad 3-9$$

The design of the accelerometer starts with the expression of the main specifications as a function of the sensitivity. On one hand, the bandwidth of the accelerometer, limited by the resonance frequency of the proof mass ω_{0m} , is inversely proportional to the square root of the sensitivity. On the other hand, because it is intended that the resolution of the accelerometer is fixed by the resolution of the nanoresonators,

the resolution of the accelerometer $a_{min,r}$ is proportional to the inverse of the sensitivity.

$$\begin{cases} a_{min,r} = \frac{\sigma_{min,r}}{S_{\sigma a}} \propto \frac{\sigma_{min,r} l S_r}{S_m L \eta_\Gamma} \left[\frac{\mathbf{m} \cdot \mathbf{s}^{-2}}{\sqrt{\mathbf{Hz}}} \right] \\ \omega_{0m} = \sqrt{\frac{k_{rc} l}{S_{\sigma a} L}} \propto \frac{l}{L} \sqrt{\frac{S_r}{S_m L_r \eta_\Gamma}} [\mathbf{rad}] \end{cases} \quad 3-10$$

Since the design objective is to maximise the bandwidth while minimising the resolution of the sensor, the ratio between bandwidth and resolution represents the figure of merit (FOM) of the accelerometer

$$FOM = \frac{\omega_{0m}}{a_{min,r}} \propto \frac{\sqrt{S_{\sigma a}}}{\sigma_{min,r}} \propto \frac{1}{\sigma_{min,r}} \sqrt{\frac{\eta_\Gamma S_m}{L_r S_r}} \left[\frac{\mathbf{rad} \sqrt{\mathbf{Hz}}}{\mathbf{m} \cdot \mathbf{s}^{-2}} \right] \quad 3-11$$

Optimising the accelerometer FOM is achieved by maximising the gain η_Γ between the motor torque and the torque on the nanoresonators, maximising the ratio S_m/S_r and minimising the detection limit of the nanoresonator $\sigma_{min,r}$.

Figure 3-10 shows the different geometrical parameters of the pendulum accelerometer architecture. The proof mass is composed of a square with side L_m completed by a triangle for a total mass footprint of $S_m = 5/4 L_m^2$ and a lever arm of length $L = 13/15 L_m$. This proof mass is suspended by two orthogonal hinges of length L_h , width w_h and thickness t_m which form a pivot point at their intersection. The nanoresonators, with compressive stiffness k_{rc} , are placed at a distance l from the centre of thrust of the pivot.

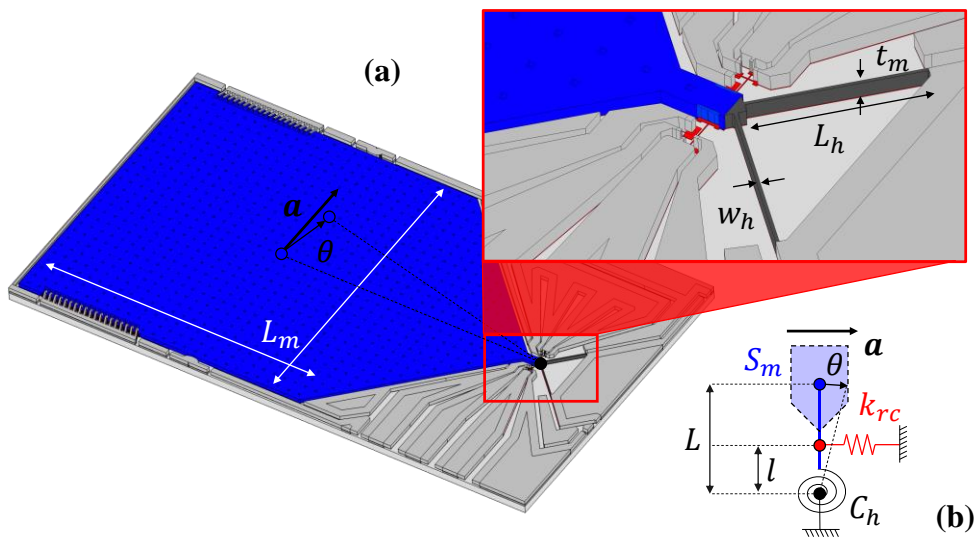


Figure 3-10 Presentation of the architecture of a pendulum accelerometer. (a) The geometry of the accelerometer and (b) its equivalent mechanical diagram. In blue the seismic mass, in red the nanoresonators and in black the flexible suspension elements.

For a pendulum accelerometer, the gain between the motor torque and the torque experienced by the nanoresonator depends on the ratio between the hinge angular stiffness relative C_h and the nanoresonator equivalent angular stiffness $l^2 k_{rc}$.

$$\eta_r = \frac{1}{1 + \frac{C_h}{l^2 k_{rc}}} [A.U] \quad 3-12$$

Maximising the gain between the motor torque and the torque experienced by the nanoresonator ($\eta_r \rightarrow 1$) is equivalent to softening the hinge's angular stiffness relative to the nanoresonator's equivalent angular stiffness ($C_h \ll k_{rc} l^2$). For this purpose it is necessary to increase the length of the hinges L_h (because $C_h \propto w_h^3 t_m / L_h$), to increase the compressive stiffness of the nanoresonator k_{rc} or to increase the distance between the nanoresonator and the pivot point l .

On one hand, if L_h or k_{rc} are increased, the equivalent nanoresonator stiffness becomes non-negligible with regards to the hinge's compression stiffness, and therefore the rotation center moves towards the nanoresonator. In other words, the arm compresses the hinge to turn around the nanoresonator. In this case, since the axis of rotation is closer to the nanoresonator than expected, the distance between the nanoresonator and the axis of rotation l is smaller. Thus, the lever arm force gain does not benefit from this increase in displacement gain. This is purely a loss of efficiency. Moreover, increasing L_h is a risky strategy because the out-of-plane sensitivity of the accelerometer is proportional to L_h^3 . On the other hand, if the nanoresonator distance l increases, the theoretical lever arm gain L/l decreases.

Another solution is to reduce the distance l of the nanoresonators by placing them closer to the hinge in order to increase the theoretical lever arm gain L/l . In this case, the lever arm force gain $L/l \times \eta_r$ increases because the benefit of the ideal gain is bigger than loss of η_r . However, for small l , $\eta_r \rightarrow 0$, and the lever arm force gain is null. There is a maximum of $L/l \times \eta_r$ when $\eta_r = 1/2$, i.e. when the hinge angular stiffness is equal to the nanoresonator equivalent angular stiffness ($C_h = k_{rc} l^2$). In other words, when there is a balanced strain energy distribution between the hinge and the nanoresonator. This balance is achieved for a specific geometry. In order to match the accelerometer design to the previous nanoresonator design, the specific geometry is set by the hinge geometry. In this way, the nanoresonator geometrical parameters S_r , L_r and l , respectively cross section, length and position are used to define the optimal hinge length :

$$L_{h,op} = \frac{2t_m w_h^3 L_r}{3l^2 S_r} [m] \quad 3-13$$

Here, the hinge thickness t_m is fixed by the manufacturing process and the hinge width w_h must be minimized to reduce the hinge length and thus the out-of-plane stiffness of the accelerometer ($\propto L_h^3$).

Maximising the area ratio between the footprint of the proof mass and the cross-section of the nanoresonator ($S_r \ll S_m$) is the main advantage of the *M&NEMS* technology. It is essential to keep a large aspect ratio between these two surfaces to propose a FOM that exceeds that of conventional micrometric architectures as well as to maintain the possibility of a three-axis sensor (this is also due to the uncentred position of NEMS layer relative to MEMS layer).

On one hand, given the properties and dimensions of the nanoresonator, i.e. $S_r, \sigma_{min,r}, L_r$ and l , an equivalent minimum acceleration imposed by the nanoresonator can be expressed as $a_{min,r} = \sigma_{min,r}/S_{\sigma a}$. On the other hand, given the properties and dimensions of the accelerometer, i.e. $S_m, S_{bm,N}$ and t_m , an equivalent minimum acceleration measurable imposed by the thermomechanical noise of the accelerometer can be expressed as $a_{min,m} = \sqrt{S_{bm,N}}/\rho t_m S_m$: this will be named MEMS noise. There exists an optimum characteristic length of the mass in which the MEMS noise is equal to the noise of the nanoresonator $a_{min,r} = a_{min,m}$:

$$L_{m,op} \propto \sigma_{min,r} \sqrt[4]{S_r^3 L_r \sqrt{Q_m l}} \quad [m] \quad 3-14$$

Figure 3-11 presents the strategy to set this optimum point. In order to show the trend in a 2D plane, the position of the nanoresonator is fixed at $l = 5 \mu m$. But this strategy is applicable to all nanoresonator positions. Figure 3-11 (a) shows the acceleration resolutions limited by the nanoresonator and the MEMS noise as a function of the proof mass length: $a_{min,r} \propto L_m^{-3}$ and $a_{min,m} \propto L_m^{-2}$. The optimum proof mass length $L_{m,op}$ is the length where $a_{min,r} = a_{min,m}$. If $L_m < L_{m,op}$ the noise of the nanoresonator dominates the MEMS noise ($a_{min,r} > a_{min,m}$) and the opposite if $L_m > L_{m,op}$. In practice, increasing the length of the mass reduces both the nanoresonator noise and the MEMS noise. In addition, Figure 3-11 (b) shows that the accelerometer bandwidth is proportional to $\omega_{0m} \propto L_m^{-2}$, so it decreases in the same way as $a_{min,m}$. Figure 3-11 (c) shows that the FOM limited by the nanoresonator's noise is proportional to L_m while the FOM limited by the MEMS noise is constant with respect to L_m .

Since the accelerometer noise is set by the dominating noise source, the accelerometer's FOM is therefore the minimum FOM of the two noise sources. In Figure 3-11 (c), the FOM of the accelerometer is represented by the black dashed line. The optimum FOM is then the constant plateau reached after the optimum proof mass length $L_{m,op}$. In other word, for each proof mass length $L_m > L_{m,op}$ the FOM is maximized. Here, the resolution/bandwidth trade-off can be set with L_m according to the required specifications. However, it is important to note that the proof mass should not exceed a specific size as the out-of-plane sensitivity of the pendulum architecture is proportional to it ($L_m < 750 \mu m$).

Furthermore, it is important to note that the improvement in wafer-level packing, i.e. increase in Q_m , can be represented as an increase in the constant plateau of the FOM bounded by $a_{min,m}$. In this way, the FOM of the accelerometer can reach a better value due to better resolution. The best case being when $Q_m > 1000$ which implies that the FOM of the accelerometer is no longer limited by the FOM of the MEMS noise but by the FOM of the nanoresonator noise.

Based on previous analysis of the M&NEMS accelerometer [67], [82]–[84], the damping of the accelerometer is assumed to be limited by the squeeze-film damping due to the packing-induced vacuum level at the wafer ($\sim mBar$) and the $5\ \mu m$ gap surrounding the proof mass. In this way, the value of the accelerometer quality factor is fixed to $Q_m < 1000$ for the first design. In conclusion, to avoid out-of-plane issues due to a large mass as well as to have the highest bandwidth for optimal FOM, the most optimal length of the proof mass is $L_m = L_{m,op}$.

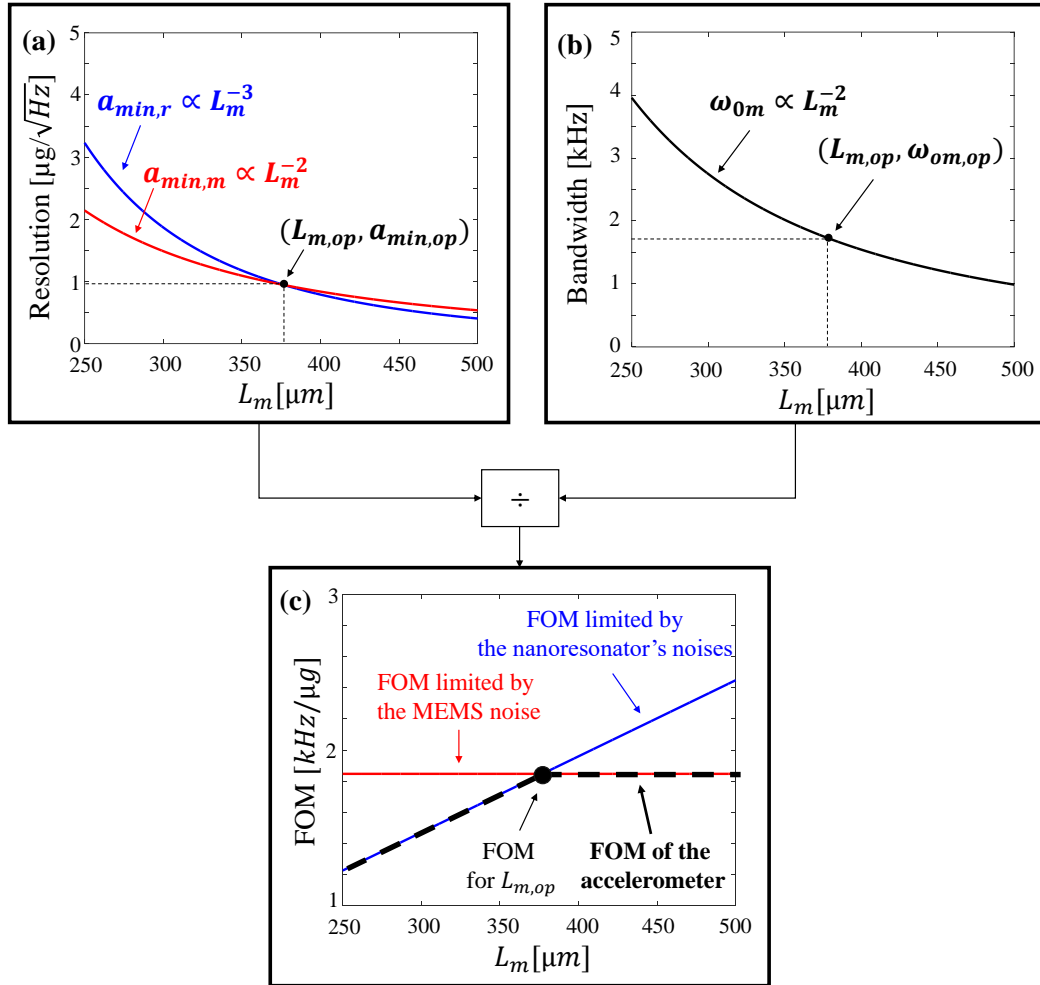


Figure 3-11 Optimization of the resolution/bandwidth ratio of the accelerometer as a function of L_m . (a) Accelerometer resolutions set by the noise of the MEMS and the noise of the nanoresonator as a function of proof mass length. (b) Accelerometer bandwidth as a function of proof mass length. (c) Accelerometer FOM as a function of proof mass length. The analytical model is done for $l = 5\ \mu m$ and $Q_m = 250$.

3.1.4 Design strategy

In this section I propose a design strategy based on the study of the designs of the resonator and the accelerometer, and then I use it to propose designs for the first generation of nano-beam resonant accelerometers. Figure 3-12 summarizes the previous design rules step by step in order to have an overview of the design strategy. The process is explained thanks to proportionality functions. The complete functions are detailed on Appendix A.

From a set of requested specifications and initial assumptions, the nanoresonator geometry (w_r, t_r, L_r) is reduced to the nanoresonator width w_r . Then, the nanoresonator optimisation, based on the improvement of piezoresistive transduction, allows expressing the nanoresonator resolution $\sigma_{min,r}$ as a function of w_r . In parallel, the energy balance condition allows expressing the hinge length as a function of w_r and l and the accelerometer sensitivity $S_{\sigma a}$ as a function of w_r , l and L_m . Through the sensitivity and the nanoresonator resolution, the acceleration resolutions $a_{min,r}$ and $a_{min,m}$ as well as the accelerometer resonance ω_{0m} can be expressed as a function of geometric parameters (L_m , w_r and l). The objective of this design strategy is to match the acceleration resolutions (MEMS and nanoresonator) in order to reduce the geometric parameters by expressing L_m as a function of l and w_r , and then setting the accelerometer specifications and other geometric parameters (L_h and L_m).

After fixing the accelerometer noise equality, the design of the accelerometer (L_m and L_h) as well as the accelerometer performance (a_{min}) can be set by the nanoresonator width w_r and the nanoresonator position l . As a consequence of the accelerometer noise equality, the accelerometer bandwidth is fixed (Figure 3-11 (c)).

In conclusion, the design strategy based on the energy balance and accelerometer noise equality reduces the design to the choice of the nanoresonator width (w_r) and position (l) at the cost of fixing only the resolution of the accelerometer (a_{min}) and not its bandwidth (ω_{0m}). This strategy is applied in our case because pendulum architecture ensures an accelerometer with a large bandwidth and a small footprint. If the strategy is to look for a high-resolution accelerometer, the equality of the acceleration noise is not necessary and the length of the proof mass must be larger than the optimal value $L_m > L_{m,op}$. This case is not implemented to ensure the operation of the pendulum architecture (a large mass results in out-of-plane sensitivity).

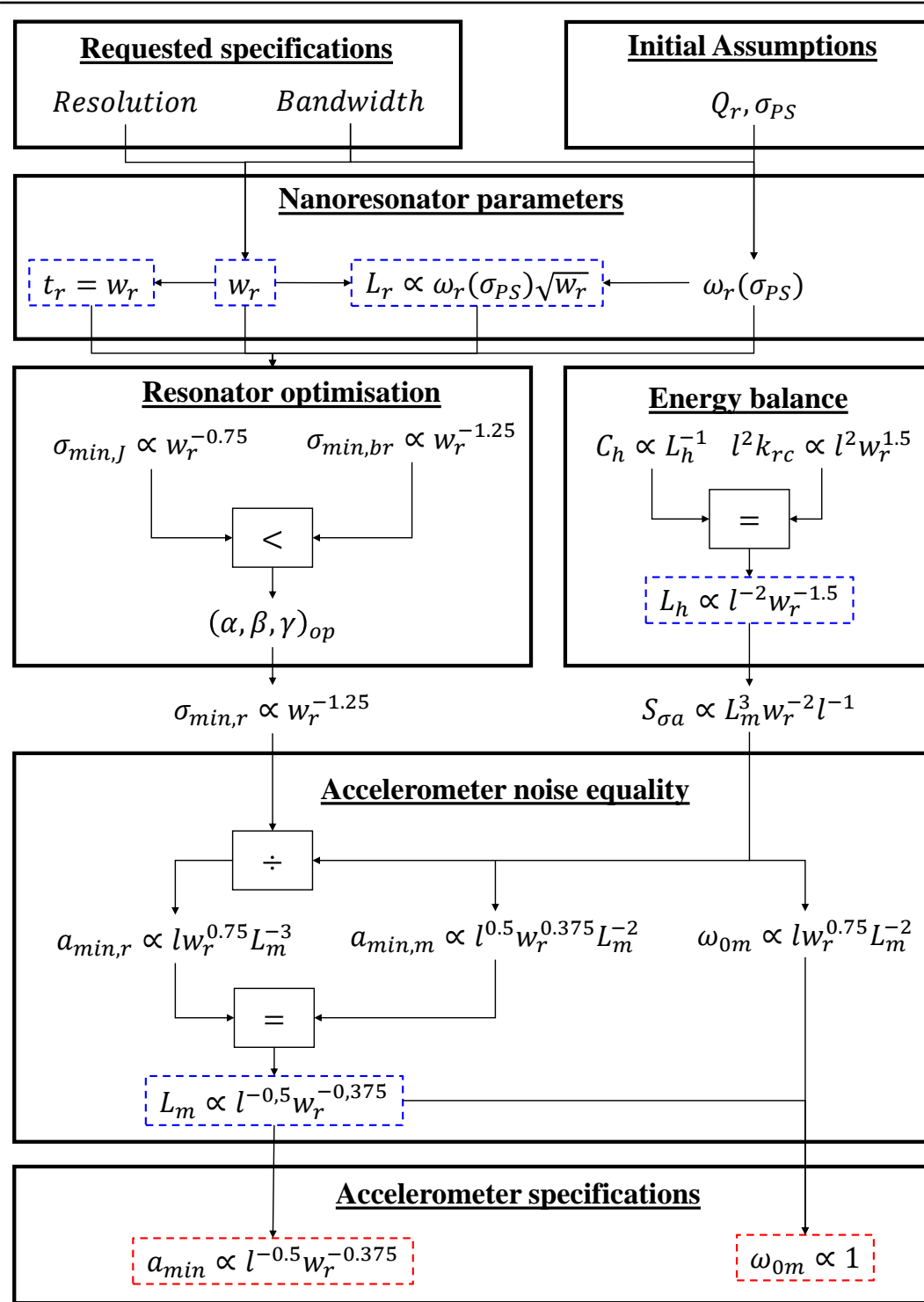


Figure 3-12 Block schematic of the design strategy: the requested specifications and initial assumptions are the beginning of the design proves, and they allow choosing ideal nanoresonator parameters. An optimization of the nanoresonator dimensions can be performed from these parameters in order to maximize its resolution. The energy balance ensures an equitable energy distribution and allows extracting the accelerometer sensitivity. The accelerometer optimization uses this sensitivity to match the nanoresonator resolution with the resolution imposed by thermomechanical noise of the accelerometer. This last step fixes the accelerometer resolution and its bandwidth.

The specifications of the first generation of nano-beam resonant accelerometers are:

- Maintain the small footprint of the M&NEMS piezoresistive accelerometer (footprint $<1 \text{ mm}^2$) and the possibility of three axis accelerometers.
- High-bandwidth accelerometer ($BW \geq 1 \text{ kHz}$).
- Resolution as high as possible (ideally, $a_{min} \leq 1 \mu g / \sqrt{Hz}$).

The following is a proposed methodology to achieve the requested specifications.

The initial assumptions on the quality factors are based on analysis of squeeze film damping [85] and quality factor of piezoresistive nanoresonators used as mass sensors [86]–[88]. Our nanoresonators are actuated with electrode with a gap of 500 nm. The proof mass is surrounded by a gap of 5 μm in average. Under the expected pressure level, the mean free path of the molecules is assumed to depopulate the electrostatic gap of the nanoresonator and thus limit its damping. However, the proof mass is still subject to this damping source because of its larger gap. We will assume here a ratio of 10 between the two effects: the expected accelerometer and nanoresonator quality factors are respectively $Q_m = 250$ and $Q_r = 2000$. Additionally the initial pre-stress imposed on the nanoresonator is $\sigma_{PS} = -150 \text{ MPa}$.

The design starts with the consequences of the choice of the sensor bandwidth. For this first generation of accelerometer, the nanoresonator must be mechanically capable of responding to the sensor bandwidth (BW). I.e. $\omega_r/2Q_r > BW$. To be large, the inverse of the nanoresonator time response ($\omega_r/2Q_r$) is set to 4 kHz

$$\frac{\omega_r(\sigma_{PS})}{4\pi Q_r} = 4 \text{ kHz} \leftrightarrow \omega_r(\sigma_{PS})/2\pi = 16 \text{ MHz} \quad 3-15$$

Thus, the nanoresonator frequency is set to 16 MHz. The impact of pre-stress in the resonance of nanoresonator is not negligible and must be taken into account in the setting of the nano-resonator response time ($\omega_r/4\pi Q_r$). For nanoresonators, quality factors above 5000 are unlikely, but even for $Q_r = 5000$ the nanoresonator time response remains superior to the accelerometer bandwidth.

Because the footprint is an important specification, accelerometer sensitivity must be maximized by minimizing the nanoresonator's cross-section. Although the nanoresonator resolution (Eq. 3-7) is inversely proportional to its width, the nanometric layer is thinned to $t_r = 250 \text{ nm}$ and the nanoresonator width is chosen to the etching limit: $w_r = 250 \text{ nm}$. On this configuration, the ratio between mass footprint and nanoresonator's cross-section is maximized, minimizing the mass footprint.

Next, the resonant beam length is fixed to obtain the resonance frequency (16 MHz) as $L_r = 10 \mu\text{m}$. On this configuration, nanoresonator has an initial resonance frequency of $\omega_{0r}/2\pi = 20 \text{ MHz}$, decreased to 16 MHz due to the initial pre-stress. As mentioned above, the pre-stress phenomenon is not negligible and lowers the

resonance frequency by 20%. In addition to the frequency reduction, the pre-stress phenomenon reduces the full scale of allowable stress. For this nanoresonator geometry, buckling appears for a compressive stress of $\sigma_{buck} \approx 350 \text{ MPa}$. With the expected prestress σ_{PS} , the maximal operating stress range is 200 MPa. The prediction of this parameter is one of the most critical points of the design, as if the usable stress range of the resonator is not large enough the nanoresonators can be buckled after their release or under acceleration operation and thus be unusable.

After the choice of resonant beam geometry, the piezoresistive transduction can be optimized. The dimensions of this particular resonant beam do not allow a complete optimization of the nanogauges. Indeed, for $w_r = 250 \text{ nm}$, the optimal PTP are $(L_t, L_g, w_g) = (500 \text{ nm}, 875 \text{ nm}, 250 \text{ nm})$ that is close to the fabrication process limit (minimum nanowire length and width are respectively 500 nm and 250 nm and nanogauge length cannot be reduced under 1 μm due to the pads contacts). For the first generation of devices, safer PTP are implemented to ensure the functioning of the piezoresistive transduction. The nanoresonator geometries and performances are summarized on Table 7 and Table 8:

w_r	250 nm
t_r	250 nm
L_r	10 μm
w_g	250 nm
L_g	2 μm

Table 7 Nanoresonator geometries

$f_{0r}(\sigma_{PS})$	16 MHz
$n_{V,J}$	4.4 nV/ $\sqrt{\text{Hz}}$
$n_{V,br}$	1.99 nV/ $\sqrt{\text{Hz}}$
v_{max}	2.78 nm
σ_{buck}	357 MPa
$S_{\sigma\omega}(\sigma_{PS})$	0.041 Hz/Pa
$\sigma_{min,J}$	18.39 Pa/ $\sqrt{\text{Hz}}$
$\sigma_{min,br}$	8.3 Pa/ $\sqrt{\text{Hz}}$
σ_{min}	20 Pa/ $\sqrt{\text{Hz}}$

Table 8 Nanoresonator performances

The hinge width is reduced as much as possible, to the limit of fabrication process $w_h = 1 \mu\text{m}$, in order to propose short hinges. The micrometric thickness layer is fixed to $t_m = 20 \mu\text{m}$. Once the nanoresonator geometry is fixed, the equitable energy distribution ($\eta_r = 1/2$) can be set by Eq. 3-13. In this case the hinge length is only fixed by the future nanoresonator position l . Because we chose to implement accelerometer noise equality, the length of the proof mass also becomes a function

of the future position of the nanoresonator l . As a result, the accelerometer bandwidth is set higher the desired bandwidth (1450 Hz) regardless of the position of the nanoresonator, and the resolution of the accelerometer also became a function of the future position of the nanoresonator l .

The last step consists in defining the position of the nanoresonator in order to obtain the best resolution a_{min} taking into account a reasonable design of the accelerometer geometries (L_m and L_h). Figure 3-13 shows an analytical simulation of a_{min} , ω_{0m} , L_h and L_m as a function of the nanoresonator position l . According to the energy balance, the nanoresonator position must be far from zero but not too large, thus l is swept from $2.5 \mu m$ to $10 \mu m$. The model considers $Q_m = 250$, $Q_r = 2000$ and $\sigma_{PS} = -150 MPa$ and it is based on the nanoresonator specifications of Table 7 and Table 8. As expected, Figure 3-13 (a) shows that the bandwidth is not a function of l . Figure 3-13 (b) shows the resolution is close to the resolution range ($\sim 1 \mu g/\sqrt{Hz}$). Thus the choice of the nanoresonator position l considers mainly the critical accelerometer geometries (L_m and L_h). Figure 3-13 (c) shows that, in order to satisfy the energy balance condition, the length of the hinges increase when the nanoresonator position decreases. On the other hand, Figure 3-13 (d) shows the accelerometer noise equality imposes a large proof mass length for a large nanoresonator position. To ensure the operation of the pendulum accelerometer, a short hinge length of $51 \mu m$ is chosen for a reasonable proof mass of $380 \mu m$.

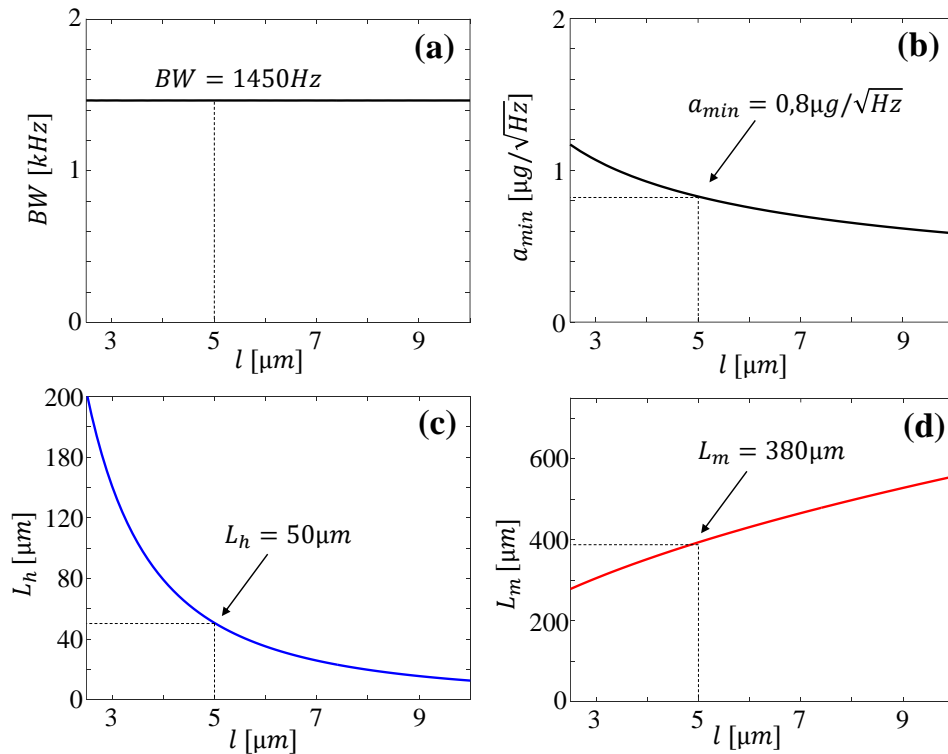


Figure 3-13 Final setting of accelerometer performances and geometries as a function of l . The bandwidth is fixed due to the accelerometer noise equality, so the resolution can be set by positioning the nanoresonator. However, due to the energy balance condition and the accelerometer noise equality the hinge and proof mass lengths depend on the nanoresonator position.

l	$5\ \mu m$
L_m	$380\ \mu m$
t_m	$20\ \mu m$
L_h	$51.41\ \mu m$
w_h	$1\ \mu m$

Table 9 Accelerometer geometry.

f_{0m}	$1450\ Hz$
$S_{\sigma a}$	$21.99\ MPa/g$
$S_{a\omega}$	$0.89\ MHz/g$
a_{max}	$9.44\ g$
$a_{min,r}$	$0.8\ \mu g/\sqrt{Hz}$
$a_{min,m}$	$0.79\ \mu g/\sqrt{Hz}$
$DR_r(\sigma_{PS})$	$139\ dB$

Table 10 Predicted accelerometer performance.

This first subsection focuses on the mechanical design of the resonant beam accelerometer. The initial consideration of the manufacturing process and the strategy due to the high-performance integrated sensor allows the design of the first generation sensor. Based on the analytical modeling of the mechanical structure, a readout electronics dedicated to the measurement of the piezoresistive nanoresonator is developed. The second sub-section presents the co-design of this electronics.

3.2 Design of the electronic readout

By driving the nanoresonator at its initial resonance frequency, an open loop electronic architecture can be used together with the phase-frequency relationship to measure frequency variations. However, this phase-frequency relationship is defined over a very small relative frequency band for nanoresonators ($> 1/2Q_r \sim 0.01\%$). It is therefore impossible to measure the relative frequency variation of a nanoresonator induced by an acceleration ($\sim 10\%$). It is thus essential to employ a closed loop to keep the nanoresonator in resonance and track its frequency in real time. Nanoresonators are passive systems that require energy input to oscillate at their resonance frequency. However, due to energy losses present in the system, the oscillation is damped so an energy input must be maintained. Oscillators are active systems that transform a DC input signal into an oscillating output signal. In combination with a feedback system, a nanoresonator forms an oscillator. In practice, it is the thermomechanical noise of the nanoresonator or other noise sources in the system that initiate the oscillations. This section aims at designing an oscillator to maintain the nanoresonator at resonance and thus to be able to measure frequency variations due to acceleration.

When the signal to be maintained operates at high frequency (> 10 MHz), NEMS based heterodyne self-oscillators [89] allow diminishing the filtering of the signal by down-mixing its frequency. In this type of setup, the down-mixed signal (at frequency $\Delta\omega$) is multiplied by the source oscillator polarising the gauges (at frequency $\omega_r + \Delta\omega$) in order to be reinjected on the feedback path. In a resonant accelerometer the down-mixed signal is modulated by the frequency variation induced by the acceleration (> 1 MHz), which significantly degrades the advantages of this technique. A force feedback loop on the mass [90]–[92] or a PLL-based architecture [50], [93] avoid problems at the cost of expensive electronics. For these reasons, a classical homodyne oscillator is implemented here. This architecture is not very costly in terms of electronics and requires only amplification and phase shifting circuits to reach self-oscillation. The design starts with the choice of low-noise readout electronics that avoid the effect of high frequency filtering. The architecture of the oscillator is then constructed to satisfy the self-oscillation conditions (Barkhausen). In parallel, the background signal due to the electrostatic actuation is compensated by a correction stage.

3.2.1 Adapted readout

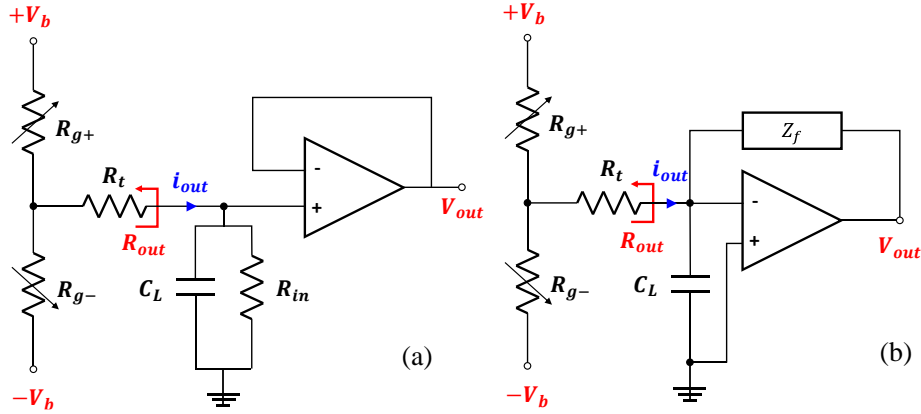


Figure 3-14 Comparison of two readout electronic schemes for a nanoresonator with piezoresistive detection. The readout suffers from filtering due to a parasitic load capacitance C_L . (a) Voltage readout implemented by a load R_{in} in parallel with the parasitic capacitance. (b) Current readout performed by a Transimpedance Amplifier (TIA) which transforms the input current into an output voltage through the impedance Z_f .

The design of the oscillator starts with the choice of the readout electronics adapted to the piezoresistive nanoresonator presented on section 2.5. The transduction architecture consists of two piezoresistive gauges $R_{g\pm} = R_g(1 \pm \delta R)$ differentially modulated by the motion of the resonant beam. These gauges are differentially biased by a DC bias voltage $\pm V_b$. The modulated current i_{out} flows through the load resistor R_t . The equivalent resistance of the strain gauge bridge R_{out} observed from the output node is

$$R_{out} = \frac{R_g}{2} + R_t \quad [\Omega] \quad 3-16$$

Figure 3-14 (a) shows a voltage readout architecture where the output node of the NEMS is loaded by a resistor R_{in} through which the current i_{out} will be transformed into a voltage V_{out} . However, this type of measurement architecture suffers directly from the parasitic capacity C_L that filters the output signal. Because the system operates at high frequency ($\omega_r/2\pi > 10\text{MHz}$) and $R_{in} \gg R_{out}$

$$\frac{V_{out}}{i_{out}} = \frac{R_{out}}{1 + jR_{out}C_L\omega} \quad [\Omega] \quad 3-17$$

Figure 3-14 (b) represents a current readout architecture where the output pin of the nanoresonator is connected to the input of a transimpedance Amplifier (TIA). The amplifier inverses the input current into an output voltage through its feedback impedance Z_f

$$\frac{V_{out}}{i_{out}} = -Z_f \quad [\Omega] \quad 3-18$$

The advantage of this type of detection is that the readout is free from the influence of the parasitic capacitance C_L and can therefore operate at high frequencies with controlled filtering effects.

The current readout offers the best operation for the homodyne detection. An equivalent model of the nanoresonator must be defined in order to integrate its impedance into the overall architecture of the oscillator. Usually, series RLC circuits are used to model the behaviour of the nanoresonator. However, this series circuit is not suitable for a piezoresistive transducing nanoresonator. For example, a DC voltage applied to the NEMS induces an unbalance of the gauge bridge and thus an output current, and the series capacitance of the conventional RLC model does not model this static behaviour. A more accurate model in this case is shown in Figure 3-15, where the capacitance is connected to ground. In this configuration, the impedance of the nanoresonator is expressed as a function of the equivalent capacitance, resistance and inductance C_{eq} , R_{eq} and L_{eq} :

$$Y_{NEMS} = \frac{i_{out}}{V_{AC}} = \frac{1/R_{eq}}{1 + \frac{L_{eq}}{R_{eq}}j\omega + L_{eq}C_{eq}(j\omega)^2} \quad [\Omega^{-1}] \quad 3-19$$

Figure 3-16 compares Y_{NEMS} with classic RCL series circuit admittance: Y_{RLC} . Figure 3-16 (a) is the frequency response of the admittance that shows Y_{NEMS} behaves like second order low-pass filter, where the static gain $|Y_{NEMS}(0)| = R_{eq}^{-1}$ corresponds to the unbalance of the bias voltage, whereas Y_{RLC} does not have a static gain $|Y_{RLC}(0)| = 0$. Figure 3-16 (b) is a complex representation that allows having clearer picture of the frequential behaviour of Y_{NEMS} : At resonance, Y_{NEMS} is purely imaginary. From Eq. 3-19 and Eq. 3-21, $|Y_{NEMS}(\omega_r)| = |1/jL_{eq} \omega_r| = Q_r/R_{eq}$. The admittance at resonance is named equivalent motional admittance $Y_m = Q_r/R_{eq}$. While the equivalent resistance R_{eq} is due to the unbalance of the bias voltage, the motional admittance represents the impedance of the nanoresonator at resonance, and it is due to the unbalance of the bias voltage amplified by the resonance phenomenon (Q_r).

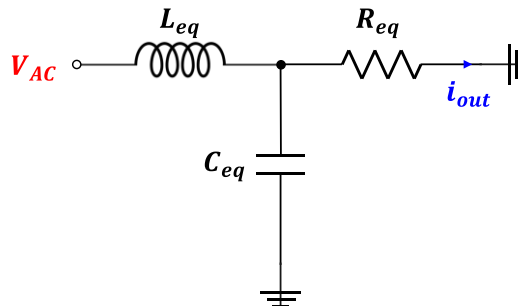


Figure 3-15 Equivalent electrical diagram of the piezoresistive nanoresonator using current readout.

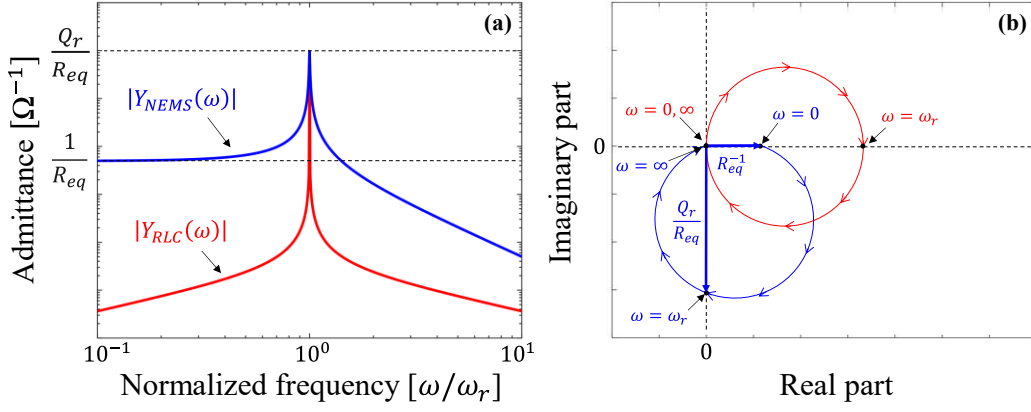


Figure 3-16 Comparison between a classic RLC circuit admittance Y_{RLC} and the model developed here Y_{NEMS} . (a) Frequency response of the admittance as a function of normalized frequency. (b) Complex representation of the admittance: the red circle is Y_{RLC} that starts and ends at $|Y_{RLC}|=0$ for $\omega = (0, \infty)$ and which is real for $\omega = \omega_r$. The blue circle is Y_{NEMS} that starts by real $|Y_{NEMS}| = R_{eq}^{-1}$ for $\omega = 0$, has an imaginary impedance $|Y_{NEMS}| = Q_r/R_{eq}$ for $\omega = \omega_r$ and ends by $|Y_{NEMS}| = 0$ for $\omega = \infty$.

From the electromechanical modelling of the nanoresonator (Figure 2-10)

$$\begin{cases} \frac{\delta R}{V_{AC}} = \frac{\eta/k_{rf}}{1 + \frac{j\omega}{Q\omega_r} + \left(\frac{j\omega}{\omega_r}\right)^2} [V^{-1}] \\ i_{out} = \frac{V_b}{R_{out}} \delta R [A] \end{cases} \quad 3-20$$

where η is the product of actuation gain η_A and sensing gain η_S , and k_{rf} is the flexural stiffness of the nanoresonator. Then, the RLC equivalent parameters can be identified with Eq. 3-20 from Eq. 3-19:

$$\begin{cases} R_{eq} = \frac{k_{rf}R_{out}}{\eta V_b} [\Omega] \\ L_{eq} = \frac{k_{rf}R_{out}}{\eta V_b \omega_r Q_r} = \frac{R_{eq}}{\omega_r Q_r} [H] \\ C_{eq} = \frac{\eta V_b Q_r}{k_{rf}R_{out} \omega_r} = \frac{Q_r}{R_{eq} \omega_r} [F] \end{cases} \quad 3-21$$

In conclusion, the nanoresonator can be considered as an equivalent impedance $Z_{NEMS} = 1/Y_{NEMS}$. In addition, current readout allows avoiding filtering effect of Eq. 3-17 due to the voltage reading performed in parallel on the parasitic capacitor C_L .

The current readout is represented in Figure 3-17 where the actuation voltage V_{AC} is transformed to output voltage V_{out} through the impedance ratio between Z_{NEMS} and Z_f :

$$\frac{V_{out}}{V_{AC}} = -\frac{Z_f}{Z_{NEMS}} = -Z_f Y_{NEMS} \text{ [A.U.]} \quad 3-22$$

Because the filtering effect is avoided, the parasitic capacitance C_L is not represented on the next representation of electronics readout.

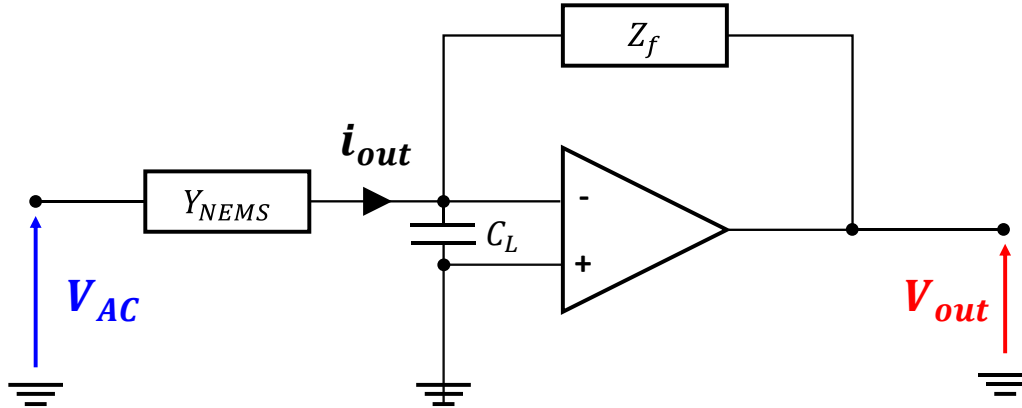


Figure 3-17 Electrical diagram of a current readout. The nanoresonator current produced by the input voltage V_{AC} is injected to the input of the TIA. The feedback impedance of the TIA transforms the input current to an output voltage V_{out} .

3.2.2 Oscillator architecture

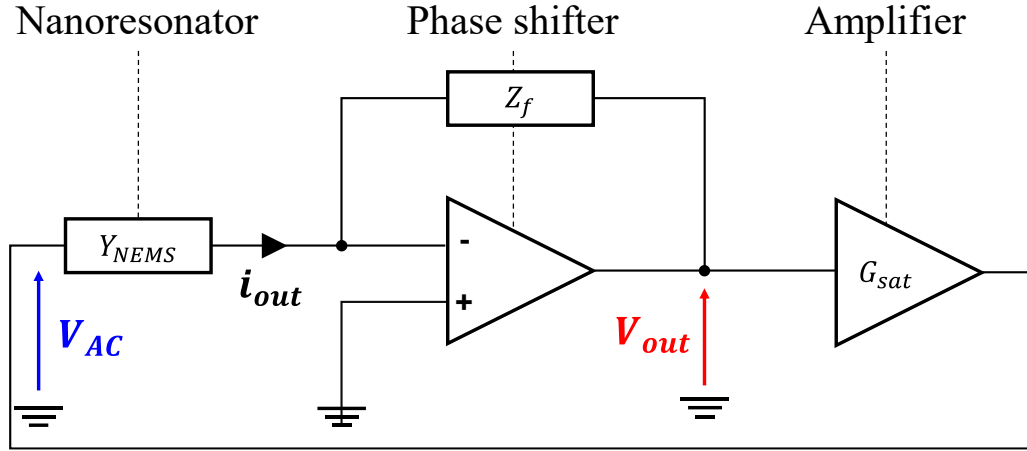


Figure 3-18 The oscillator architecture consists of three parts: the nanoresonator of impedance Z_{NEMS} , the phase shifter implemented by a TIA and the amplifier realised by a saturation stage.

This subsection describes the implementation of an amplification stage as well as a phase shift stage in order to satisfy the oscillation conditions of the system. As a reminder, the Barkausen conditions are met when the total gain of the closed loop is $|H_{CL}| = 1$ and the phase shift between the input and output of the oscillator is $Arg(H_{CL}) = 360^\circ$. Figure 3-18 represents the architecture of the oscillator, which consists of a nanoresonator ($i_{out}/V_{AC} = Y_{NEMS}$), a phase shifter (the TIA) and an amplification stage (G_{sat}). Because the nanoresonator operates at resonance, the current i_{out} is shifted with respect to the drive voltage V_{AC} by -90° and amplified by the inverse of the motional admittance Y_m . The phase shift stage inverts the output voltage V_{out} with respect to the nanoresonator current i_{out} , which induces an initial phase shift of -180° . The feedback impedance is a parallel RC $Z_f = R_f // C_f$ where the cut-off frequency is well below the working angular frequency $\omega_r \gg 1/\sqrt{R_f C_f}$. Thus, the impedance Z_f behaves as a low-pass filter to add the missing phase shift of -90° . Finally, the saturation stage satisfies $|H_{CL}| = 1$ with $G_{sat} > R_m C_f \omega_r$. The saturation stage consists in using the non-linear regime (saturation) of the components, in practice the gain G_{sat} is fixed by the supply of these components.

Stage	Nanoresonator	Phase shifter	Amplifier
Output/Input	$\frac{i_{out}}{V_{AC}} = Y_{NEMS}$	$\frac{V_{out}}{i_{out}} = -Z_f$	$\frac{V_{AC}}{V_{out}} = G_{sat}$
Gain(ω_{CL})	Y_m	$(C_f \omega_r)^{-1}$	G_{sat}
$\varphi(\omega_{CL})$	-90°	$-180^\circ - 90^\circ$	0°

Table 11 Summary of the operation of each stage when the oscillation frequency is equal to the resonance frequency of the nanoresonator $\omega_{CL} = \omega_r$.

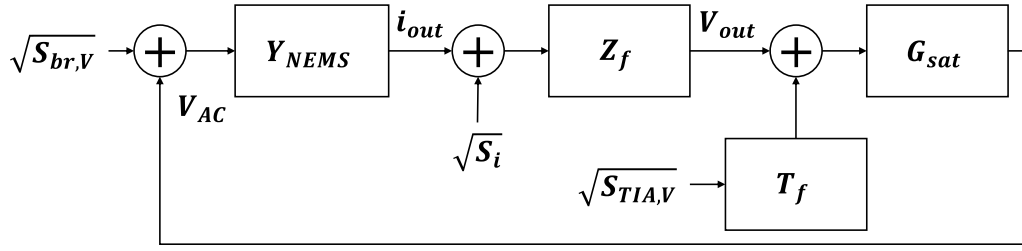


Figure 3-19 Block diagram of the oscillator completed with the different noise sources.

As explained in Section 2.4, the main limitation on the frequency stability of a short-term oscillator comes from the noise of the amplifier. It is the case here, as the noise of the Transimpedance Amplifier (TIA) is not negligible compared to that of the nanoresonator. Besides, the noise introduced by the saturation stage (amplifier) is negligible compared to the output voltage V_{out} of the TIA, so its induced phase noise is negligible. The block diagram in Figure 3-19 is equivalent to the oscillator architecture showing the considered noise sources: the thermomechanical noise of the nanoresonator $S_{br,V}$ can be modeled as a noise source on the actuation voltage V_{AC} . In addition, the output current i_{out} of the nanoresonator suffers from several sources of current noise S_I . The first one is the gauge-intrinsic Johnson noise $S_{J,I} = 4k_B T / R_{out}$ expressed as output current noise. Then the TIA input current noise $S_{TIA,I}$, which is in practice chosen negligible compared to the output current noise of the nanoresonator. The Johnson noise of the feedback resistor R_f , which is in practice neglected because $R_f \gg R_{out}$. Finally, the referenced voltage noise of the TIA, which is the limiting noise added by the TIA. It is expressed as a voltage noise at the input of the phase shifter $S_{TIA,V}$ but must be integrated into the system with the TIA transfer function $T_f(\omega_r) \sim C_L / C_f$ in order to be expressed as a noise source on the TIA output. The phase noise induced by these additive noises is expressed on the V_{AC} node of the oscillator using these transfer functions at resonance $Y_{NEMS}(\omega_r)$, $Z_f(\omega_r)$ $T_f(\omega_r)$ and using $G_{sat} = R_m C_f \omega_r$:

$$\left\{ \begin{array}{l} S_{br,\phi} = \frac{S_{br,V}}{V_{AC}^2/2} \left[\frac{rad^2}{Hz} \right] \\ S_{J,\phi} = \frac{S_{J,I} Y_m^{-2}}{V_{AC}^2/2} \left[\frac{rad^2}{Hz} \right] \\ S_{TIA,\phi} = \frac{S_{TIA,V} |C_L \omega_r Y_m^{-1}|^2}{V_{AC}^2/2} \left[\frac{rad^2}{Hz} \right] \end{array} \right. \quad 3-23$$

Consequence of the Barkhausen phase condition is that any perturbation phase $\Delta\theta$ in the loop is directly compensated by a phase variation $\Delta\theta$ in the resonator causing a variation in the frequency of the oscillator output signal. Considering ω_s the frequency of the fluctuation, if these fluctuations are faster than the response time of the nanoresonator they are filtered. Thus the power spectral density of these phase fluctuations S_ϕ are equal to the power spectral density of the phase of the

oscillator signal S_ϕ . If the fluctuations are slower than the response time of the nanoresonator ($\omega_S < \omega_r/2Q_r$), the nanoresonator corrects them by inducing a frequency variation of the oscillator signal. The consequence is $S_\phi = S_\phi \left(\frac{\omega_r}{2Q_r}\right)^2 \frac{1}{\omega_S^2}$. Both regimes are represented in the Leeson formula [94]:

$$S_\phi = S_\phi \left(1 + \left(\frac{\omega_r}{2Q_r}\right)^2 \frac{1}{\omega_S^2}\right) \left[\frac{\text{rad}^2}{\text{Hz}}\right] \quad 3-24$$

The consequence of the Leeson formula is illustrated in Figure 3-20. The power spectral density of the oscillator signal frequency $S_\omega = S_\phi \omega_S^2$ is calculated from the nanoresonator's mechanical noise, the detection noise $S_{r,\omega} = (S_{br,\phi} + S_{j,\phi}) \omega_S^2$ and the electronics noise, especially from the input voltage noise source of the TIA $S_{TIA,\omega} = S_{TIA,\phi} \omega_S^2$. The noise spectral density shows the impact of phase noise is amplified after the cut off frequency $\omega_r/2Q_r$. This is a disadvantage of the oscillator architecture but is not problematic here because the operation bandwidth of the sensor is lower than the cut-off frequency. Figure 3-20 represents the noise spectral density of the oscillator signal frequency for the specific accelerometer designed in section 3.1.4. For this accelerometer architecture, the accelerometer resolution is dominated by Johnson noise (main contributor of $S_{r,\omega}$). By choosing a low-noise transimpedance amplifier ($\sqrt{S_{TIA,V}} = 4 \text{ nV}/\sqrt{\text{Hz}}$), the detection limit imposed by the electronics overcomes the detection limit imposed by the nanoresonator if $C_L > 5 \text{ pF}$.

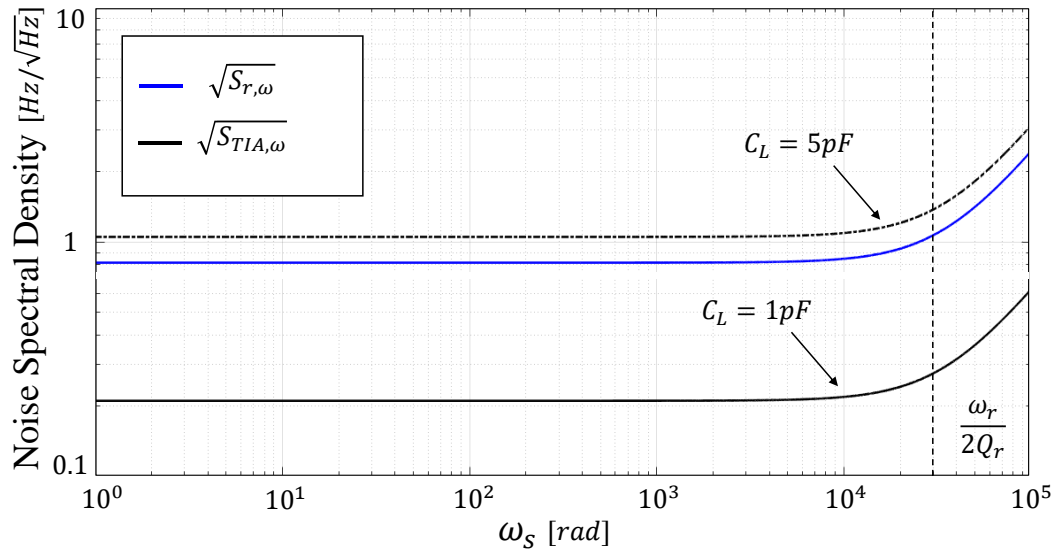


Figure 3-20 Frequency spectrum of the dominant frequency noises of the oscillator, in terms of power spectral density of frequency fluctuations. The output noises of the nanoresonator (Johnson and voltage noise of the TIA) have a corner frequency characteristic of the Leeson formula.

3.2.3 Feedthrough correction

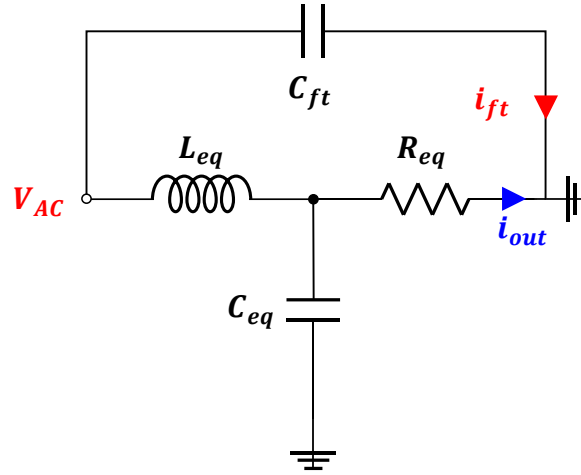


Figure 3-21 Equivalent electrical diagram of the piezoresistive nanoresonator using current readout. Because of the electrostatic actuation, the feedthrough capacitance C_{ft} between drive and sense induces a feedthrough current i_{ft} .

As explained in section 2.5, the electrostatic actuation causes a feedthrough current to flow from the actuation to the output of the nanoresonator. This current is added to the useful current and degrades the output signal measurement. Figure 3-21 represents the equivalent circuit of nanoresonator including a feedthrough capacitance C_{ft} to model this effect. Due to the actuation voltage V_{AC} , the output current is the sum of the useful current i_{out} and the background current i_{ft} . As shown in Figure 2-21, the SBR impacts the measurement. The feedthrough modelling aims at estimating the degradation due to the expected feedthrough capacitances and implementing a correction stage on the oscillator to suppress the background signal.

The admittance of the equivalent nanoresonator model including the feedthrough capacitance is

$$Y_{NEMS,ft} = \frac{1/R_{eq}}{1 + \frac{L_{eq}}{R_{eq}}j\omega + L_{eq}C_{eq}(j\omega)^2} + jC_{ft}\omega \quad [\Omega^{-1}] \quad 3-25$$

Besides, the closed-loop transfer function of the oscillator can be expressed as a function of the open loop transfer function $H_{OL} = Y_{NEMS,ft}Z_fG_{sat}$ as

$$H_{CL} = \frac{H_{OL}}{1 - H_{OL}} \quad [A.U.] \quad 3-26$$

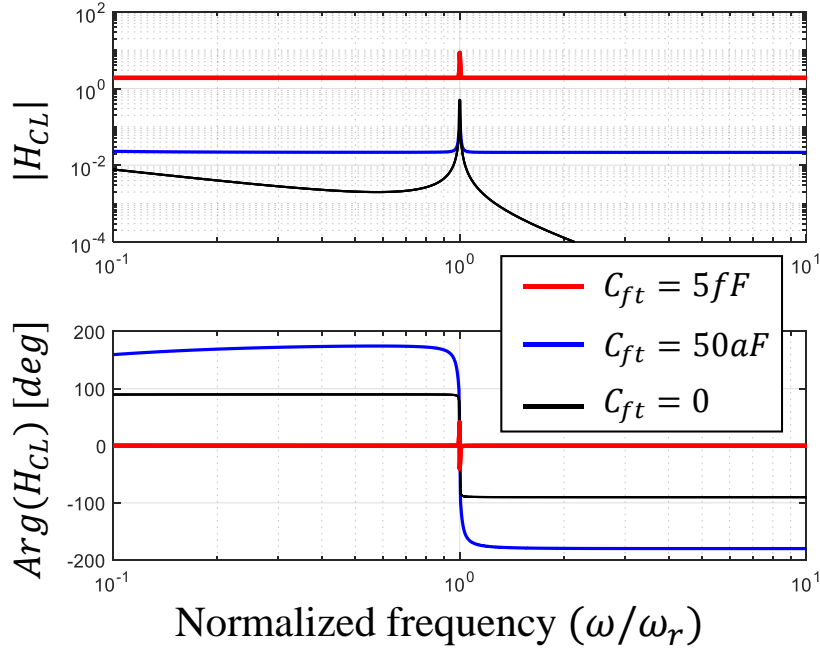


Figure 3-22 Frequency response of the close-loop transfer function as a function of normalized frequency. Different values of feedthrough capacitance are considered, the smallest from the electrostatic actuation design, the largest considering a worst case where silicon design, socket and bonding add capacitances.

Figure 3-22 shows the close-loop transfer function of the oscillator. The black curve considers H_{CL} without feedthrough capacitance. The increasing feedthrough capacitance doesn't affect the phase at resonance $Arg[H_{CL}(\omega_r)] = 0^\circ$. However, the Signal to Background Ratio (SBR) is deteriorated by the high feedthrough capacitance. With a self-oscillator, the oscillation condition cannot be met with a degraded SBR.

In order to avoid the SBR degradation due to the feedthrough capacitance, a correction stage must be implemented. The objective is an equivalent feedthrough current of opposite sign on the output of the nanoresonator. Figure 3-23 shows the correction stage architecture. An inverting amplifier with correction capacitance C_{fc} are connected in parallel to the nanoresonator. The actuation voltage induces a current from the nanoresonator $i_{out} + i_{ft}$ and a current from the correction stage i_{fc} . The advantage of this architecture is to compensate feedthrough current independently of the frequency of operation, as $i_{ft} = \omega_r C_{ft} V_{AC}$ and $i_{fc} = -\omega_r C_{fc} V_{AC}$. The feedthrough capacitance must match perfectly $C_{ft} = C_{fc}$ to fully correct the feedthrough current in terms of amplitude and phase. However, the amplifier might filter the signal due to the high working frequency (>10 MHz), which is equivalent to a reduction of the feedthrough capacitance. In any case, as long as the SBR allows achieving the oscillation conditions, the amplitude mismatch is acceptable. It is essential to control precisely the phase shift $\Delta\phi_{fc}$ induced on the feedthrough current because it affects the phase condition ($Arg[H_{CL}(\omega_r)]$).

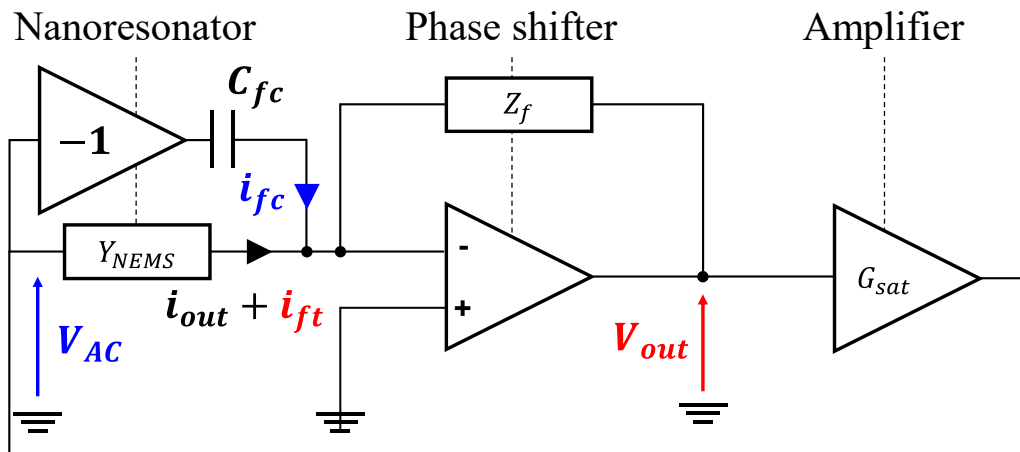


Figure 3-23 The oscillator architecture is completed by a correction stage in parallel to the nanoresonator admittance. The correction stage is composed of an inverting amplifier and a correction capacitance.

3.2.4 Implementation of the oscillator

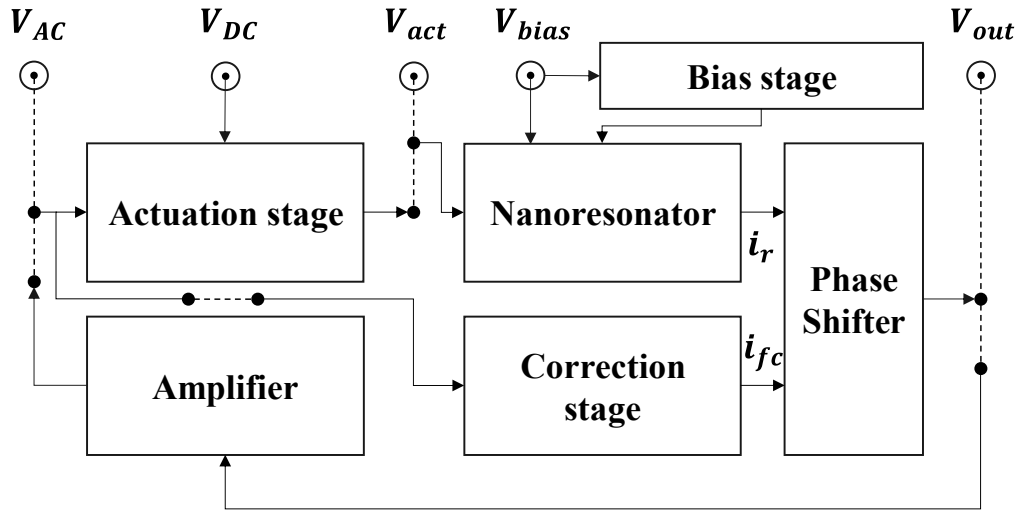


Figure 3-24 Schematic of the global oscillator architecture. Switches and connectors are included on the design to test the operation of the different stages.

This last subsection presents the implementation of the oscillator architecture. In order to validate the operation of the different stages, the architecture must allow measuring the different functional blocks separately.

Figure 3-24 presents the global architecture of the oscillator, which allows validating the main function of the oscillator in open loop. The current readout can be validated by directly actuating the nanoresonator, with $V_{act} = V_{AC} + V_{DC}$ and V_{bias} , and reading the Phase shifter output on V_{out} . The actuation stage can be tested by driving the nanoresonator through V_{AC} and V_{DC} . Likewise, the correction stage can be connected or not. After setting an operation point, the feedback path can be closed in order to allow self-oscillation, and the output signal is measured on the V_{AC} node.

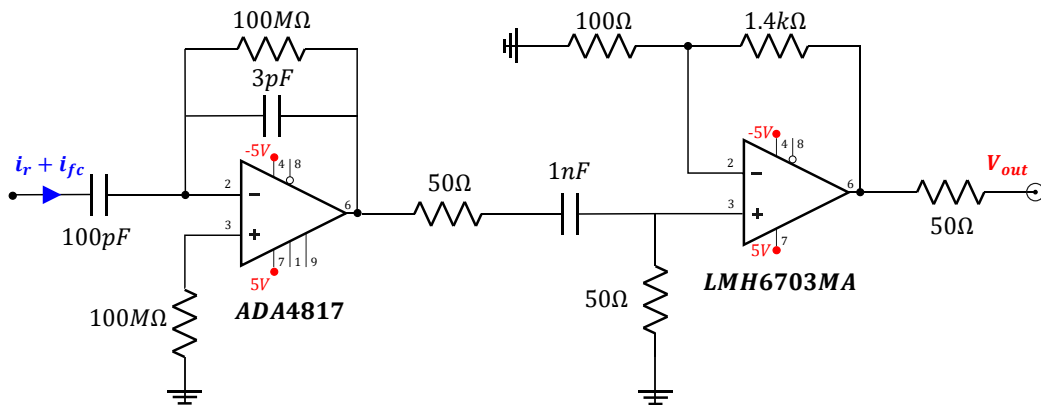


Figure 3-25 Electronic schematics of the Phase shifter composed of the transimpedance amplifier (ADA4817) and a non-inverting amplifier (LMH6703MA).

Figure 3-25 presents the electronic schematics of the Phase shifter. The stage aims at transforming an input current to an output voltage while adding a -270° phase shift at resonance. This stage is composed of two blocks: The first one is a TIA which converts the input current (with $i_r = i_{out} + i_{ft}$) to output voltage. The feedback of the TIA has a gain and a phase shift close to the operation frequency $|Z_f(15MHz)| = 3600$ and $\Delta\varphi = -90.23^\circ$ due to a 500 Hz cut-off frequency. A low-noise ($\sqrt{S_{V,TIA}} = 4 \text{ nV}/\sqrt{\text{Hz}}$ and $\sqrt{S_{i,TIA}} = 2.5 \text{ fA}/\sqrt{\text{Hz}}$) and large bandwidth ($> 100 \text{ MHz}$) amplifier is chosen for the TIA. The next non-inverting amplifier has a gain of 15 due to its feedback resistance. This is also a large bandwidth amplifier ($> 100 \text{ MHz}$). Then, the impedance of the Phase shifter is

$$\frac{V_{out}}{i_r + i_c} = -\frac{15R_f}{1 + jC_fR_f\omega} [\Omega] \quad 3-27$$

In practice, passive components must be integrated on the electronics. 50 Ω resistances are plugged to the amplifier outputs to adapt their impedances to the next blocks. A 100M Ω resistance is plugged to the “+” input of the TIA in order to compensate the high feedback resistance (R_f). A 100pF capacitance is connected between the nanoresonator and the “−” input of the TIA in order to filter the DC offset due to unbalanced gauges. A high pass filter (1nF/50 Ω) is connected to the non-inverting amplifier in order to filter the DC offset on the TIA output. The supply voltage of the amplifier is also clean by a capacitance.

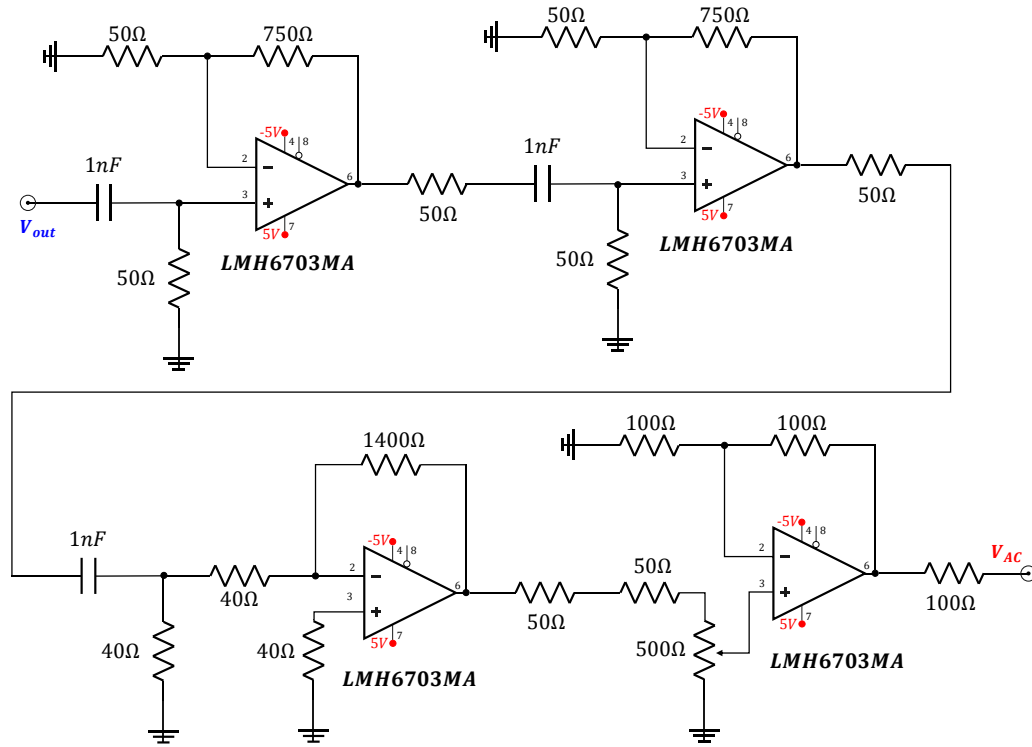


Figure 3-26 Electronic schematics of the saturation stage, composed of a non-inverting amplifier, one inverting amplifier and an adjustable non-inverting amplifier.

Figure 3-26 presents the schematic of the saturation stage. The operating frequency ω_r presents large shifts during the accelerometer's operation, spanning several MHz. In practice, the gain is adjusted superior to the Barkausen condition $G_{sat} > R_m C_f \omega_{r,max}$, with $\omega_{r,max}$ the maximum expected frequency, in order to amplify the signal until the saturation of the amplifier. The last non-inverting amplifier is adjustable in order to set the desired V_{AC} actuation. The two first non-inverting amplifiers have a gain of 16, the inverting amplifier has a gain of -35 and the adjustable non-inverting amplifier has a gain of $2(1 - x)$ where $0 < x < 1$ is set by a 50Ω -trimmer resistance. Because the high bandwidth of the amplifier LMH6703MA, the saturation stage does not induce a phase shift at the operation frequency and its total gain is

$$\frac{V_{AC}}{V_{out}} = 17920(1 - x) [A.U.] \quad 3-28$$

Figure 3-27 (a) presents how V_{AC} is used to actuate the nanoresonator thanks to an AC+DC actuation. The previous saturation stage allows tuning the AC component of the drive voltage, in order to set the desired amplitude. Then, the actuation stage aims at adding a DC offset. The actuation amplitude is

$$V_{act} = -(V_{AC} + V_{DC}) [V] \quad 3-29$$

Figure 3-27 (b) presents the background compensation circuit. Because the feedthrough capacitance C_{ft} is not known beforehand, a large value is used for the correction capacitance C_{fc} . Then, the division of V_{AC} on the input of the non-inverting amplifier allows tuning the correction current through a trimmer resistance x as

$$i_{fc} = [j2(1 - x)C_{fc}\omega]V_{AC} [A] \quad 3-30$$

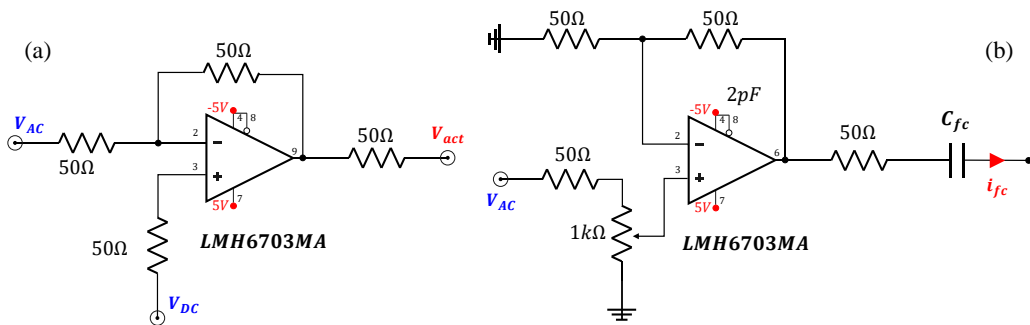


Figure 3-27 Electronic schematics of (a) the actuation stage composed of an inverting amplifier and (b) the correction stage composed of a non-inverting amplifier with an adjustable gain.

4 Experimental characterization

This chapter presents the characterization results of nano-beam resonant accelerometers. The objective is to prove the concept of this type of accelerometer, measure its performance and identify issues in this first generation of devices. To this end, the characterisation chapter focuses on measurements of the piezoresistive nanoresonators acting of the sensing element of the accelerometer. These nanoresonators are tested to validate their piezoresistive transduction independently of the accelerometer, their use as force sensor and their integration with their readout electronics. In order to be consistent between each characterisation step, the nanoresonators are tested on the same measurement set-up and with the same measuring instrumentation.

The measurement setup is shown in Figure 4-1. The main challenge in the development of the set-up was the minimization of acoustic noise and vibrations that interfere with the measurements of the accelerometers, as well as to have the most stable environment possible in terms of temperature. The packaged chips containing the nanoresonators are wire-bonded to LCC48 ceramic sockets and then integrated into a dedicated support on a PCB, which can be a test board or the electronic oscillator board. The PCBs are mounted in a closed metal box that provides a stable thermal environment, avoids acoustic wave interference and provides electromagnetic shielding. The housing is attached to a rotating table to adjust the applied acceleration by changing its orientation. The rotating table is attached to a stabilising table that filters out low frequency disturbances. Then, the PCB is connected to the measuring instrument by short SMA cables that minimise parasitic capacitances. However, these cables transmit high frequency acoustic harmonics from the external environment to the PCB. Therefore, these cables are attached to a clamp that acts as a low-pass filter.

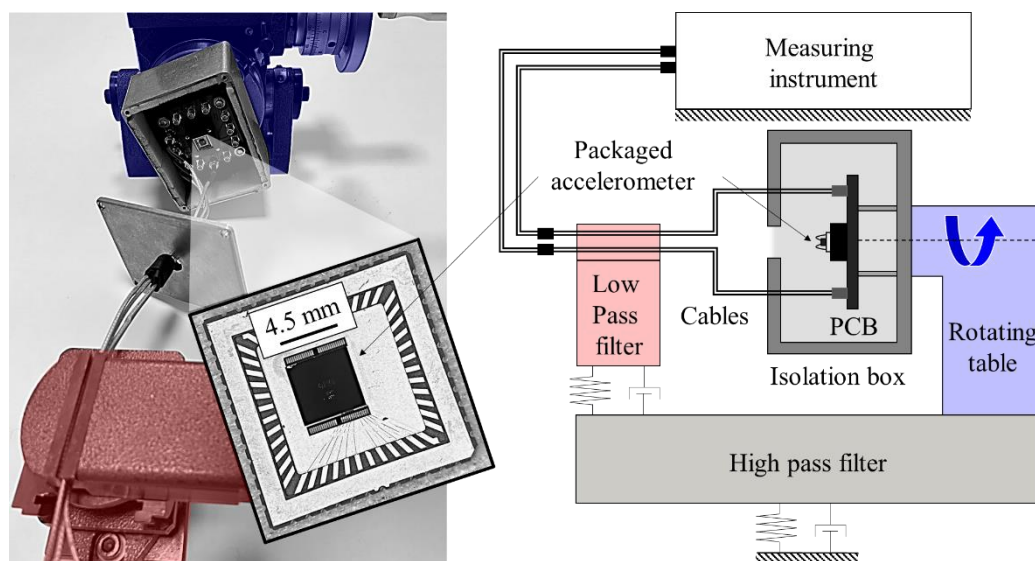


Figure 4-1 Measurement set-up of nano-beam resonant accelerometers.

The measurements of the piezoresistive nanoresonator are performed by an FPGA-based lock-in amplifier (LIA) which allows implementing a large number of functionalities. To begin with, this measuring instrument is used to perform different detection methods such as homodyne or heterodyne detection. Furthermore, this tool allows implementing a Phase-Locked Loop (PLL) to continuously drive the nanoresonator at its resonance frequency under acceleration. Finally, some extension tools can be used to realize a current reading similar to the one used in the oscillator electronics.

In general, a LIA measures a signal by demodulating it with a reference oscillator. This principle can be used for the homodyne detection of nanoresonators (Figure 4-2 (a)). A source oscillator generates the electrostatic drive $V_{AC}(\omega_a)$ at one output. Another output generates a static voltage $\pm V_b$ to bias the gauges. In this configuration, the nanoresonator's output voltage is therefore modulated at the source oscillator frequency $V_{out}(\omega_a)$ by the motion of the resonant beam, and the measured at the input of the LIA. The demodulation of the nanoresonator voltage using the source oscillator is shown in Figure 4-2 (b). The objective is to measure the phase φ_a and the amplitude $|V_{out}|$ of the nanoresonator's voltage. Indeed, the lock-in detection is performed by mixing the voltage $V_{out} = |V_{out}| \cos(\omega_a t + \varphi_a)$, with in-phase ($\cos \omega_a t$) and out-of-phase ($\sin \omega_a t$) components of the source oscillator. Thus, the real part V_X and the imaginary part V_Y after demodulation are

$$\begin{cases} V_X = |V_{out}| \cos \varphi_a + |V_{out}| \cos(2\omega_a t + \varphi_a) & [V] \\ V_Y = |V_{out}| \sin \varphi_a + |V_{out}| \sin(2\omega_a t + \varphi_a) & [V] \end{cases} \quad 4-1$$

A low-Pass Filter (LPF) rejects the unwanted signals ($2\omega_a$). Only the real and imaginary part of the phasor are retained, respectively $X = |V_{out}| \cos \varphi$ and $Y = |V_{out}| \sin \varphi$. These static terms are sampled and transferred to the workstation in order to calculate the magnitude and phase of the signal based on its real and imaginary parts: $|V_{out}|^2 = X^2 + Y^2$ and $\varphi_a = \arctan(Y/X)$.

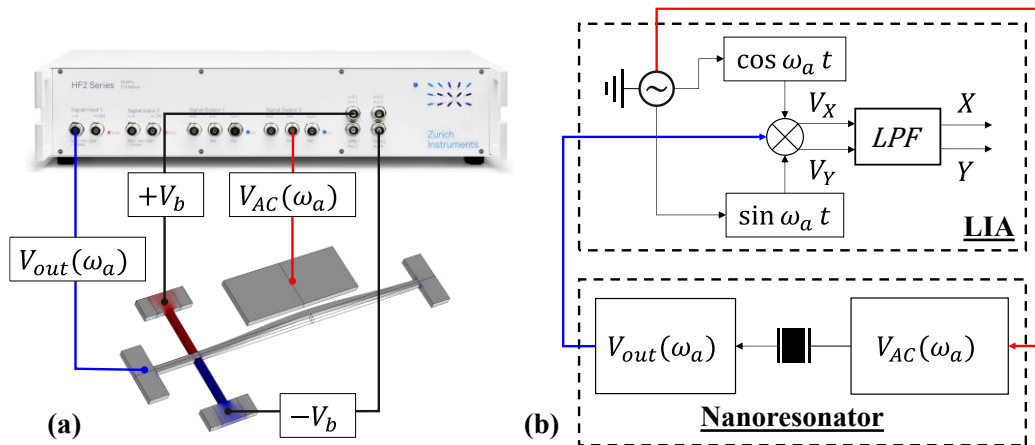


Figure 4-2 Homodyne detection of a piezoresistive resonator implemented by a Lock In Amplifier. (a) Measurement set-up. (b) Demodulation principle.

4.1 Isolated nanoresonators

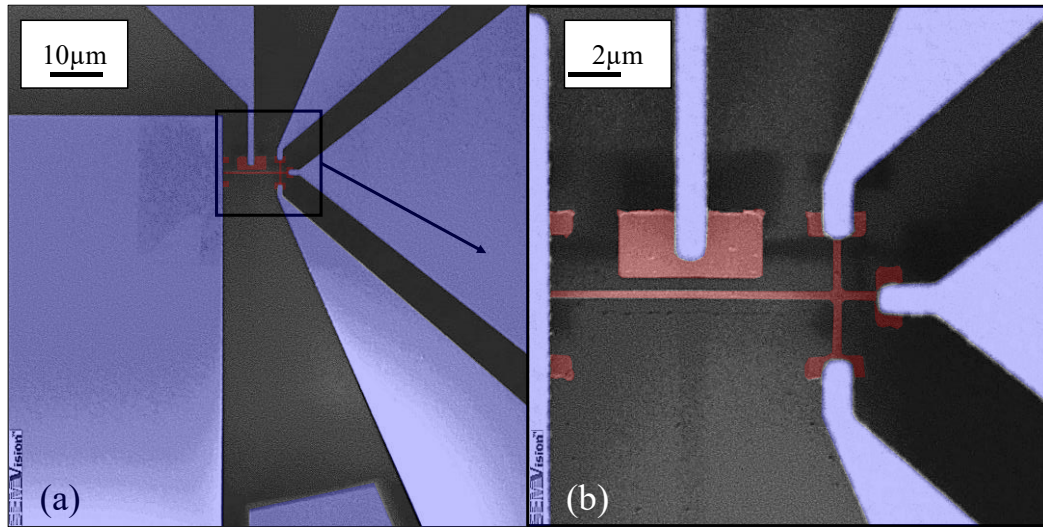


Figure 4-3 Scanning electron microscope (SEM) images of the nanoresonator. In blue, the micrometric layer, in red, the nanometric layer. (a) The nanoresonators are fixed to an unreleased proof mass equivalent to a clamped anchor. (b) Zoom on the nanoresonator where gauges, beam-end and electrode are clamped.

In this first section, the nanoresonators are attached to an unreleased proof mass in order to clamp each sensing element anchor. In practice, they are then tested as a pre-stressed doubly-clamped beams. Figure 4-3 shows a SEM of the 20 MHz nanoresonators: they are defined on a 250 nm thick layer, with a length and width of 10 μm and 250 nm respectively. The length and width of the gauges are 2 μm and 250 nm respectively. The length and width of the beam-end are 1.5 μm and 250 nm respectively.

A previous study of the *M&NEMS* manufacturing process quantified the standard deviation of the nanowire geometries. It was found that the standard deviation of the 250nm-nanowire widths, on 72 samples, follows a normal distribution. The error on the nanowire width can then be expressed as 3σ : $\Delta w_r = \pm 13.5 \text{ nm}$. In addition, a study of 306 samples shows that the standard deviation of the nanowire thickness does not follow a normal distribution. Therefore, the error on the thickness of the nanowires is expressed as 1σ : $\Delta t_r = \pm 10 \text{ nm}$. Moreover, a pre-stress induced by the release of the nanoscale patterns is expected to be in the order of 100 MPa.

In this section, the transfer function of the nanoresonator is studied to validate the model of the piezoresistive transduction. Then a noise analysis is performed to study the frequency stability of the system. Finally, a measurement of the non-linearities is made to optimize the performance of the nanoresonators. These measurements serve as a reference for the intrinsic performance limits of the nanoresonator.

As presented in section 2.5, the homodyne detection with voltage readout suffers from two parasitic effects. First, the high-frequency output voltage of the nanoresonator is filtered by parasitic capacitances on the load. Second, the direct current caused by the electrostatic actuation induces a background signal on the output voltage. In contrast, heterodyne detection helps overcoming the impossibility of isolating the motional signal from the background signal and to avoid high frequency filtering. This method, used commonly for the measurement of piezoresistive nanoresonators [44], [89], can be implemented with the LIA.

The heterodyne measurement is presented on Figure 4-4. Here, two reference oscillators are used on the LIA: one at the actuation angular frequency ω_a , the other at the fixed "down-mixed" angular frequency $\Delta\omega$. These reference signals are mixed to generate the gauge bias signal at the frequency $\omega_a + \Delta\omega$. The reference signal ω_a is used to drive the nanoresonator. Due to the modulation between $V_{AC}(\omega_a)$ and $V_b(\omega_a + \Delta\omega)$, the output voltage of the nanoresonator is composed of two harmonics : one at $\Delta\omega$, the other one at $2\omega_a + \Delta\omega$. The reference signal $\Delta\omega$ is used to demodulate the harmonic $\Delta\omega$ of the output voltage, which is proportional to the motion of the nanoresonator, as in the case of homodyne detection. The same principle of Figure 4-2 is used to demodulate the $\Delta\omega$ harmonic of V_{out} .

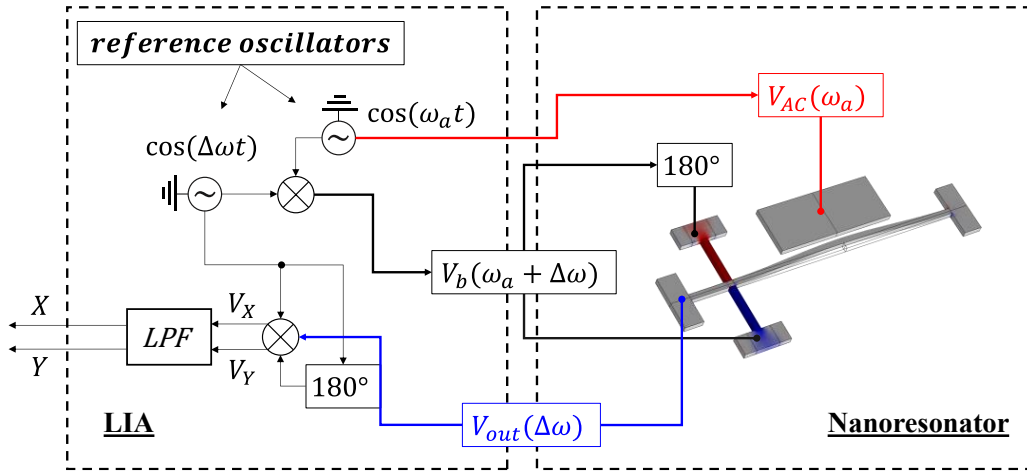


Figure 4-4 Heterodyne measurement implemented by Lock-In Amplifier for piezoresistive nanoresonators. Here the nanogauges are differentially polarized by a signal at angular frequency $(\omega_a + \Delta\omega)$. The nanoresonator is actuated at ω_a . The mixing of the nanogauge resistance variation and polarization creates the nanoresonator output voltage with angular frequency components at $2\omega_a + \Delta\omega$ and $\Delta\omega$. By mixing the nanoresonator output voltage with the reference oscillator at angular frequency $\Delta\omega$, V_X and V_Y are measured.

4.1.1 Frequency response

Here, the frequency response of the nanoresonator is characterized to study its resonance frequency and the amplitude at resonance. The measurement of the amplitude at resonance allows validating the transduction model of the nanoresonator. The measurement of the resonance frequency allows validating the modal analysis of a pre-stressed doubly-clamped beam, and then quantify the pre-stress due to the fabrication process. As a reminder (Chapter 2)

$$\begin{cases} \omega_r(\sigma_{PS}) = \omega_{0r}\sqrt{1 + \sigma_{PS}/\sigma_{buck}} \quad [\text{rad}] \\ V_{out}(\omega_r(\sigma_{PS})) = V_{AC}\eta_A H_r(\omega_r(\sigma_{PS}))\eta_S \quad [\text{V}] \end{cases} \quad 4-2$$

In order to measure the transfer function of the nanoresonator, the detection method of Figure 4-4 is implemented by sweeping ω_a around the resonance frequency. Figure 4-5 plots the measured (blue) and modelled (red) transfer function. As expected, the measured resonance frequency is not the natural unstressed frequency of a doubly clamped beam. The standard deviation of the fabrication process cannot explain this frequency mismatch which would correspond to $w_r \approx 190 \text{ nm}$. In order to match the experimental resonance frequency a compressive pre-stress of 190 MPa is applied on the analytical modelling. Moreover, the experimental amplitude at resonance is lower than the value predicted analytically by a factor ~ 2.5 . The mismatch is probably due to losses on the transduction gain as explained on Table 12 and Table 15. Table 11 compares the analytical modelling, FEM (COMSOL) simulations and experimental results.

	Analytical model	FEM simulation	Experimental
$\omega_r(\sigma_{PS})/2\pi$	$14.7 \pm 0.17 \text{ MHz}$	13.8 MHz	14.8 MHz
$V_{out}(\omega_r(\sigma_{PS}))$	$4.44 \pm 0.5 \text{ } \mu\text{V}$	—	$1.9 \text{ } \mu\text{V}$

Table 11 Comparison of the resonance properties. The analytical model supposes an actuation $V_{AC} = 2.5 \text{ mV}$, $V_{DC} = 3.5 \text{ V}$ and $V_{bias} = 1.25 \text{ V}$, the measured quality factor $Q_r = 8700$ is fitted from phase measurement, the standard deviation of the nanometric layer and 190MPa of pre-stress (for FEM simulation too).

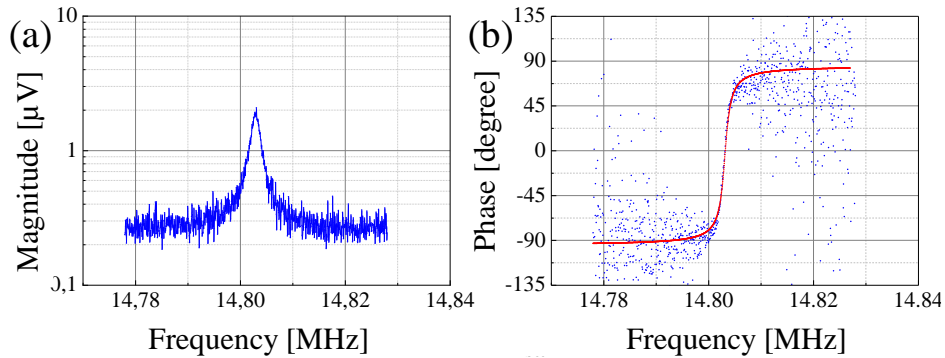


Figure 4-5 Measurement of the nanoresonator's transfer function. (a) Magnitude measurement and (b) phase measurement. The actuation is: $V_{AC} = 2.5 \text{ mV}$, $V_{DC} = 3.5 \text{ V}$ and $V_{bias} = 1.25 \text{ V}$. The measured quality factor is $Q_r = 8700$.

4.1.2 Noise analysis

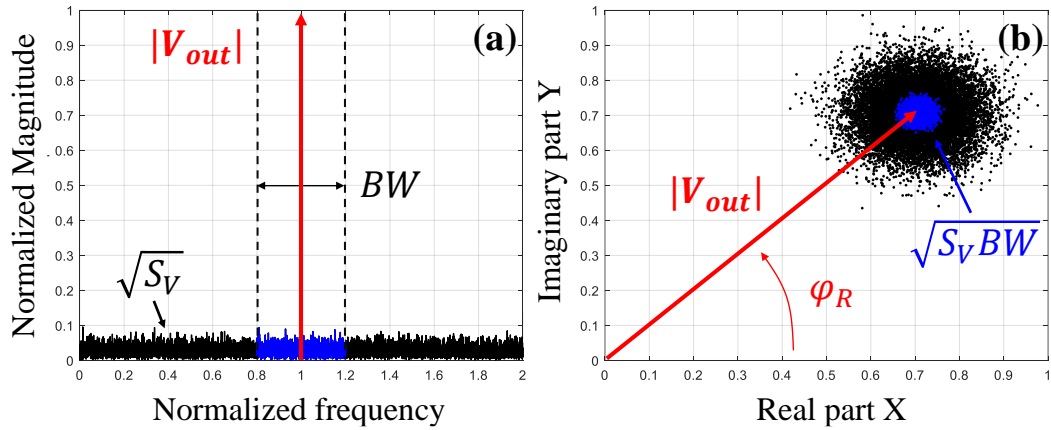


Figure 4-6 Representation of the nanoresonator's output voltage. (a) Frequency domain representation. (b) Complex representation.

This section aims at measuring the stability of nanoresonator frequency measurement. Here, the nanoresonator is not coupled to the proof mass. As explained in section 2.4, the stability measurement is usually limited by additive noise in short timescales and by intrinsic frequency drifts in long timescales. In order to compare this noise analysis with the one of the whole accelerometer (section 4.2.2), the short-term stability must be studied up to the accelerometer bandwidth (>1 kHz). Closed-loop measurements, for instance with a PLL or a self-oscillator, suffer from trade-offs between resolution and speed [95], so the most effective way to perform this noise analysis is an open-loop frequency measurement. In open loop, the maximum speed are fixed by the nanoresonator response time, superior to the target bandwidth, and the measurement's integration time. In practice, the nanoresonator is driven at its resonance angular frequency ($\omega_a = \omega_r$) and the open loop measurement is performed thanks to the method presented in Figure 4-4.

Figure 4-6 (a) shows a representation of the spectrum of the nanoresonator output voltage at resonance in the frequency domain. The signal contains additive white noise S_V distributed in frequency. Figure 4-6 (b) is the complex representation of the nanoresonator output voltage where the amplitude $|V_{out}|$ and the phase φ_R with regards to an ideal reference signal. As detailed on the operation of the lock-in detection, both parameters can be processed from the real part (X) and imaginary part (Y) of the signal. Thus, in order to measure resonance frequency fluctuations $\Delta\omega_r$, the phase fluctuations $\Delta\varphi_r$ are computed as a function of X and Y:

$$\Delta\varphi_r = \arctan\left(\frac{Y}{X}\right) \text{ [rad]} \quad 4-3$$

Because the resonance properties of Figure 2-6, the frequency fluctuations $\Delta\omega_r$ can be processed from the phase fluctuations $\Delta\varphi_r$.

$$\Delta\omega_r = \left[\frac{\omega_r}{2Q_r} \right] \Delta\varphi_r \text{ [rad]} \quad 4-4$$

During the measurements, the low-pass filtering of X and Y results in an integration of the nanoresonator output voltage (magnitude and phase) on specific bandwidth, which is represented in blue on Figure 4-6.

In other words, the open-loop measurement is based on the measurement over time of the output voltage of the nanoresonator operated close to resonance. The operation close to the resonance ensures a known and linear phase-frequency relationship [78], [95]. Because the calculation of frequency fluctuations is deduced from this linear relationship, the open-loop measurement cannot measure frequency fluctuations that would fall outside this linear range. This is why open-loop measurements are performed over short times (100 s) in order to study short-term stability. Longer measurements are carried out in section 4.2.4 in order to study the long-term stability.

When acquiring the signal at resonance, the phase as well as the amplitude of the signal are computed through X and Y measurements. In section 2.4.1 the relationship between additive noises and phase noise is explained. The noise analysis aims at identifying phase noise coming from additive noise and other noise sources by representing amplitude noise and phase noise from the measurement. There are several representations that can be used to plot the noise in a signal. FFT-based signal analysis allows the power spectral density (PSD) of amplitude and phase signals to be determined. Because the nanoresonator operates in resonance, the PSD of the phase signal has an equivalence in terms of resonance frequency. The expected noise sources are characterized on the PSD by constant plateaus that indicate white noise and 1/f slopes that indicate flicker noise.

Noise analysis begins by the measurement of the additive noises S_V on the output voltage V_{out} . The measurement conditions are a 1 kHz bandwidth and 10 kHz of sampling frequency. The down-mixed frequency is $\Delta f = 161753 \text{ Hz}$. The expected noises are the Johnson noise, thermomechanical noise of the nanoresonator, and readout electronics noise. The signal is proportional to V_{bias} and V_{AC} (for a fixed V_{DC}). The thermomechanical noise $S_{br,N}$ can be modelled by an actuation force on the resonant beam. Projected to the output signal V_{out} , the thermomechanical noise $S_{br,V}$ is proportional to V_{bias} . In the limited operation range of V_{bias} , the influence of temperature due to Joule heating is neglected. In other words, the Johnson noise imposes the $\text{SNR} \propto V_{bias}V_{AC}$.

Figure 4-7 shows the measured PSD of V_{out} , representative of noise originating from additive noise sources. First, the LIA performs the open-loop measurement using a 50 Ohms plug at its input, so it demodulates the signal consisting only of its intrinsic electronic noise $S_{LIA,V}$. Then, the input of the LIA is connected to the output of the nanoresonator and the outputs of the LIA are connected to the gauges with bias voltage of 0 Volt. In this configuration, the LIA demodulates the signal composed of the quadratic sum of the electronic noise $S_{LIA,V}$ and the Johnson noise $S_{J,V}$ of the gauges. Finally, the bias voltage is turned on, which allows to transduce the motion of the resonant beam coming from its thermomechanical noise. Thus, the LIA demodulates, in addition to the other noise sources, the thermomechanical noise of the resonant beam reported as additive noise on the output voltage $S_{br,V}$.

Table 12 allows comparing the measured additive noise with the analytical modelling. The modelled thermomechanical noise $S_{br,V}$ is larger than the experimental one, but Figure 4-5 shows a similar mismatch on the output signal that can probably be explained by losses on the sensing gain η_S

	Analytical model	Experimental
$\sqrt{S_{LIA,V}}$	-	$1 \text{ nV}/\sqrt{\text{Hz}}$
$\sqrt{S_{J,V}}$	$4.4 \text{ nV}/\sqrt{\text{Hz}}$	$3.97 \text{ nV}/\sqrt{\text{Hz}}$
$\sqrt{S_{br,V}}$	$3.84 \text{ nV}/\sqrt{\text{Hz}}$	$< 1 \text{ nV}/\sqrt{\text{Hz}}$

Table 12 Comparison of the measured white noise with analytical modelling.

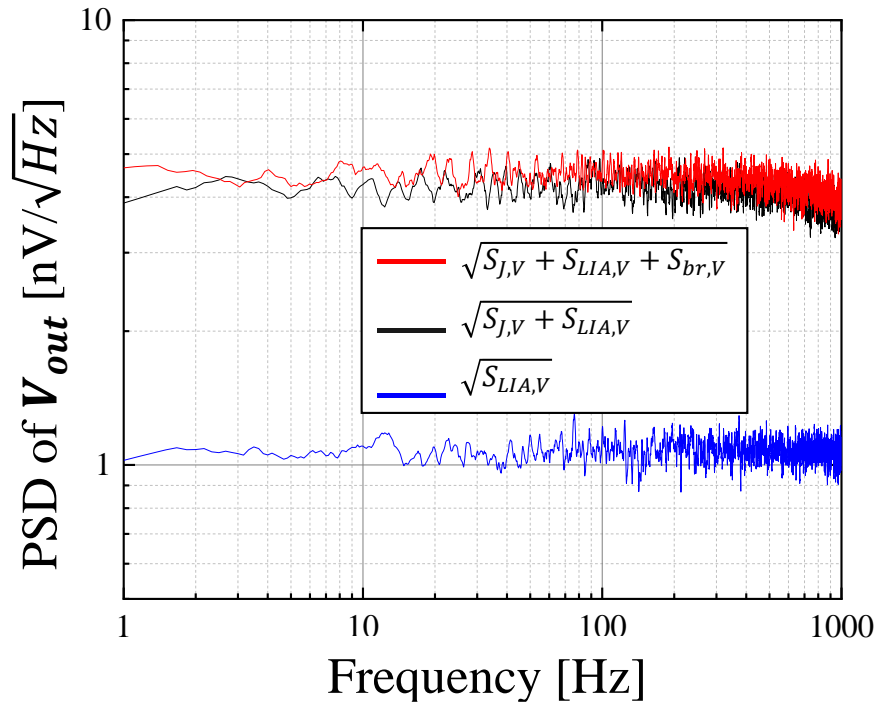


Figure 4-7 Power spectral density (PSD) of the nanoresonator output voltage.

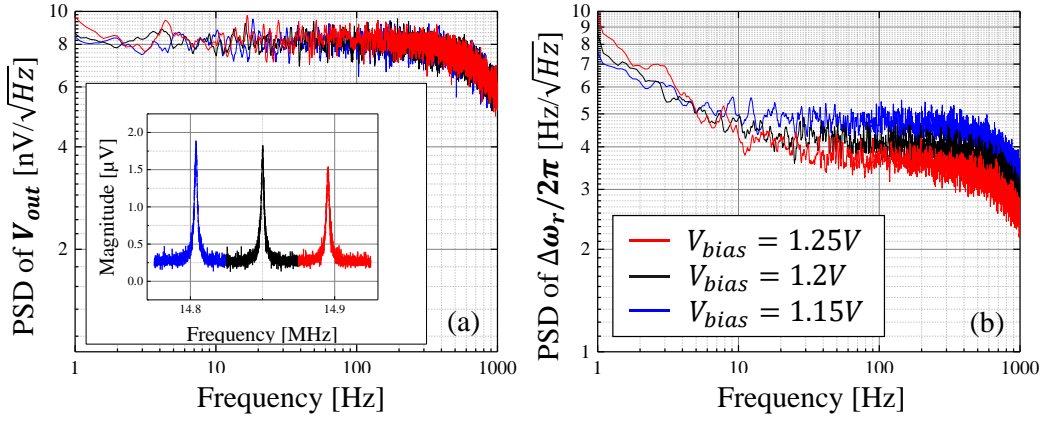


Figure 4-8 (a) Power spectral density of the additive noise for different bias voltage values. (a-inset) Nanoresonator magnitude for different bias voltages. (b) Power spectral density of resonance frequency fluctuations for different bias voltages. The actuation set is $V_{AC} = 2.5\text{ mV}$ and $V_{DC} = 3.5\text{ V}$.

In a first step, the nanoresonator is driven. The AC actuation is $V_{AC} = 2.5\text{ mV}$, the DC actuation is $V_{DC} = 3.5\text{ V}$ and bias voltage V_{bias} is swept. Figure 4-8 (a-inset) shows that the magnitude increases with the bias actuation and Figure 4-8 (a) shows that additive white noise is not affected by the bias actuation. Thus, the thermomechanical noise, which should be proportional to V_{bias} , is negligible. However, the white noise level has increased compared to the expected value measured in Figure 4-7 (from $5\text{ nV}/\sqrt{\text{Hz}}$ to $8\text{ nV}/\sqrt{\text{Hz}}$), which could be explained by Joule heating. The quality factor $Q_r = 8700$ is not affected in this polarisation range. However, the resonance frequency decreases with increasing bias voltage, again probably due to the temperature increase caused by heat dissipation from the nanogauges to the resonant beam. The resonant element is then eager to expand but its double anchoring imposes a fixed condition that causes a compressive axial stress (σ_{bias}), hence a frequency down.

For each bias voltage, the resonance frequency fluctuations $\Delta\omega_r/2\pi$ are deduced from phase fluctuations $\Delta\phi_r$. The PSD of $\Delta\omega_r$ is then plotted in Figure 4-8 (b). The PSD curves show a $1/f$ behaviour at low frequency ($<10\text{ Hz}$) which is not affected by the bias polarisation. A constant plateau that decreases with the improvement of the SNR, probably due to additive noises. Table 13 presents the consistency of the white noise of $\Delta\omega_r$ (S_ω) as a function of the measurement SNR ($V_{out}/\sqrt{S_V}$).

V_{bias}	V_{out}	$\sqrt{S_V}$	$\sqrt{S_\omega}/2\pi$
1.15 V	1.5 μV	$8\text{ nV}/\sqrt{\text{Hz}}$	$4.56\text{ Hz}/\sqrt{\text{Hz}}$
1.2 V	1.65 μV	$8\text{ nV}/\sqrt{\text{Hz}}$	$4.13\text{ Hz}/\sqrt{\text{Hz}}$
1.25 V	1.75 μV	$8\text{ nV}/\sqrt{\text{Hz}}$	$3.88\text{ Hz}/\sqrt{\text{Hz}}$

Table 13 Consistence with the noise of the resonance frequency fluctuations S_ω and the SNR = $V_{out}/\sqrt{S_V}$ deduced from Eq. 2-37.

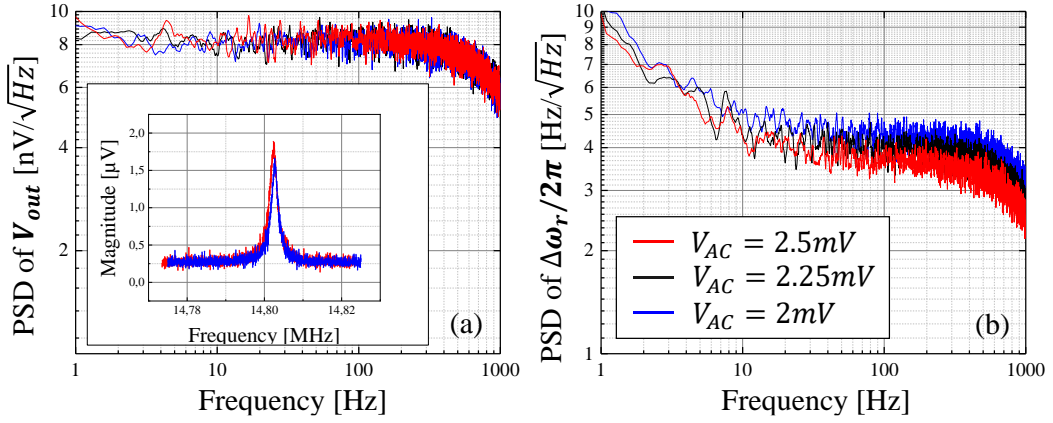


Figure 4-9 (a) Power spectral density of the additive noise for different AC actuations. (a-inste) Nanoresonator magnitude for different AC actuations. (b) Power spectral density of resonance frequency fluctuations for different AC actuations.

In a second step, the AC actuation amplitude V_{AC} is swept. The bias polarisation is $V_{bias} = 1.25 \text{ V}$ and the DC actuation is $V_{DC} = 3.5 \text{ V}$. Figure 4-9 (a-inset) shows the nanoresonator magnitude increase with the AC actuation and the Figure 4-9 (a) shows that the additive white noise remains constant.

For each amplitude, we measured the corresponding relative frequency fluctuations. The PSD of these signals is then plotted in Figure 4-9 (b). The PSD curves show a $1/f$ behaviour at low frequency ($<10 \text{ Hz}$) which is not affected by the AC actuation, and a constant plateau, representative of the white noise, which decreases with the improvement of the SNR as expected.

Table 14 compares the additive white noise S_V , the magnitude at resonance V_{out} and the white noise plateau S_ω . The experimental additive white noise S_V is higher than the analytical model. Because phase is proportional to $V_{out}/\sqrt{S_V}$, the experimental white noise plateau S_ω is higher than its analytical model.

	Analytical model	Experimental
$\sqrt{S_V}$	$5.95 \text{ nV}/\sqrt{\text{Hz}}$	$8 \text{ nV}/\sqrt{\text{Hz}}$
V_{out}	$1.9 \text{ } \mu\text{V} *$	$1.9 \text{ } \mu\text{V}$
$\sqrt{S_\omega}/2\pi$	$2.6 \text{ Hz}/\sqrt{\text{Hz}}$	$3.5 \text{ Hz}/\sqrt{\text{Hz}}$

Table 14. Comparison between experimental and analytical model of the SNR and $S_\omega/2\pi$. The experimental additive noise is higher than the analytical model but the S_f is coherent with this mismatch. The open-loop frequency measurement is performed with $V_{AC} = 2.5 \text{ mV}$, $V_{bias} = 1.25 \text{ V}$ and $V_{DC} = 3.5 \text{ V}$. * For the model, the measured output voltage is used for calculation.

The PSD highlights the white noise S_ω of the resonance frequency fluctuations measurements at short timescales (>10 Hz). However, in the relatively short term (<10 Hz), the $1/f$ noise and long term drifts are difficult to discern. In order to provide complementary measurements, the resonance frequency fluctuations $\Delta\omega_r/2\pi$ can be represented in terms of Allan deviation from the same set of data. The Allan deviation is a well-known statistical tool to characterise the frequency stability of oscillators. It was developed to compensate for the weaknesses of the standard deviation, which does not converge for some noise sources [96]. The Allan deviation $\sigma_f(\tau)$ is the root mean square of the frequency difference between two successive frequency samples:

$$\sigma_f(\tau) = \sqrt{\frac{1}{2(M-1)} \sum_{i=1}^{M-1} (\overline{f_{i+1}} - \overline{f_i})^2} \quad [\text{A.U.}] \quad 4-5$$

where M is the number of samples, τ the integration time and $\overline{f_{i+1}}$ the averaged relative frequency. A slope $\tau^{-1/2}$ on the Allan variance, shown in Figure 4-10, corresponds to the plateau of white noise on the PSD. Therefore, by increasing the AC actuation or the bias of the polarisation, the offset of the slope $\tau^{-1/2}$ decreases for short integration times. The slope of $1/f$ noise identified on the PSD corresponds to a plateau on the Allan variance [97]. This representation allows identifying the bias instability of the measurement. On one hand, the V_{AC} sweep does not affect the noise in $1/f$ so, improving the SNR by increasing V_{AC} induces better white noise S_ω (improving the position of the slope $\tau^{-1/2}$) but does not improve the bias instability (Allan deviation plateau) of the measurement. This behaviour is consistent with resonance frequency fluctuations, as presented in section 2.4. On the other hand, the V_{bias} sweep affects the white and $1/f$ noises: increasing V_{bias} induces better white noise S_ω (by improving the SNR, i.e. the position of the slope $\tau^{-1/2}$) but somewhat degrades the bias instability (Allan deviation plateau) of the measurement. This effect could be induced by the heating of the nanoresonator at large bias voltages, which changes its resonance frequency and quality factor.

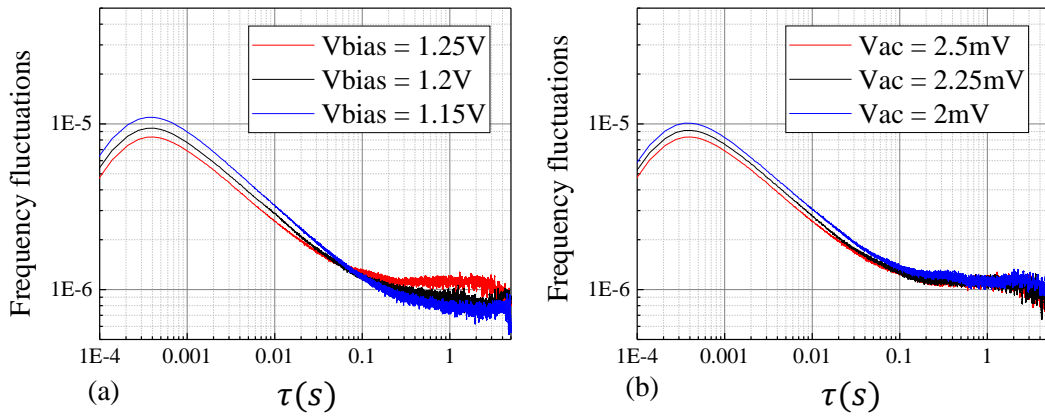


Figure 4-10 Allan deviation of the open-loop frequency measurement (a) for different bias voltages; (b) for different AC actuation voltages.

4.1.3 Non linearity

Considering only the additive noise sources (Johnson + thermomechanical + electrical) imposed by the design, an efficient way to improve frequency resolution (short-term stability) is to improve the SNR. When the thermomechanical noise becomes larger than the Johnson noise, especially at high polarisation V_{bias} , the SNR is not improved. The only way to robustly improve the SNR without increasing the additive noise is to maximise V_{AC} actuation. However, the AC actuation has a maximum value V_{max} that corresponds to the critical amplitude before nonlinearity v_{max} .

Figure 4-11 shows the magnitude response of the nanoresonator for several AC actuation voltages. The bias voltage is $V_{bias} = 1.25\text{ V}$ and the DC actuation is $V_{DC} = 3.5\text{ V}$. The critical amplitude is due to a large elongation of the beam that induces an increase of rigidity as explained in [73]. We expected a resonance frequency shift due to the presence of nonlinear terms in the stiffness but not of the order of the offset observed for $V_{AC} = 7.5\text{ mV}$. This could be explained by environment-induced drifts (ex. temperature) of the resonance frequency. The formulation of Eq. 2-28 allows the critical amplitude to be modelled. In the measurement, the amplitude of the vibration at the bifurcation point, i.e. the infinite slope in magnitude, is almost reached. Table 15 compares the measured critical magnitude with the analytical model.

	Analytical model	Characterization
Critical magnitude	$9.8\text{ }\mu\text{V}$	$>5.5\text{ }\mu\text{V}$

Table 15 Comparison of the measured critical amplitude and corrected analytical modelling.

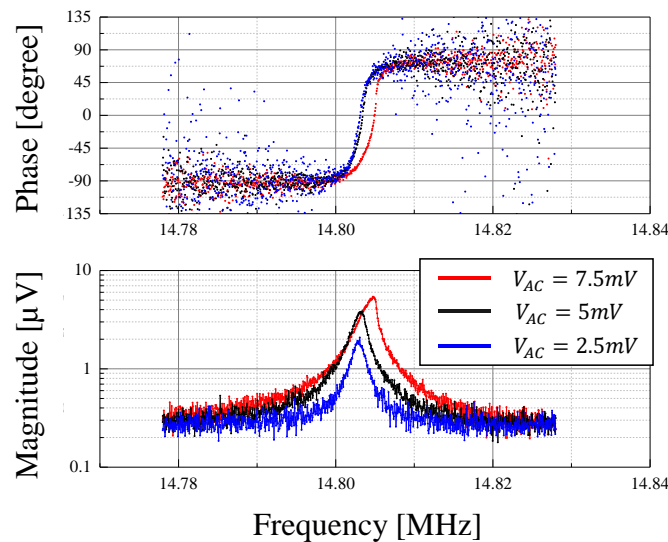


Figure 4-11 Measurement of the nanoresonator's transfer function as a function of AC actuation. The bias polarization is $V_{bias} = 1.25\text{ V}$ and the DC actuation is $V_{DC} = 3.5\text{ V}$. The magnitude shape appearing for $V_{AC} = 7.5\text{ mV}$ is typical of the geometrical non-linearity.

4.2 Accelerometer

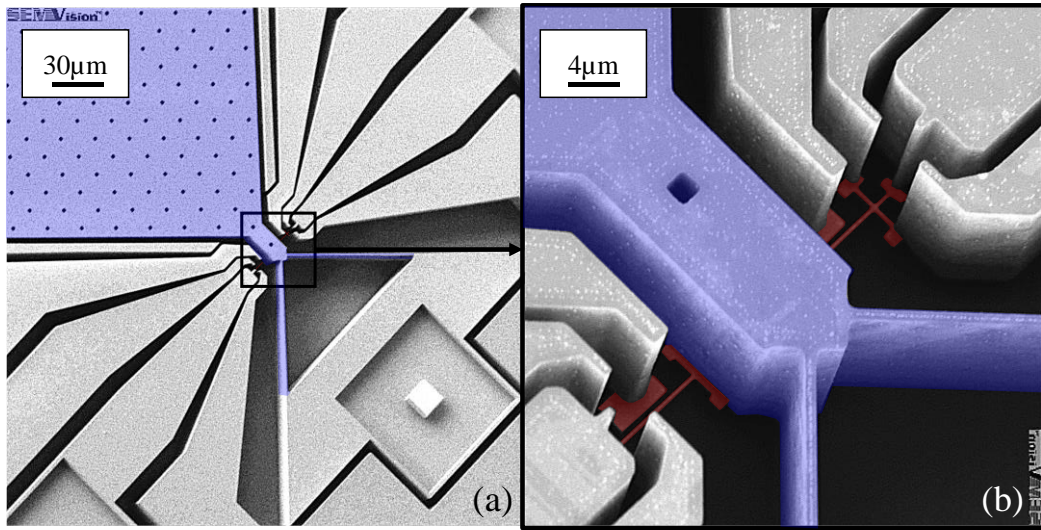


Figure 4-12 Scanning electron microscope (SEM) images of the accelerometer. (a) Nano resonators are fixed to a proof mass. (b) Zoom on the nano resonators. In blue the micrometric released proof mass. In red the nano resonators coupled to the proof mass.

In this second section, the nano resonators are tested as clamped pre-stressed beams used as force sensors. Here, they are attached to a micrometric released proof mass that affects the anchoring conditions on one side of the nano resonator. Figure 4-12 shows the design of the 20 MHz nano resonators shown in Figure 4-3, but coupled to an accelerometer with the following geometrical characteristics: proof mass length: $L_m = 380 \mu m$, hinges length $L_h = 51 \mu m$ and position of the nano resonator $l = 5 \mu m$ (i.e. the design presented in Figure 3-10).

A previous study of the M&NEMS fabrication process quantified the standard deviation of the nanowire geometries and micrometric geometries. The nanowires are subject to the above standard deviations defined in section 4.1. The $1 \mu m$ width of micrometric patterns, over 153 samples, was found to follow a normal distribution. The standard deviation on the micrometric width can then be expressed as $3\sigma: \Delta w_h = \pm 75 nm$. Furthermore, a study on 306 samples, shows that the standard deviation of $20 \mu m$ micrometric thickness follows a normal distribution. Therefore, the error on the micrometric thickness is expressed as $3\sigma: \Delta t_m = \pm 1.5 \mu m$

Here, the measurements consist in measuring the nano resonators under acceleration and comparing the results to the operation of the doubly-clamped nano resonator studied in Section 4.1. In addition, the operation of a nano-beam resonant accelerometer features some unexpected issues that were analysed in order to solve them.

4.2.1 Frequency response

Here, the frequency response of the nanoresonators are studied in terms of resonance frequency and amplitude at resonance as a function of acceleration. The measurement of the resonance amplitude aims at validating the modelling of the transduction of the nanoresonator. The measurement of the resonance frequency is used to validate the modal analysis of the clamped pre-stressed beam. In contrast to subsection 4.1, the analytical modelling allows the prediction of the resonance properties through the previously studied pre-stress σ_{PS} and the acceleration-induced stress σ_r . In order to validate the proof of concept of the accelerometer, the resonances' properties are measured using the detection principle of Figure 4-4 for several applied accelerations set by the angle of the rotation table described in Figure 4-1.

Figure 4-13 shows the measurement of the resonance properties of the coupled nanoresonator for an acceleration from $-1g$ to $1g$. The conditions for the $0g$ nanoresonator are $f_r(\sigma_{PS}) = 14.25 \text{ MHz}$ and $Q_r(\sigma_{PS}) = 750$. The low quality factor indicates a degraded vacuum environment. The nanoresonators are actuated by $V_{AC} = 0.2 \text{ V}$, $V_{DC} = 3.5 \text{ V}$ and $V_{bias} = 1.5 \text{ V}$. Figure 4-13 (a) shows that the resonance frequencies depend on the applied acceleration, as expected. The resonance frequency at $0g$ is close to but not equal to the resonance frequency of Figure 4-5. The mismatch is probably caused by a close but not equal σ_{PS} , another compressive stress σ_{bias} caused by a higher bias polarisation, and/or the uncertainty on the nanoresonator dimensions as explained on Table 11.

The blue dotted-line of Figure 4-13 (b) shows the measured quality factor as a function of the applied acceleration. If the damping coefficient b_r comes only from to squeeze film, the quality factor could be increased by the resonance frequency $Q_r(\sigma_r) \propto \omega_r(\sigma_r)/b_r$. In practice, the quality factor increases well with resonance frequency, but the increase is not linear, which could be explained by the anchoring conditions changing with the applied acceleration.

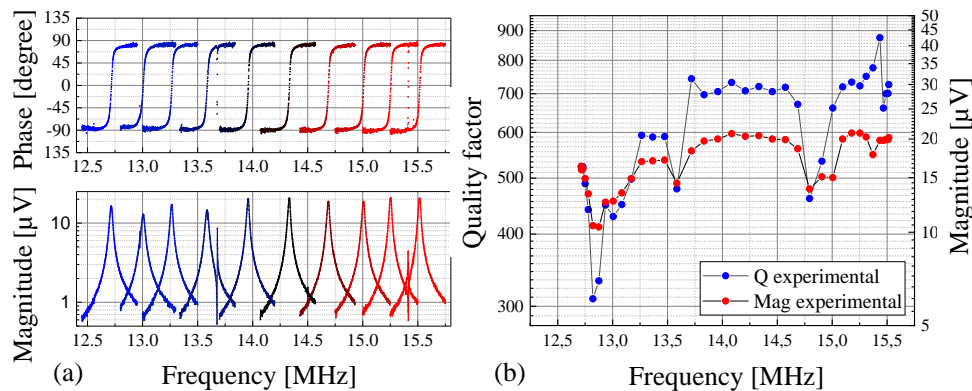


Figure 4-13 Resonance properties of nanoresonator used as force sensor. (a) The transfer functions of accelerometer for applied accelerations from $-1g$ (red plot) to $1g$ (blue plot) with steps of $0.2g$. (b) Measured quality factor and magnitude as a function of resonance frequency compared to the analytical predictions.

The red dotted-line of Figure 4-13 (b) shows the measured output voltage as a function of the applied acceleration. The magnitude of the nanoresonator should be decreased by the resonance frequency $V_{out} \propto Q_r(\sigma_r)/\omega_r^2(\sigma_r) \propto 1/\omega_r(\sigma_r)b_r$. However, the magnitude of the nanoresonator increases with the resonance frequency and presents the same nonlinearity of the quality factor. Anchoring conditions likely have a dominant effect on both quality factor and magnitude.

The 0 g resonance frequency of the nanoresonators is mapped across the wafer, when the accelerometers are subjected to -1g out of plane. Figure 4-14 presents a mapping of a wafer containing 37 samples. Figure 4-14 (a) shows that 4 nanoresonators do not work while 34 do, which indicates an operating rate of over 90%. Figure 4-14 (b) shows that the distribution of 0g resonance frequencies spans from 13.5 MHz to 16.2 MHz with an average resonance frequency of 15.02 MHz and a standard deviation of 0.67 MHz. The distribution of resonance frequencies on the wafer could be due to a stress gradient generated by the fabrication process. The yield on a wafer is sometimes lower than 90% due to the fact that the geometry is not adapted to the protection of the nanoresonators, which can be destroyed by mechanical or electrostatic shocks.

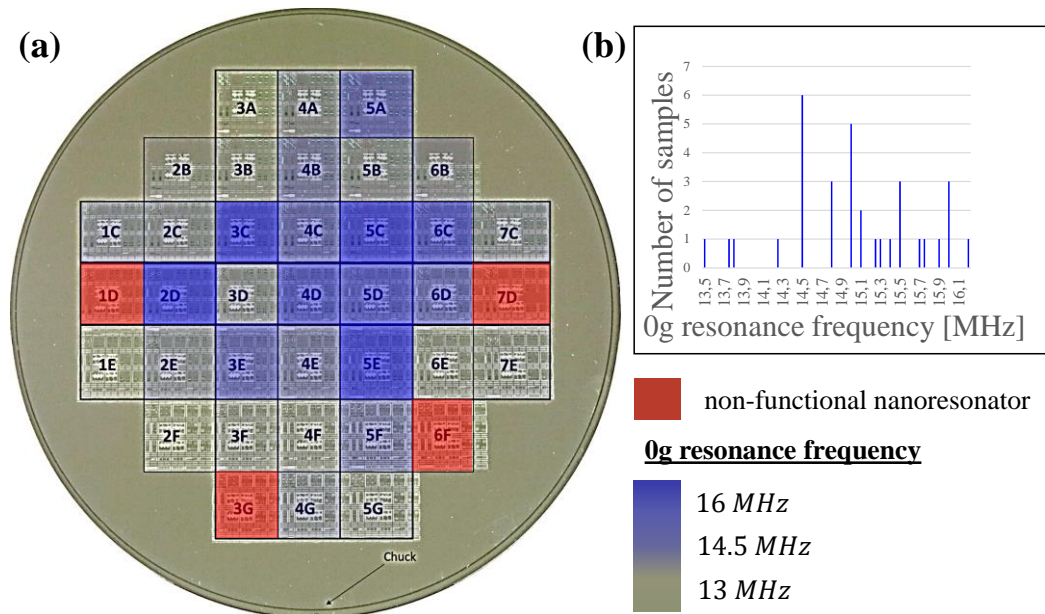


Figure 4-14 Mapping of the 0g-frequency of nanoresonators coupled to the accelerometers. The wafer consists in 37 chips that are named from 1 to 7 for the column and from A to G for the line.

After mapping, the wafers are cut and the individual chips are packaged and tested under acceleration. The new measured 0g frequencies of the nanoresonators presented in Figure 4-15 are reduced by a few hundred kilohertz, which could be due to strain relaxation during cutting.

The frequency sensitivity to axial stress (thus acceleration) is then measured for five sensors representative of the mean results in the wafer. Figure 4-15 (a) plots the open-loop sensitivity measurement performed on both nanoresonators coupled to the same accelerometer (Figure 4-12). The differential measurement shows the 0g-resonance frequencies are not matched between the nanoresonators. This mismatch is probably due to an initial proof mass rotation caused by residual shear deformation of the proof mass anchor, which induces differential 0g-stress σ_ϵ , as discussed in Figure 4-24. In first order, both sensitivities are equivalent $\pm 1.4 \text{ MHz/g}$. This is because for small σ_ϵ the resonance frequencies are close to $\sim 14.5 \text{ MHz}$, so their frequency sensitivity are equivalent. Moreover, some chips, which are randomly distributed on the wafer, have a higher σ_ϵ . For instance, one nanoresonator can operate at 13MHz while the other operates at 16 MHz. In these particular cases the two sensitivities are not equivalent and the differential measurement should be less effective. The previous mapping performed in the whole wafer allow identifying low σ_ϵ accelerometers.

Figure 4-15 (b) plots the frequency as a function of applied acceleration on five different sensors with and low σ_ϵ and the design of Figure 4-12. Sensors are named 5C, 5F, 5D, 5G and 3E due to their position on the wafer. Each sensitivity is measured under the same conditions using the measurement setup of Figure 4-1.

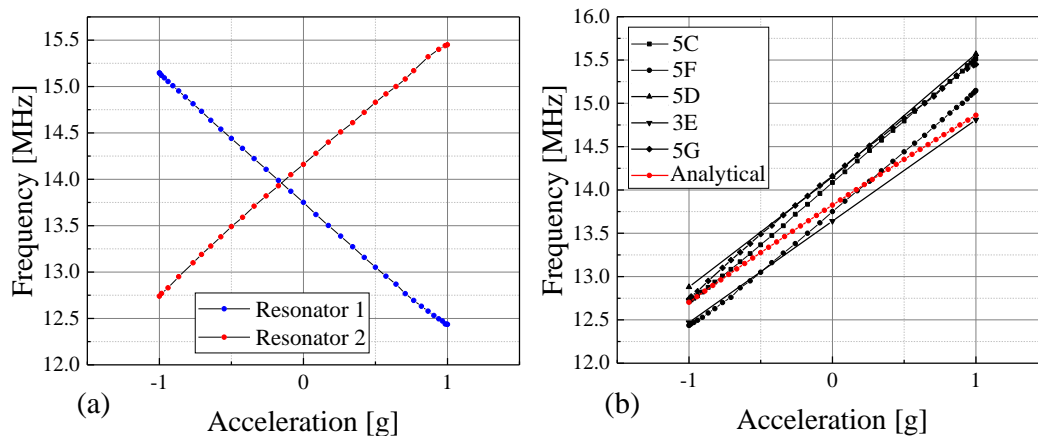


Figure 4-15 Experimental characterization of the accelerometer. Five similar sensors are tested on the same conditions: using a rotating table from -1g to 1g. (a) Differential frequency sensitivities of both nanoresonators of one accelerometer. (b) Single frequency sensitivities of the five accelerometers compared to analytical modelling.

Value	Minimum	Maximum
Resonance frequency	13.62 MHz	14.2 MHz
Frequency sensitivity	1.21 MHz/g	1.39 MHz/g

Table 16 Experimental resonance frequency and frequency sensitivity of the measured accelerometers. The minimum and maximum of their value are indicated in order to compare them with the assumed dispersion sources.

Considering the nanoresonator geometries shown in Figure 4-3, the resonance frequency and frequency sensitivity are calculated from an analytical modelling and FEM (COMSOL) simulations. The initial stress is involved in the resonance frequency and frequency sensitivity. It consists of the initial pre-stress σ_{PS} , the stress induced by the bias voltage σ_{bias} , and the 0g-stress which is close to $\sigma_\epsilon \approx 0$. Here, the initial stress of the nanoresonator is taken as $\sigma_{init} = -190MPa$ in order to match the analytical modelling.

Methods	Resonance frequency	Frequency sensitivity
FEM simulations	11.75 MHz	1.18 MHz/g
Analytical modelling	14.06 MHz	1.05 MHz/g

Table 17 Expression of the resonance frequency and frequency sensitivity from analytical modelling and FEM simulation. The initial stress is $\sigma_{init} = -190MPa$.

However, an initial stress does not allow to fit both the resonance frequency and the frequency sensitivity. Here, the mismatch is discussed as a combination of pre-stress and the standard deviation of the fabrication process. The nanoresonator width is the only geometrical parameter that can affect both the resonance frequency and the frequency sensitivity because it affects the in-plane bending mode of the nanoresonator (Eq. 2-17), the frequency to stress sensitivity of the nanoresonator (Eq. 2-19) and the rigidity of the accelerometer. The other parameters t_m , w_h and t_r affect the accelerometer rigidity, thus the accelerometer sensitivity (Eq. 2-4). Table 18 presents the minimum and maximum resonance frequency and frequency sensitivity as a function of the standard deviations of the fabrication process presented in section 4.1 and 4.2.

Standard deviation parameters	Resonance frequency [min, max]	Frequency sensitivity [min, max]
$w_r(\pm 3\sigma)$	[12.21 – 15.91] MHz	[1.03 – 1.33] MHz/g
$t_m(\pm 3\sigma)$	–	[1.13 – 1.23] MHz/g
$w_h(\pm 3\sigma)$	–	[1.07 – 1.29] MHz/g
$t_r(\pm 1\sigma)$	–	[1.16 – 1.2] MHz/g

Table 18 Expression of the maximum and minimum value of the resonance frequency and frequency sensitivity as a function of the standard deviation of the fabrication process. The initial stress is $\sigma_{init} = -190MPa$

4.2.2 Noise analysis

In this subsection, a noise analysis is performed using the heterodyne detection scheme of Figure 4-4. The noise in terms of resonance frequency fluctuations is deduced from the open-loop frequency measurement scheme presented in section 4.1.2, by measuring the phase fluctuation $\Delta\phi_r$ around the resonance frequency and deducing the resonance frequency fluctuations using the linear phase-frequency relationship. The measurement conditions used in the next experiment are an integration bandwidth of 10 kHz and a sampling rate of 100 kHz. In this experiment, two different accelerometers are tested. Both are the design presented in Section 4.2, but one operates at a high pressure level while the other operates at a low pressure level. They are named low-Q accelerometer and high-Q accelerometer respectively.

Figure 4-16 shows noises analysis of low-Q accelerometer for different values of AC actuation. The DC actuation and bias polarisation voltages are kept constant at 3.5 V and 1.5 V respectively. Here, the coupled nanoresonator has low quality factor $Q_r = 1000$. Figure 4-16 (a-inset) shows that the magnitude of $|V_{out}|$ depends on the AC actuation. The PSD of $|V_{out}|$, presented in Figure 4-16 (a), shows that additive white noise S_V is not affected by the AC actuation, as expected. Figure 4-16 (b) shows the PSD of resonance frequency fluctuations $\Delta\omega_r$. After 1 kHz, the PSD of $\Delta\omega_r$ is consistent with the phase noise because its noise level is inversely proportional to the SNR. However, the PSD of $\Delta\omega_r$ before 1 kHz is not consistent with the phase noise because the noise level is not dependant of the SNR. Here, there are two source of noise that affect the frequency fluctuation measurement $\Delta\omega_r$: the effect of additive noise on the frequency measurement, called phase noise, and the effect of thermomechanical noise of the accelerometer on the resonance frequency, called frequency noise. These effects are detailed in Figure 4-17.

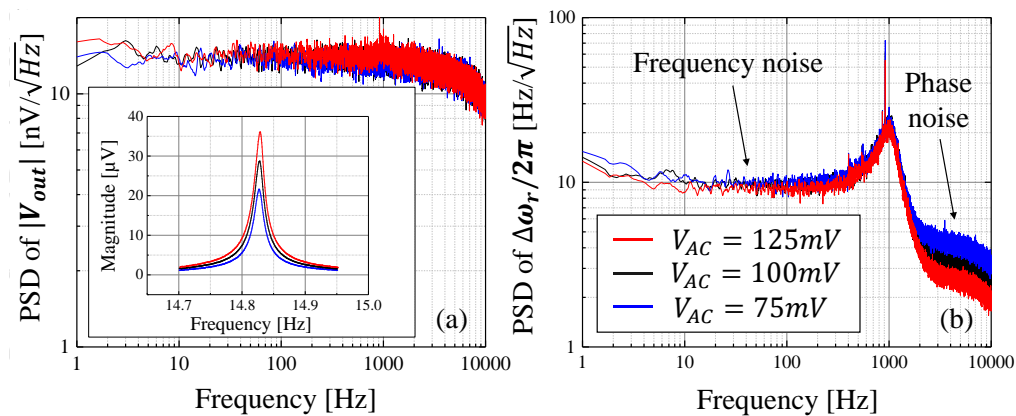


Figure 4-16 Open-loop frequency measurement of a nanoresonator coupled to a low-Q accelerometer. The bias actuation is $V_{bias} = 1.5V$ and the DC actuation is $V_{DC} = 3.5V$. (a) PSD of $|V_{out}|$ as a function of different AC actuation voltages. (a-inset) Magnitude of $|V_{out}|$ as a function of AC actuation. (b) PSD of $\Delta\omega_r$, calculated from the phase fluctuations $\Delta\phi_r$ and the phase-frequency relationship. This PSD can be divided in two parts, the frequency noise, which is the variation of resonance frequency due to thermomechanical noise of the accelerometer, and the phase noise, due to the additive noise of the nanoresonator.

Figure 4-17 shows how the different noise sources affect the frequency fluctuation measurement. On one hand, Figure 4-17 (a.1) represents the PSD of the thermomechanical noise of the accelerometer $S_{bm,N}$. This force spectral density is a white noise. $S_{bm,N}$ is transmitted to the nanoresonator as an axial stress spectral density through the mechanical response of the accelerometer H_m , represented in Figure 4-17 (a.2), and the transduction gain η_σ . As mentioned in section 2.2, an axial stress applied on nanoresonator induces resonance frequency shift through the frequency sensitivity to the stress $S_{\omega\sigma}$. Then, the force spectral density $S_{bm,N}$, equivalent to white noise, is transduced to a resonance frequency noise $S_{bm,\omega}$, represented on the PSD of ω_r (Figure 4-17 (a.3)). This frequency noise has the shape of the transfer function of accelerometer. In the next $S_{bm,\omega}$ is considered only before the accelerometer resonance (<1 kHz). When the open loop measurement of section 4.1.2 is performed, the noise of the resonance frequency ω_r is equivalent to the noise on the frequency fluctuations $\Delta\omega_r$. On the other hand, Figure 4-17 (b.1) represents the PSD of the additive noises S_V of the nanoresonator output voltage expressed in section 2.4.1. Figure 4-17 (b.2) represents the output voltage of the nanoresonator close to the resonance for different AC actuations. As detailed on Eq. 2-36, half of the additive noise is distributed as phase noise and it is inversely proportional to $|V_{out}|$. At resonance, the phase-frequency relationship allows expressing the effect of additive noises on the frequency fluctuation measurement, represented by S_ω (Eq. 2-37). Figure 4-17 (b.3) represents the impact of additive noise on the frequency fluctuations measurement as a function of the output voltage of Figure 4-17 (b.2).

In conclusion, the output signal of the sensor is the measurement of the resonance frequency fluctuations of the nanoresonator $\Delta\omega_r$. The open loop frequency measurement allows measuring the PSD of $\Delta\omega_r$ (Figure 4-17 (c)). This PSD can be dissociated in two parts: The noise called “frequency noise” comes from the noise of the resonance frequency $S_{bm,\omega}$. The noise called “phase noise” comes from the additive noise of the nanoresonator distributed as phase fluctuations and thus as an uncertainty in the measurement of ω_r . In our case, the frequency noise is dominant in the target bandwidth (1 kHz). In the section 3.1.3, the accelerometer is designed in order to match the noise coming from the thermomechanical noise of the accelerometer with the additive noises of the nanoresonator. This noises equality is performed under the assumptions of $Q_m = 250$ and $\omega_{0m} = 1.5 \text{ kHz}$. However, using Figure 4-16 (b), these accelerometer parameters are fitted to $Q_m = 2$ and $\omega_{0m} = 1 \text{ kHz}$. Under these experimental conditions, the measurement results fit the analytical modelling as shown in Table 19.

	Analytical modelling	Experimental
$\sqrt{S_{bm,\omega}}$	12.9 Hz/ $\sqrt{\text{Hz}}$	10 Hz/ $\sqrt{\text{Hz}}$

Table 19 Comparison of analytical modelling and experimental results of $S_{bm,\omega}$. The noise of the frequency fluctuations is expressed as white noise (Hz/ $\sqrt{\text{Hz}}$) because only the noise under $\frac{\omega_{0m}}{2\pi} = 1 \text{ kHz}$ is considered.

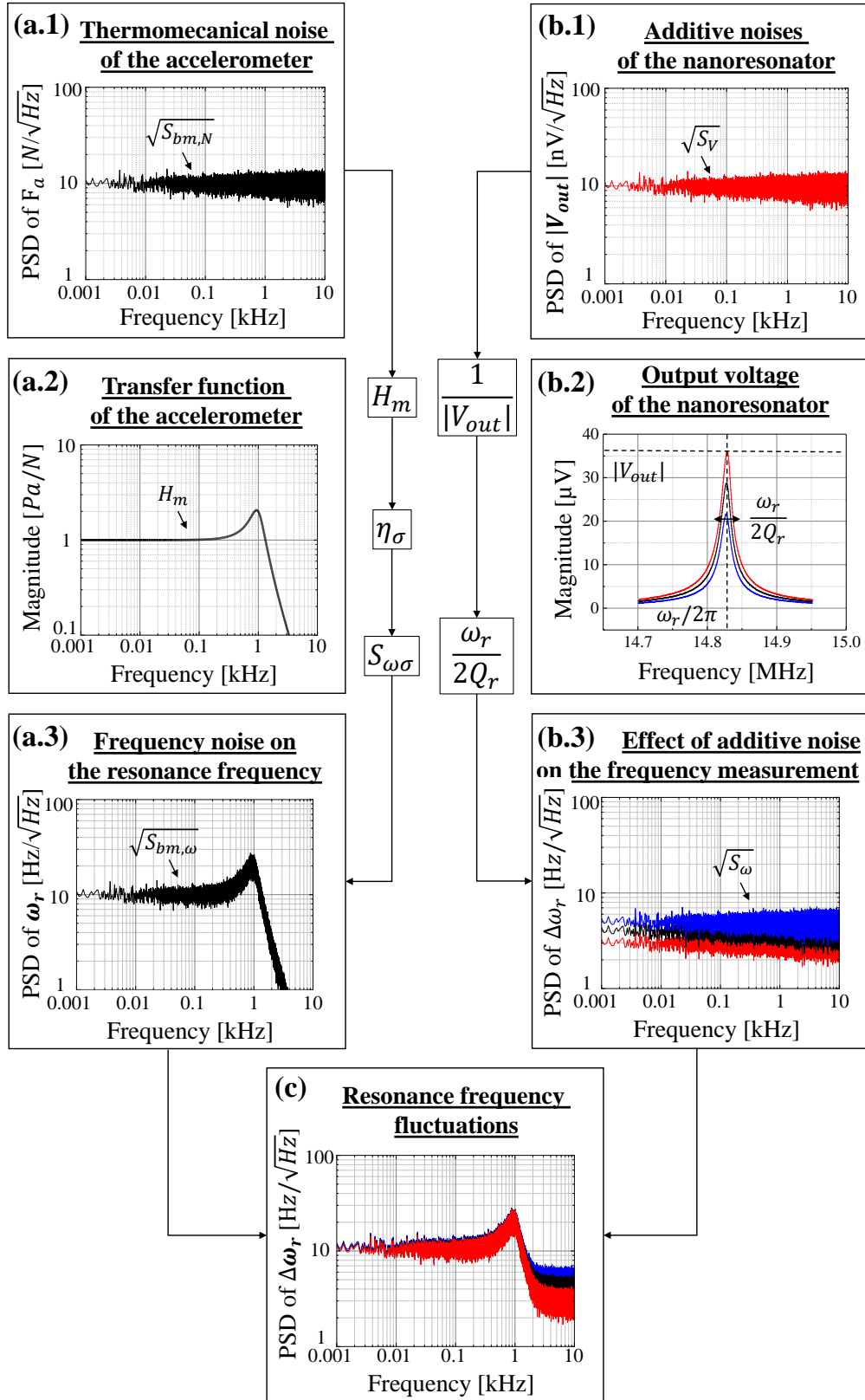


Figure 4-17 Comparison of the different noise sources of the frequency measurement. Left figures (a) represent the frequency noise of the nanoresonator's resonance coming from the thermomechanical noise of the proof mass. Right figures (b) represent the effect of additive noise on the frequency measurement. (c) Represents the PSD of the resonance frequency fluctuations arising from a combination of both sources.

The PSD of the frequency fluctuations $\Delta\omega_r$ gives the short term stability (>1 Hz) of the nanoresonator signal, i.e. its frequency. Because the accelerometer is designed to operate before its resonance (ω_{0m}), frequency fluctuations must be integrated below 1 kHz. For the low-Q accelerometer, the short-term stability of $\Delta\omega_r$ is then dominated by the thermomechanical noise of the accelerometer. Under these conditions increasing the nanoresonator output voltage does not improve the short-term stability of the frequency fluctuations, because the fluctuations of the resonance frequency themselves are more important than the measurement uncertainty induced by phase noise. Increasing the quality factor of the accelerometer by improving the level of vacuum is a solution to reach the nanoresonator detection limit. Figure 4-18 shows an equivalent noise analysis on samples with an improved packaging at wafer-level, in particular in terms of vacuum. Here, the coupled nanoresonator has high quality factor $Q_r = 5600$. On this measurement, AC actuation sweep is performed in open-loop frequency measurements. The measurement conditions are 5 kHz of integration bandwidth and 50 kHz of sampling frequency. Figure 4-18 (a-inset) shows that the nanoresonator magnitude is proportional to the AC actuation voltage. Figure 4-18 (a) shows the additive white noise is not affected by the AC actuation, as expected. There are some residual harmonics (70 Hz) on the PSD of V_{out} probably due to the experimental environment. Figure 4-18 (b) shows the PSD of the frequency fluctuations. Here, the accelerometer resonance can be identified at 1 kHz too but with an higher quality factor ($Q_m > 2$). Before the accelerometer resonance (<1 kHz) the PSD of resonance frequency fluctuations is affected by the AC actuation in the same way as after the accelerometer resonance, indicating that the contribution from thermomechanical noise of the accelerometer is negligible in regard to the effect of the additive noises of the nanoresonator. Indeed, $S_{bm,\omega}$ is inversely proportional to Q_m , which depends on the level of vacuum. Moreover, the $1/f$ behaviour at low frequency (<10 Hz) shows that the bias instability of nanoresonator is reached similarly to Figure 4-8.

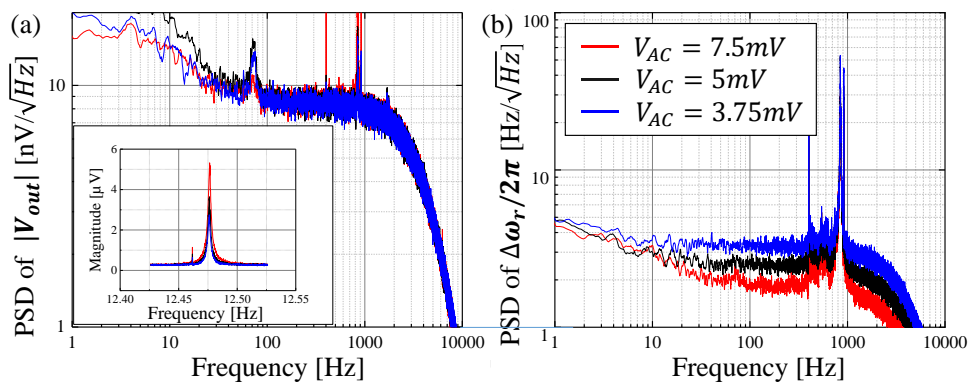


Figure 4-18 Open-loop frequency measurement of a nanoresonator coupled to a high-Q accelerometer. The bias actuation voltage is $V_{bias} = 1.25V$ and the DC actuation is $V_{DC} = 3.5V$. (a) PSD of $|V_{out}|$ as a function of different AC actuation voltages. (a-inset) Magnitude of $|V_{out}|$ as a function of AC actuation voltage. (b) PSD of $\Delta\omega_r$, calculated from the phase fluctuations $\Delta\phi_r$ and the phase-frequency relationship. This PSD can be divided in two parts, before and after the resonance frequency of the accelerometer (1 kHz). In both cases, the noise of $\Delta\omega_r$ is dominated by the additive noise of the nanoresonator.

In Figure 4-18 (b), the short-term stability of the frequency measurements can be represented as white noise from 50 Hz to 1 kHz. On this bandwidth, the noise density of $\Delta\omega_r$ is inversely proportional to V_{AC} and ranges from $4 \text{ Hz}/\sqrt{\text{Hz}}$ to $2 \text{ Hz}/\sqrt{\text{Hz}}$. However, from 1 Hz to 50 Hz, the noise density is dominated by $1/f$ noise. That is why the Allan deviation is used in order to calculate the bias instability of both low-Q accelerometers and high-Q accelerometers.

Here the Allan deviation is then expressed in terms of acceleration: from the frequency fluctuations measurement $\Delta\omega_r$, $\sigma_f(\tau)$ is processed from Eq. 4-5, and expressed in acceleration by using the accelerometer sensitivity $S_{a\omega}$ as $\sigma_a(\tau) = [\omega_r/S_{a\omega}] \sigma_f(\tau)$. Figure 4-19 (a) shows the Allan deviation of the low-Q accelerometer ($Q_r = 1000$) as a function of the measurement time τ . On the 1 kHz-bandwidth ($\tau \in [1\text{ms} - 1\text{s}]$), the Allan deviation has $\tau^{-1/2}$ slope typical of white noise. The noise level on this range is not affected by the AC actuation, suggesting that this limit corresponds to the thermomechanical noise of the accelerometer, which is a frequency noise and therefore independent of SNR. After 1 s of integration time, the Allan deviation reaches a plateau, probably due to long-term drifts induced by the fluctuation of environmental parameters. Figure 4-19 (b) shows the Allan deviation of the high-Q accelerometer ($Q_r = 5600$). For $\tau \in [1\text{ms} - 0.1\text{s}]$, the Allan deviation presents again a $\tau^{-1/2}$ slope representative of white noise. However, in this case the deviation is affected by the AC actuation: this suggests that the dominating noise source in this case is additive noise, which is proportional to the SNR. After 0.1 s of integration time the Allan deviation reaches a plateau probably caused by the same detection limit as the nanoresonator presented in Figure 4-10. In conclusion, the improvement of wafer level packaging allows reaching the detection limit of the nanoresonator: the equivalent acceleration noise on 1 kHz-bandwidth ranges from to $7.14 \mu\text{g}/\sqrt{\text{Hz}}$ for the low-Q accelerometer to $1.75 \mu\text{g}/\sqrt{\text{Hz}}$ for high-Q accelerometer. The bias instability ranges from $10 \mu\text{g}$ at 1s of integration for low-Q accelerometer to $5 \mu\text{g}$ at 1s of integration for the low-Q accelerometer.

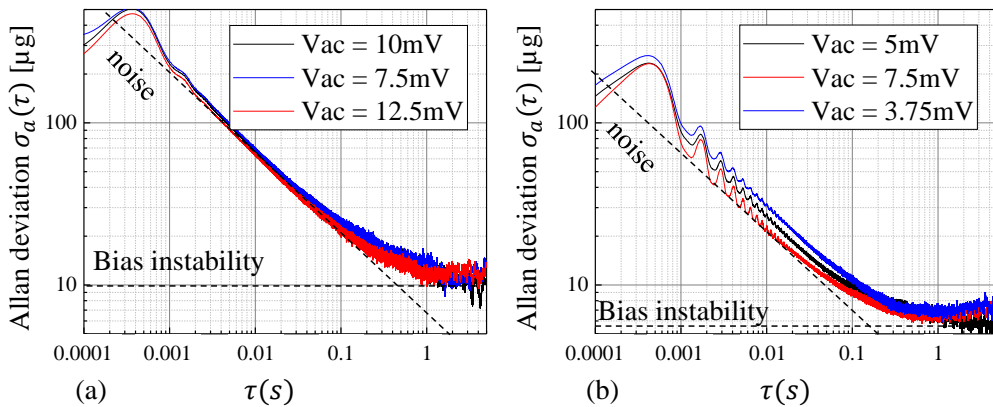


Figure 4-19 Allan deviation of acceleration as a function of the driving voltage of the nanoresonator V_{AC} . (a) The Allan deviation of low-Q accelerometer is dominated by the thermomechanical noise of the proof mass $S_{bm,\omega}$. (b) The Allan deviation of the high-Q accelerometer is dominated by additive phase noise (section 2.4.1).

4.2.3 Non linearities

Here the critical amplitude is studied on coupled nanoresonators. Eq. 2-28 shows that the critical amplitude depends on the quality factor Q_r and the axial stress applied on the beam. The subsequent analysis compares the critical amplitude v_{max} of two different coupled nanoresonators as a function of applied stress and quality factor. Figure 4-20 shows the frequency response of coupled nanoresonators with $Q_r < 1000$ for several AC actuation voltages. The bias polarisation is $V_{bias} = 1.5 V$ and the DC actuation is $V_{DC} = 3.5 V$. The critical amplitude is probably limited by spring hardening as expected. Table 20 compares the nanoresonator critical amplitude for different accelerations. The resonance properties (f_r and Q_r) depend on the acceleration and have been taken into account on the analytical modelling.

	acceleration	v_{max}	$v_{max}\eta_S$	V_{max}
$Q_r = 730$				
$f_r = 14.98 MHz$	0.5 g	4.1 nm	34.7 μV	< 40 μV
$Q_r = 443$				
$f_r = 12.92 MHz$	-1 g	4.58 nm	38.77 μV	< 40 μV

Table 20 Comparison of the analytical modelling of v_{max} , the analytical modelling of critical magnitude $v_{max}\eta_S$ and the measured critical amplitude V_{max} .

Because the quality factor depends on the operating frequency of the nanoresonator (Figure 4-13 (b)), so does the critical amplitude, the operating AC actuation must be fixed by the minimum critical amplitude of the frequency range. For low- Q_r nanoresonators, the operation limit (in terms of critical amplitude) is relatively uniform for the whole working frequency range. Thus, the actuation voltage can be set for an initial position and ensures the linear response over the whole operating frequency range of the nanoresonator.

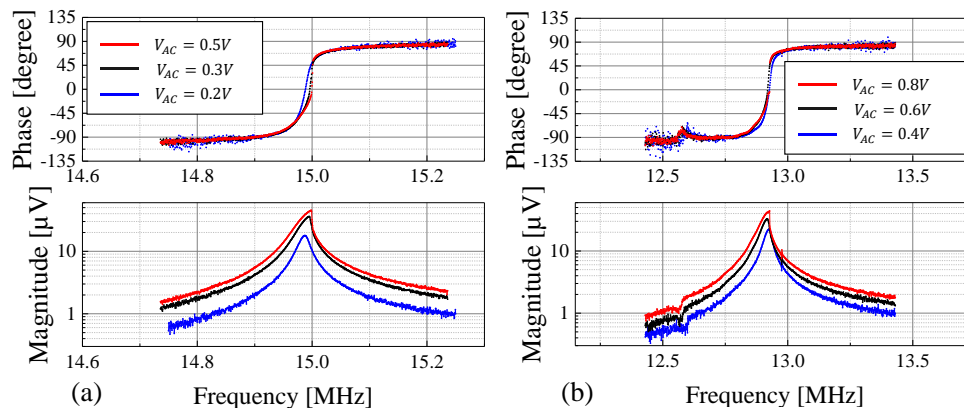


Figure 4-20 Measurement of the transfer function of coupled nanoresonator as a function of AC actuation voltage. The DC actuation is $V_{DC} = 3.5 V$. The shape of the magnitude response suggests that the spring hardening appears for $V_{AC} > 0.5 V$. (a) Coupled nanoresonator operating under 0.5 g of acceleration. (b) Coupled nanoresonator operating under -1 g of acceleration.

Figure 4-21 shows the frequency response of coupled nanoresonator, with $Q_r > 4000$, in terms of magnitude and phase for several AC actuation voltages. The bias polarisation is $V_{bias} = 1.25 \text{ V}$ and the DC actuation is $V_{DC} = 3.5 \text{ V}$. In the case of the nanoresonator of Figure 4-21 (b) operating at 12.5 MHz, the critical amplitude is probably limited by spring hardening. However, on Figure 4-21 (a) another non-linearity appears before the expected critical amplitude, which is not understood for the moment. Therefore, the maximum AC voltage ensuring the linearity of the nanoresonator response over the frequency operation range is lower than the one required to achieve spring hardening effect. The SNR will not be maximised under these conditions. Table 21 compares the analytically modelled nanoresonator's critical amplitude for different accelerations.

	acceleration	v_{max}	$v_{max}\eta_S$	V_{max}
$Q_r = 4500$				
$f_r = 14.98 \text{ MHz}$	0.5 g	1.66 nm	14.1 μV	$< 5 \mu\text{V}$
$Q_r = 6300$				
$f_r = 12.47 \text{ MHz}$	-1 g	1.18 nm	9.98 μV	$< 10 \mu\text{V}$

Table 21 Comparison of the analytical modelling of v_{max} , the analytical modelling of critical magnitude $v_{max}\eta_S$ and the measured critical amplitude V_{max} .

Several experiments yield the following conclusions with respect to the unexpected non-linear phenomenon of high-Q resonators: (1) This non-linearity is reproducible on every coupled nanoresonator with $Q_r > 4000$. (2) Figure 4-11 shows that uncoupled nanoresonators operating at the same frequency do not suffer from this effect. (3) The applied acceleration has an impact on this non-linearity for coupled nanoresonators with $Q_r > 4000$ but not for $Q_r < 1000$. A first hypothesis is that when the nanoresonator damping is not dominated by its air environment but by dissipation on the anchor ($Q > 4000$), the coupling to the proof mass changes these anchor conditions as a function of the applied acceleration.

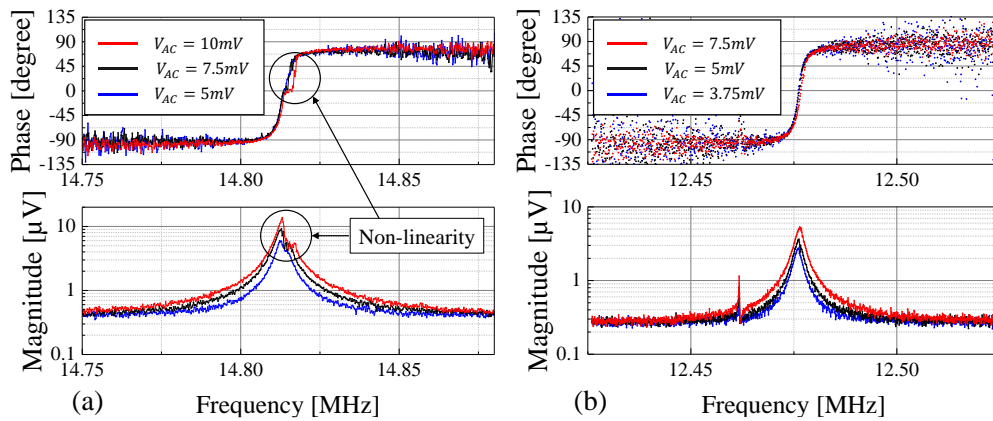


Figure 4-21 Measurement of the transfer function of a coupled nanoresonator as a function of AC actuation voltage. The DC actuation is $V_{DC} = 3.5 \text{ V}$. The shape of the magnitude response suggests that the spring hardening appears for $V_{AC} > 0.5 \text{ V}$. (a) Coupled nanoresonator operating under 0.5 g of acceleration. (b) Coupled nanoresonator operating under -1 g of acceleration.

4.2.4 Closed loop operation

A closed-loop measurement method to track the resonance frequency in real time is mandatory in order to be able to monitor large frequency variations. It is well-established that resonators with high quality factors offer a better phase-frequency relationship at the expense of a slow mechanical response. For the nanoresonators studied here, their mechanical response is larger than the desired bandwidth of the accelerometer ($\omega_{0m} < \omega_r/2Q_r$). Therefore, a self-oscillating circuit is chosen to implement the closed-loop operation. However, this oscillating circuit only works optimally if the feedthrough capacitance is corrected, as explained in section 3.2.3. Here, a first closed-loop measurement is implemented to study the behaviour of nanoresonators used as force sensors, in particular (1) their thermal drift and (2) their frequency variations under acceleration.

To do this, the heterodyne detection presented in Figure 4-4 is combined with a PLL using the LIA (Figure 4-22). Unlike the open-loop frequency measurement, the resonator always operates at its resonance in a closed loop. The resonance frequency is monitored by a PLL which adjusts the frequency of the actuation signal to correct the phase error with respect to a reference. A variable-frequency oscillator at frequency ω_r is used to actuate nanoresonator. The fixed-frequency oscillator at frequency $\Delta\omega$ is used to demodulate the nanoresonator's output in order to process its phase ($\tan^{-1}(Y/X)$). This phase is compared with a previously-measured phase at resonance φ_0 , then a phase error is generated and fed into a PI controller. In this specific case, these coefficients are calculated using the previously calculated linear frequency/phase relationship and the desired PLL response time τ_{PLL} . Finally, the PI controller calculates the correction to the frequency of the oscillator ω_r as a function of this phase error.

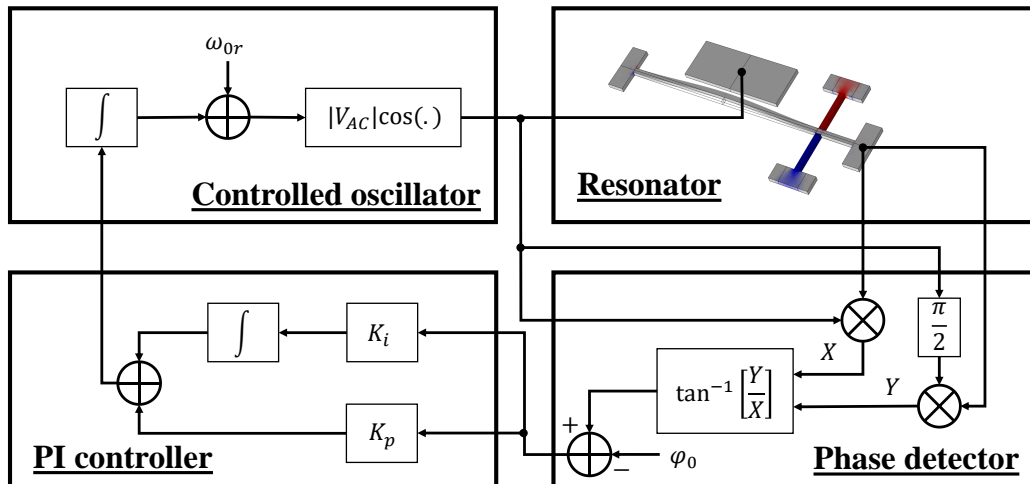


Figure 4-22 PLL-based closed loop of nanoresonator using heterodyne detection. The controlled oscillator frequency is initially set to ω_{0r} and then maintained to ω_r . The heterodyne part of the PLL (bias voltages at $\omega_r + \Delta\omega$ angular frequency and output at $\Delta\omega$ angular frequency) is omitted in this figure.

4.2.4.1 Thermal drift

Using a PLL-based closed loop, long-term frequency measurements are made on accelerometers with two measurable nanoresonators in differential configuration. The specificity of their nanoresonators is that they have 1 μm -long nanogauges. In this configuration, the transduction is less efficient in the sense that the Johnson noise is higher than in the previously tested nanoresonators. This does not matter because the purpose of these measurements is to quantify the long-term stability of the frequency measurement, especially due to the thermal environment. The expected behaviour is that the thermal drift will induce a common mode signal on the sensing elements that can be compensated by a differential measurement.

Figure 4-23 (a) shows the differential closed-loop frequency measurement as a function of time. The frequency fluctuations of both nanoresonators, $\Delta\omega_1(t)$ and $\Delta\omega_2(t)$, are normalized by their initial resonance frequencies, respectively ω_{01} and ω_{02} . The temperature is acquired in real time as close as possible to the accelerometer. Relative frequencies are measured in real time during 1800 seconds. Contrary to the expected behaviour, the nanoresonators are differentially affected by the temperature drift: when the temperature increases, $\Delta\omega_1$ decreases whereas $\Delta\omega_2$ increases. These results are reproducible on three similar accelerometers. The hypothesis is the one nanoresonator is compressed when the temperature increase whereas the other one is elongated, such as during an acceleration. As the differential effect is indistinguishable from an acceleration, it is not possible to compensate temperature fluctuations with this architecture. Indeed, Figure 4-23 (b) shows the Allan deviation of each frequency measurement and the processed Allan deviation of their differential measurement. Because both nanoresonators are measured in real time, differential measurement consists in the subtraction of their frequency $\Delta\omega_{diff}(t) = |\Delta\omega_1(t) - \Delta\omega_2(t)|$. As expected from the differential closed-loop measurement, the long-term frequency stability is degraded by the differential measurement because temperature drift is differential.

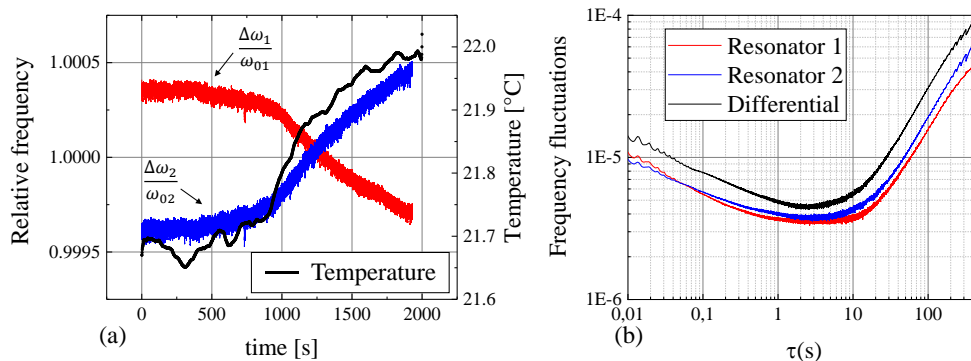


Figure 4-23 Differential closed loop measurement. (a) Frequency measurements of both nanoresonators and temperature acquisition. (b) Allan deviation of the frequency response of each nanoresonator, and Allan deviation of their differential response.

Assuming a steady state is reached, the increase of temperature of the environment induces an increase of the temperature of the silicon structure as well as of the packaging. The measurements are performed on the accelerometer design of Figure 4-24 (a.1). The silicon structure is perfectly symmetrical except for the proof mass anchor which has a slight asymmetry. The silicon chip is initially glued (Figure 4-24 (c)) to its ceramic substrate with a rigid adhesive under its entire surface. Considering the whole system comprising the integrated accelerometer, several hypotheses can be made about the origin of this differential drift.

In practice, the dilatation of the proof mass induces compressive stress on both nanoresonators. This effect is reproduced by FEM (COMSOL) simulations (Figure 4-24-(a.2)), where an increase of $\Delta T = 100^\circ\text{C}$ is applied to the accelerometer and induces a common-mode stress on both nanoresonators. The first hypothesis is that the asymmetry of the proof mass anchor induces, in addition to the expected common mode, a differential mode. In order to quantify this effect by FEM simulations, the axial stress induced in both nanoresonators, $\sigma_{x,R1}$ and $\sigma_{x,R2}$, and differential stress $\sigma_{x,diff} = |\sigma_{x,R1} - \sigma_{x,R2}|$, are compared to the maximum allowable stress σ_{max} . The maximum stress corresponds to the stress applied on the nanoresonator when the proof mass reaches the stoppers. Table 22 compares these stress ratio and shows the relative differential stress $\sigma_{x,diff}/\sigma_{max}$ is negligible to the relative common-mode stress $\sigma_{x,R1}/\sigma_{max}$.

The second assumption is that the difference in the coefficient of thermal expansion (CTE) between the ceramic substrate and the silicon generates a shear effect on the chip, which is transmitted to all accelerometer anchors due to die-attach [98]–[100]. This effect, called package stress, has been known for a long time [101] and can be limited by using single anchor [103]. Due to the need of pads for piezoresistive transduction, the current design is not based on a single anchor architecture. The base strain sensitivity is a specification of the entire accelerometer (silicon chip + packaging) that is typically expressed for a hundred microstrain [23] for strain-critical application. In order to quantify the phenomenon on our design, a FEM simulation reproduces the effect of shear deformation on the accelerometer anchors. In Figure 4-24-(c), where a shear deformation of $\epsilon_{XY} = 100 \text{ ppm}$ is applied to all accelerometer anchors and induces differential stress on both nanoresonators. In order to compare this effect, the same criterion is used than the previous hypothesis. Table 22 compares these stress ratio and shows the relative differential stress $\sigma_{x,diff}/\sigma_{max}$ is important in regards to the one of $\Delta T = 100^\circ\text{C}$.

	$\sigma_{x,R1}/\sigma_{max}$	$\sigma_{x,R2}/\sigma_{max}$	$\sigma_{x,Diff}/\sigma_{max}$
$\epsilon_{XY} = 100 \text{ ppm}$	26.59%	-26.59%	53.18%
$\Delta T = 100^\circ\text{C}$	-120.46%	-119.96%	0.51%

Table 22 Comparison of axial stresses (σ_x) calculated from FEM simulations for the two hypothesis ($\Delta T = 100^\circ\text{C}$) and ($\epsilon_{XY} = 100 \text{ ppm}$). The stress is normalized by full-scale stress σ_{max} .

As $\epsilon_{XY} = 100 \text{ ppm}$ is the dominant effect of this FEM comparison, different gluing strategies are proposed, shown in Figure 4-24 (d). The aim is to minimize the shear effect induced by the difference in CTE between the substrate and the chip. Soft glue (d.1) should absorb the shear stress better than a rigid glue (c) and a silicon buffer (d.2) allows matching the CTE between the buffer and the substrate to avoid the shear deformation. The comparison of these different packages through simulation and experimentation is an important pending task for the future development of such accelerometers. However, efforts to be more robust against thermal drift have rather focused on improving the architecture of the accelerometers in the second generation to be presented in section 5.2.2.

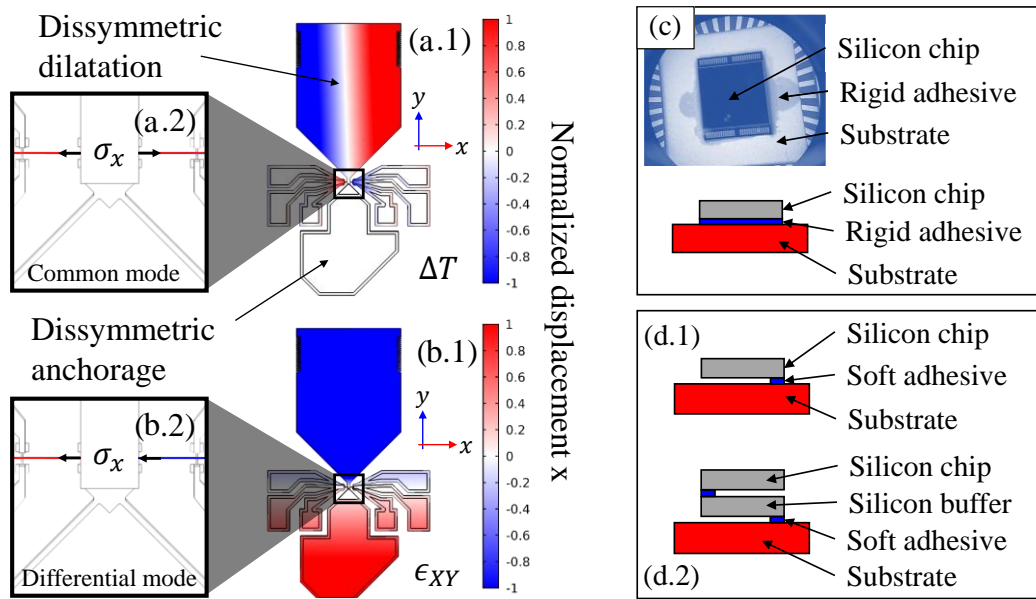


Figure 4-24 (a.1) FEM simulations of $\Delta T = 100^\circ\text{C}$. The displacement in the “x” direction induced by thermal dilatation has a small dissymmetry due to proof mass anchor’s dissymmetry. (a.2) Common-mode stress induced by thermal dilatation. For an increase of temperature, the stress is in compression. (b.1) FEM simulations of a shear stress in the substrate $\epsilon_{XY} = 100\text{ppm}$. The displacement in the “x” direction induced by the shear effect shows that the proof mass tilts, similarly than under an acceleration. (b.2) The whole proof mass tilts in one direction induces a differential axial stress. (c) Current packaging used for experimental results. (d) Proposed new packaging to avoid package stress. (d.1) The soft adhesive helps to absorb some of the shear strain induced by the CTE mismatch, and positioning the adhesive on only one corner reduces the contact area, and thus the shear strain. (d.1) Adding a silicon buffer helps absorb the ceramic-induced shear stress and matches the CTE of the buffer stage with that of the silicon chip.

4.2.4.2 Spurious mode coupling

Next, a PLL-based closed loop allows performing a measurement of the sensitivity of the accelerometer, in other words, to measure in real time the frequency shift due to the acceleration. For this measurement, the accelerometer is integrated in the measurement set-up of Figure 4-1. The PLL-based closed loop of Figure 4-22 is implemented. The actuation parameters are $V_{AC} = 0.2\text{ V}$ / $V_{bias} = 1.5\text{ V}$ / $V_{DC} = 3.5\text{ V}$. The rotating bench sets a varying rotation angle, hence an acceleration, from -1g to 1g during a 10s period.

Figure 4-25 compares the open-loop sensitivity measurement with the closed-loop sensitivity measurement. In general, both sensitivities are perfectly matched. The magnitude and quality-factor variations shown on Figure 4-13 do not affect the operation of the PLL. Close to the 0g position, the resonance frequencies of both nanoresonators should cross, but we observe no evidence of coupling between nanoresonators. However, at two specific positions, -0.5g and 0.75g, at frequencies 13.68MHz and 15.41MHz respectively, the PLL apparently loses tracking of the resonance frequency. This is a major issue affecting the accelerometer because it reduces the useful working frequency range of the nanoresonator and thus the acceleration range (here -0.5g to 0.75g).

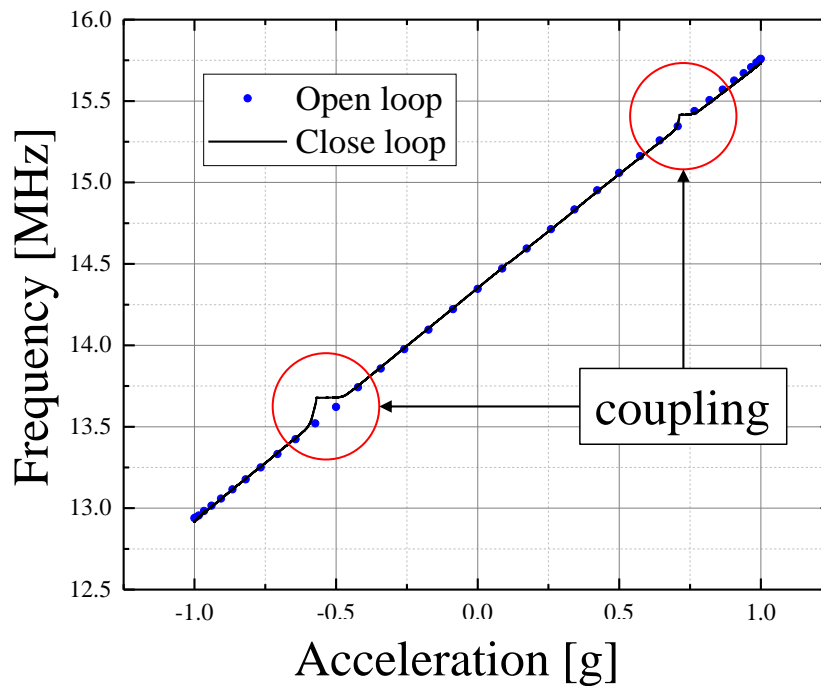


Figure 4-25 Comparison between open-loop sensitivity measurement and closed-loop sensitivity measurement from -1 to +1g. The closed-loop sensitivity measurement hints at a coupling phenomenon of the nanoresonator's first bending mode.

Figure 4-26 shows the transfer function of the nanoresonator around the specific position of 0.75 g for different accelerations. The magnitude shape suggests that the nanoresonator is subject to mode coupling. In its most basic form, the mode coupling is represented by a damped spring-mass, like on Figure 6-3. Its operation assumes a stiffness coupling. In this configuration, one spring-mass system represents the nanoresonator used as force sensor, where the flexural stiffness is modulated by the acceleration. The other one represents the other resonator of unknown origin. A spring coupling both elements represents the coupling in stiffness. From the basic form of the mode coupling, the shape of the nanoresonator's resonance is discussed in order to find the origin of the mode coupling. The different springs of the systems are supposed, one after the other, to be modulated by the acceleration in order to match the shape of the basic form with the shape of Figure 4-26. The different cases are discussed in Appendix C. The most likely case is that only the spring representing the flexural stiffness of the nanoresonator is modulated by the acceleration. The spring coupling and the spring of the unknown system are not modulated by the acceleration. This case can represent mode coupling originating from modes of the MEMS structure that are not affected by the acceleration.

Mode-coupled resonators have been the subject of several works [104], [105] and a recent work takes advantage of coupling control to implement a resonator-based mode-localized accelerometer [106]–[108]. On resonant beam accelerometers using nanoresonators, the mode-localized coupling is not desired. But the MEMS structure (accelerometer) is composed of micrometric elements (proof mass and hinge), and therefore its first resonance frequencies are close to the kHz. The nanoresonator operates at the MHz and its resonance frequency sweeps a large several-MHz frequency range during operation. It is therefore very probable that the working mode of the nanoresonator intersects with higher modes of the MEMS structure, for instance the n -th mode of flexible elements.

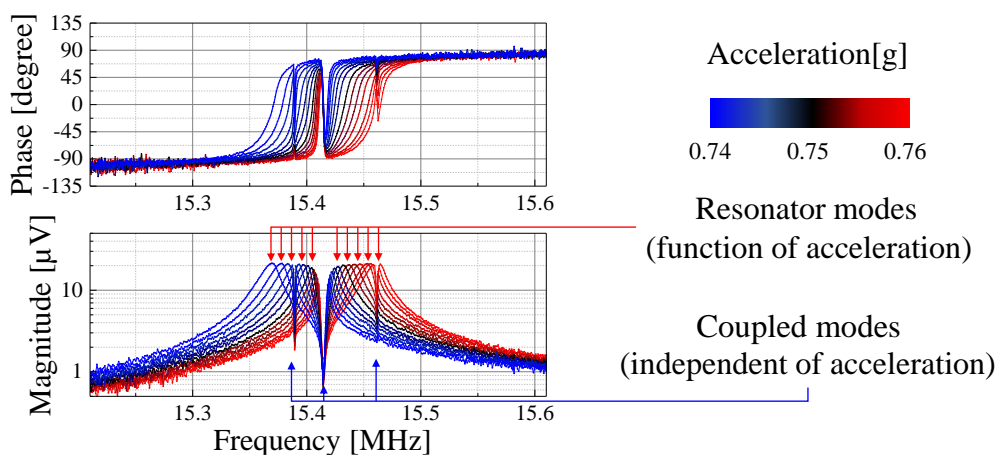


Figure 4-26 Transfer function of a nanoresonator as a function of applied acceleration. Around 15.41 MHz, the transfer function shows a dominant coupling and two “soft” couplings at 15.39 MHz and 15.46 MHz that affect the closed loop measurement less importantly than the dominant one. The actuation parameters are $V_{AC} = 0.2 V / V_{bias} = 1.5 V / V_{DC} = 3.5 V$.

The challenge is then to identify the origin of the coupled modes. An investigation is first carried out in order to rule out certain hypotheses, and then a tool to identify parasitic modes is implemented using FEM (COMSOL) simulations. Figure 4-27 compares mode-coupling measurements for different accelerometer architectures. The objective is to relate features of the mode-coupling phenomena to differences in the accelerometer structures. The two versions of accelerometer are: the one of Figure 4-26, named M1-accelerometer because its proof mass length is $L_m = 380\mu\text{m}$, another one with proof mass length $L_m = 600\mu\text{m}$, named M2-accelerometer. Two specific coupled modes appear at the same frequency (13.68MHz and 15.41MHz) and have the same insensitivity to acceleration, as described in Figure 4-26. In Figure 4-27 another coupled mode appears at 15.5 MHz for the M2 accelerometer. This difference will be an evidence for the FEM simulation identification method. The geometrical features shared by the two accelerometer structures are the resonant beam length ($L_r = 10\mu\text{m}$), the nanoresonator position ($l = 5\mu\text{m}$) and the hinges' geometries ($L_h = 51.41\mu\text{m}$, $t_h = 20\mu\text{m}$ and $w_h = 1\mu\text{m}$). The geometrical difference between the three accelerometer structures is the proof mass characteristic length L_m . The M1 accelerometer allows differential measurements and shows that coupled modes appear at the same frequencies for both nanoresonators, named respectively Res1 and Res2 on the Figure 4-27.

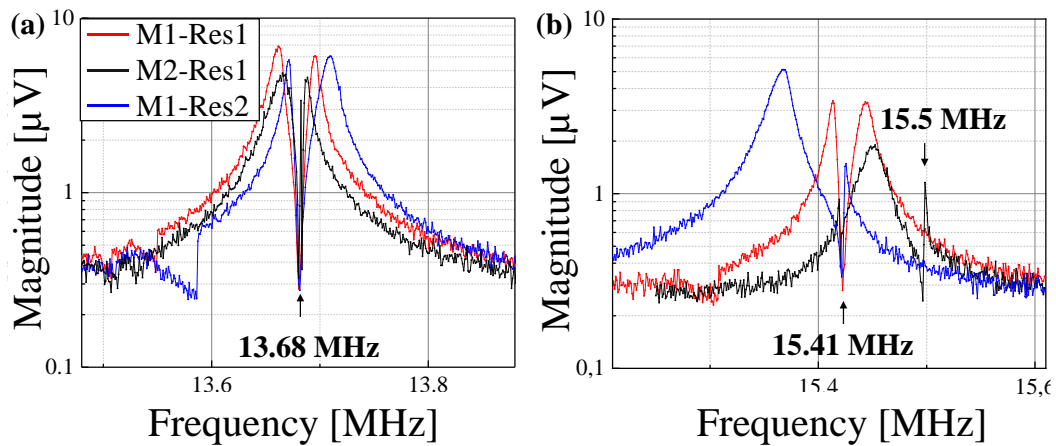


Figure 4-27 Transfer functions of nanoresonators coupled to different MEMS structures. (a) Measurement of mode coupling of the 13.68 MHz-mode. (b) Measurement of mode coupling of the 15.41 MHz-mode and 15.5 MHz. On the M1-accelerometer the differential measurement is allowed and coupled modes are measured on both nanoresonators, respectively Res1 and Res2. The M2-accelerometer has an additional coupling at 15.5 MHz.

What can be deduced from the above information is that: (1) The out-of-plane mode is close but not superposed with the in-plane mode and both are affected by acceleration. It is therefore unlikely that the coupling is due to the interaction between different nanoresonator modes. (2) For a differential structure with a low initial stress (σ_ϵ), the two nanoresonators operate in a similar frequency range and they have equal resonance frequency for a certain acceleration value. However, at this frequency intersection, there is no evidence of coupling. On the contrary, the coupled modes appear at the extreme ends of the frequency range, when the

frequencies are far apart as shown in Figure 4-15 (a). It could be that the out-of-plane mode of one resonator intersects the in-plane mode of the other at these positions. In this case, the mode coupling would be dependent on the acceleration, and that is not the case. In conclusion, the behaviour does not seem consistent with a coupling between resonance modes of two nanoresonators. (3) As predicted by the analytical modelling of the problem, the coupling is probably induced by the interaction between the MEMS structure and the nanoresonators. As the change of the proof mass does not affect the position of the coupling, the coupled modes are probably due to the flexible elements of the MEMS structure, in particular the pivot: Two hinges, placed at 45 degrees of the sensitive direction, allow the mass to rotate around a central node. The nanoresonators are placed at $l = 5 \mu m$ from the central node of the pivot that connects all the flexible elements to the proof mass.

A FEM simulation method is developed to validate the hypothesis that the hinges are responsible for these coupled modes. The objective is to identify the modes of the MEMS structure that are coupled to the in-plane mode of the nanoresonators. The identification method is detailed in Appendix C. Here, the identification method is applied to the M1 and M2-accelerometer architecture but it can be applied to any other design. Figure 4-28 and Figure 4-29 show the results of the identification method used for the M1-accelerometer and M2-accelerometer architectures respectively. For each figure, sub-figure (a) shows the evolution of all the accelerometer modes as a function of acceleration. It can be seen that the resonator modes vary with acceleration while the MEMS modes are not affected. Here only the in-plane mode of one nanoresonator is studied because the problem is symmetric. Some crossings between the nanoresonator modes and the MEMS modes are circled. These are the likely couplings observed experimentally named m-x, where x is the mode number. In order to highlight the coupling, the method studies the relative modal mass, which is calculated from the FEM simulation. It consists in a ratio between the integrated modal mass of the nanoresonator and the integrated modal mass of the whole accelerometer. For the in-plane mode of the nanoresonator, this fraction must be equal to 1 because all the modal mass must be concentrated on the nanoresonator. When the in-plane mode of nanoresonator crosses coupled modes, part of the nanoresonator modal mass is displaced somewhere else on the accelerometer. Sub-figure (b) represents the relative modal mass of the in-plane mode of the right-nanoresonator. The relative modal mass is represented as a function of frequency because the in-plane mode of the nanoresonator is a function of acceleration. For this nanoresonator, the relative modal mass is calculated over the entire operating range of the nanoresonator mode [12.5 MHz to 16 MHz] corresponding to an acceleration [-1g to +1g]. It can be clearly seen that for certain frequencies, sub-figure (b) shows a black peak that means the relative modal mass is distributed outside the nanoresonators: these are the couplings.

As identified on the sub-figures (a) and (b) of Figure 4-28 and Figure 4-29, there is an important population of MEMS modes that could be identified as coupled modes thanks to the identification criterion. Comparison between FEM simulations and measurements allows identifying, in this population of MEMS modes, which are the observed coupled modes. The comparison is based on the relative frequency difference between these modes. The experimental frequencies of the coupled modes are extracted from sub-figures (m-x.1) where the shape of the nanoresonator magnitude highlights the coupling modes. The corresponding modal deformation, calculated by the FEM simulation, is shown in sub-figures (m-x.2). This modal deformation represents the MEMS mode shape when the nanoresonator mode is far from the coupling frequency. The sub-figures (m-x.3) show the modal deformation of the MEMS mode shape when the nanoresonator mode is close to the coupling frequency. In this configuration, the MEMS mode shape has the shape of the in-plane mode shape of the nanoresonator, which is representative of the mode coupling. This is because the coupling mode shape is a linear combination of the nanoresonator bending mode and the MEMS structure mode, which are normalized by the maximum vibration amplitude of the whole structure. Since the amplitude of vibration of the nanoresonator is much higher than that of the MEMS, so it is normalized and we do not see the MEMS.

Table 23 compares the relative frequency difference between these modes. The experimental modes at 13.68 MHz and 15.41 MHz have quasi-equivalent frequencies on both M1-accelerometer and M2-accelerometer's FEM simulations. A frequency mismatch of $\Delta f_{init} = 200 \text{ kHz}$ is found, which can be due to the absence of release holes on the FEM simulation model. The other modes are identified thanks to this frequency mismatch. Looking at the shape of the identified modes, the hinges seem to be at the origin of the coupling.

In conclusion, the developed FEM method will be able to predict such coupling phenomena in advance. The first identification criterion predicts more coupled modes than the ones observed experimentally. Based on these first experimental results, the method must be completed by other criteria in order to identify the most probable coupled mode and to reject the others. However, efforts have been focused on the development of mechanical structures to avoid mode coupling.

M1-accelerometer			M2-accelerometer		
f_{exp}	f_{FEM}	δf	f_{exp}	f_{FEM}	δf
13.68MHz	13.2MHz	2.4	13.68MHz	13.3MHz	1.9
			14.1MHz	13.62MHz	2.4
14.5MHz	14.28MHz	1.1			
			14.7MHz	14.22MHz	2.4
15.4MHz	15.19MHz	1.05	15.41MHz	15.21MHz	1
			15.5MHz	15.36MHz	0.7

Table 23 Comparison of the measured coupled modes f_{exp} and the probable MEMS modes f_{FEM} found by the FEM simulation method. The mismatch δf correspond to the relative frequency error $|f_{exp} - f_{FEM}|/\Delta f_{init}$.

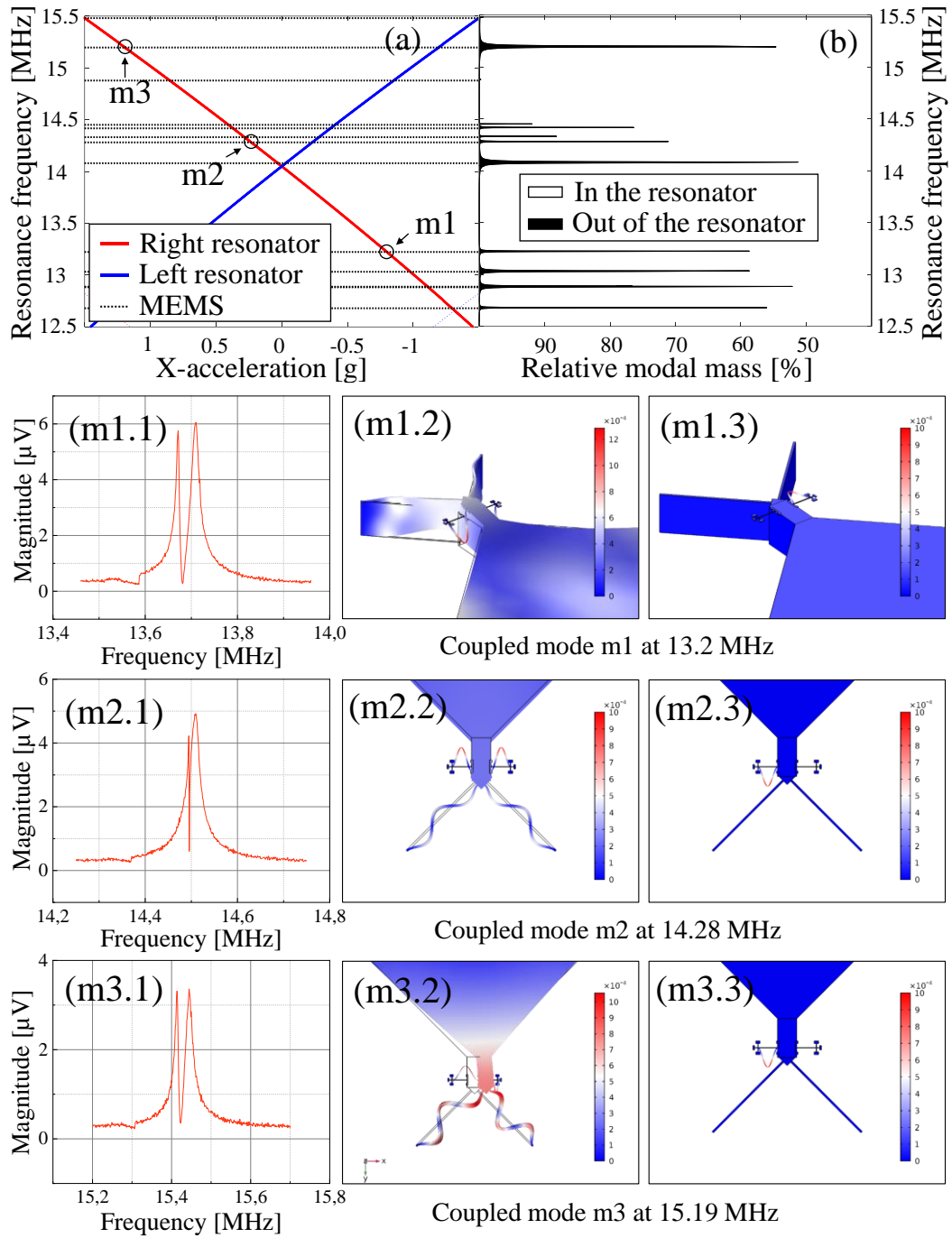


Figure 4-28 FEM identification method for the M1 accelerometer. (a) Frequencies as a function of the acceleration of the MEMS and nanoresonator modes. (b) Relative modal mass as a function of frequency of the in-plane nanoresonator modes. (m-x.1) Measurement of the nanoresonator magnitude close to mode coupling. (m-x.2) Shape of the corresponding MEMS mode when the nanoresonator mode is far from the coupling frequency and (m-x.3) when the nanoresonator mode is close to the coupling frequency.

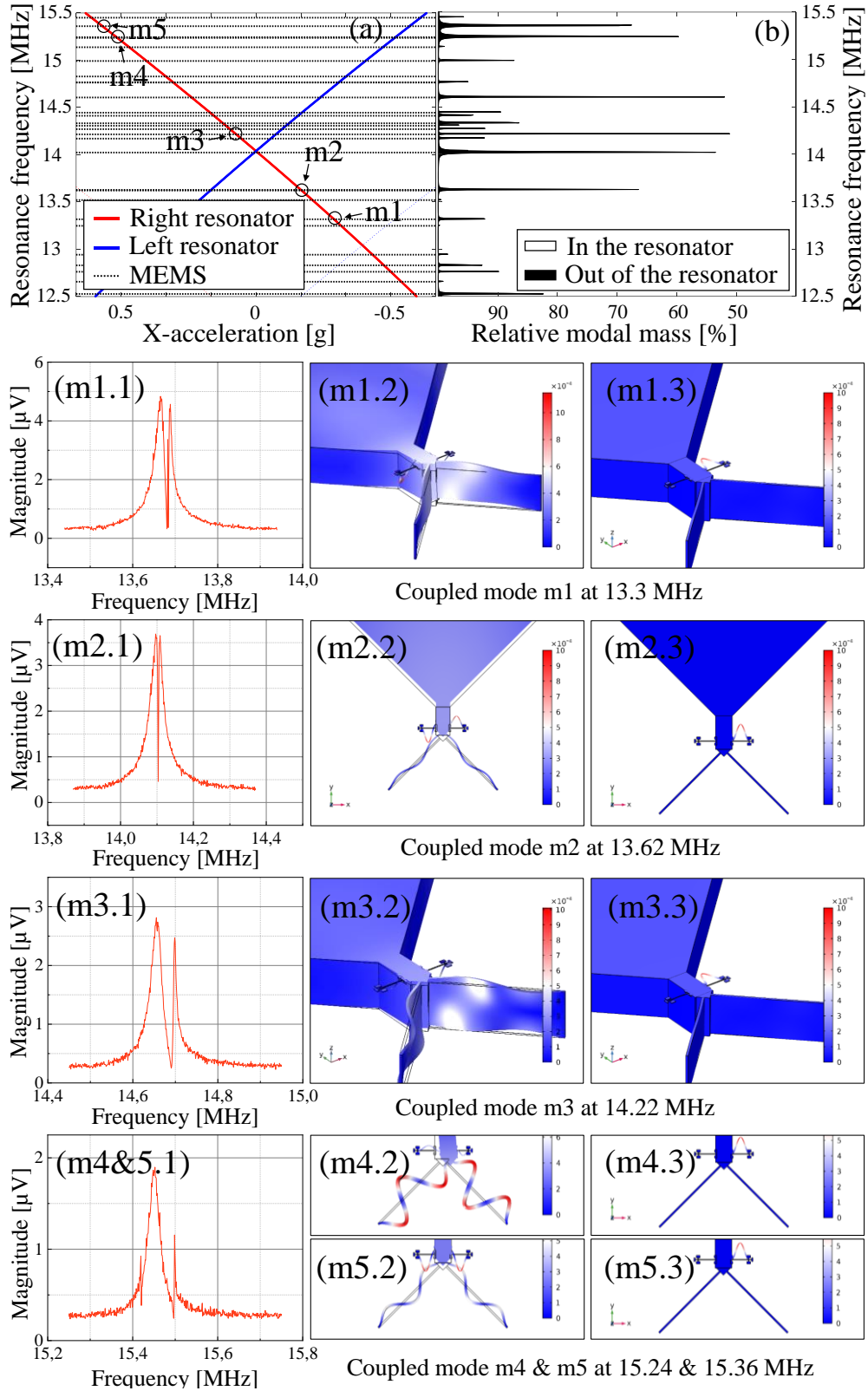


Figure 4-29 FEM identification method for the M2 accelerometer. (a) Frequencies as a function of the acceleration of the MEMS and nanoresonator modes. (b) Relative modal mass as a function of frequency of the in-plane nanoresonator mode. (m-x.1) Measurement of the nanoresonator magnitude close to mode coupling. (m-x.2) Shape of the corresponding MEMS mode when the nanoresonator mode is far from the coupling frequency and (m-x.3) when the nanoresonator mode is close to the coupling frequency.

4.3 Self-oscillating circuit

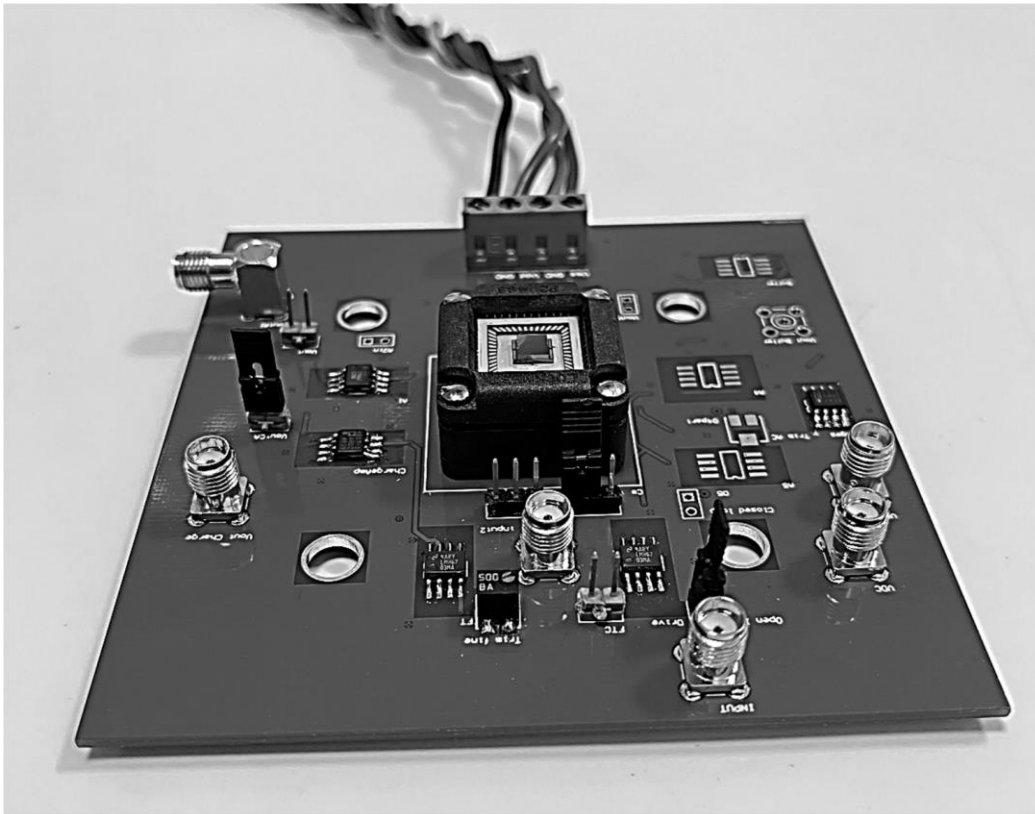


Figure 4-30 Photo of the self-oscillator circuit. The packaged accelerometer is integrated on the PCB by a specific socket. SMA connectors are used to apply an AC+DC actuation voltage and a gauge polarization voltage. A variable trigger resistance is used to tune the correction stage and an output SMA connector allows measuring the output voltage after the readout TIA.

The objective of this section is to present the first results of the readout electronics dedicated to the measurement of a resonant accelerometer based on nanoresonators. The operation of several stages of the system presented in Figure 3-24 has been demonstrated: the actuation stage that combines the DC and AC actuation signals, the polarization stage that provides a static differential bias on the gauges, and the compensation stage that allows a large part of the feedthrough signal to be removed. Because the feedthrough capacitance is larger than expected, the oscillation conditions at resonance are not met and we are not able to close the loop, so the saturation stage is not tested. Therefore, with the current sensors, we could not perform a demonstration of the complete system.

Before testing the readout circuit, feedthrough capacitance measurements are performed for several configurations on the test PCB, i.e. with direct activation/readout of the nanoresonator. The objective is to successively add the different elements to the system and thus quantify the sources of capacitance between the actuation and readout.

Figure 4-31 shows a schematic of the measurement setup: a transimpedance amplifier (TIA) is used to achieve a current reading similar to the operation of the readout circuit. The TIA's gain, fixed by G_1 and R_1 , ensures a flat bandwidth of 50 MHz [109]. The feedthrough capacitances are quantified on the test PCB between two connectors named V_{AC} and I_{out} . V_{AC} is connected to the output of the LIA for AC drive application while V_{out} is connected to the input of the TIA to perform current sensing. The output of the TIA is then connected to the 50-Ohms input of the LIA. The parasitic capacitance at the output of the LIA is neglected here because its impedance is low (50-Ohms). An AC frequency sweep is performed at the V_{AC} node from 10 kHz to 50 MHz, and measured at V_{out} with the homodyne detection scheme presented in Figure 4-2. Because the expected impedance between V_{AC} and V_{out} is capacitive, the logarithmic representation of the measurement can be used to calculate the capacitance value.

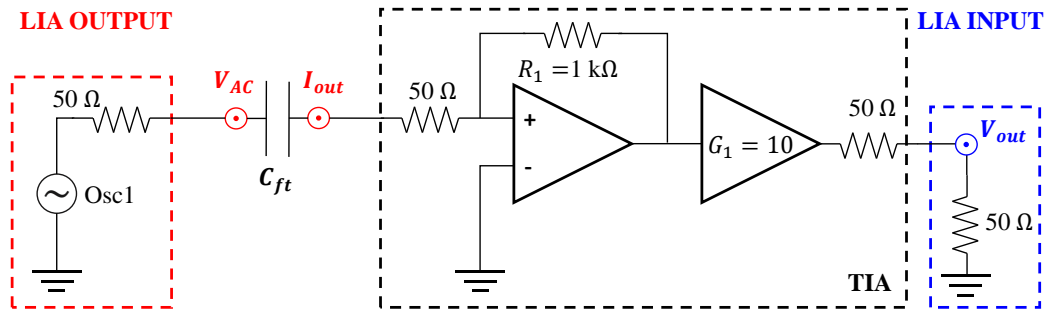


Figure 4-31 Measurement set-up of the feedthrough capacitance. The feedthrough capacitance is measured between V_{AC} and I_{out} , two specific connectors on the PCB used for the nanoresonator's actuation and sensing.

Finally, the accelerometer chip is integrated on the PCB thanks to a ceramic support LCC48 where it is wire-bonded. The support is connected to its dedicated socket soldered on the PCB. Thus, there are three possible elements contributing to the feedthrough capacitance: (1) the PCB and the LCC48 socket, mainly due to the soldering of the socket's pads (2) the ceramic, and (3) the wire bonding of the accelerometer chip and the intrinsic feedthrough capacitance of the chip. In order to quantify separately these three contributors, 3 different test structures are implemented. Figure 4-32 (a) represents the measured V_{out} as a function of the actuation frequency (from 10 kHz to 50 MHz) for the different structures. The filtering at 50 MHz represents the bandwidth limit of the LIA. The capacitance value can be extracted from the slope of the measurement.

The Figure 4-32 (p.x) shows the different test structures: (p.1) represents the initial one where only the PCB and socket are used. Here a small feedthrough capacitance of 16 fF is measured, probably due to the soldering of the socket. In an early version of the PCB, capacitances of 300 fF were measured due to the fact that the actuation and readout paths were too close. Therefore, the input and output of the nanoresonator should be as far apart as possible on the PCB. (p.2) represents the second structure where the PCB, the socket and the support are connected. Here a feedthrough capacitance of 28 fF is measured. (p.3) represents the third structure where the PCB, the socket and the support with a wire-bonded accelerometer chip are used. Here, the bias voltage of the nanoresonator is turned off so as not to transduce its mechanical response. A large feedthrough capacitance of 320 fF is measured. The main source of parasitic capacitance is induced by the accelerometer chip itself, probably due to the long contact paths and the floating potential present around the device. An electrostatic FEM simulation could be performed to validate this hypothesis and propose an optimized design. In addition, the capacitance originated by the carrier and socket can be avoided by directly connecting the accelerometer chip to the PCB.

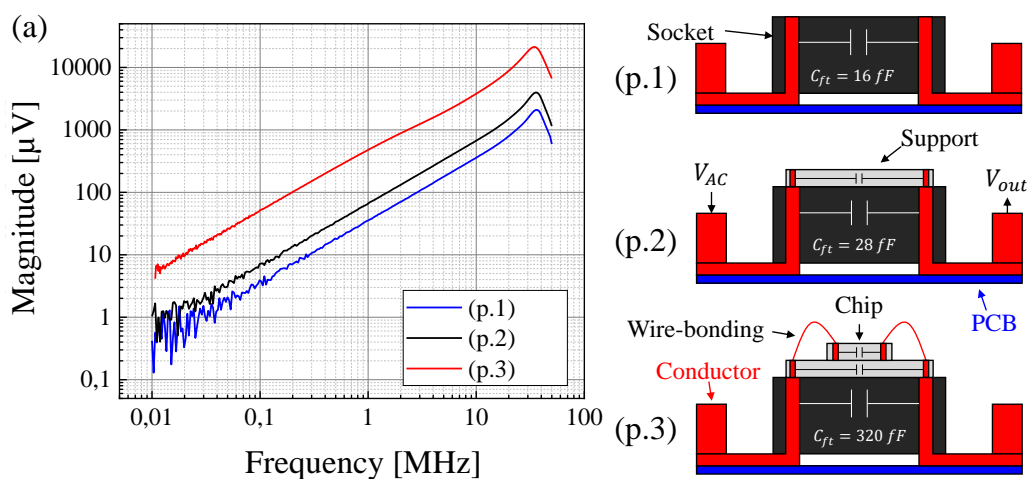


Figure 4-32 Measurement of the feedthrough capacitance originating from different elements of the packaging. The AC actuation is $V_{AC} = 0.1 \text{ V}$. The slope of $f^{0.5}$ in logarithmic scale is representative of a capacitance measurement. The resonance and filtering after 50 MHz are due to the TIA.

4.3.1 Adapted readout analysis

In order to validate the benefits of current readout over voltage readout (section 3.2.1), both detection systems are implemented. The current readout is first based on the TIA presented in the previous section to have a reference to the designed electronics.

For the current readout presented in the Figure 4-33, the measurement is similar to one performed in Figure 4-32 (p.3) but the bias voltage is turn on and the sweep is performed around the nanoresonator resonance. In other words, in the equivalent schematic of Figure 4-33 (a), the nanoresonator admittance Y_{NEMS} (Eq. 3-19) is added in parallel to the previous measured feedthrough capacitance $C_{ft} \approx 320 \text{ fF}$. The measurement is performed on the nanoresonator presented in section 4.1. However, the actuation is $V_{AC} = 25 \text{ mV} / V_{DC} = 0.35 \text{ V} / V_{bias} = 1.25 \text{ V}$ to be consistent with the electronic circuit measurement. In practice, having an lower AC/DC ratio allows reducing the background signal (proportional to V_{AC}) while keeping the nanoresonator actuation (proportional to $V_{AC}V_{DC}$). The blue curve of Figure 4-33 (b) shows the frequency response, in phase and magnitude, of the nanoresonator. According the TIA's gain ($R_1 \times G_1$), the previous quality factor ($Q_r \approx 8700$) and the impedance $Y_{NEMS,ft}$ of Eq. 3-25, the analytical model of V_{out} (red curve) allows adjusting the measurement by fitting the capacitance values to $C_{ft} = 339 \text{ fF}$. The mismatch with the previous value could be due to the fact that the bias voltage path is no longer floating. The phase shift at resonance $\Delta\phi$ is smaller than expected due to the large feedthrough capacitance. From the frequency response, the signal can be characterized by its SBR detailed in Table 24:

Signal	Background	SBR	$\Delta\phi$
13 μV	2.77 mV	0.0047	0.4°

Table 24 Experimental results of current readout.

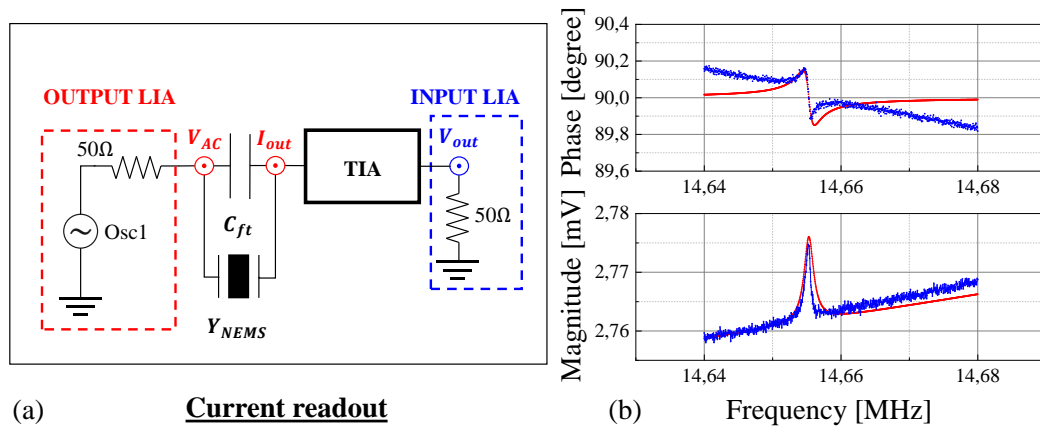


Figure 4-33 Measurement of the response of the nanoresonator using a current readout. (a) Schematic of the measurement using homodyne detection and a TIA. (b) Comparison of the experimental results (blue) with the analytical modelling (red).

For the voltage readout presented in the Figure 4-34, the measurement is similar to one performed in Figure 4-2. Here, the measurement is performed at high frequency (homodyne detection) and therefore the associated loss must be taken into account. The equivalent schematic of Figure 4-34 (a) uses the transfer function $H(\omega)$ shown in Eq. 2-43 which considers both the losses associated with the high-frequency voltage readout as well as the feedthrough capacitance. To be consistent with the current readout, the voltage readout is performed with the actuation $V_{AC} = 25 \text{ mV} / V_{DC} = 0.35 \text{ V} / V_{bias} = 1.25 \text{ V}$. The blue curve plotted in Figure 4-34 (b) represents the frequency response, in phase and magnitude, of the nanoresonator. The analytical modelling considers both the feedthrough capacitance measured previously ($C_{ft} = 339 \text{ fF}$) and the parasitic capacitance C_L . The analytical modelling of V_{out} (red curve) allows adjusting the measurement with $C_L = 112 \text{ pF}$. In this case, the loss associated to the voltage readout, represented by the gain G_L in Eq. 2-43, is $G_L(15 \text{ MHz}) \approx 0.07$, i.e. more than 90% of losses. The phase shift at resonance $\Delta\phi$ is smaller than expected due to the large feedthrough capacitance. From the frequency response, the signal can be characterized by its SBR detailed in Table 25.

Signal	Background	SBR	$\Delta\phi$
0.4 μV	81 μV	0.0049	0.4 $^\circ$

Table 25 Experimental results of voltage readout.

Although current readout is free from the high-frequency losses that appear in the voltage readout, both suffer from the effect of feedthrough capacitance. Indeed, the Signal-to-Background Ratio (SBR) imposes the phase shift at resonance as explained in Figure 2-21. In the case of the voltage readout, the filtering due to C_L is performed both in the signal and in the background, so the SBR is not changed. The results presented on Table 24 and Table 25 are consistent with this theory. In the end, the current readout is more efficient to operate at high frequencies but still requires electronics to compensate for the feedthrough capacitance.

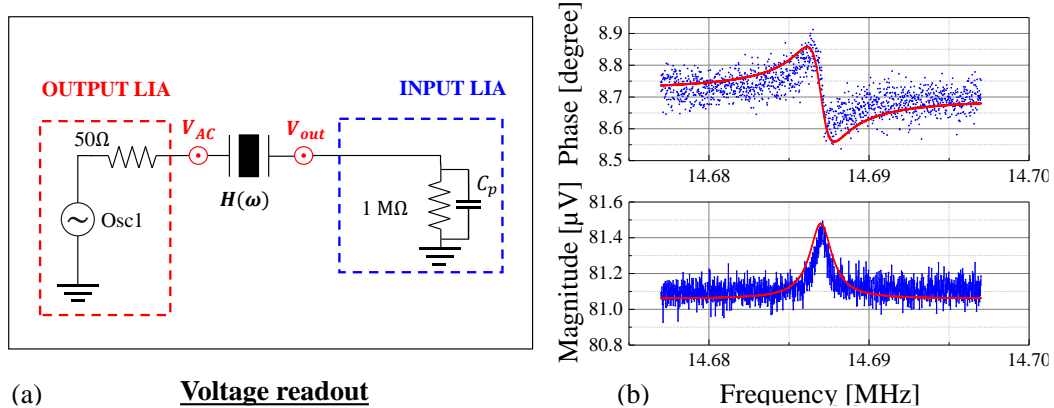


Figure 4-34 Measurement of the response of the nanoresonator using a voltage readout. (a) Schematic of the measurement using homodyne detection and TIA. (b) Comparison of the experimental results (blue) with the analytical modelling (red).

4.3.2 Feedthrough correction

In order to avoid the feedthrough phenomenon, the electronic circuit presented in section 3.2.4 is partially tested, only in open loop configuration. The measurement results are presented in Figure 4-35 (a): the output of the LIA is connected to V_{AC} , which supplies the actuation stage and correction stage. Static voltages corresponding to the DC actuation and the gauges polarisation are respectively connected to V_{DC} and V_{bias} . The bias stage provides differential polarization of the gauges. The actuation stage combines an AC voltage and a DC voltage to provide a 1ω actuation on the nanoresonator, which induces a motional current as well as a feedthrough current to the phase shifter. In parallel, the AC voltage supplies the correction stage, which theoretically injects an opposite feedthrough current to the phase shifter. A variable resistance allows setting the magnitude of the correction current in order to match the magnitude of the feedthrough current. A switch allows deactivating the correction stage to compare its operation. The 50-Ohms input of the LIA is connected to the output of the phase shifter to read the corrected output current of the nanoresonator.

In practice, the bias stage has no problem providing a differential polarization voltage in the required amplitude range. However, the actuation stage starts to be unstable for large DC supplies ($V_{DC} > 1V$). For this reason, the AC/DC ratio has been increased. The actuation stage must be redesigned to minimize the background signal by minimizing the AC/DC ratio. In order to validate the operation of the correction stage, the open loop measurements are performed with the actuation parameters : $V_{AC} = 20\text{ mV}$ / $V_{DC} = 0.16\text{ V}$ and $V_{bias} = 1.25\text{ V}$. Figure 4-35 (b) shows the frequency response of the nanoresonator for a corrected (red) and not corrected (blue) feedthrough current. Both measurements are compared in the Table 26. The correction stage allows improving the SBR by on order of magnitude, as well as the phase shift at resonance, but is not sufficient to allow self-oscillation in the electronics ($\Delta\phi \sim 4^\circ$).

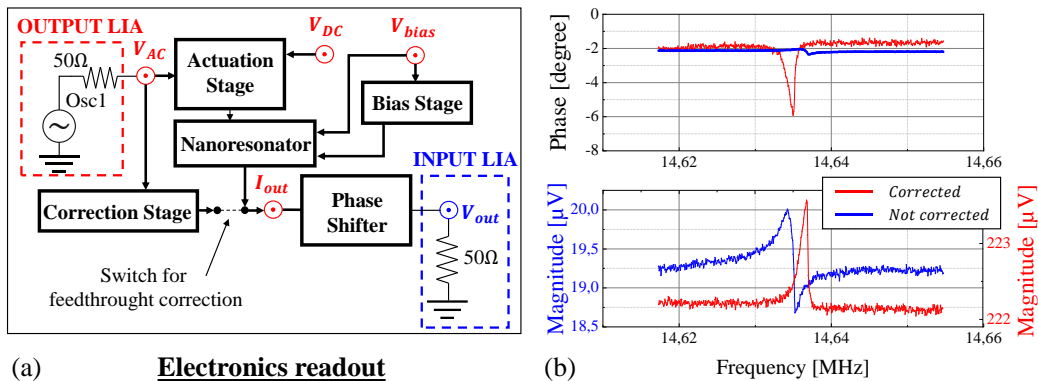


Figure 4-35 Open loop homodyne measurement implemented with the electronic circuit. (a) Schematics of the open-loop measurement. (b) Experimental frequency response of the nanoresonator with (red) and without (blue) the feedthrough correction stage.

	Signal	Background	SBR	$\Delta\phi$
Corrected	1.25 μV	19.25 μV	0.065	4°
Not corrected	1.41 μV	222.15 μV	0.0063	0.4°

Table 26 Comparison of the open loop homodyne measurement implemented with the electronics circuit with the correction stage (correction) and without the correction stage (not corrected).

A phase shift of several degrees between the feedthrough current and the nanoresonator current is observed by independently measuring the output of the correction stage and the nanoresonator (using the two TIA inputs shown in Figure 4-31). The delay is likely due to the limit of ideal operation of the AOPs used in these stages.

In conclusion, the readout electronic shows its capabilities to drive and detect the nanoresonator as well as to correct the feedthrough current. However, due to several issues, such as the instability of the actuation stage and the delay of the correction stage, a closed-loop operation cannot be implemented. Therefore, the architecture of the oscillator needs to be redesigned. However, efforts have been focused on minimizing the feedthrough capacitance, especially in the silicon design by proposing a push-pull actuation where differential actuation should cancelled the feedthrough current.

5 Towards next generations of resonant accelerometers

As explained in section 1.3.3, sub- μg resonant beam accelerometers suffer from single-layer trade-offs between noise density, bandwidth and footprint. The objective of this work is to overcome this trade-off by using two active layers. The experimental results presented in chapter 4 showed the proof of concept of the accelerometer, especially through the highest sensitivity of the state of the art (100,000 ppm/g) obtained with a small mass footprint (0.18 mm²). This made possible to address at the same time a large bandwidth and a low noise. The PSD of Figure 4-18 (b) highlights the high-Q accelerometer is dominated by a noise density of $1.75 \mu\text{g}/\sqrt{\text{Hz}}$ under 1kHz-bandwidth. Figure 5-1 compares these results to those of single layer accelerometers. Although the first generation of Nano-beam Resonant Pendulum-Accelerometer (NRPA-gen1) does not surpass the resolution-bandwidth trade-off set by [52], it does reach the resolution-footprint trade-off set by [55]. Therefore, it achieves the best FOM_{tot} (Table 27) defined in Eq. 1-2, opening the field to extend the sub- μg resonant beam accelerometer to larger applications. Leveraging the results and experience gained with the first-generation accelerometers, this chapter aims at discussing the perspectives of improvement of nano-beam resonant accelerometers.

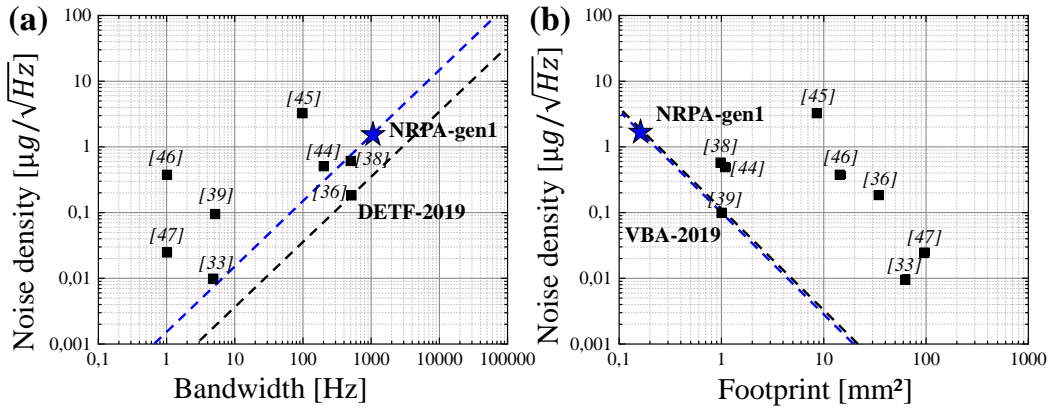


Figure 5-1 Representation of the trade-offs of sub- μg resonant beam accelerometers. (a) Resolution-bandwidth trade-off held by DETF-2019. (b) Footprint-resolution trade-off held by VBA-2019 and achieved by the first generation of nano-resonant beam accelerometer (NRPA-2018).

Ref & Type	Noise [$\mu\text{g}/\sqrt{\text{Hz}}$]	Bandwidth [Hz]	Footprint [mm ²]	FOM_{tot}
[110] Miani <i>et al.</i> NRPA-gen1	1.75	1000	0.18	3174
[55] Zaho <i>et al.</i> VBA-2019	0.098	5	>1	51
[52] Han <i>et al.</i> DETF-2019	0.18	500	35	79

Table 27 Comparison of the state of the art of sub- μg resonant beam accelerometers and the first generation of nano-beam resonant accelerometer.

5.1 Mode-decoupling solution

The main drawback of the first generation of accelerometers is mode coupling, as it significantly reduces the frequency operating range by unlocking the closed-loop resonance frequency, as shown in Figure 4-25. The acceleration range is then reduced in the frequency range between two coupling modes. In this subsection, a mechanical decoupling structure is presented to avoid the coupling effect.

Figure 5-2 summarizes the principle of the mode coupling. The coupling is represented by two damped spring-mass systems coupled by a stiffness k_c in the Figure 5-2 (a). The first system represents a MEMS mode of the accelerometer. The second system represents the first in-plane mode of the nanoresonator. Figure 5-2 (b) illustrates the coupling of the nano-beam resonant accelerometer: the transduction path (solid line) shows the transformation of the applied acceleration γ to axial stress σ on the nanoresonator bending stiffness $k_2(\sigma)$. The dotted line represents the path that maintains the bending motion of the nanoresonator x_2 thanks to an actuation force F_2 . The nanoresonator is driven at its resonance frequency $\propto k_2(\sigma)$. The coupling path (dashed line), through the stiffness k_c , induces the movement of the MEMS mode x_1 according to the motion of the nanoresonator x_2 . This has an impact on the nanoresonator as illustrated in graph (c) which plots the frequency response of the nanoresonator (x_2/F_2) as a function of the applied acceleration. Here, the nanoresonator resonance is close to the coupling frequency and the stiffness k_c is sensitive to this coupling ($k_c \neq 0$). Under these conditions, the nanoresonator frequency response is not Lorentzian anymore, so the methods employed to track the resonance frequency are not valid for this range of frequencies.

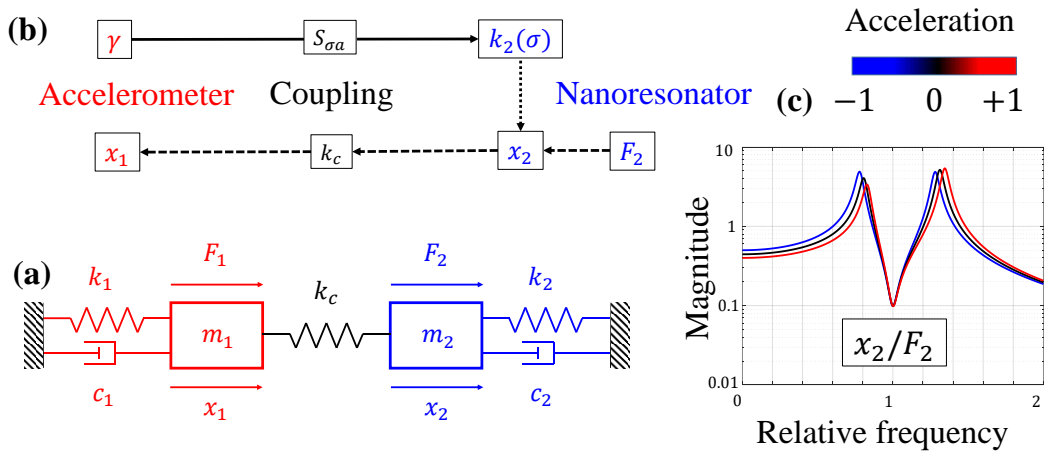


Figure 5-2 Principle of the mode coupling between the resonance modes of the nanoresonator and the MEMS accelerometer. The damped spring mass model (a) describes the mechanical problem of coupling. The schematic (b) represents the different elements involved in the coupling phenomenon. The graph (c) illustrates the frequency response of the coupling model as a function of acceleration.

5.1.1 Presentation and modelling of the decoupling mechanism

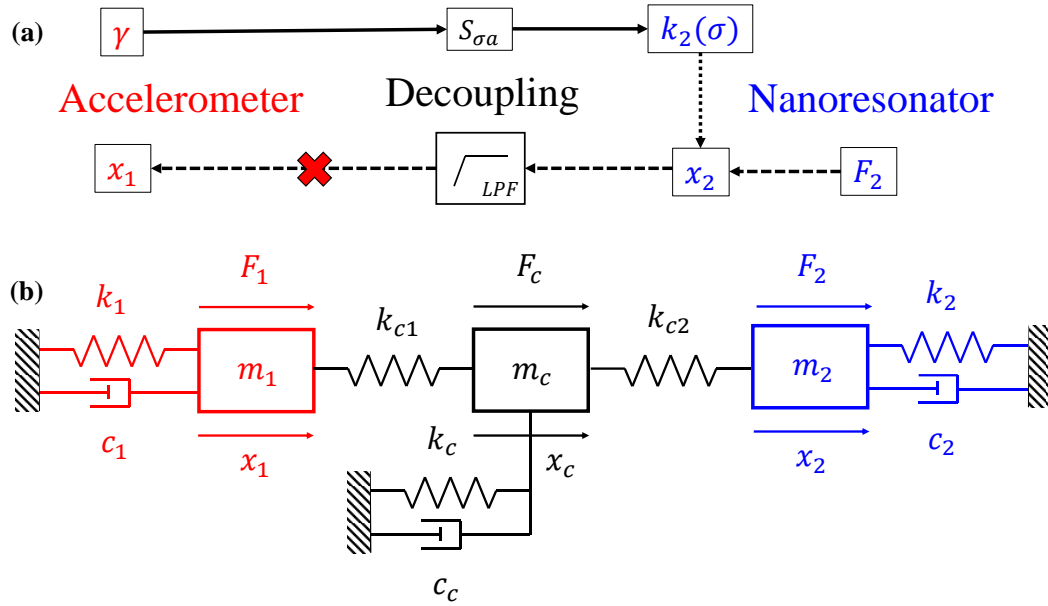


Figure 5-3 Principle of the decoupling solution between the resonance modes of the nanoresonator and the MEMS accelerometer. The schematic (a) represents the different elements that act during the decoupling phenomenon. (b) A damped spring mass system (with coefficient k_c , c_c and m_c) models the mechanical solution of decoupling.

The main issue of the coupling between the nanoresonator and the MEMS structural modes is that there is a large amount of MEMS modes within the working frequency range of the nanoresonator, and it is difficult to identify which MEMS modes are receptive to the actuation of the nanoresonator ($k_c \neq 0$). The proposed solution is to control the stiffness coupling by implementing a mechanical decoupling structure. Figure 5-3 (a) shows that this mechanical structure acts as a low-pass filter that prevents the nanoresonator actuation F_2 from driving the structural mode x_1 through the motion of the nanoresonator x_2 . Figure 5-3 (b) represents this mechanical structure added to the damped spring mass system used to describe the coupling phenomenon. Here, the damped spring mass system 1 (in red) represents the MEMS mode coupled to the nanoresonator. The damped spring mass system 2 (in blue) represents the in plane mode of the nanoresonator. The system “c” (in black) represents the decoupling mechanical structure. The decoupling mechanical structure consists in a damped spring mass system of mass m_c , spring k_c and damping coefficient c_c , in addition to two springs that are added to connect the mechanical decoupling structure to systems 1 and 2, respectively k_{c1} and k_{c2} . The objective is to be able to adjust the cut-off frequency f_c of the low-pass filter in order to make the filtering operate in the targeted bandwidth. Here the designer controls the cut-off frequency through the design of the mass m_c and the flexible elements k_c , k_{c1} and k_{c2} . The tuning of the parameters of the mechanical decoupling structure requires special attention. The general strategy is to design a decoupling mechanism that allows a coupling between the MEMS and the

nanoresonator at the range of frequencies of the acceleration, but decouples them at higher frequencies. Figure 5-4 represents the transfer function (x_2/F_2) of the coupled nanoresonator as a function of the acceleration, extracted from the solution of the coupled equations of the global system of Figure 5-3 (b) (described in Appendix C). In this system with three inputs (F_1, F_c, F_2) and three outputs (x_1, x_c, x_2), only the output of interest (x_2) as a function of the input of interest (F_2) is plotted. Figure 5-4 (a) shows the frequency response of the nanoresonator coupled to a structural mode of the accelerometer, when the cut-off frequency f_c is a decade higher than the operating frequency of the nanoresonator $f_2(\gamma)$. Here, the frequency of the MEMS mode f_1 is equal to the frequency of the nanoresonator mode $f_2(\gamma = 0)$ as in Figure 5-3 (c). Thus, the shift of the nanoresonator's resonance frequency due to acceleration cannot be measured properly. In contrast, Figure 5-4 (b) shows the frequency response of the nanoresonator, with the MEMS mode of the accelerometer such that $f_1 = f_2(\gamma = 0)$, but for a cut-off frequency f_c a decade lower than the operating frequency of the nanoresonator $f_2(\gamma)$. In this configuration, the MEMS mode is not actuated anymore, and the frequency response of the nanoresonator recovers its Lorentzian shape. Thus, the shift of the nanoresonator's resonance frequency due to acceleration can be properly measured.

In conclusion, the first requirement for the mechanical decoupling structure to work is to set its cut-off frequency at list a decade lower than the frequency range of the nanoresonator to be sure that all of the MEMS structural modes are filtered out. However, this is not a sufficient condition. In order not to add new sources of coupling, it is important to consider the internal dynamics of the mechanical decoupling structure. Each flexible elements (k_c, k_{c1}, k_{c2}) must be tuned to avoid that their modes also cross the operating frequency range of the nanoresonator. An example is implemented in the next subsection.

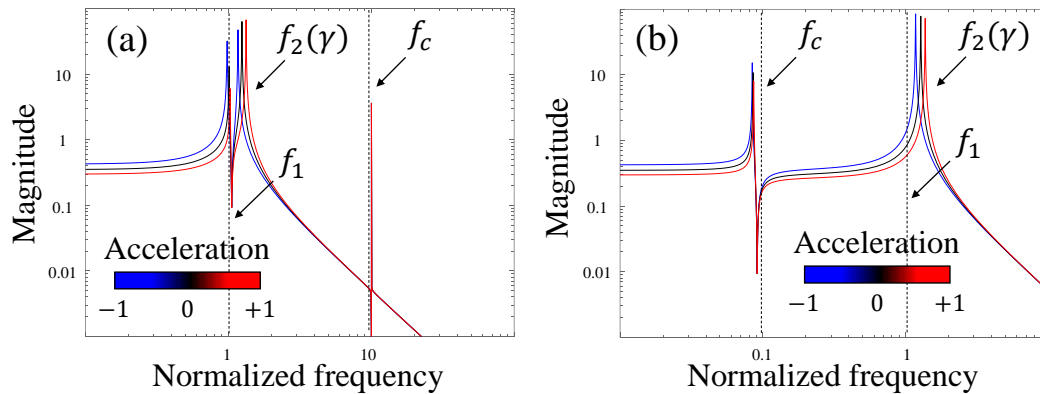


Figure 5-4 Working principle of the mechanical decoupling structure. The resonance frequency of the MEMS mode is represented by the f_1 line. The resonance frequency of the nanoresonator's in-plane mode by $f_2(\gamma)$, where γ is the applied acceleration. The cut-off frequency of the mechanical decoupling structure is represented by the f_c vertical line. (a) Nano-resonator response (x_2/F_2) when $f_c \gg f_2(\gamma)$: mode coupling is not avoided. (b) Nanoresonator response (x_2/F_2) when $f_c \ll f_2(\gamma)$: mode coupling is avoided.

5.1.2 Implementation

The implementation of the mechanical decoupling structure is performed for the pendulum accelerometer structure presented in Figure 5-5 (a). Its equivalent damped spring-mass system is presented in Figure 5-5 (b). Here, the mechanical decoupling structure consists of a small test mass (m_2) supported by bending beams (k_{f2}) and connected to the lever arm by a compression beam (k_{c1}). In the spring-damped mass system that represents the nanoresonator (Figure 5-2 (a)), k_2 represents the bending stiffness of the resonant beam. In the spring-damped mass system that represents the accelerometer, the nanoresonator is represented by a compressive stiffness k_{r2} ($\neq k_2$) that is clamped to the mechanical decoupling structure. I.e. the spring that connects the mechanical decoupling structure to the nanoresonator is considered as infinite ($k_{c2} \rightarrow \infty$).

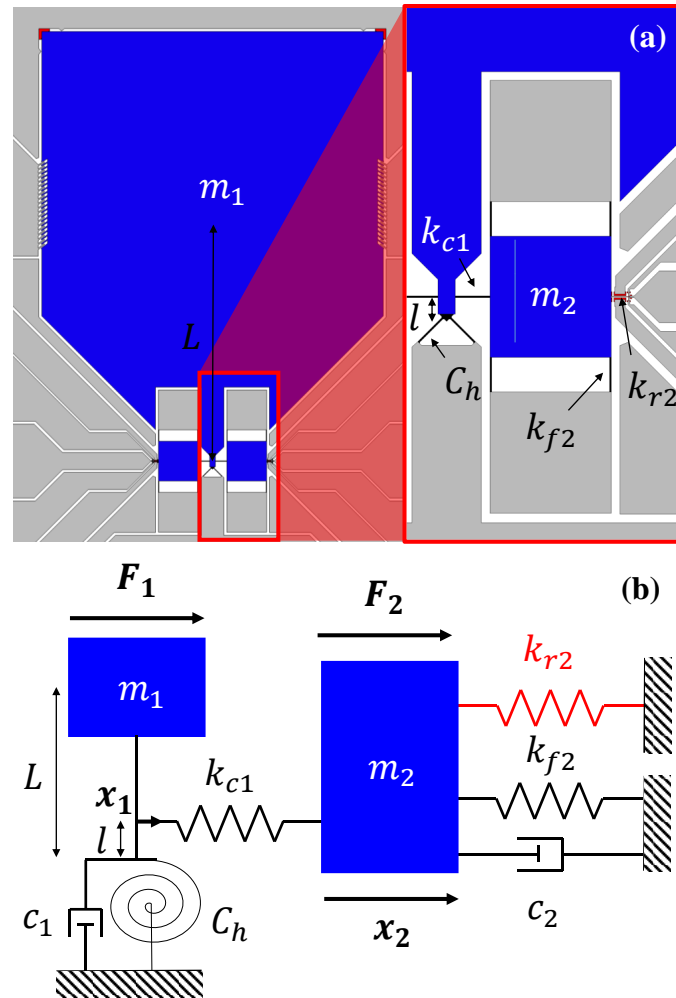


Figure 5-5 Implementation of mechanical decoupling structure for the pendulum accelerometers. The transduction of the accelerometer is similar to the first generation of devices: the proof mass m_1 is coupled to a lever arm L/l and the hinges are represented by their rotating stiffness C_h . The motion of the proof mass is represented by x_1 and the acceleration force by F_1 . The axial force on the nanoresonator is represented by F_2 and its displacement by x_2 .

The design of a mechanical coupling structure must take into consideration two effects induced by this structure on the accelerometer. The first one is the need to have a correct operation of the structure, i.e. to set the cut-off frequency and the internal dynamics of the structure. The second one, discussed in section 5.2.2, is the impact of the mechanical coupling structure on the global stiffness of the accelerometer $K_{eq} = F_1/x_2$. In other words, the mechanical coupling structure reduces the sensitivity of the accelerometer and increases its bandwidth, by increasing K_{eq} . It is therefore important to find a trade-off between the operation of the mechanical decoupling structure and not increasing the global stiffness of the accelerometer too much.

For the pendulum accelerometer architecture, the global stiffness of the accelerometer is

$$K_{eq} = \frac{F_1}{x_2} = \frac{C_h + l^2 \frac{k_{c1}(k_{r2} + k_{f2})}{k_{c1} + k_{r2} + k_{f2}}}{L^2} \begin{bmatrix} N \\ m \end{bmatrix} \quad 5-1$$

The details of the calculation are explained in Appendix D. In practice, k_{c1} is the compressive stiffness of the coupling micrometric beams, k_{f2} is the bending stiffness of micrometric beams of the decoupling structure and k_{r2} is the compressive stiffness of the nanoresonator. In order to minimize the impact of the mechanical decoupling stage, i.e. to reach the equivalent stiffness of the first generation of pendulum accelerometers (Eq. 6-18), the most optimal way is to maximize the stiffness in series with the nanoresonator $k_{c1} \gg k_{r2}$ and to minimize the stiffness in parallel with the nanoresonator $k_{r2} \gg k_{f2}$. In other words:

$$\begin{cases} k_{r2} \gg k_{f2} \leftrightarrow l_{f2} \gg \sqrt[3]{l_{r2} \frac{S_{f2}}{S_{r2}} w_{f2}^2} \quad [m] \\ k_{c1} \gg k_{r2} \leftrightarrow l_{c1} \ll \frac{S_{c1}}{S_{r2}} l_{r2} \quad [m] \end{cases} \quad 5-2$$

where S_{f2} , S_{c1} and S_{r2} are respectively the cross section of the beams associated to the stiffness k_{f2} , k_{c1} and k_{r2} respectively. In this way $K_{eq}^* = (C_h + l^2 k_{r2})/L^2$.

The cut-off frequency of the mechanical decoupling structure can be evaluated from the equivalent stiffness of the structure, i.e. k_{r2} , k_{f2} and k_{c1} in parallel, and the mass of the structure m_2 :

$$\omega_2 = \sqrt{\frac{k_{f2} + k_{r2} + k_{c1}}{m_2}} \underset{k_{c1} \gg k_{r2} \gg k_{f2}}{\approx} \sqrt{\frac{k_{c1}}{m_2}} \propto \frac{1}{\sqrt{L_{m2}^2 l_{c1}}} \text{ [rad]} \quad 5-3$$

Where L_{m2} is the length of the square mass m_2 . Here, the cut-off frequency of the mechanical decoupling structure can be set by the flexible element k_{c1} in addition to the proof mass m_2 . In a first approach, the internal dynamics of the mechanical decoupling structure consist in bending modes of the flexible elements associated to k_{f2} and k_{c1} :

$$\begin{cases} \omega_{c1} = \sqrt{\frac{k_{f,c1}}{m_{c1}}} \propto \frac{1}{l_{c1}^2} \text{ [rad]} \\ \omega_{f2} = \sqrt{\frac{k_{f,f2}}{m_{f2}}} \propto \frac{1}{l_{f2}^2} \text{ [rad]} \end{cases} \quad 5-4$$

where $k_{f,c1}$ and m_{c1} are respectively the bending stiffness and the effective mass of the beams associated to k_{c1} while $k_{f,f2}$ and m_{f2} are respectively the bending stiffness and the effective mass of the beams associated to k_{f2} . In practice, for the second generation of nano-beam accelerometers, the operating frequency range of the nano-resonator is chosen from 10 MHz to 20 MHz. Thus, the cut-off frequency must be close to $\omega_2/2\pi \approx 1$ MHz. As the operating frequency range must be free of the internal resonance modes of the mechanical decoupling structure, it is appropriate to anticipate the harmonics of the flexible elements k_{c1} and k_{f2} by imposing the conditions $\omega_{c1}/2\pi$ $\omega_{f2}/2\pi > 20$ MHz. To minimize the stiffness in parallel with the nanoresonator and maximize the stiffness in series with the nanoresonator, it is effective to fix the beam widths at their minimum $w_{f2} = w_{c1} = 1 \mu m$. The thickness of the micrometric layer is fixed by the fabrication process to $t_{f2} = t_{c1} = 20 \mu m$. Depending on the chosen nanoresonator, which sets l_{r2} and S_{r2} , the requirements of the mechanical decoupling structure (Eq. 5-4), can be achieved by tuning the lengths l_{f2} and l_{c1} . In addition, the cut-off frequency can be defined separately by setting the proof mass length L_{m2} (Eq. 5-3). A design proposal that meets the requirements of the mechanical decoupling structure, especially adapted to a nanoresonator with $l_{r2} = 10.5 \mu m$ and $w_{r2} = t_{r2} = 250 mn$, is $L_{m2} = 70 \mu m$, $l_{f2} = 20 \mu m$ and $l_{c1} = 20 \mu m$. Table 28 compares the analytical modelling of the dynamics of the mechanical decoupling structure for this specific design with FEM simulations.

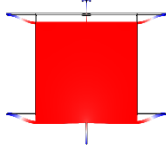
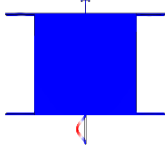
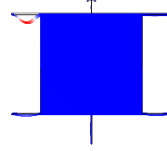
	ω_2	ω_{c1}	ω_{f2}
Analytical modelling	4.36MHz	22MHz	22MHz
FEM Simulations	4.11MHz	21.5MHz	21.12MHz
Mode Shape			

Table 28 Internal dynamics (resonance modes) of the mechanical decoupling structure designed for the pendulum accelerometer.

The mechanical decoupling structure has a drawback. Indeed, to achieve $\omega_{f2}/2\pi > 20$ MHz, the minimum length of $20\text{ }\mu\text{m}$ results in $k_{f2} = 422\text{ N/m}$ that is not much lower than $k_{r2} \approx 1\text{ kN/m}$. In other words, part of the acceleration energy is consumed as strain energy in k_{f2} . To match $k_{c1} \gg k_{r2}$ and $\omega_2/2\pi \approx 1\text{ MHz}$ it is easier to set $\omega_{c2}/2\pi > 20\text{ MHz}$. With $l_{c2} = 20\text{ }\mu\text{m}$, $k_{c1} = 169\text{ kN/m}$ which is much higher than k_{r2} . In practice, no deformation energy is consumed in k_{c2} . In the whole accelerometer, the k_{c1} and k_{r2} springs are represented by two beams in compression and the k_{f2} springs are represented by 2×4 flexural beams. In this way:

$$\begin{cases} k_{c1} = 2 \frac{E w_{c1} t_{c1}}{l_{c1}} = \mathbf{338\text{ kN/m}} \\ k_{r2} = 2 \frac{E w_{r2} t_{r2}}{l_{r2}} = \mathbf{1965\text{ N/m}} \\ k_{f2} = 2 \frac{4 E w_{f2}^3 t_{f2}}{l_{f2}^3} = \mathbf{3380\text{ N/m}} \end{cases} \quad 5-5$$

Then, from Eq. 5-1, we obtain that the equivalent stiffness of the accelerometer K_{eq} is 2.3 time superior to the ideal equivalent stiffness $K_{eq}^* = (C_h + l^2 k_{c2})/L^2$. In other words, the mechanical decoupling structure costs half the sensitivity. However, this cost is necessary and overcomes the limited acceleration range of the nanoresonator due to mode coupling.

K_{eq} - decoupling	K_{eq}^* - no decoupling
2.15 N/m	0.93 N/m

Table 29 Comparison of the equivalent stiffness for a pendulum accelerometer with a mechanical decoupling structure and the ideal case corresponding to the same accelerometer without mechanical decoupling structure.

5.1.3 FEM simulations method

In order to validate the operation of the mechanical decoupling structure, the method based on FEM simulations [presented in section 4.2.4.2] is implemented to identify the coupling modes in the designs of the second generation of pendulum accelerometers. The results of the FEM simulation method are presented in Figure 5-6.

Figure 5-6 (a) shows a plot of the frequencies as a function of acceleration of all the resonance modes of the accelerometer between 9 MHz and 21 MHz. The MEMS modes are shown as black dotted lines and they are not dependent on the acceleration. The density of modes in this frequency range is significant. Nanoresonator modes are represented by blue and red lines. Because the nanoresonator modes are acceleration-dependent, they intersect with all the MEMS modes in the frequency range at some value of acceleration. The risk of mode coupling is then important.

However, the relative modal mass of the left nanoresonator (blue line), presented in Figure 5-6 (b), shows that there is no coupling mode from 9 MHz to 20 MHz, as intended by the design of the mechanical decoupling structure. This is an encouraging sign of the effectiveness of the mechanical decoupling structure. The relative mass modal highlights a coupling of two modes at 20.3 MHz and 9.3 MHz.

Figure 5-6 (m1.1) shows the modal deformation, calculated by FEM simulations, of the 20.3 MHz when the in-plane mode of the nanoresonator is far from the coupling frequency. From the mode shape, it can be deduced that it is a combination of the torsion modes of the mechanical decoupling structure around the two in-plane axis (X and Y). Figure 5-6 (m1.2) shows the modal deformation of the 20.3 MHz when the in-plane mode of the nanoresonator is close to the coupling frequency. In this configuration, the MEMS mode shape has the shape of the in-plane mode shape of the nanoresonator, which is representative of the mode coupling. Figure 5-6 (m2.1) and (m1.2) represent the modal deformation of the 9.3 MHz mode when the nanoresonator's in plane mode is respectively far from and close to the coupling frequency. Here the MEMS mode is the torsion mode of the mechanical decoupling structure around the out-of-plane axis (Z).

In conclusion, the mechanical decoupling structure is able to reject the mode coupling between the MEMS modes and the nanoresonator's in-plane mode. However, the internal dynamics of the mechanical decoupling structure needs further modal analysis in order to predict the main mode of the structure. The next step is to experimentally verify the operation of the mechanical decoupling structure, which will be the subject of future research.

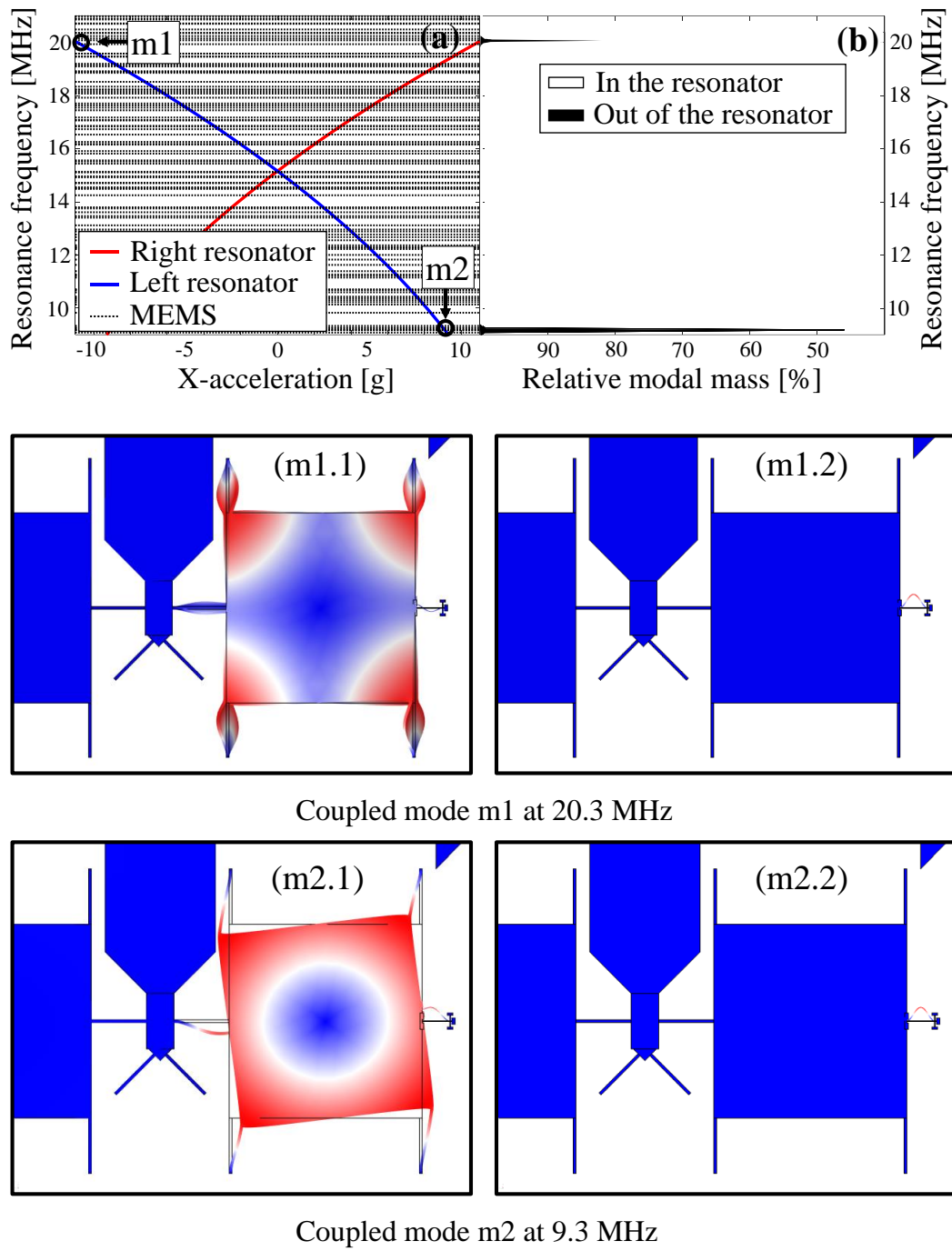


Figure 5-6 Study of the mode-decoupling structure using the FEM method for second generation of pendulum accelerometers. (a) Frequencies as a function of the acceleration of the MEMS and nanoresonator modes. (b) Relative modal mass as a function of frequency of the in-plane nanoresonator mode. (m-x.1) Shape of the corresponding MEMS mode when the nanoresonator mode is far from the coupling frequency and (m-x.2) when the nanoresonator mode is close to the coupling frequency.

5.2 Design of the second generation of resonant accelerometers

In this subsection, new designs of nano-beam resonant accelerometers are presented. Each design implements the mechanical decoupling structure to avoid mode coupling in the frequency operation of the nanoresonators. The designs aim at overcoming the issues encountered in the characterization of the first generation of accelerometers and addressing other applications beyond high-bandwidth accelerometers. These designs were implemented in a second layout and they will be fabricated with two variants of nanolayer thickness (250 nm and 500 nm) to compare wider nanoresonator advances, which is one of the goals of the batch.

As a reminder, the first generation of accelerometers is based on a pendulum architecture. These accelerometers take advantage of the lever effect achieved by hinges, which allows addressing a mass with small footprint. The use of a small mass allows addressing 1 kHz-bandwidth applications and the lever effect ensures a high measurement stability close to 1 μg . To improve this measurement stability, it is more difficult to design a large-mass sensor with a pendulum architecture. This is because the lever arm is proportional to the mass footprint that also acts out of plane: a large test mass causes a large out-of-plane deformation, which may cause the out-of-plane stoppers to be reached and prevent in-plane operation. In addition, the pendulum architecture has shown sensitivity to shear deformation induced by the package stress (Section 4.2.4.1). This makes it a poor candidate for harsh environments, requiring a costly integration of temperature-compensation electronics to avoid thermal drifts. The objective for the second generation of designs is to improve the robustness of the sensors to thermal drifts and their cross-axis sensitivity. In this way, two new accelerometer architectures are proposed to reach both lower measurement stability ($<1 \mu\text{g}$) and higher bandwidth ($>1 \text{ kHz}$).

As a reminder, the first design of the nanoresonators is based on the thinnest cross-section allowed by the manufacturing process (250 nm \times 250 nm) in order to achieve the highest sensitivity of the accelerometer. However, the reduction of the nanoresonators width reduces its dynamic range and thus that of the accelerometer. The piezoresistive transduction of these nanoresonators is not optimized and their electrostatic actuation induces a problematic feedthrough current. Moreover, for nanoresonators with a high quality factor ($Q_r > 4000$), the critical amplitude before nonlinearity imposed a rather low output voltage of the nanoresonator ($V_{max} < 10 \mu\text{V}$). The objective of the second design of the nanoresonators is to improve the piezoresistive transduction in order to reach their detection limit and to implement a push-pull actuation to avoid the feedthrough current. In addition, the dynamic range of the nanoresonators is improved by increasing their cross-section and pinned anchors are proposed to increase the critical amplitude of vibration before non-linearity.

5.2.1 Second generation of nanoresonators

In order to be consistent with the first generation of nanoresonators, the new designs target the same operating frequency (20 MHz) and are equipped with a push-pull actuation architecture.

The first nanoresonator, called RCGC-250 for Resonator Clamped-Gauged-Clamped 250nm, is presented in Figure 5-7 (a). This version is based on the same geometry as the first generation: the resonant beam width and length are respectively $w_r = 250\text{nm}$ and $L_r = 10\mu\text{m}$, that ensures a 20MHz-operation frequency. But here, the piezoresistive transduction is improved through the transduction gain η_s by reducing the length of the beam-end to $L_t = 500\text{nm}$. As detailed in section 3.1.2, the optimum design of 250 nm-wide nanoresonators is to use a nanogauge length and width of respectively $L_g = 875\text{nm}$ and $w_g = 250\text{nm}$. However, Figure 5-7 (a) shows the critical dimension of the nanogauges length ($L_{g,min}$). Here, the beam-end optimisation ($L_t = 500\text{nm}$), is sufficient to reach the detection limit of the nanoresonator fixed by thermomechanical noise, as detailed in Table 30. Reducing the beam-end length has several benefits: the transduction gain is doubled and the Johnson noise is reduced, improving the minimum measurable strain $\sigma_{min,r}$. Moreover, the effective length of the nanoresonator ($\propto L_r + L_t$) is reduced, thereby increasing its buckling stress (σ_{buck}). In conclusion, the dynamic range ($\propto \sigma_{buck}/\sigma_{min,r}$) is improved but the critical amplitude before nonlinearity is not improved. This nanoresonator represents an intermediate optimisation step, sharing some features with both generations of accelerometers in order to study the optimizations separately.

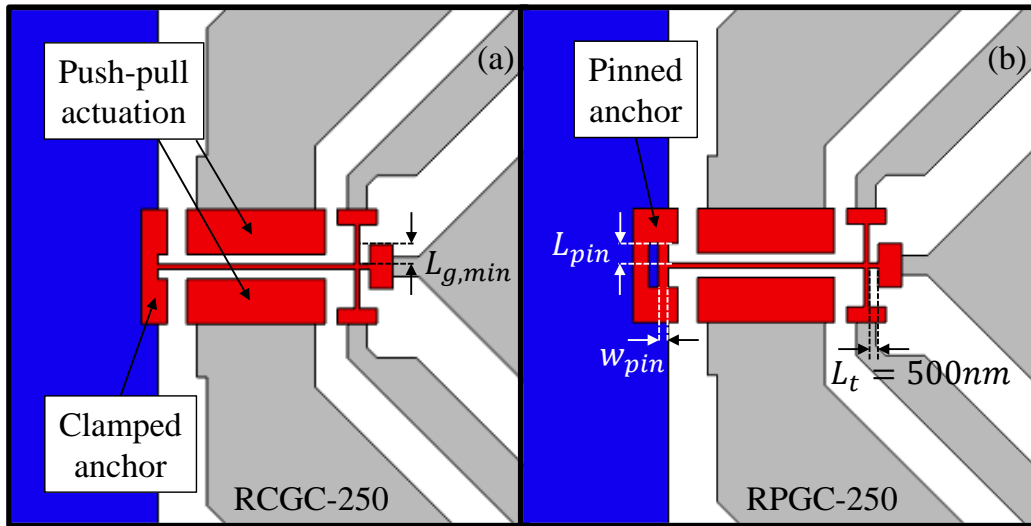


Figure 5-7 Second generation of nanoresonators with a beam width of 250 nm. The nanoresonators are composed of piezoresistive nanogauges $(w_g, L_g, L_t) = (250\text{ nm}, 2\text{ }\mu\text{m}, 500\text{ nm})$, the resonant beam $(w_r, L_r) = (250\text{ nm}, 10\text{ }\mu\text{m})$ and push pull actuation. (a) Design of a clamped nanoresonator. (b) Design of a pinned nanoresonator with a pin anchors size of $(L_{pin}, w_{pin}) = (1\text{ }\mu\text{m}, 500\text{ nm})$.

The first variant focuses on the pin anchor: the RPGC-250, for Resonator Pinned-Gauged-Clamped 250nm, has the same geometry as the RCGC-250 but the anchor of the resonant beam (that is fixed to the proof mass) is pinned. Pin anchors have been shown to improve the detection limit of nanoresonators, for instance in mass spectrometry applications [111], [112], by increasing the critical amplitude arising from nonlinearity. The principle is to add a degree of freedom (rotation) at the anchors to push back the geometrical effects of spring hardening presented in section 2.3.1. The pin anchors consist in not fixing the end of the resonant beam directly on the proof mass, but in fixing the end of the resonant beam to two smaller orthogonal beams, with length and width respectively L_{pin} and w_{pin} , themselves fixed to the proof mass. These anchors are illustrated in Figure 5-7 (b). For nanoresonators used as force sensors, the effects of pin anchors are more complicated. This is because the frequency sensitivity to axial stress ($S_{\omega\sigma}$) depends on how the input force is distributed as axial stress in the resonant beam. In the case of pin anchors, part of the input force is distributed in the bending deformation of the pin anchors and part in the axial deformation of the resonant beam. Moreover, as detailed in the modal analysis in section 2.2.2, the buckling stress depends on the coefficient β_0 that comes from the boundary conditions. For pin anchors, the buckling stress is higher than with clamped anchors. As a first approach, the buckling stress and $S_{\omega\sigma}$ are calculated from FEM simulations. Based on CEA-LETI team's experience, the critical amplitude of resonant beams using pin anchors is roughly twice the critical amplitude (v_{max}) of resonant beams using clamped anchors.

The second variant consists in increasing the nanoresonator width. The RCGC-500, for Resonator Clamped-Gauged-Clamped 500 nm, is the first design of 500 nm-width nanoresonator ($w_r = 500 \text{ nm}$). For this specific design, the thickness of the nanolayer must be increased to 500 nm, otherwise the out-of-plane buckling stress would limit the dynamic range of the nanoresonator. In order to be consistent with the 20 MHz-operation frequency, the length of the nanoresonator is adapted to $L_r = 15 \text{ }\mu\text{m}$. Here too, the piezoresistive transduction is improved through by setting the beam-end to $L_t=500 \text{ nm}$, the nanogauges dimensions to $w_g = 250 \text{ nm}$ and $L_g = 2 \text{ }\mu\text{m}$. The possibility to reduce the nanogauge width to 250 nm with respect to a resonant beam width of 500 nm allows improving the transduction gain η_v by a factor 2. By increasing the nanoresonator width, the critical amplitude before nonlinearity is improved, as well as the minimum measurable stress $\sigma_{min,r}$. In addition the buckling limit is higher, thus the dynamic range is larger. An equivalent pinned version (RPGC-500), for Resonator Pinned-Gauged-Clamped 500 nm, is also implemented in order to compare the trade-off of using this type of anchor. Figure 5-8 (a) represents the RCGC-500 and Figure 5-8 (b) represents the RPGC-500.

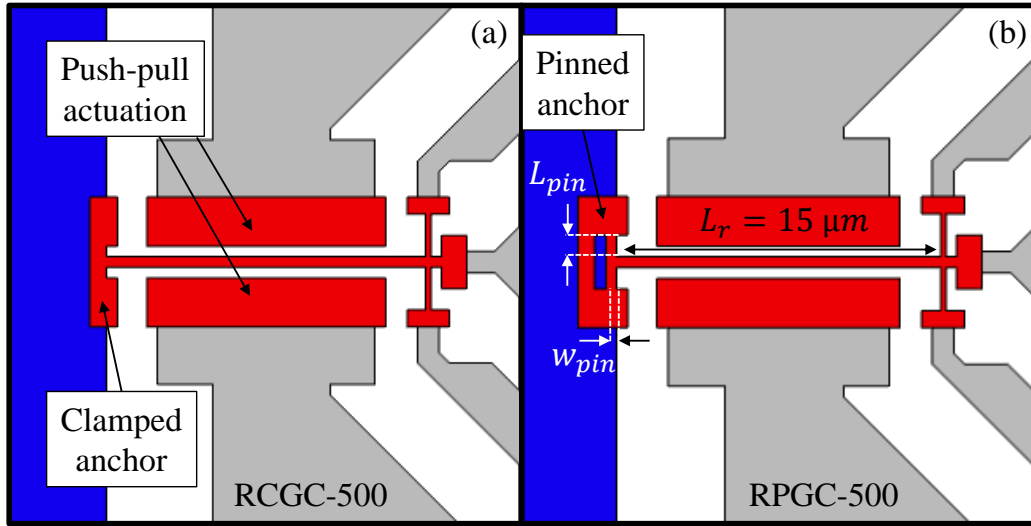


Figure 5-8 Second generation of nanoresonators with a beam width of 500 nm. The nanoresonators are composed of piezoresistive nanogauges $(w_g, L_g, L_t) = (250 \text{ nm}, 2 \mu\text{m}, 500 \text{ nm})$, the resonant beam $(w_r, L_r) = (500 \text{ nm}, 15 \mu\text{m})$ and push pull actuation. (a) Design of a clamped nanoresonator. (b) Design of a pinned nanoresonator with the pin anchors size of $(L_{pin}, w_{pin}) = (1 \mu\text{m}, 500 \text{ nm})$.

Table 30 compares the expected performances of the second generation of nanoresonators. Each nanoresonator reaches their detection limit ($\sigma_{min,J} < \sigma_{min,br}$) thanks to their optimized piezoresistive transduction. Increasing the nanoresonator width improves both the buckling stress and the detection limit imposed by the thermomechanical noise of the nanoresonator ($\sigma_{min,br}$). The pinned anchors increase both the critical amplitude before non-linearity and the buckling stress.

	R-v1**	RCGC-250	RPGC-250	RCGC-500	RPGC-500
$S_{\omega\sigma}/2\pi \text{ [Hz/Pa]}$	0.041	0.044	0.04*	0.02	0.02*
$\sigma_{min,J} \text{ [Pa}/\sqrt{\text{Hz}}]$	18.39	7.08	3.5	2	1
$\sigma_{min,br} \text{ [Pa}/\sqrt{\text{Hz}}]$	8.3	8.3	4.15	3.35	1.675
$\sigma_{min} \text{ [Pa}/\sqrt{\text{Hz}}]$	20	10.9	5.45	3.92	1.96
$\sigma_{max} \text{ [MPa]}$	207	207	252*	488	596*
$DR \text{ [dB]}$	140	145	153	161	169

Table 30. Comparison of the second generation of nanoresonators. The performances are calculated from analytical modelling with fixed parameters: $Q_r = 2000$, $\sigma_{ps} = -150 \text{ MPa}$. For the pinned version, the critical amplitude before nonlinearity is considered as twice the clamped one. The maximum allowable stress consists of the pre-stress in addition to the buckling stress $\sigma_{max} = \sigma_{buck} - \sigma_{ps}$. *For the pin anchors, the buckling stress and $S_{\omega\sigma}$ are calculated from FEM simulations. ** Analytical model of first nanoresonator (named R-v1) from Table 8

In conclusion, the four new nanoresonator designs can be compared with each other and with the previous nanoresonator design. The objective is to quantify the gain of the piezoresistive optimization, the nanoresonator enlargement and the pin anchor. In the next subsection, three new accelerometer architectures are presented. Each of them will be adapted to the use of each new design of nanoresonators

5.2.2 Second generation of accelerometers

In addition to improving the operation of the high-sensitivity accelerometer, the second generation of accelerometers is focused on addressing different applications. The second fabrication batch includes three different accelerometer architectures. Each design incorporates the mechanical decoupling structure of section 5.1.

Among the architectures, there are the second-generation pendulum accelerometers, called Nano-Resonant beam Pendulum Accelerometer (NRPA-gen2). These accelerometers take advantage of a lever effect that allows them to address small footprints, 1 kHz bandwidths and low noise level, but suffer from increased thermal sensitivity. This type of architecture is a good candidate for inertial sensor requiring high-integration and high-performance

The second design, called Nano-Resonant beam Translation Accelerometer (NRTA-gen2) consist in using the movement of a mass in translation, without amplification effect, to compress the nanoresonator. In fact, this architecture offers a low sensitivity, thus a high bandwidth and high full-scale at the expense of degraded noise level. However, it is a promising architecture for accelerometers requiring bandwidths larger than 10 kHz such as vibration measurement, where it can offer a good noise level compared to similar devices in the state of the art.

The third design, called Nano-Resonant beam Lever arm Accelerometer (NRLA-gen2) consist in using the movement of a mass in translation, with amplification effect, to compress the nanoresonator. Unlike the pendulum accelerometer, this architecture is suitable for large proof masses and allows addressing high-sensitivity accelerometers. The use of a nanoresonator allows maintaining a proof mass footprint lower than 1 mm², which allows keeping a wide bandwidth (>500 Hz). These accelerometers are candidates for very high-resolution applications such as seismometers.

5.2.2.1 Pendulum accelerometer (NRPA-gen2)

Figure 5-9 shows the architecture of the second generation of the pendulum accelerometer (NRPA-gen2). The accelerometer consists of a rotating proof mass, mechanical decoupling structures and nanoresonators. The proof mass is suspended by hinges and connected to the mechanical decoupling structure by a compressive beam. The mechanical decoupling structure is guided in translation by bending beams. Here, the mechanical decoupling structure has the advantage of transmitting only an axial compression to the nanoresonator where the first generation also induced a rotation. In this way, the mechanical decoupling structure is also useful to reject transverse sensitivities. In addition, the mechanical decoupling structure can be used to set a maximum allowable axial stress in the nanoresonator when the rotating mass reaches the stoppers, in other words, taking advantage of the decrease of sensitivity caused by the mechanical decoupling structure to protect the nanoresonator. Four version of NRPA-gen2, with the same proof mass, are adapted to the four types of nanoresonators. Table 31 compares the expected performances of these accelerometers. Such accelerometers take advantage of 500 nm-nanoresonators dynamic range to increase their full scale.

	RCGC-250	RPGC-250	RCGC-500	RPGC-500
Scale Factor [MPa/g]	12	9.2	5.6	4.6
Full scale* [g]	± 13	± 10	± 50	± 50
Noise [$\mu g/\sqrt{Hz}$]	0.9	0.59	0.7	0.42
Bandwidth [kHz]	2	2	2.4	2.4

Table 31. Comparison of NRPA-gen2 relying on various nanoresonator designs. * Full scale is limited by half the buckling stress (greater than scale factor nonlinearity)

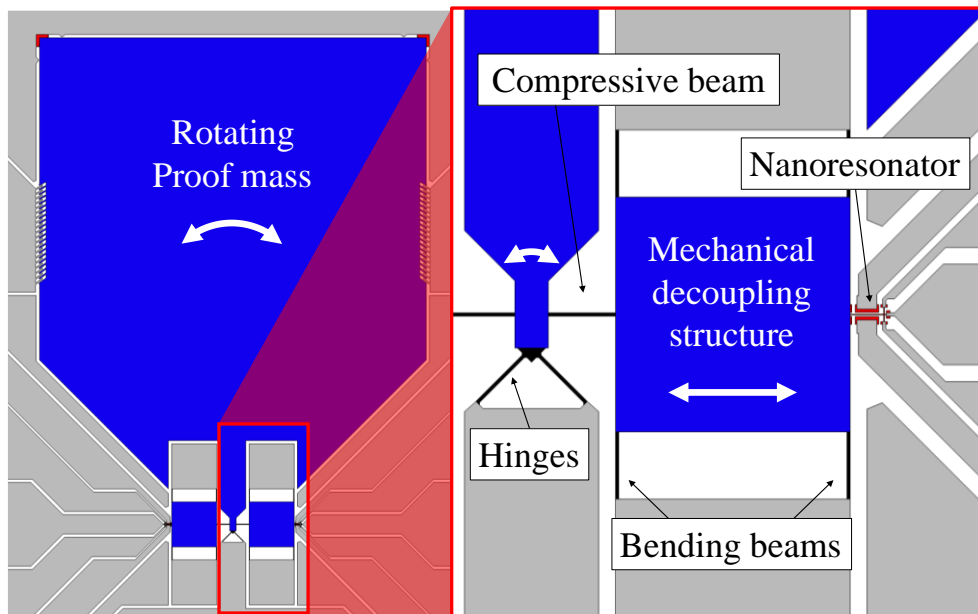


Figure 5-9 Second generation of pendulum accelerometer. The proof mass under acceleration rotates by means of hinges. The rotation is transmitted as a translation to the decoupling stage which transmits it in compression to the nanoresonators.

5.2.2.2 Translation accelerometer (NRTA-gen2)

Figure 5-10 shows the architecture of the translation accelerometer (NRTA-gen2). This accelerometer consists of a translational proof mass, mechanical decoupling structures and nanoresonators. The proof mass is held by a guiding structure and connected to the mechanical decoupling structure by a compression structure. Here, the compression and the guiding structures are made of flexural folded beams. These beams are particularly good at rejecting the effect of unwanted disturbances on the nanoresonator, such as shear deformation, thermal expansion, or transverse sensitivity. Because this architecture does not benefit from the lever arm effect, it can address a large full-scale acceleration. The small proof mass ($<1 \text{ mm}^2$) guarantees a large bandwidth ($>10 \text{ kHz}$). It is a candidate for vibration applications that require immunity to repetitive shocks, insensitivity to temperature environments and a flat frequency response from DC to 10 kHz . Table 32 compares the expected performance of these accelerometers adapted to the second generation of nanoresonators.

	RCGC-250	RPGC-250	RCGC-500	RPGC-500
Scale Factor [MPa/g]	0.35	0.3	0.17	0.15
Full scale [g]	± 380	± 400	± 2500	± 2500
Noise [$\mu g/\sqrt{\text{Hz}}$]	31	18	23	13
Bandwidth [kHz]	10	10	25	25

Table 32 Comparison of NRTA-gen2 relying on various nanoresonator designs.

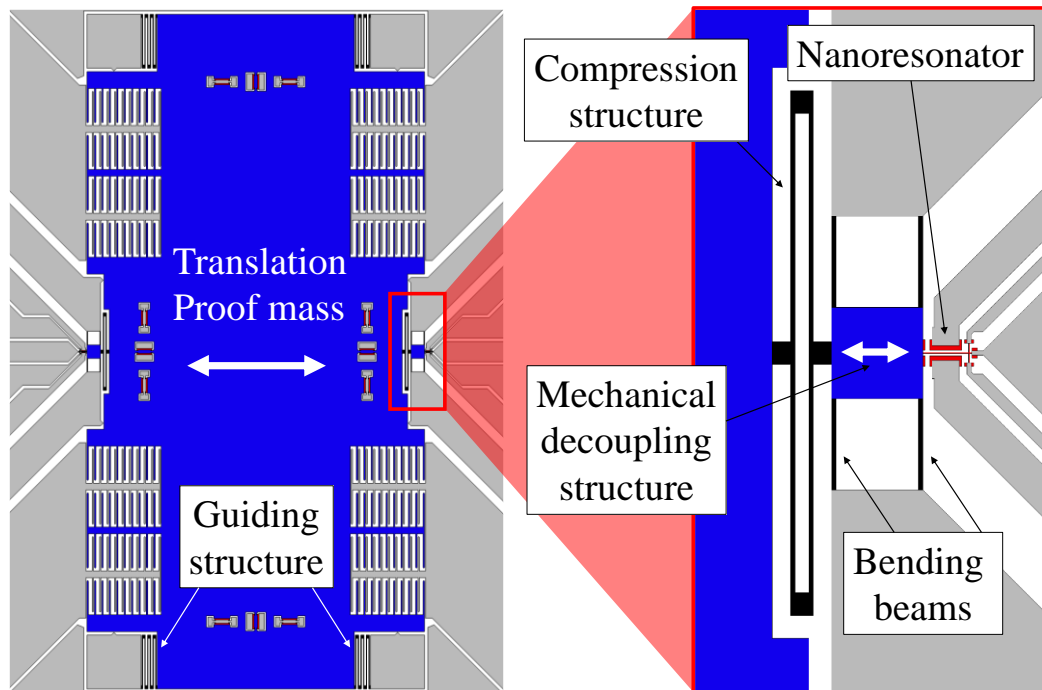


Figure 5-10 First generation of translation accelerometers. The proof mass under acceleration is guided by means of translation beams. The translation is transmitted to the decoupling stage which transmits it in compression to the nanoresonators.

5.2.2.3 Lever arm accelerometer (NRLA-gen2)

Figure 5-11 shows the architecture of the first generation of the lever arm accelerometer (NRLA-gen2). The accelerometer consists of a proof mass in translation, lever arm mechanisms, mechanical decoupling structures, and nanoresonators. The proof mass is guided by translational structure and connected to the lever arm mechanism by a connecting structure. The lever arm mechanism consists of an arm rotated around hinges and connected to the mechanical decoupling structure by a compressive structure. Guiding structure, composed of bending folded beams, are ideal to reject shear deformations, additionally the connecting structure helps reduce transverse sensitivity. Because this architecture benefits from the lever arm effect, it allows addressing high-resolution applications. In addition, the small mass footprint ($<1 \text{ mm}^2$) due to the use of nanoresonators, allows to address a bandwidth higher than 500 Hz. These characteristics make NRLA-gen2 a good candidate for high-resolution applications in harsh environments, such as seismometers. Table 33 compares the expected performance of these accelerometers adapted to the second generation of nanoresonators.

	RCGC-250	RPGC-250	RCGC-500	RPGC-500
Scale factor [MPa/g]	50	42	29	24
Full scale * [g]	± 2	± 2	± 5	± 5
Noise [$\mu g/\sqrt{\text{Hz}}$]	0.21	0.11	0.14	0.08
Bandwidth [kHz]	750 Hz	750 Hz	950 Hz	950 Hz

Table 33 Comparison of NRLA-gen2 relying on various nanoresonator designs. * Full scale is limited by half the buckling stress (greater than scale factor nonlinearity). The version RCGC-250 and RPGC-250 take advantage of 125 lever arm ratio whereas the version RCGC-500 and RPGC-500 take advantage of 85 lever arm ratio. The FEM simulation highlights the compressive beams consumes a part of the inertial energy as strain energy. This loss is taken into account in the analytical modelling presented on this Table.

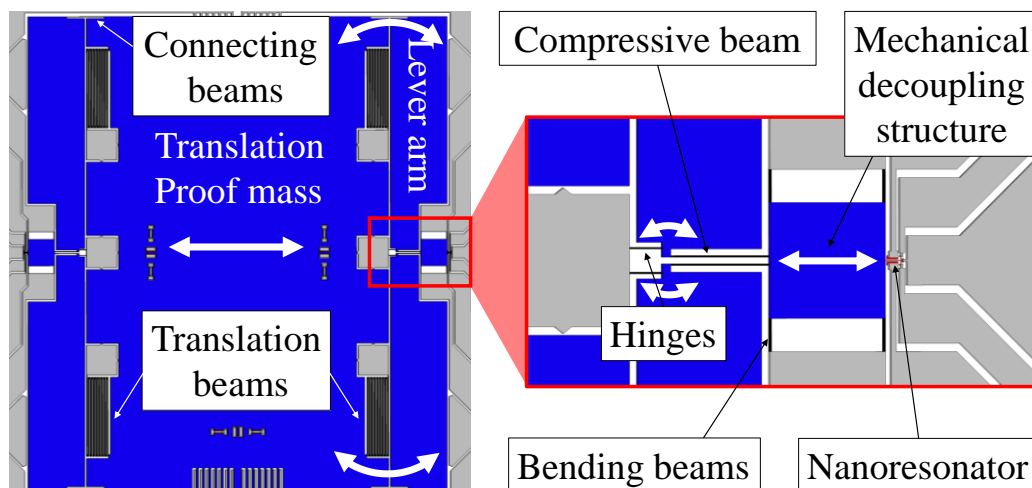


Figure 5-11 First generation of lever arm accelerometer. The proof mass under acceleration is translated by means of translation beams. The resulting force is amplified by lever arm effect. The amplified force is transmitted to the decoupling stage which transmits it in compressive stress in the nanoresonators.

In conclusion, the main characteristics of the second generation of accelerometers are compared to the first generation of accelerometer (NRA-2018) in Table 34. To be consistent with NRA-2018, only the versions with the RCGC-250 nanoresonator are mentioned. In addition to the different targeted applications (determined by the bandwidth and noise targets), the dynamic range of the second generation is higher because the improved nanoresonator allows reaching the detection limit of the nanoresonator ($\sigma_{min,br}$) and because the decoupling stage allows using a larger frequency range (coupling mode are rejecting from 10 MHz to 20 MHz), thus acceleration range.

	NRPA-gen1	NRPA-gen2	NRTA-gen2	NRLA-gen2
Sensitivity [MPa/g]	20	12	0.35	50
Bandwidth [Hz]	1.000	2.000	10.000	750
Noise [$\mu\text{g}/\sqrt{\text{Hz}}$]	1.75	3	13	0.5
Full scale [g]	0.5	13	380	2
Dynamic range [dB]	109	133	131	132

Table 34 Comparison of the main performance of the nano-beam resonant accelerometer. The NRPA-gen1 shows experimental results that considers coupling phenomenon in the full scale whereas the second generation of accelerometer considers analytical modelling. Here, the dynamic range of the accelerometer is less than the dynamic range of the RCGC-250, because the proof mass stoppers are set before reaching the buckling stress.

In order to begin a more in-depth analysis of the accelerometers, several simulations, detailed in Appendix D, were performed to benchmark the designs. The first simulation evaluates the sensitivities of the transverse axis in-plane (cross-axis Y) and the transverse axis out-of-plane (cross-axis Z) by comparing them to the sensitivity of the accelerometer. The results are expressed as a ratio between both sensitivities in Table 35. The second generation of accelerometer is less sensitive to cross-axis due to the mechanical decoupling stage that is designed to transmit only the axial strain to the nanoresonator in addition to the use of folder beams for guiding proof mass.

	NRPA-gen1	NRPA-gen2	NRTA-gen2	NRLA-gen2
Cross-axis Y [% Sensitivity]	3.14	0.00006	0.0015	0.0014
Cross-axis Z [% Sensitivity]	3.14	0.00023	0.00075	0.00044

Table 35 Comparison of the cross-axis sensitivity ratio of the nano-beam resonant accelerometers, simulated by FEM.

Since the nanoresonator has a low buckling limit due to its nanoscale size, in addition to the pre-stressing phenomenon that reduces the allowable axial stress, the protection of the nanoresonator is important. The second simulation consists in evaluating the robustness of the nanoresonator against the motion of the proof mass. Here, the simulation, detailed in Appendix D, consists in moving the proof mass towards its 3-axis stoppers in order to evaluate the axial stress induced on the nanoresonators. In the first generation of accelerometers, the stoppers in the X direction are set to have a maximum allowable stress close to the buckling limit (~ 250 MPa). Due to the high pre-stress, the second generation of sensors takes a larger margin and sets the maximum allowable stress at ~ 150 MPa. The simulations of the NRTA-gen2 show that a 20,000 g shock is needed to reach the Z stoppers, and those on the NRPA-gen2 show that a shock of 5,000,000 g is needed to reach the Y stoppers. Both values are due to the high stiffness of the mechanical structure in these directions. Table 36 compares the maximum stress induced in the nanoresonator by the maximum allowed proof mass motion.

	NRPA-gen1	NRPA-gen2	NRTA-gen2	NRLA-gen2
X-stopper [MPa]	265	162	151	112
Y-stopper [MPa]	14	294	0.26	0.0005
Z-stopper [MPa]	0.16	7.9	184	1.5

Table 36 FEM simulations of the stress on the nanoresonator at the maximum displacement of the proof mass, limited by the position of the stoppers.

The pendulum accelerometer (NRPA type) showed significant sensitivity to temperature during the experimental characterizations. The most likely hypothesis is that the thermal package stress induces a tilt of the proof mass, which induces differential stress on the nanoresonators (such as in section 4.2.4.1). Here, we perform FEM simulations, detailed in Appendix D, applying a shear deformation and an increase in temperature to compare the impact on the different accelerometer architectures. Because the accelerometers are based on a differential measurement architecture, the differential stress on the nanoresonators is compared. Even with a mechanical decoupling structure, the NRPA-gen2 shows sensitivity to shear deformation. However, having a translational proof mass in both the NRTA-gen2 and NRLA-gen2 induces a better compensation of the thermal effect through the differential measurement. In other words, the shear deformation induces a common-mode stress when the proof mass is in translation. Table 37 compares the compensation of thermal effects by differential measurements in the different geometries.

	NRPA-gen1	NRPA-gen2	NRTA-gen2	NRLA-gen2
$\Delta T = 100^\circ\text{C}$ [% FS]	53.2	38	0.1	0.01
$\epsilon_{xy} = 100\text{ppm}$ [% FS]	0.5	0.35	0.78	0.61

Table 37 Comparison of the differential strain on the nanoresonators caused by thermal effect. This strain is modelled using FEM simulations when submitting the accelerometer to temperature variations or a shear deformation of the substrate. The differential measurements are expressed as a fraction of the full-scale acceleration.

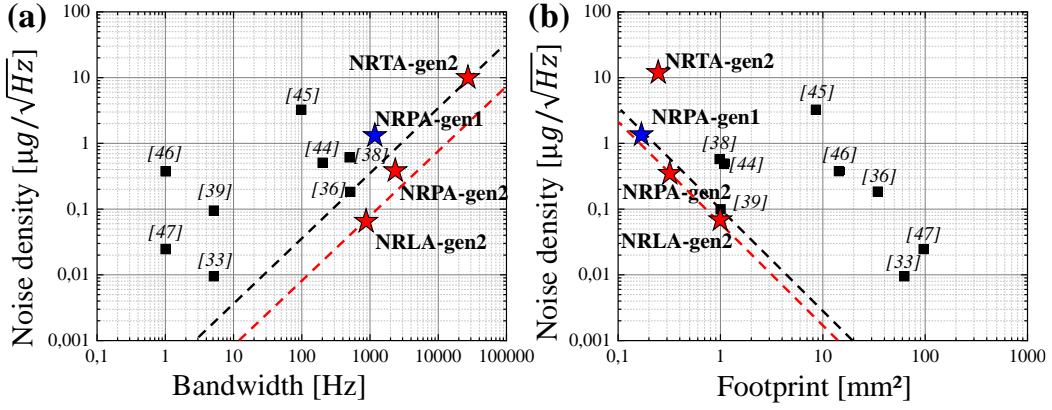


Figure 5-12 Representation of the trade-offs of sub- μg resonant beam accelerometer. (a) the resolution bandwidth trade-off. (b) the footprint resolution trade-off. Combination of both trade-off are held by VBA-2017. The analytical modelling of the second generation of nano-resonant beam accelerometer are compared to the state of the art.

In conclusion, the expected performances of the next generation of nano-resonant beam accelerometers are illustrated in Figure 5-12 and compared in Table 38 to the resonant beam accelerometer that achieves the best FOM_{tot} [54]. The pendulum accelerometer (NRPA-gen2) provides the best FOM_{tot} , making this type of architecture an ideal solution for sub- μg accelerometers with high bandwidth and small footprint. The VBA-2017 is also based on a pendulum architecture and presents an interesting thermal robustness for this type of architecture that could be the next evolution of the NRPA type.

Ref & Type	Noise [$\mu g/\sqrt{Hz}$]	Bandwidth [Hz]	Footprint [mm^2]	FOM_{tot}
[110] <i>Miani at al.</i> NRPA-gen1	1.75	1000	0.18	3174
NRPA-gen2	0.42	2400	0.3	19047
NRTA-gen2	13	25000	0.25	7692
NRLA-gen2	0.08	950	1	11875
[54] <i>Kenny at al.</i> VBA-2017	0.6	500	1	833

Table 38 Comparison of the analytical performance of the next generation of nano-resonant beam accelerometers with the state of the art of sub- μg resonant beam accelerometers.

As a new approach, we could imagine a different implementation of a multilayer process to achieve a resonant beam accelerometer. As demonstrated for NRPA-gen1 and predicted for NRPA-gen2, the pendular architecture is the best candidate to realize a sub- μg accelerometer with high bandwidth and small footprint. However, the proposed pendular architecture suffers from high thermal sensitivity due to the large amount of anchors (7 in total) required to realize the piezoresistive transduction of the nanoresonator. An efficient solution to conserve the pendular architecture and the resonant beam detection was developed in [54] and showed the previous highest current FOM_{tot} in addition to being robust against thermal drifts. This accelerometer is particularly robust against thermal fluctuations because the proof mass and the two resonant beams are connected to a single anchor. Because this accelerometer is based on a single-layer manufacturing process, the

electrostatic transduction are both efficient due to the large capacitive area and allows single anchor accelerometer. In contrast, in piezoresistive nanoresonators, the nanogauges are mechanically linked to the resonant beam, which makes it an inappropriate method for the single anchor. The nanoresonator has a poor capacitive surface due to its nanoscale making it unsuitable for electrostatic detection. In order to combine the use of a similar structure with the use of nanoresonators to overcome the compromise of monolayers, it would be judicious to imagine an efficient transduction at the nanoscale that would not mechanically affect the nanoresonators and thus allow the implementation of a pendular accelerometer with a single anchor. Optomechanical transduction has shown its capabilities in high precision measurement of the nanoresonator [113]. Here the optomechanical transduction, presented consists in a ring resonator that transduces 11 MHz-resonance frequency of a nanobeam. The nanobeam has the similar dimensions ($L \times w \times t = 5 \mu\text{m} \times 160 \text{ nm} \times 220 \text{ nm}$) as nanoresonator used as force sensor, so it seems realistic to use this transduction in the measurement of the nanoresonator resonance. In addition, optomechanical transduction [17], [114], [115] has demonstrated the capability to measure wide bandwidth signals. Therefore, an optomechanical transduction could be a good candidate to measure the large frequency variation induced by using the nanoresonator as a force sensor. However, the thermal stability of silicon optical properties can be a challenge for optomechanical transduction and requires feedback to operate in a temperature environment. In conclusion, it may be appropriate to combine the accelerometer of Figure 5-13 (a) using a nanobeam instead of a microbeam. In addition, the optomechanical transduction of Figure 5-13 (b) should be implemented for the transduction of the nanoresonator, as shown in Figure 5-13 (c).

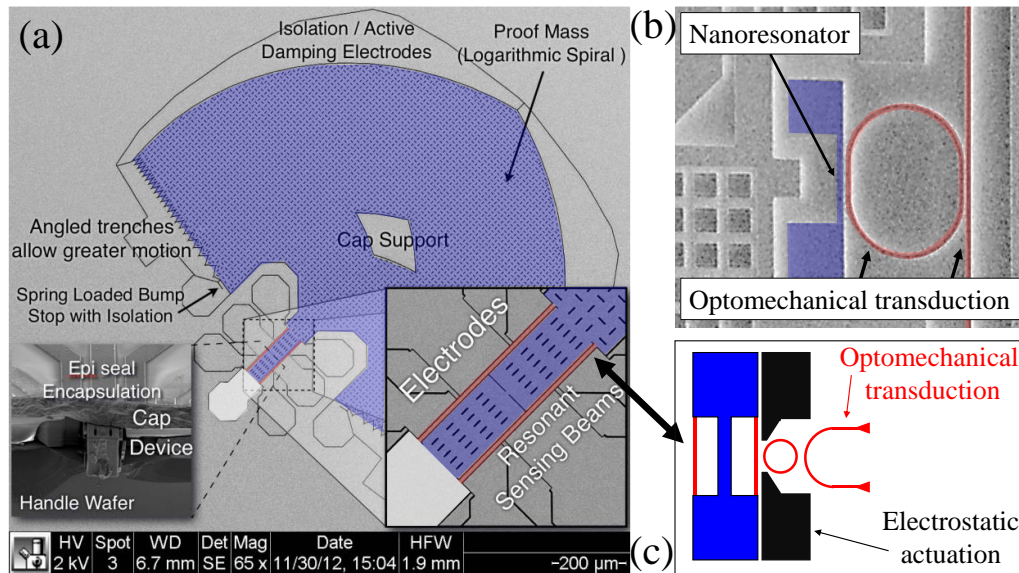


Figure 5-13 Proposition of pendulum accelerometer using a nanoresonator and optomechanical detection. (a) Pendulum architecture with a single anchor. Extracted from [54] (b) Optomechanical transduction of a nanoresonator. Extracted from [113]. (c) Proposed design, combining the pendulum architecture with an optomechanical detection.

Conclusions

In this work, a novel bilayer concept for resonant MEMS inertial sensors was presented and demonstrated for the first time with a single-axis accelerometer. This approach enables the realization of resonant beam accelerometers with high resolution, while keeping a large bandwidth and a small footprint thanks to the coupling between a micrometric-size accelerometer with an ultra-sensitive piezoresistive nanoresonator-based detection.

A first sensor design was performed by analytical modeling and FEM simulations. A force-measuring pendulum accelerometer and a piezoresistive nanoresonator were first studied separately and then combined to design the complete sensor. The sensors were then fabricated with a 200-mm fabrication process in Leti's clean room, using the *M&NEMS* technology. Measurements were performed at chip level in order to implement a proof of concept of in-plane accelerometer, and to validate the analytical models. These first devices demonstrated the best sensitivity in the state of the art, of 100,000 ppm/g, and a noise density of $1.75 \mu\text{g}/\sqrt{\text{Hz}}$ over a 1 kHz bandwidth, in a footprint of only 0.18 mm^2 . A dedicated electronic oscillator circuit was developed in parallel with the MEMS design, but issues in some individual modules prevented us to demonstrate its full operation. Globally, the first generation of devices show the advantages of the bilayer technology to simultaneously achieve μg resolution, wide bandwidth, and a small footprint.

However, these first designs also highlight several issues related to the use of the nanoresonators as force sensors, and of the pendulum architecture: (1) The high vacuum level provided by the wafer-level packaging induces high quality factors in the nanoresonator, and therefore a rapid apparition of nonlinearities. (2) A mode-coupling phenomenon between the nanoresonator and the MEMS modes reduces the dynamic range of the accelerometer. (3) The pendulum architecture showed an important sensitivity to thermal drifts. For this reason, a new generation of accelerometers that address these issues was designed and implemented in a subsequent tape-out (the corresponding lots are being fabricated). These devices present several advantages with respect to the first generation of designs: (1) while maintaining a high thickness ratios between the two active layers, larger nanoresonators with pinned anchors were designed to push the nonlinearities of the nanoresonators and to reach their detection limit. (2) Mechanical decoupling structures were developed to avoid mode-coupling phenomena. (3) Temperature stability has been taken into account in the specifications of the new designs, resulting in robust sensors against packaging-induced stress.

6 Appendix

Appendix A

In a resonant beam accelerometer, the resonant beam is both the sensing element and the mechanical actor of the entire structure. In order to be able to optimize the design of the whole structure it is necessary to model the intrinsic behavior of the resonant beam and its impact on the environment. For piezoresistive nanoresonators, the mechanical transduction of the resonant beam motion into a strain on the gauges is so far modelled using FEM simulation. Because it is an expensive modelling, it is time consuming to optimize both the piezoresistive transduction and the use of the nanoresonator as a force sensor for each accelerometer design. Therefore, a closed form of the piezoresistive transduction is proposed here to be implemented in the analytical modelling of the nanoresonator.

Because piezoresistive nanoresonator is here mainly used in its in-plane bending mode and consists in an assembling of nano-beams, we develop here a tool for assembling different 1D-elementary beam in order to study the static mechanical behaviour of the whole structure. This model assumes that each beam constituting the nanoresonator can be considered as ideal beams, i.e. that they have a sufficient length to width ratio, and that each beam has similar dimensions, i.e. that we do not model the assembly of a micrometric beam with a nanometric beam. A 1D elementary beam is composed of two nodes named N_k and N_n to which are associated (1) 3 degrees of freedom $v_{k,n}$, $u_{k,n}$, and $\theta_{k,n}$ corresponding respectively to the translation perpendicular and parallel to the neutral fibre of the beam as well as to the rotation of its cross section. (2) 3 reactions $T_{k,n}$, $F_{k,n}$ and $M_{k,n}$ which are respectively the reactions associated to the degree of freedom, namely the transverse reaction, the compressive reaction and the reaction moment.

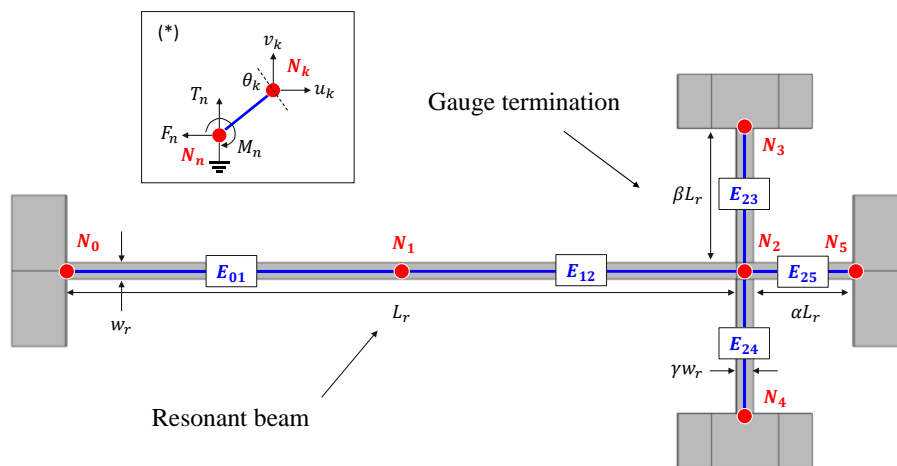


Figure 6-1 Decomposition of the nanoresonator on elementary beam: the resonant beam is decomposed in two element E_{01} and E_{12} . The nanogauges are represented by E_{23} and E_{24} and the beam end is represented by E_{25} . (inset) Description of the degrees of freedom and associated reaction on a node.

Because we looking for simple closed form of the displacement gain, we represent the mechanical equilibrium of 1D-elementary beam in quasi-static regime under the Bernoulli assumption:

$$\begin{cases} YS \frac{\partial^2 u}{\partial x^2} = 0 \\ YI \frac{\partial^4 v}{\partial x^4} = 0 \end{cases} \quad \& \quad \begin{cases} u\left((-1)^k \frac{L}{2}\right) = u_k \\ v\left((-1)^k \frac{L}{2}\right) = v_k \\ v_{,x}\left((-1)^k \frac{L}{2}\right) = \theta_k \end{cases} \quad \text{pour } k = \{1,2\} \quad 6-1$$

Where Y, S, L and I are respectively the Young modulus, the cross section, the length and the quadratic moment of the 1D-elementary beam. By naming w, t and L respectively the beam width thickness and length, we have $S = wt$ and $I = w^3 t / 12$. Moreover u and v are respectively the beam's displacement perpendicular and parallel to the neutral axis.

The displacement vector of the 1D-elementary beam $X(x) = \{u(x), v(x), \theta(x)\}$ can be calculated in function of the characteristic length L and the degrees of freedom $\bar{X} = \{u_1, v_1, \theta_1, u_2, v_2, \theta_2\} : X(x) = A(x)\bar{X}$.

$$A = \begin{pmatrix} \frac{1}{2} - \frac{x}{L} & 0 & 0 & \frac{1}{2} + \frac{x}{L} & 0 & 0 \\ 0 & \frac{1}{2} - \frac{3x}{2L} + \frac{2x^3}{L^3} & \frac{L}{8} - \frac{x}{4} - \frac{x^2}{2L} + \frac{x^3}{L^2} & 0 & \frac{1}{2} + \frac{3x}{2L} - \frac{2x^3}{L^3} & -\frac{L}{8} - \frac{x}{4} + \frac{x^2}{2L} + \frac{x^3}{L^2} \\ 0 & -\frac{3}{2L} + \frac{6x^2}{L^3} & -\frac{1}{4} - \frac{x}{L} + \frac{3x^2}{L^2} & 0 & \frac{3}{2L} - \frac{6x^2}{L^3} & -\frac{1}{4} + \frac{x}{L} + \frac{3x^2}{L^2} \end{pmatrix} \quad 6-2$$

We can then expressed the stiffness matrix K of the beam in the base \bar{X} by using the definition of strain energy \mathcal{V}_{int} and the elasticity matrix H [68]. As the same manner we can express the load matrix in the base \bar{X} by using the definition of external energy \mathcal{V}_{ext} and assuming axial load $F = \{0, f, 0\}$

$$K = \begin{pmatrix} \frac{YS}{L} & 0 & 0 & -\frac{YS}{L} & 0 & 0 \\ 0 & \frac{12YI}{L^3} & \frac{6YI}{L^2} & 0 & -\frac{12YI}{L^3} & \frac{6YI}{L^2} \\ 0 & \frac{6YI}{L^2} & \frac{4YI}{L} & 0 & -\frac{6YI}{L^2} & \frac{2YI}{L} \\ -\frac{YS}{L} & 0 & 0 & \frac{YS}{L} & 0 & 0 \\ 0 & -\frac{12YI}{L^3} & -\frac{6YI}{L^2} & 0 & \frac{12YI}{L^3} & -\frac{6YI}{L^2} \\ 0 & \frac{6YI}{L^2} & \frac{2YI}{L} & 0 & -\frac{6YI}{L^2} & \frac{4YI}{L} \end{pmatrix} \quad \& \quad F = \begin{pmatrix} 0 \\ \frac{fL}{2} \\ \frac{fL^2}{12} \\ 0 \\ \frac{fL}{2} \\ -\frac{fL^2}{12} \end{pmatrix} \quad 6-3$$

We can then express the mechanical equilibrium of an elementary 1D beam in a matrix way $F = K\bar{X}$. For the following, we name the mechanical equilibrium of the element E_{12} : $F_{12} = K_{12}\bar{X}_{12}$

Using the 1D elementary beam stiffness matrix, the nanoresonator assembly can be realized. To begin, we defined a projection basis where all degrees of freedom are brought back. For simplicity, we use the base of the element E_{12} . Then, for each element associated with E_{12} , that is to say each element that shares the node N_1 and N_2 , we associate a rotation matrix that allows us to express the reactions associated with the blocked degree of freedom. From a matrix point of view this operation is illustrated by the report of element E_{23} in the base of E_{12} :

$$F_{12} - K_{12}\bar{X}_{12} = \pi_{2,3}F_{23} - \pi_{2,3}K_{23}^T \pi_{2,3}^T \bar{X}_{23} \quad 6-4$$

This operation is repeated for each element associated to E_{12} . The stiffness matrix K of the nanoresonator element must consider the width, thickness and length defined in Figure 6-1. I.e. considering the resonant beam length L_r and w_r and the associated ratio α, β and γ . The final assembling stiffness matrix is K_{ass} :

$$\begin{pmatrix} \frac{4twY}{L} & 0 & 0 & -\frac{2twY}{L} & 0 & 0 \\ 0 & \frac{16tw^3Y}{L^3} & 0 & 0 & -\frac{8tw^3Y}{L^3} & \frac{2tw^3Y}{L^2} \\ 0 & 0 & \frac{4tw^3Y}{3L} & 0 & -\frac{2tw^3Y}{L^2} & \frac{tw^3Y}{3L} \\ -\frac{2twY}{L} & 0 & 0 & \frac{2twY}{L} + \frac{twY}{L\alpha} + \frac{2tw^3Y\gamma^3}{L^3\beta^3} & 0 & 0 \\ 0 & -\frac{8tw^3Y}{L^3} & -\frac{2tw^3Y}{L^2} & 0 & \frac{8tw^3Y}{L^3} + \frac{tw^3Y}{L^3\alpha^3} + \frac{2twY\gamma}{L\beta} & -\frac{2tw^3Y}{L^2} + \frac{tw^3Y}{2L^2\alpha^2} \\ 0 & \frac{2tw^3Y}{L^2} & \frac{tw^3Y}{3L} & 0 & -\frac{2tw^3Y}{L^2} + \frac{tw^3Y}{2L^2\alpha^2} & \frac{2tw^3Y}{3L} + \frac{tw^3Y}{3L\alpha} + \frac{2tw^3Y\gamma^3}{3L\beta} \end{pmatrix} \quad 6-5$$

The mechanic equilibrium of the reduced nanoresonator is then $F_{12} = K_{ass}X_{12}$ with $X_{12}^T = \{u_1, v_1, \theta_1, u_2, v_2, \theta_2\}$. The problem can be return by $X_{12} = F_{12}K_{ass}^{-1}$. Assuming that F_{12} results in a linear load on the beam, the transduction of the displacement is $\eta_v = v_2/v_1$

$$\eta_v = \frac{A}{\left(\frac{L_r}{w_r}\right)^2 + B} \quad 6-6$$

With

$$\begin{cases} A = \frac{\beta((11 + 52\alpha + 41\alpha^2)\beta + 104\alpha^2\gamma^3)}{2\alpha\gamma((8 + 19\alpha)\beta + 16\alpha\gamma^3)} \\ B = \frac{\beta((2 + 19\alpha + 73\alpha^2 + 112\alpha^3 + 56\alpha^4)\beta + 16\alpha(1 + 14\alpha^3)\gamma^3)}{2\alpha^3\gamma((8 + 19\alpha)\beta + 16\alpha\gamma^3)} \end{cases} \quad 6-7$$

The closed form of displacement gain η_v is compared with FEM simulation in Figure 6-2. Here, only 3 geometric parameters are swept in order to validate the consistency of the analytical model over a specific geometric range. We fix the resonant beam length $L_r = 10 \mu m$ and $\gamma = 1$. Nanoresonator width w_r are swept from 250 nm to 750 nm. The Figure 6-2 (a) shows nanogauge length sweep from 0 μm to 2 μm . The analytical modelling has ratio two with FEM simulation. The Figure 6-2 (b) shows beam-end length sweep from 0 μm to 2 μm . The analytical modelling is closed to FEM simulation for $w_r = 250 \text{ nm}$ but shows ratio 1.5 for $w_r = 750 \text{ nm}$. Moreover, the optimal position of the gauge α_{op} has mismatch that increase with the nanoresonator width.

However, for a 1D modelling with only 5 elements, the static behaviour of the nanoresonator is close enough to the FEM simulations in our geometry range. It will therefore be integrated into our model analytic to provide a tool for transduction optimization (section 3.1.2).

This method could be applied to the assembly of resonators with pin terminations for example. Moreover, the initial beam description (Eq. 6-1) could be completed by a more precise description (Timoshenko [68]) and the number of elements could be doubled to reach more precision.

However, this technique aims at improving the computation time for design optimization tools. If the equation of closed form becomes too laborious, this method loses its interest. This is why a dynamic analysis of the assembly has not been developed to express for example a closed form resonance frequency of the assembled nanoresonator.

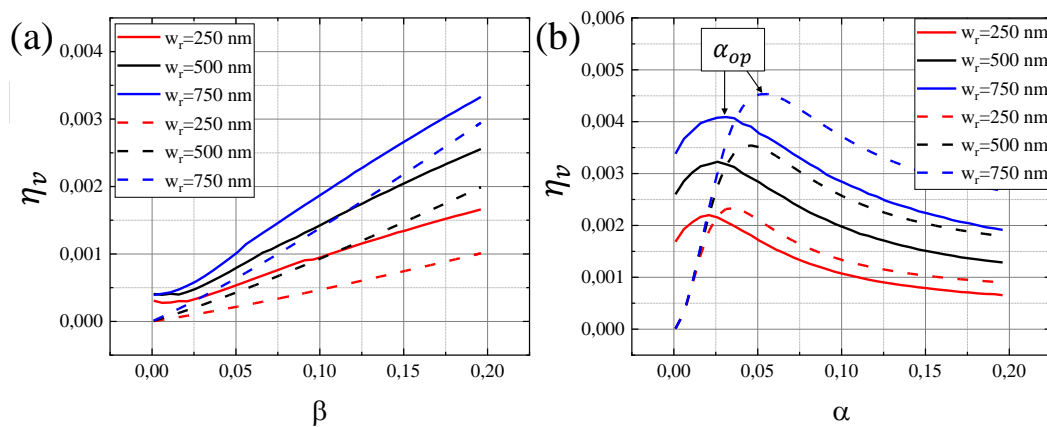


Figure 6-2 Comparison of the analytical model and FEM simulation of the displacement transduction for several nanoresonator width (w_r). The nanoresonator length is $L_r = 10 \mu m$. The dash line represent the analytical model and the full line the FEM simulation. (a) the β parameter (gauge length) is swept for $\alpha = 0.15$ and $\gamma = 1$. (b) the α parameter is swept for $\beta = 0.2$ and $\gamma = 1$.

Appendix B

In this section, the design strategy of the MEMS structure (section 3.1) is developed.

(1) Accelerometer parameters	(1) Nanoresonator parameters
$S_{\sigma a} = \rho t_m \frac{S_m L}{S_r l} \eta_r$	$\omega_{0r} = \frac{\alpha_0 w_r}{2\pi L_r^2} \sqrt{\frac{E}{12\rho}}$
$\omega_{0m} = \sqrt{\frac{C_h + k_{rc} l^2}{\rho t_m S_m L^2}}$	$\sigma_{buck} = \frac{E w_r^2}{12\beta_0 L_r^2}$
$a_{min,m} = \sqrt{\frac{4k_B T \omega_{0m}}{\rho t_m S_m Q_m}}$	$S_{\sigma\omega} = \frac{\omega_{0r}}{2\sigma_{buck} \sqrt{1 + \frac{\sigma_{PS}}{\sigma_{buck}}}}$
$a_{min,r} = \frac{\sigma_{min,r}}{S_{\sigma a}}$	$\omega_r = \omega_{0r} \sqrt{1 + \frac{\sigma_{PS}}{\sigma_{buck}}}$
(2) Nanoresonator optimized SNR	
$v_{max} = w_r \frac{\bar{v}_0}{\sqrt{3Q_r}} \left(1 + \frac{\sigma_{PS}}{\sigma_{buck}}\right)^{0.5}$	$n_{br} = \sqrt{\frac{4k_B T Q_r}{\omega_{0r}^3 0.39\rho}} \frac{(t_r w_r L_r)^{-0.5}}{\left(1 + \frac{\sigma_{PS}}{\sigma_{buck}}\right)^{0.75}}$
(3) Nanoresonator design rules	
$\begin{cases} t_r = w_r \\ L_r = \bar{L} w_r^{0.5} \end{cases}$	$\bar{L} = \sqrt{\frac{\alpha_0}{2\pi\omega_{0r}}} \sqrt{\frac{E}{12\rho}}$
(4) Impact on SNR_{br}	
$SNR_{br} = \frac{\bar{v}_0}{Q_r} \sqrt{\frac{\omega_{0r}^3 0.39\rho \bar{L}}{12k_B T}} \left(1 + \frac{\sigma_{PS}}{\sigma_{buck}}\right)^{1.25} w_r^{2.25}$	
$\sigma_{min,r} = \left[\sqrt{\frac{k_B T}{\bar{L}^5 12\omega_{0r}^3 0.39\rho}} \frac{E}{\bar{v}_0 \beta_0} \right] \left(1 + \frac{\sigma_{PS}}{\sigma_{buck}} w_r^{-1}\right)^{-0.25} w_r^{-1.25} = \Phi w_r^{-1.25}$	
(5) Accelerometer robustness $\eta_r = 1/2$	$L_h = \frac{2w_h^3 t_m \bar{L}}{3l^2 w_r^{1.5}}$
(6) Impact on accelerometer parameters	
$\omega_{0m} = \Omega \frac{l w_r^{0.75}}{L_m^2}$	$\Omega = \frac{15}{13} \sqrt{\frac{4Enb_r}{5\eta_r \bar{L} \rho t_m}}$
$a_{min,m} = A_M \frac{l^{0.5} w_r^{0.375}}{L_m^2}$	$A_M = \sqrt{\frac{16k_B T \Omega}{5\rho t_m Q_m}}$
$a_{min,r} = A_R \frac{l w_r^{0.75}}{L_m^3}$	$A_R = \frac{60nb_r \Phi}{65 \rho t_m \eta_r}$
(7) Optimisation	
$(a_{min,r} = a_{min,m})$	$L_m = \frac{A_R}{A_M} l^{0.5} w_r^{0.375}$
$\omega_{0m} = \Omega A_M^2 A_R^{-2}$	$a_{min} = A_M^3 A_R^{-2} l^{-0.5} w_r^{-0.375}$

Table 2 Analytical modelling of the optimisation of a nano-beam resonant accelerometer

Appendix C

In this section, an analytical model and an FEM-based model are developed to study the coupling of the nanoresonator mode. In addition, the analytical model of the decoupling stage developed in the second generation of the accelerometer (section 5.1.1) is developed.

Coupling modelling

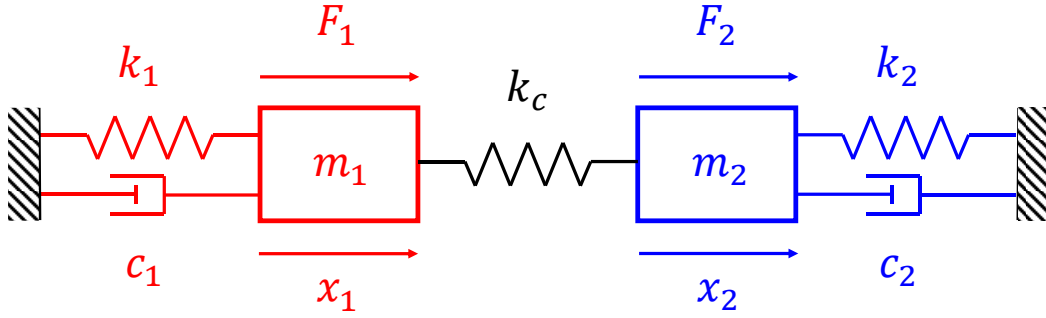


Figure 6-3 Principle of the coupling between nanoresonator and structural mode. (blue) the nanoresonator. (black) the coupling stiffness. (red) an MEMS mode coupled to nanoresonator.

The coupling concept between the nanoresonator and the MEMS mode can be modelled by two damped spring mass systems associated by a spring k_c . Here the first system represents the MEMS mode with m_1 its effective mass, k_1 its effective stiffness and c_1 its damping coefficient. F_1 represents the force that drives the effective mode and x_1 its natural displacement. Similarly, the second system represents the nanoresonator with m_2 its effective mass, k_2 its bending stiffness and c_2 its damping coefficient. F_2 represents the actuation force of the nanoresonator and x_2 its flexural displacement. The system of Figure 6-3 can be calculated from

$$\begin{pmatrix} m_1 & 0 \\ 0 & m_2 \end{pmatrix} \begin{pmatrix} \ddot{x}_1 \\ \ddot{x}_2 \end{pmatrix} + \begin{pmatrix} c_1 & 0 \\ 0 & c_2 \end{pmatrix} \begin{pmatrix} \dot{x}_1 \\ \dot{x}_2 \end{pmatrix} + \begin{pmatrix} k_1 + k_c & -k_c \\ -k_c & k_2 + k_c \end{pmatrix} \begin{pmatrix} x_1 \\ x_2 \end{pmatrix} = \begin{pmatrix} F_1 \\ F_2 \end{pmatrix} \quad 6-8$$

Here, the problem is addressed with the state space approach discussed in [116]. The principle is to reduce two second degree equations to four first degree equations. From a matrix point of view:

$$M\ddot{X} + C\dot{X} + KX = F \leftrightarrow \begin{cases} \dot{X} = AX + BF \\ \ddot{X} = CX + DF \end{cases} \quad 6-9$$

By posing $u_{1,2} = \omega_{1,2}x_{1,2}$, $v_{1,2} = \dot{x}_{1,2}$, $\omega_{1,2}^2 = k_{1,2}/m_{1,2}$ and $Q_{1,2} = \omega_{1,2}m_{1,2}/c_{1,2}$

$$\begin{cases} \begin{pmatrix} \dot{u}_1 \\ v_1 \\ \dot{u}_2 \\ v_2 \end{pmatrix} = \begin{pmatrix} 0 & \omega_1 & 0 & 0 \\ -\omega_1 & -\frac{\omega_1}{Q_1} & \frac{k_c}{\omega_2 m_1} & 0 \\ 0 & 0 & 0 & \omega_2 \\ \frac{k_c}{\omega_1 m_2} & 0 & -\omega_2 & -\frac{\omega_2}{Q_2} \end{pmatrix} \begin{pmatrix} u_1 \\ v_1 \\ u_2 \\ v_2 \end{pmatrix} + \begin{pmatrix} 0 & 0 \\ \frac{1}{m_1} & 0 \\ 0 & 0 \\ 0 & \frac{1}{m_2} \end{pmatrix} \begin{pmatrix} F_1 \\ F_2 \end{pmatrix} \\ \begin{pmatrix} x_1 \\ x_2 \end{pmatrix} = \begin{pmatrix} \frac{1}{\omega_1} & 0 & 0 & 0 \\ 0 & 0 & \frac{1}{\omega_2} & 0 \end{pmatrix} \begin{pmatrix} u_1 \\ v_1 \\ u_2 \\ v_2 \end{pmatrix} + \begin{pmatrix} 0 & 0 \\ 0 & 0 \end{pmatrix} \begin{pmatrix} F_1 \\ F_2 \end{pmatrix} \end{cases} \quad 6-10$$

The solution of Eq. 6-10 can be modelled in Matlab as Two-Input-Two-Output system. Here, the input / output of interest are F_2 and x_2 . The Figure 6-4 plots the magnitude of coupled nanoresonator as a function of frequency. The aims at identifying the origin of the stiffness k_1 and k_c . The characterization in Figure 4-26 shows the coupling frequency is not a function of the acceleration. Using the model with two coupled spring mass system, several cases are simulated. The first case (d) is the one where the two stiffnesses k_1 and k_2 are differentially modulated by the acceleration. This configuration may correspond to the case where coupling appears between the two nanoresonators. The second case (c) is the one where the two stiffnesses k_1 and k_2 are modulated in common mode by the acceleration. This configuration may correspond to the case where coupling appears between two modes in the nanoresonator (in plane and out of plane for instance). The third case (b) is the one where the two stiffnesses k_c and k_2 are modulated in common mode by the acceleration. This configuration may correspond to the case where coupling appears between the nanoresonators and another MEMS mode of the accelerometer that is affected by the acceleration. In these first three cases, the coupling frequency is a function of the acceleration, so they cannot represent the coupling. The last case (a) is the one where only the nanoresonator stiffnesses k_2 is modulated by the acceleration. This configuration may correspond to the case where the structural mode of the accelerometer coupled to the nanoresonator is not affected by the acceleration. This is the most likely configuration because the coupling frequency is not a function of the acceleration.

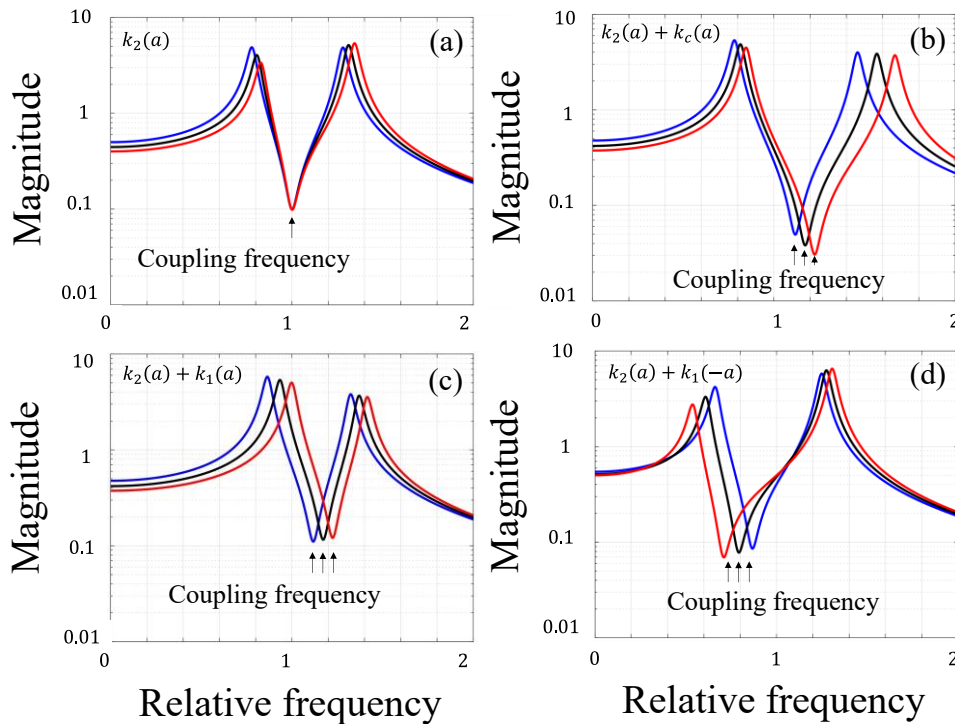


Figure 6-4 Magnitude of coupled nanoresonator as a function of acceleration. The coupling frequency is modulated by the acceleration in the first three cases (b), (c) and (d). The most likely case is the (a) because the coupling frequency is not modulated by acceleration.

FEM-simulation identification method

The objective of the FEM simulation method is to observe which MEMS modes are likely to couple to nanoresonator modes.

To achieve this, the proposed method allows: (1) to identify by a numerical criterion the modes of the nanoresonator. (2) to reproduce the operation of nanoresonator used as force sensor, i.e. its frequency variations under the effect of acceleration, by considering the whole structure of the accelerometer. (3) to quantify the coupling effects by the variation of this numerical criterion. (4) to visually observe the MEMS modes responsible for the variation of the numerical criterion and conclude.

In order to reproduce the behaviour of the accelerometer, and in particular the coupling phenomenon, a modal analysis of the complete structure of the accelerometer must be achieved. This modal analysis focuses the frequency range of interest, i.e. the operating frequency range of the nanoresonators. Then all the eigenmodes of the structure, i.e. the MEMS modes and the nanoresonator modes, are calculated.

Because the large frequency range (>MHz) and the different sizes of the elements involved (MEMS structure + nanoresonator), the simulation will find large number of eigenmodes. The first challenge is to focus on the modes of nanoresonators. In order to identify precisely this mode, we rely on the definition of a resonator: a resonator is a passive system that, at resonance, exchanges kinetic energy to strain energy. In other words, the eigenmode of the nanoresonator can be identified by its effective mass and its effective stiffness. We choose to base our numerical criterion on the effective mass because the evaluation of the effective stiffness in our case will be time consuming due to the non-linearity of the strain energies. According to its definition [68], the kinetic energy E_k can be evaluated for a specific eigenmode ω_n in a volume V :

$$(E_{k,n})_V = \frac{1}{2}(j\omega_n)^2 \iiint_V \rho_{Si}(u^2 + v^2 + w^2)dV \quad 6-11$$

By simulation, we evaluate the effective mass of the mode ω_n on a given volume

$$(m_{eff,n})_V = \frac{(E_{k,n})_V}{2(j\omega_n)^2} = \iiint_V \rho_{Si}(u^2 + v^2 + w^2)dV \quad 6-12$$

It is interesting to parameterize the FEM simulation tool in such a way as to project the ω_n mode on a normalized base, i.e. where the maximum amplitude of each eigenmodes is equal to 1. In this way, the evaluation of $m_{eff,n}$ on the nanoresonator's volume, represented on Figure 6-5 (a), allows identifying the

nanoresonator's mode among all the modes ω_n . Indeed, for the normalized base, the effective mass of the nanoresonator's mode is 0.39 (Eq. 2-20).

To go further, we base our numerical criterion on a relative value. Then, for each mode ω_n , we evaluate the effective mass on the volume of the nanoresonator, named V_r , as well as on the total volume of the accelerometer, named V_a . Thus, the nanoresonator's mode is then identify by 100%. Indeed, when the mode ω_n is different of the nanoresonator's mode, part of its effective mass is distributed out of the nanoresonator, thus, the Relative Mass Modal (RMM) is less than 100%. On the other hand, if the eigenmode ω_n is the nanoresonator's mode, the RMM should be closed to 100%. We define our numerical criterion as the ratio:

$$RMM = \frac{(m_{eff,n})_{V_r}}{(m_{eff,n})_{V_a}} = \frac{\iiint_{V_r} \rho(u^2 + v^2 + w^2) dV}{\iiint_{V_a} \rho(u^2 + v^2 + w^2) dV} \quad 6-13$$

where u, v and w are the displacement in the three direction and ρ the density of the material.

In conclusion, the RMM is a numerical value that allows quantifying the distribution of effective mass in the whole structure. In this specific case the ratio highlights the distribution in the nanoresonator, but we can define other ratio to quantify the distribution in other part of the structure. If we evaluate the RMM for each eigenmodes, the maximum value (close to 100%) corresponds to the nanoresonator's mode.

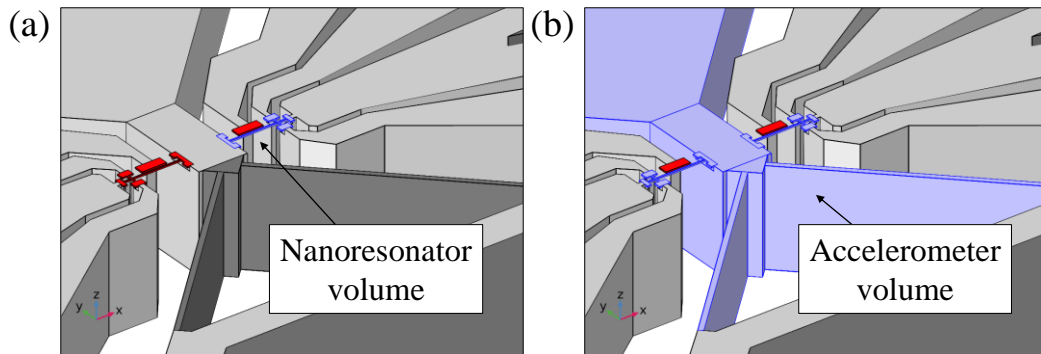


Figure 6-5 Illustration of the both volumes used in the calculation of the Relative Mass Modal. Here the structure is the first pendulum accelerometer architecture but it can be any other accelerometer architecture. (a) represents the nanoresonator's volume and (b) represents the accelerometer's volume.

For the moment, the RMM doesn't allow identifying the coupling. We must first reproduce the operation of the accelerometer by FEM simulation. I.e. the frequency variation of the nanoresonator due to acceleration. In this way, the modal analysis is completed by initial step that introduces load before the modal analysis. This load consists in applied acceleration in the sensitive direction to the accelerometer. In order to observe variation of nanoresonator's mode, we consider the non-linearity in the initial step of the FEM simulation (because the modulation of flexural stiffness by axial stress is due to second order deformation terms). The nonlinear-modal analysis must be repeated for each acceleration in the operation range, i.e. the acceleration range necessary to shift nanoresonator's mode in the defined frequency range. The simulation generates 2D array of results that consists in the evaluation of RMM for each eigenmodes (on the frequency range) for each accelerations (on the acceleration range). In order to illustrate the FEM simulation results, the Table 39 shows arbitrary example of 2D array of results:

	a_1	a_2	a_3	a_4
ω_1	0.5 %	0.5 %	0.5 %	0.5 %
ω_2	100 %	77 %	77 %	77 %
ω_3	77 %	100 %	0.005 %	0.005 %
ω_4	0.005 %	0.005 %	100 %	17%
ω_5	17%	17%	17%	100 %
ω_6	59 %	59 %	59 %	59 %

Table 39 Example of RMM calculated on frequency range of 6 eigenmodes and acceleration range of 4 accelerations.

By identification, we can extracted the nanoresonator mode for each acceleration by researching the maximum value of the FMM. In practice the FMM is not always equal to 100% but still the maximum value for the nanoresonator's mode. In order to have an idea of the interest of the FMM, Table 40 presents the same simulation results but where the frequency is evaluated.

	a_1	a_2	a_3	a_4
ω_1	11.5 MHz	11.5 MHz	11.5 MHz	11.5 MHz
ω_2	12.5 MHz	12.9 MHz	12.9 MHz	12.9 MHz
ω_3	12.9 MHz	14.5 MHz	15 MHz	15 MHz
ω_4	15 MHz	15 MHz	16.5 MHz	18.1 MHz
ω_5	18.1 MHz	18.1 MHz	18.1 MHz	18.5 MHz
ω_6	20.5 MHz	20.5 MHz	20.5 MHz	20.5 MHz

Table 40 Example of frequency calculated on frequency range of 6 eigenmodes and acceleration range of 4 accelerations

Because the FEM simulation cannot isolate the nano-resonator mode by itself, it always presents the frequencies in increasing order. Thus, FMM allows to post-process the FEM simulation results in an efficient way to classify the modes into two families: the modes that vary with the acceleration, i.e. the nanoresonator's modes and the modes that do not, i.e. the MEMS modes.

The Figure 6-6 (a) represents the two families of mode classified in function of the acceleration. Here, the results come from to real simulations performed in the second generation of pendulum architecture (section 5.2.2.1). We can identify properly the variation of nanoresonator's modes as a function of acceleration whereas the MEMS modes are not affected by acceleration. The Figure 6-6 (b) plots the RMM of the Left resonator: If we imagine Table 39 and Table 40 represent real results of FEM simulation, the x axis represents the RMM, i.e. the red values of Table 39 and the y axis its associated frequency i.e. the red values of Table 40. Here, there are two "black peaks" that represent the degraded value of the RMM ($<100\%$). In other words there are acceleration values where the modal mass of the nanoresonator's mode is distributed out of the nanoresonator. This is unusual because the RMM ensure that the eigenmode is the nanoresonator's mode (because he keeps the maximum RMM). Looking at the position of these peaks in Figure 6-6 (a), the $\sim 9\text{MHz}$ peak corresponds to an acceleration where nanoresonator's mode crosses the MEMS mode named "m2". At the intersection, the RMM is close to 50%, i.e. the modal mass of the nanoresonator is half distributed in the nanoresonator and half out of the nanoresonator. At this step, we can conclude that the mode "m2" is likely to be a coupling mode. But we need to study the FEM simulation results further to conclude.

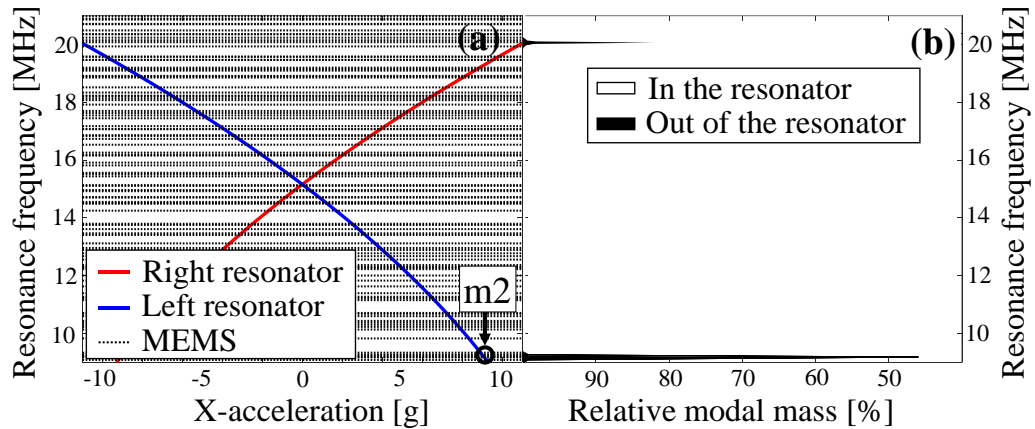


Figure 6-6. Post-processed FEM simulation results. (a) Eigenmodes classified into two families: nanoresonator modes (blue and red) and MEMS modes (black). The nanoresonator modes are acceleration dependent while the MEMS modes are not. (b) The calculated RMM for the left resonator as a function of acceleration. The white area represents the relative modal mass in the resonator and the black area represents the relative modal mass out of the resonator. The black peaks are probably indicative of coupling.

The last step consists in investigating more closely the specific suspect mode, here "m2". We choose to focus on the mode shape to validate the mechanism involved. The objective is to determine if the mode of the structure is really likely to couple to the mode of the resonator. The shape of the MEMS mode and the nanoresonator mode is first represented away from the coupling, i.e., for an acceleration where the nanoresonator resonance is far from the MEMS mode frequency. The Figure 5-13 (m2.1) represents the MEMS mode shape that is the z-torsion mode of the mechanical decoupling structure. Its frequency is 9.18 MHz. The Figure 5-13 (mR.1) represents the nanoresonator mode shape at 20 MHz, thus far to the MEMS mode. In both case the scale is normalized by the maximal displacement. Since these modes are identified structure modes (mechanical decoupling structure and nanoresonator), a fitted view above these structures allows to clearly identify the displacements involved. The Figure 5-13 (m2.2) and (mR.2) represents respectively the MEMS mode and nanoresonator mode for matched frequency (i.e. for acceleration position where the both modes are crossed). Their frequency are respectively 9.18 MHz and 9.17 MHz. his configuration corresponds to the likely coupling of the "m2" mode with the nanoresonator mode identified in Figure 6-6. Remember in this configuration the modal mass of the nanoresonator is half distributed in the nanoresonator and half out of the nanoresonator. When we observe the shapes of the modes, both resemble the bending mode of the nanoresonator. In fact, this is due to the fact that the scale is normalized by the maximum displacement. Because of the large size difference between the nanoresonator and the mechanical decoupling structure, the displacement of the MEMS mode is not perceptible. The Figure 5-13 (m2.3) and (mR.3) shows the mode shapes for scale amplification of 1000. Here we can clearly identify both mode are the linear combination of the MEMS mode and nanoresonator mode.

In this particular case, we can conclude that both the numerical and visual criteria are realistic and that coupling is very likely to happen. This visual criterion takes time but is still necessary to ensure the validity of the coupling.

As explained in Section 4.2.4.2, the identification of the most likely coupling modes is based on the numerical criterion, the visual criterion and the experimental results. The experimental results allow to validate or not that a coupling identified by the FEM method happen.

It is now necessary to develop the method based on the experimental results. The objective would be to find the combination of numerical criteria that are sufficient to demonstrate why one coupling happen and not another.

We can start by establishing new ratios based on the structures most likely to be coupled in order to quantify where the effective mass is distributed during coupling (e.g. from the nanoresonator to the hinge for stiffness coupling).

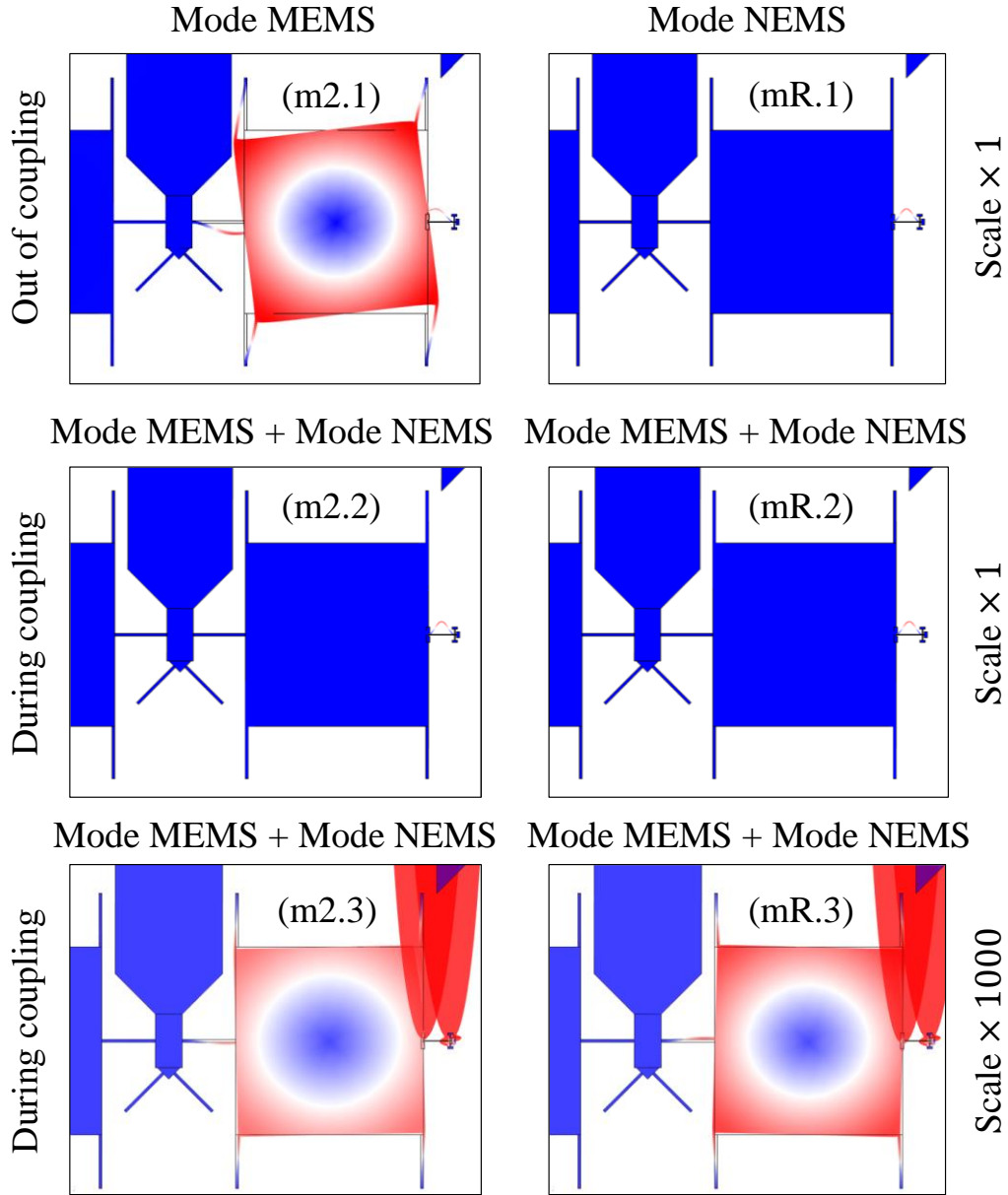


Figure 6-7 Representation of the "m2" coupling that could happen in the second generation of the pendulum accelerometer at 9.18 MHz. The MEMS mode consists of a z-torsion mode of the mechanical decoupling structure. When this coupling happens, both the MEMS mode and the nanoresonator mode are a linear combination of the bending mode of the beam and the z-torsion mode of the mechanical decoupling structure.

Decoupling modelling

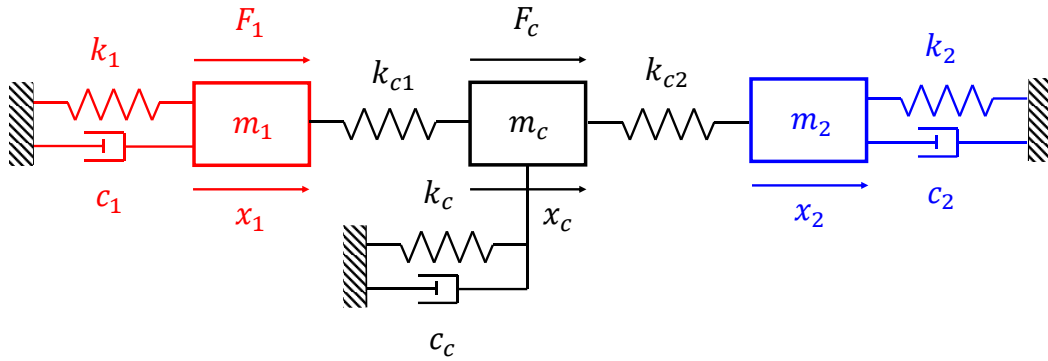


Figure 6-8 Schematic of the mechanical solution of decoupling.

The mechanical decoupling structure can be modeled by the schematic of Figure 6-8. Its dynamics can be modelled by three second order equations

$$\begin{pmatrix} m_1 & 0 & 0 \\ 0 & m_c & 0 \\ 0 & 0 & m_2 \end{pmatrix} \begin{pmatrix} \ddot{x}_1 \\ \ddot{x}_c \\ \ddot{x}_2 \end{pmatrix} + \begin{pmatrix} c_1 & 0 & 0 \\ 0 & c_c & 0 \\ 0 & 0 & c_2 \end{pmatrix} \begin{pmatrix} \dot{x}_1 \\ \dot{x}_c \\ \dot{x}_2 \end{pmatrix} + \begin{pmatrix} k_1 + k_{c1} & -k_{c1} & 0 \\ -k_{c1} & k_c + k_{c1} + k_{c2} & -k_{c2} \\ 0 & -k_{c2} & k_2 + k_{c2} \end{pmatrix} \begin{pmatrix} x_1 \\ x_c \\ x_2 \end{pmatrix} = \begin{pmatrix} F_1 \\ F_c \\ F_2 \end{pmatrix} \quad 6-14$$

or reduced to six first-order equations:

$$\begin{cases} \begin{pmatrix} u_1 \\ v_1 \\ u_c \\ v_c \\ u_2 \\ v_2 \end{pmatrix} = \begin{pmatrix} 0 & \omega_1 & 0 & 0 & 0 & 0 \\ -\omega_1 & -\frac{\omega_1}{Q_1} & \frac{k_{c1}}{m_1\omega_c} & 0 & 0 & 0 \\ 0 & 0 & 0 & \omega_c & 0 & 0 \\ \frac{k_{c1}}{m_c\omega_1} & 0 & -\omega_c & -\frac{\omega_c}{Q_c} & \frac{k_{c2}}{m_c\omega_2} & 0 \\ 0 & 0 & 0 & 0 & 0 & \omega_2 \\ 0 & 0 & \frac{k_{c2}}{m_2\omega_c} & 0 & -\omega_2 & -\frac{\omega_2}{Q_2} \end{pmatrix} \begin{pmatrix} u_1 \\ v_1 \\ u_c \\ v_c \\ u_2 \\ v_2 \end{pmatrix} + \begin{pmatrix} 0 & 0 & 0 \\ \frac{1}{m_1} & 0 & 0 \\ 0 & \frac{1}{m_c} & 0 \\ 0 & 0 & 0 \\ 0 & 0 & 0 \\ 0 & 0 & \frac{1}{m_2} \end{pmatrix} \begin{pmatrix} F_1 \\ F_c \\ F_2 \end{pmatrix} \\ \begin{pmatrix} x_1 \\ x_c \\ x_2 \end{pmatrix} = \begin{pmatrix} \frac{1}{\omega_1} & 0 & 0 & 0 & 0 & 0 \\ 0 & 0 & \frac{1}{\omega_c} & 0 & \frac{1}{\omega_2} & 0 \\ 0 & 0 & 0 & 0 & 0 & 0 \end{pmatrix} \begin{pmatrix} u_1 \\ v_1 \\ u_c \\ v_c \\ u_2 \\ v_2 \end{pmatrix} + \begin{pmatrix} 0 & 0 & 0 \\ 0 & 0 & 0 \\ 0 & 0 & 0 \end{pmatrix} \begin{pmatrix} F_1 \\ F_c \\ F_2 \end{pmatrix} \end{cases} \quad 6-15$$

With

$$\begin{aligned} u_1 &= \omega_1 x_1, v_1 = \dot{x}_1, \omega_1^2 = \frac{k_1}{m_1} \text{ and } Q_1 = \frac{\omega_1 m_1}{c_1} \\ u_c &= \omega_c x_c, v_c = \dot{x}_c, \omega_c^2 = \frac{k_c}{m_c} \text{ and } Q_c = \frac{\omega_c m_c}{c_c} \\ u_2 &= \omega_2 x_2, v_2 = \dot{x}_2, \omega_2^2 = \frac{k_2}{m_2} \text{ and } Q_2 = \frac{\omega_2 m_2}{c_2} \end{aligned}$$

The matrix system can be solve as the same manner of Eq. 6-9 using the state space approach [116].

Appendix D

In this section there is a methodology to model and quantify the performances of different accelerometers. The method follows the following steps:

- (1) Presentation of the design geometry and reduced damped spring mass model.
- (2) Expression of motions equation in the form of second order matrix system
- (3) Reduction to first order matrix systems
- (4) Expression of equivalent stiffness of the accelerometer
- (5) Expression of the dynamics of the accelerometer
 - Resonance frequency of the accelerometer
 - Cut-off frequency of the mechanical decoupling structure
 - Internal dynamics of the mechanical decoupling structure
- (6) Example of geometry
- (7) Comparison of analytical model and FEM simulation
 - For the accelerometer sensitivity
 - For the different dynamics
- (8) Simulation of the structure stability/robustness
 - Cross axis simulation : 1g of acceleration are applied on each axis. The axial strain are evaluated on both nanoresonator (σ_{R1} and σ_{R2}). The differential sensitivity $\Delta\sigma = |\sigma_{R1} - \sigma_{R2}|$ is compared with the in plane sensitivity $\delta\sigma = \Delta\sigma/\Delta\sigma_X$.
 - Shocks simulation: the proof mass is move to the 3-axis stoppers. The axial strain are evaluated on both nanoresonator (σ_{R1} and σ_{R2}). The stress average $\Delta\sigma = (\sigma_{R1} + \sigma_{R2})/2$ is evaluated and compared with the Full scale stress (FS)
 - Package stress simulations: strain ϵ_{XX} , ϵ_{YY} or ϵ_{XY} of 100ppm are applied at all the accelerometer anchors in order to reproduce package stress due to thermal effect. The axial strain are evaluated on both nanoresonator (σ_{R1} and σ_{R2}). The differential sensitivity $\Delta\sigma = |\sigma_{R1} - \sigma_{R2}|$ is compared as a ratio of the Full Scale stress.

Pendulum accelerometer generation 1

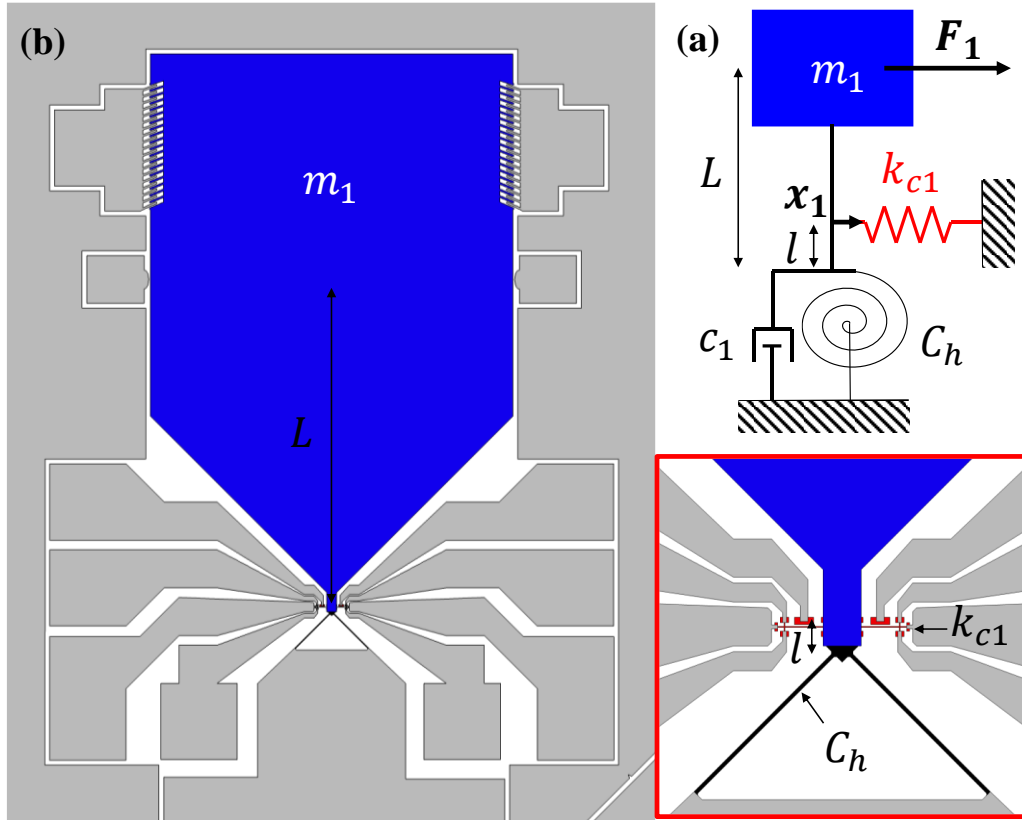


Figure 6-9 Presentation of the first generation of pendulum accelerometer. (a) is the reduced damped spring mass system and (b) is the design of the accelerometer

The first generation of pendulum accelerometer can be modelled by the schematic of Figure 6-9 (a). Its dynamics can be modelled by a second order equations

$$F_1 \frac{l}{L} = m_1 \ddot{x}_1 + \frac{c_1}{L^2} \dot{x}_1 + \frac{C_h + k_{c1} l^2}{L^2} x_1 \quad 6-16$$

or reduced to two first-order equations by posing $u_1 = \omega_1 x_1$, $v_1 = \dot{x}_1$, $\omega_1^2 = K_{eq}/m_1$ and $Q_1 = \omega_1 m_1 L^2 / c_1$

$$\begin{cases} \begin{pmatrix} \dot{u}_1 \\ \dot{v}_1 \end{pmatrix} = \begin{pmatrix} 0 & \omega_1 \\ -\omega_1 & -\frac{\omega_1}{Q_1} \end{pmatrix} \begin{pmatrix} u_1 \\ v_1 \end{pmatrix} + \begin{pmatrix} 0 \\ \frac{l}{L m_1} \end{pmatrix} (F_1) \\ x_1 = \left(\frac{1}{\omega_1} \quad 0 \right) \begin{pmatrix} u_1 \\ v_1 \end{pmatrix} + (0)(F_1) \end{cases} \quad 6-17$$

With $K_{eq} = F_1/x_1$ the equivalent stiffness of the accelerometer:

$$K_{eq} = \frac{C_h + k_{c1} l^2}{L^2} \quad 6-18$$

The accelerometer resonance can be estimated

$$\omega_{0m} = \sqrt{\frac{K_{eq}}{m_1}} \quad 6-19$$

Here the analytical modelling is compared to FEM simulation for this pendulum accelerometer (generation 1) geometry:

Geometry	Value
L_g	$2 \mu m$
L_t	$0.5 \mu m$
L_r	$10 \mu m$
w_r	$250 nm$
L_m	$379.8 \mu m$
L_h	$51.41 \mu m$

Table 41 Geometry of the pendulum accelerometer

Parameters	Analytics modelling	COMSOL
$S_{\sigma a} = m_1 E / K_{eq} L_r$	$22.97 MPa/g$	$22.42 MPa/g$
ω_{0m}	$1.6 kHz$	$1.3 kHz$

Table 42 Comparison between analytical modeling and FEM simulation of accelerometer parameters

The next part is based only on the FEM simulation and allows quantify the cross-axis sensitivities, the thermal effect and the protection of the nanoresonator by stoppers.

acceleration	$\sigma_{R1} [MPa]$	$\sigma_{R1} [MPa]$	$\Delta\sigma [MPa]$	$\delta\sigma [\%]$
$a_x = 1g$	22.442	-22.453	44.895	100
$a_y = 1g$	0.71	-0.71	1.41	3.14
$a_z = 1g$	0.703	-0.708	1.41	3.14

Table 43 Differential sensitivities as a function 1g-acceleration applied on each directions.

displacement	$\sigma_{R1} [MPa]$	$\sigma_{R1} [MPa]$	$\Delta\sigma [MPa]$
$x = 1 \mu m$	265.14	-265.27	$FS = 265.2$
$y = 1 \mu m$	13.91	-13.9	13.9
$z = 0.8 \mu m$	-0.14	-0.18	0.16

Table 44 Maximum stress applied on the nanoresonator when proof mass contacts stoppers.

effect	$\sigma_{R1}[MPa]$	$\sigma_{R1}[MPa]$	$\Delta\sigma[MPa]$	%FS
$\epsilon_{XX} = 100ppm$	3.56	3.59	0.03	0.01
$\epsilon_{YY} = 100ppm$	119.25	118.72	0.53	0.2
$\epsilon_{XY} = 100ppm$	70.52	-70.52	141.04	53.184
$\Delta T = 100^\circ C$	319.47	-318.13	1.34	0.5

Table 45 Differential sensitivities as a function of substrate deformation (ϵ_{XX} , ϵ_{YY} , ϵ_{XY}) and thermal expansion (ΔT).

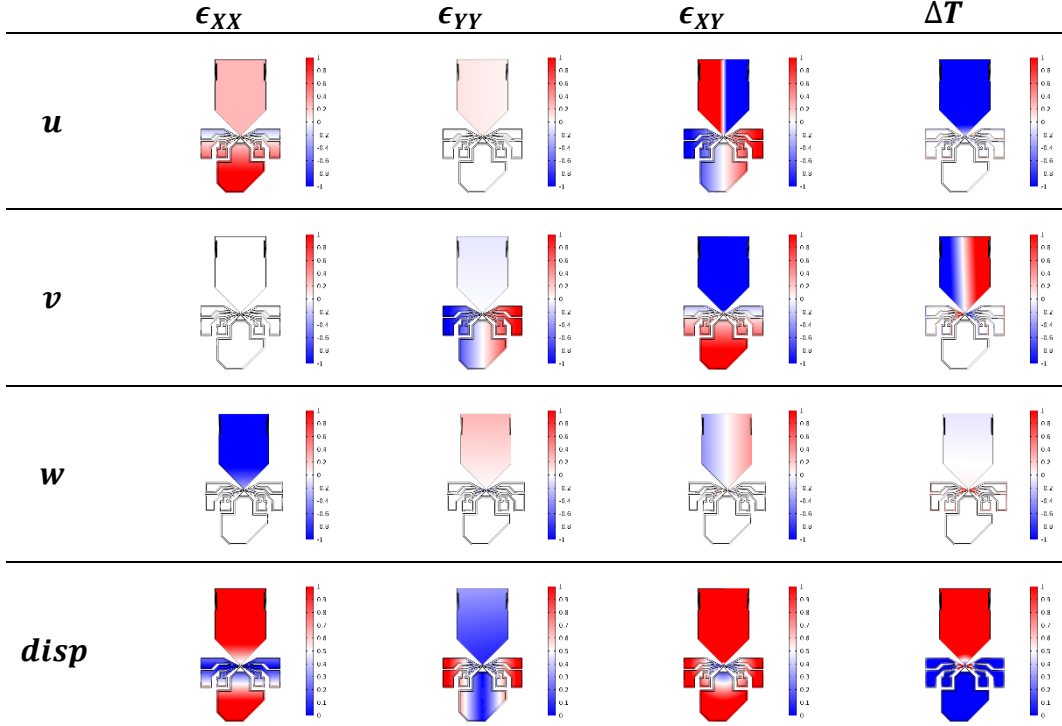


Table 46 Displacement profile induced by substrate deformation (ϵ_{XX} , ϵ_{YY} , ϵ_{XY}) and thermal expansion (ΔT).

Pendulum accelerometer generation 2

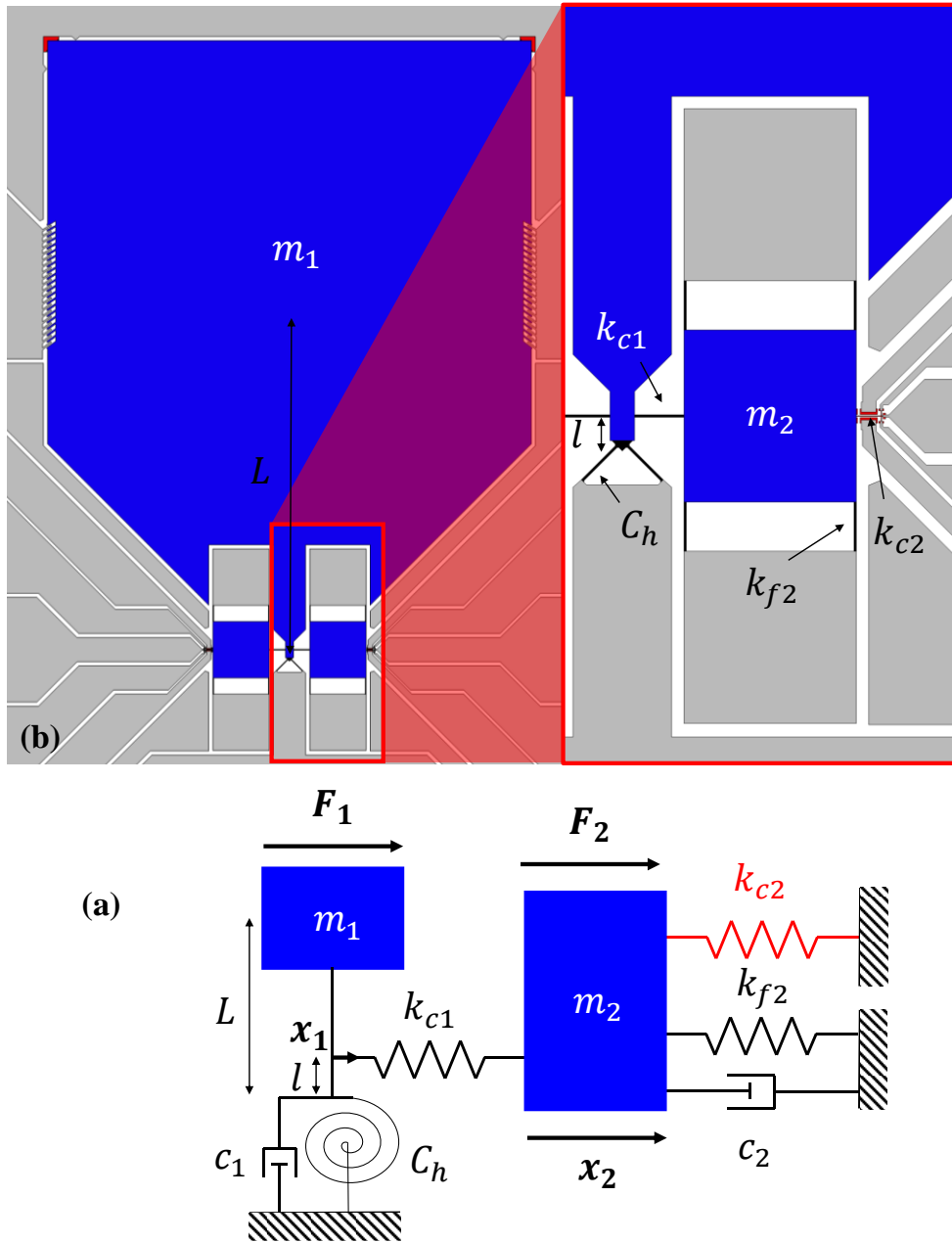


Figure 6-10 Presentation of the first generation of pendulum accelerometer. (a) is the reduced damped spring mass system and (b) is the design of the accelerometer

The second generation of pendulum accelerometer can be modelled by the schematic of Figure 6-10 (a). Its dynamics can be modelled by two second order equations

$$\begin{pmatrix} m_1 & 0 \\ 0 & m_2 \end{pmatrix} \begin{pmatrix} \ddot{x}_1 \\ \ddot{x}_2 \end{pmatrix} + \begin{pmatrix} \frac{c_1}{L^2} & 0 \\ 0 & c_2 \end{pmatrix} \begin{pmatrix} \dot{x}_1 \\ \dot{x}_2 \end{pmatrix} + \begin{pmatrix} \frac{C_h + k_{c1}l^2}{L^2} & -k_{c1}\frac{l^2}{L^2} \\ -k_{c1} & k_{f2} + k_{c2} + k_{c1} \end{pmatrix} \begin{pmatrix} x_1 \\ x_2 \end{pmatrix} = \begin{pmatrix} \frac{F_1 l}{L} \\ F_2 \end{pmatrix} \quad 6-20$$

or reduced to four first-order equations by posing $u_{1,2} = \omega_{1,2}x_{1,2}$; $v_{1,2} = \dot{x}_{1,2}$, $\omega_1^2 = C_h + k_{c1}l^2/m_1L^2$, $\omega_2^2 = (k_{f2} + k_{c2} + k_{c1})/m_2$, $Q_1 = \omega_1m_1L^2/c_1$ and $Q_2 = \omega_2m_2/c_2$:

$$\begin{cases} \begin{pmatrix} \dot{u}_1 \\ \dot{v}_1 \\ \dot{u}_2 \\ \dot{v}_2 \end{pmatrix} = \begin{pmatrix} 0 & \omega_1 & 0 & 0 \\ -\omega_1 & -\frac{\omega_1}{Q_1} & \frac{k_{c1}l^2}{\omega_2m_1L^2} & 0 \\ 0 & 0 & 0 & \omega_2 \\ \frac{k_{c1}}{\omega_1m_2} & 0 & -\omega_2 & -\frac{\omega_2}{Q_2} \end{pmatrix} \begin{pmatrix} u_1 \\ v_1 \\ u_2 \\ v_2 \end{pmatrix} + \begin{pmatrix} 0 & 0 \\ \frac{l}{m_1L} & 0 \\ 0 & 0 \\ 0 & \frac{1}{m_2} \end{pmatrix} \begin{pmatrix} F_1 \\ F_2 \end{pmatrix} \\ \begin{pmatrix} x_1 \\ x_2 \end{pmatrix} = \begin{pmatrix} \frac{1}{\omega_1} & 0 & 0 & 0 \\ 0 & 0 & \frac{1}{\omega_2} & 0 \end{pmatrix} \begin{pmatrix} u_1 \\ v_1 \\ u_2 \\ v_2 \end{pmatrix} + \begin{pmatrix} 0 & 0 \\ 0 & 0 \end{pmatrix} \begin{pmatrix} F_1 \\ F_2 \end{pmatrix} \end{cases} \quad 6-21$$

The equivalent stiffness of the accelerometer $K_{eq} = x_2/F_1$ consists in k_{c2} in parallel with k_{f2} , all in series with k_{c1} . This equivalent stiffness integrated in the lever arm:

$$K_{eq} = \frac{C_h + l^2 \frac{k_{c1}(k_{c2} + k_{f2})}{k_{c1} + k_{c2} + k_{f2}}}{L^2} \quad 6-22$$

Considering $m_1 \gg m_2$ the accelerometer resonance can be estimated

$$\omega_{0m} = \sqrt{\frac{K_{eq}}{m_1}} \quad 6-23$$

The dynamics of the mechanical decoupling structure can be estimated by

$$\begin{cases} \omega_2 = \sqrt{\frac{k_{f2} + k_{c2} + k_{c1}}{m_2}} \\ \omega_{f2} = \sqrt{\frac{k_{f,f2}}{m_{f2}}} \\ \omega_{c1} = \sqrt{\frac{k_{f,c1}}{m_{c1}}} \end{cases} \quad 6-24$$

where ω_2 is the cut-off frequency of the mechanical decoupling structure. ω_{f2} is the bending mode of the beam represented by the stiffness k_{f2} , with $k_{f,f2}$ and m_{f2} , which are respectively its flexural stiffness and effective mass. ω_{c1} is the bending mode of the beam represented by the stiffness k_{c1} , with $k_{f,c1}$ and m_{c1} , which are respectively its flexural stiffness and effective mass.

Here the analytical modelling is compared to FEM simulation for this pendulum accelerometer (generation 2) geometry:

Geometries	Values
L_g	$2\ \mu m$
L_t	$0.5\ \mu m$
L_r	$10\ \mu m$
w_r	$250\ nm$
L_{m11}	$600\ \mu m$
L_{m12}	$500\ \mu m$
L_h	$20\ \mu m$
L_{m2}	$60\ \mu m$
l_{f2}	$20\ \mu m$
l_{c1}	$20\ \mu m$

Table 47 Geometry of the pendulum accelerometer

Parameters	Analytics modelling	FEM simulation
$S_{\sigma a} = m_1 E / K_{eq} L_r$	$17\ MPa/g$	$12.43\ MPa/g$
ω_{0m}	$2.1\ kHz$	$2\ kHz$

Table 48 Comparison between analytical modeling and FEM simulation of accelerometer parameters.

	ω_2	ω_{c1}	ω_{f2}
Analytic	4.36 MHz	22 MHz	22 MHz
FEM Simulation	4.11 MHz	21.5 MHz	21.12 MHz

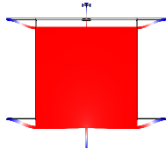
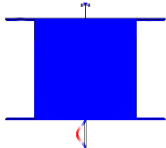
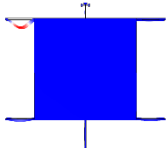
Mode shape			
------------	---	--	---

Table 49 Comparison between analytical modeling and FEM simulation of mechanical decoupling structure.

The next part is based only on the FEM simulation and allows quantify the cross-axis sensitivities, the thermal effect and the protection of the nanoresonator by stoppers.

acceleration	$\sigma_{R1}[MPa]$	$\sigma_{R1}[MPa]$	$\Delta\sigma[MPa]$	$\delta\sigma[\%]$
$a_x = 1g$	12.433	-12.438	24.871	100
$a_y = 1g$	$5.4E - 5$	$6.8E - 5$	$1.4E - 5$	$6E - 5$
$a_z = 1g$	0.06993	0.06999	$6E - 5$	$2.3E - 4$

Table 50 Differential sensitivities as a function 1g-acceleration applied on each directions.

displacement	$\sigma_{R1}[MPa]$	$\sigma_{R1}[MPa]$	$\Delta\sigma[MPa]$
$x = 1\mu m$	161.99	-161.32	$FS = 161.655$
$y = 1\mu m$	295.56	292.6	294.08
$z = 0.8\mu m$	7.71	8.04	7.87

Table 51 Maximum stress applied on the nanoresonator when proof mass contacts stoppers.

effect	$\sigma_{R1}[MPa]$	$\sigma_{R1}[MPa]$	$\Delta\sigma[MPa]$	%FS
$\epsilon_{XX} = 100ppm$	-1.07	-1.03	0.05	0.02
$\epsilon_{YY} = 100ppm$	202.46	202.63	0.17	0.1
$\epsilon_{XY} = 100ppm$	-30.58	30.80	61.38	37.96
$\Delta T = 100^\circ C$	-523.61	-524.18	0.57	0.35

Table 52 Differential sensitivities as a function of substrate deformation (ϵ_{XX} , ϵ_{YY} , ϵ_{XY}) and thermal expansion (ΔT).

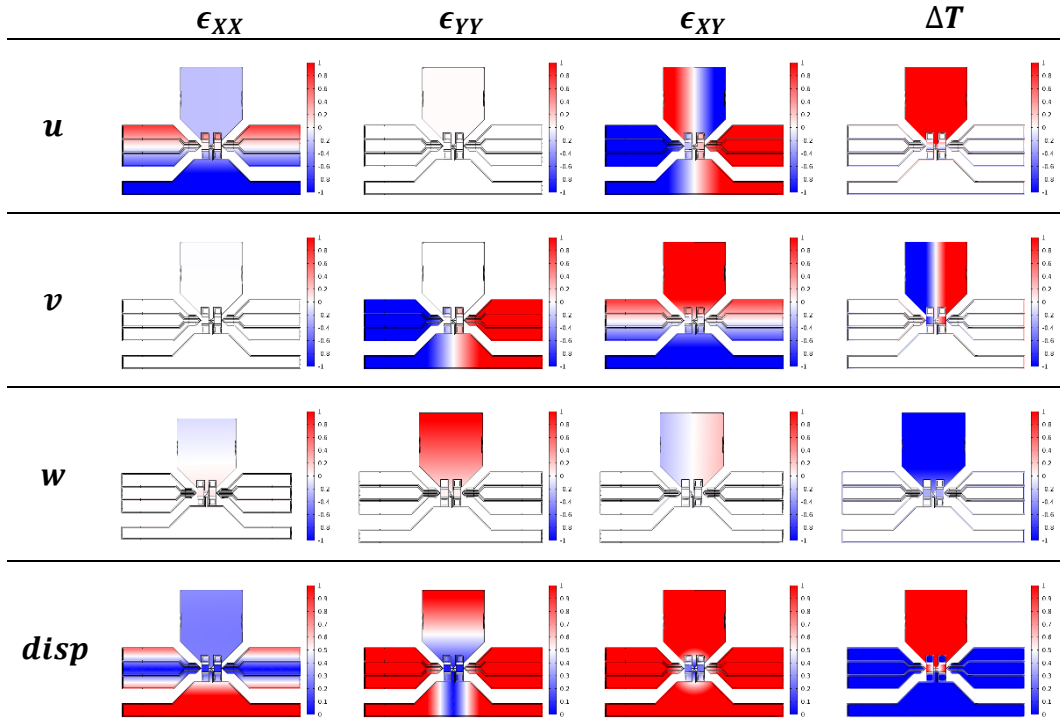


Table 53 Displacement profile induced by substrate deformation (ϵ_{XX} , ϵ_{YY} , ϵ_{XY}) and thermal expansion (ΔT).

Translation accelerometer

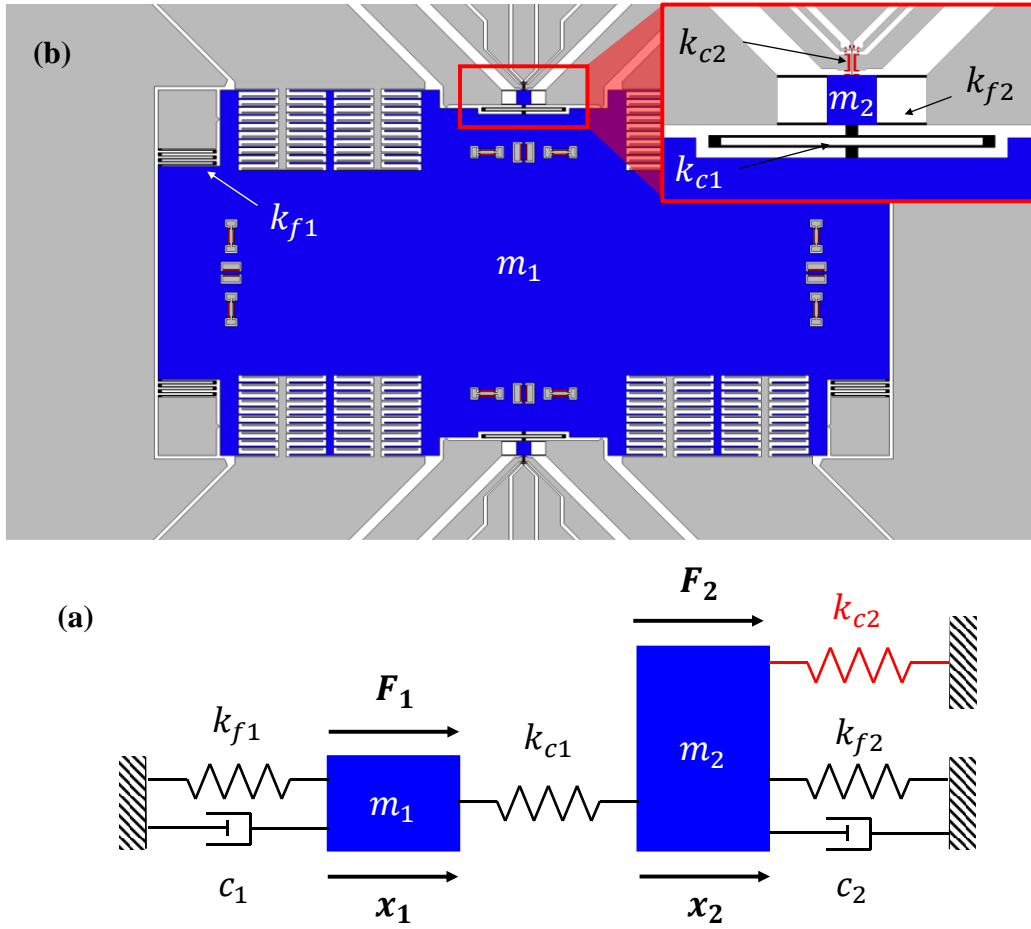


Figure 6-11 Presentation of the first generation of translation accelerometer. (a) is the reduced damped spring mass system and (b) is the design of the accelerometer

The translation accelerometer can be modelled by the schematic of Figure 6-11 (a). Its dynamics can be modelled by two second order equations

$$\begin{pmatrix} m_1 & 0 \\ 0 & m_2 \end{pmatrix} \begin{pmatrix} \ddot{x}_1 \\ \ddot{x}_2 \end{pmatrix} + \begin{pmatrix} c_1 & 0 \\ 0 & c_2 \end{pmatrix} \begin{pmatrix} \dot{x}_1 \\ \dot{x}_2 \end{pmatrix} + \begin{pmatrix} k_{f1} + k_{c1} & -k_{c1} \\ -k_{c1} & k_{f2} + k_{c2} + k_{c1} \end{pmatrix} \begin{pmatrix} x_1 \\ x_2 \end{pmatrix} = \begin{pmatrix} F_1 \\ F_2 \end{pmatrix} \quad 6-25$$

or reduced to four first-order equations by posing $u_{1,2} = \omega_{1,2}x_1$, $v_{1,2} = \dot{x}_{1,2}$, $\omega_1^2 = (k_{f1} + k_{c1})/m_1$, $\omega_2^2 = (k_{f2} + k_{c2} + k_{c1})/m_2$, $Q_1 = \omega_1 m_1/c_1$ and $Q_2 = \omega_2 m_2/c_2$:

$$\begin{cases} \begin{pmatrix} \dot{u}_1 \\ \dot{v}_1 \\ \dot{u}_2 \\ \dot{v}_2 \end{pmatrix} = \begin{pmatrix} 0 & \omega_1 & 0 & 0 \\ -\omega_1 & -\frac{\omega_1}{Q} & \frac{k_{c1}}{\omega_2 m_1} & 0 \\ 0 & 0 & 0 & \omega_2 \\ \frac{k_{c1}}{\omega_1 m_2} & 0 & -\omega_2 & -\frac{\omega_2}{Q} \end{pmatrix} \begin{pmatrix} u_1 \\ v_1 \\ u_2 \\ v_2 \end{pmatrix} + \begin{pmatrix} 0 & 0 \\ \frac{1}{m_1} & 0 \\ 0 & 0 \\ 0 & \frac{1}{m_2} \end{pmatrix} \begin{pmatrix} F_1 \\ F_2 \end{pmatrix} \\ \begin{pmatrix} x_1 \\ x_2 \end{pmatrix} = \begin{pmatrix} \frac{1}{\omega_1} & 0 & 0 & 0 \\ 0 & 0 & 1 & 0 \\ 0 & 0 & 0 & 0 \end{pmatrix} \begin{pmatrix} u_1 \\ v_1 \\ u_2 \\ v_2 \end{pmatrix} + \begin{pmatrix} 0 & 0 \\ 0 & 0 \end{pmatrix} \begin{pmatrix} F_1 \\ F_2 \end{pmatrix} \end{cases} \quad 6-26$$

The equivalent stiffness of the accelerometer $K_{eq} = x_2/F_1$ consists in k_{c2} in parallel with k_{f2} , all in series with k_{c1} . The equivalent stiffness in parallel with k_{f1}

$$K_{eq} = k_{f1} + \frac{k_{c1}(k_{f2} + k_{c2})}{k_{c1} + k_{c2} + k_{f2}} \quad 6-27$$

Considering $m_1 \gg m_2$ the accelerometer resonance can be estimated

$$\omega_{0m} = \sqrt{\frac{K_{eq}}{m_1}} \quad 6-28$$

The dynamics of the mechanical decoupling structure can be estimated by

$$\left\{ \begin{array}{l} \omega_2 = \sqrt{\frac{k_{f2} + k_{c2} + k_{c1}}{m_2}} \\ \omega_{f2} = \sqrt{\frac{k_{f,f2}}{m_{f2}}} \\ \omega_{c1} = \sqrt{\frac{k_{f,c1}}{m_{c1}}} \end{array} \right. \quad 6-29$$

where ω_2 is the cut-off frequency of the mechanical decoupling structure. ω_{f2} is the bending mode of the beam represented by the stiffness k_{f2} , with $k_{f,f2}$ and m_{f2} , which are respectively its flexural stiffness and effective mass. ω_{c1} is the bending mode of the beam combination represented by the stiffness k_{c1} , with $k_{f,c1}$ and m_{c1} , which are respectively its flexural stiffness and effective mass. Here the analytical modelling is compared to FEM simulation for this translation accelerometer:

Geometries	Values
L_g	$2 \mu m$
L_t	$0.5 \mu m$
L_r	$10 \mu m$
w_r	$250 nm$
L_{m11}	$1 mm$
L_{m12}	$500 \mu m$
l_{f1}	$70 \mu m$
l_{f2}	$20 \mu m$
l_{c1}	$50 \mu m$
L_{m2}	$20 \mu m$

Table 54 Geometry of the translation accelerometer

Parameters	Analytics modelling	COMSOL
$S_{\sigma a} = m_1 E / K_{eq} L_r$	0.54 MPa/g	0.39 MPa/g
ω_{0m}	10.4 kHz	9.95 kHz

Table 55 Comparison between analytical modeling and FEM simulation of accelerometer parameters

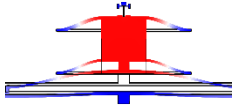
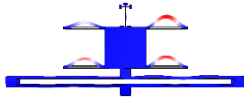
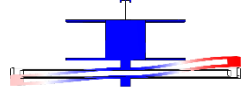
	ω_2	ω_{f2}	ω_{c1}
Analytic	1.7 MHz	22 MHz	0.48 MHz
Simulation	1.63 MHz	21.42 MHz	0.65 MHz
Mode shape			

Table 56 Comparison between analytical modeling and FEM simulation of mechanical decoupling structure.

The next part is based only on the FEM simulation and allows quantify the cross-axis sensitivities, the thermal effect and the protection of the nanoresonator by stoppers.

acceleration	$\sigma_{R1}[MPa]$	$\sigma_{R1}[MPa]$	$\Delta\sigma[MPa]$	$\delta\sigma[\%]$
$a_Y = 1g$	0.39	-0.39	0.78	100
$a_Y = 1g$	$8.8E - 6$	$2.1E - 5$	$1.18E - 5$	0.0015
$a_Z = 1g$	0.01	0.01	$6E - 6$	$7.5E - 4$

Table 57 Differential sensitivities as a function 1g-acceleration applied on each directions.

displacement	$\sigma_{R1}[MPa]$	$\sigma_{R1}[MPa]$	$\sigma_{mean}[MPa]$
$x = 1\mu m$	151.76	-151.76	$FS = 151.79$
$y = 1\mu m$	0.365	0.17	0.26
$z = 0.8\mu m$	184.58	184.62	184.6

Table 58 Maximum stress applied on the nanoresonator when proof mass contacts stoppers.

effect	$\sigma_{R1}[MPa]$	$\sigma_{R1}[MPa]$	$\Delta\sigma[MPa]$	%FS
$\epsilon_{XX} = 100ppm$	-31.78	-32.27	0.49	0.32
$\epsilon_{YY} = 100ppm$	49.46	49.49	0.03	0.02
$\epsilon_{XY} = 100ppm$	-0.18	-0.02	0.16	0.1
$\Delta T = 100^\circ C$	-45.97	-44.79	1.19	0.78

Table 59 Differential sensitivities as a function of substrate deformation (ϵ_{XX} , ϵ_{YY} , ϵ_{XY}) and thermal expansion (ΔT).

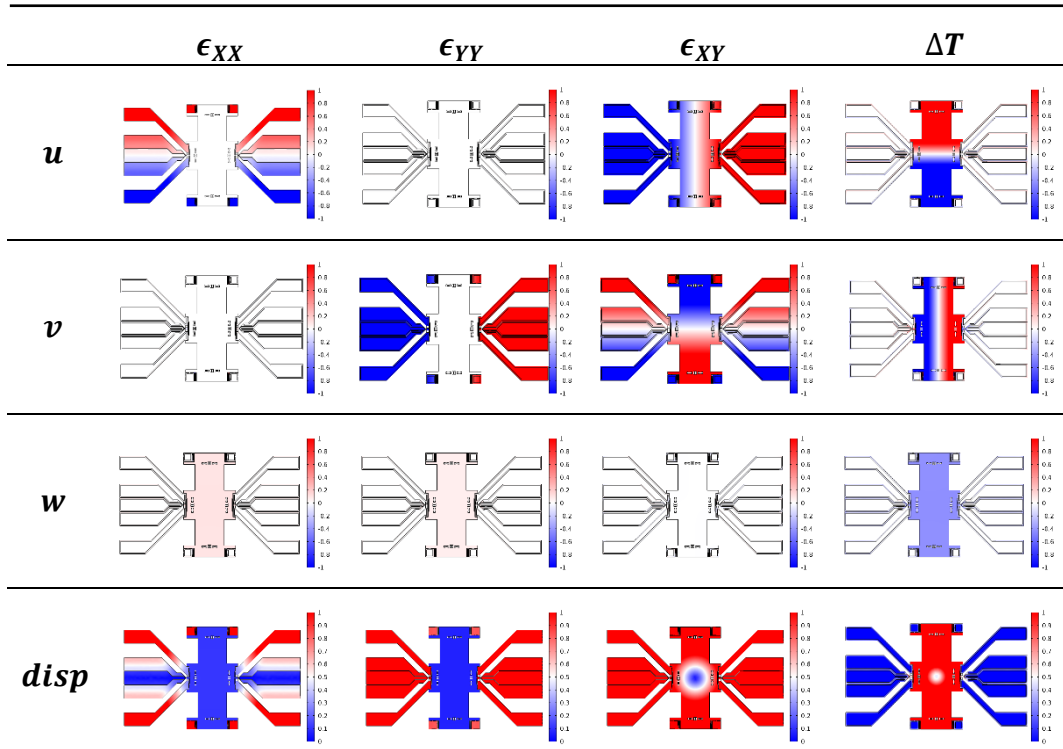


Table 60 Displacement profile induced by substrate deformation ($\epsilon_{XX}, \epsilon_{YY}, \epsilon_{XY}$) and thermal expansion (ΔT).

Lever arm accelerometer

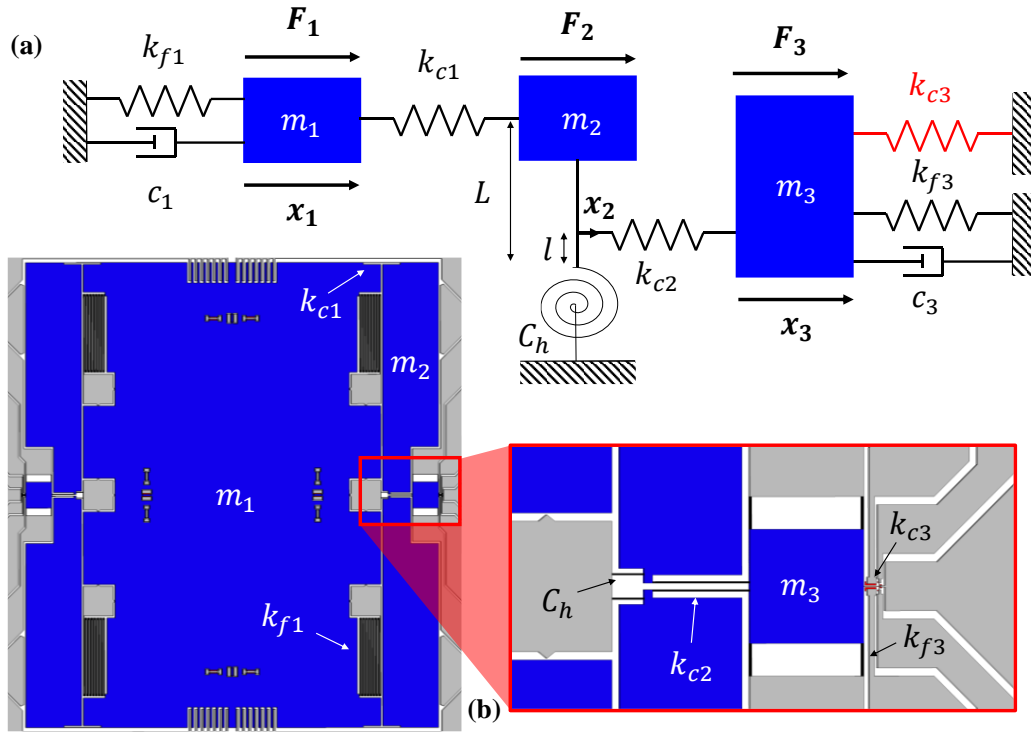


Figure 6-12 Presentation of the first generation of lever arm accelerometer. (a) is the reduced damped spring mass system and (b) is the design of the accelerometer

The translation accelerometer can be modelled by the schematic of Figure 6-12 (a). Its dynamics can be modelled by two second order equations

$$\begin{cases} F_1 = m_1 \ddot{x}_1 + c_1 \dot{x}_1 + (k_{f1} + k_{c1})x_1 - x_2 \frac{L}{l} k_{c1} \\ F_2 \frac{l}{L} = m_2 \ddot{x}_2 + \frac{c_2}{L^2} \dot{x}_2 + \frac{(C_h^* + l^2 k_{c2} + L^2 k_{c1})}{L^2} x_2 - x_1 \frac{l}{L} k_{c1} - x_3 \frac{l^2}{L^2} k_{c2} \\ F_3 = m_3 \ddot{x}_3 + c_3 \dot{x}_3 + (k_{f3} + k_{c3} + k_{c2})x_3 - x_2 k_{c2} \end{cases} \quad 6-30$$

or reduced to four first-order equations by posing $u_{1,2,3} = \omega_{1,2,3} x_1$, $v_{1,2,3} = \dot{x}_{1,2,3}$,

$$\begin{cases} \begin{pmatrix} \dot{u}_1 \\ \dot{v}_1 \\ \dot{u}_2 \\ \dot{v}_2 \\ \dot{u}_3 \\ \dot{v}_3 \end{pmatrix} = \begin{pmatrix} 0 & \omega_1 & 0 & 0 & 0 & 0 \\ -\omega_1 & -\frac{\omega_1}{Q} & \frac{L}{l} \frac{k_{c1}}{m_1 \omega_2} & 0 & 0 & 0 \\ 0 & 0 & 0 & \omega_2 & 0 & 0 \\ \frac{k_{c1} l}{m_2 \omega_1 L} & 0 & -\omega_2 & -\frac{\omega_2}{Q} & \frac{k_{c2} l^2}{m_2 L^2 \omega_3} & 0 \\ 0 & 0 & 0 & 0 & 0 & \omega_3 \\ 0 & 0 & \frac{k_{c2}}{m_3 \omega_2} & 0 & -\omega_3 & -\frac{\omega_3}{Q} \end{pmatrix} \begin{pmatrix} u_1 \\ v_1 \\ u_2 \\ v_2 \\ u_3 \\ v_3 \end{pmatrix} + \begin{pmatrix} 0 & 0 & 0 \\ \frac{1}{m_1} & 0 & 0 \\ 0 & 0 & 0 \\ 0 & \frac{l}{m_2 L} & 0 \\ 0 & 0 & 0 \\ 0 & 0 & \frac{1}{m_3} \end{pmatrix} \begin{pmatrix} F_1 \\ F_2 \\ F_3 \end{pmatrix} \\ \begin{pmatrix} x_1 \\ x_2 \\ x_3 \end{pmatrix} = \begin{pmatrix} \frac{1}{\omega_1} & 0 & 0 & 0 & 0 & 0 \\ 0 & 0 & \frac{1}{\omega_2} & 0 & 0 & 0 \\ 0 & 0 & 0 & \frac{1}{\omega_3} & 0 & 0 \end{pmatrix} \begin{pmatrix} u_1 \\ v_1 \\ u_2 \\ v_2 \\ u_3 \\ v_3 \end{pmatrix} + \begin{pmatrix} 0 & 0 & 0 \\ 0 & 0 & 0 \\ 0 & 0 & 0 \end{pmatrix} \begin{pmatrix} F_1 \\ F_2 \\ F_3 \end{pmatrix} \end{cases} \quad 6-31$$

with

$$\left\{ \begin{array}{l} \omega_1^2 = \frac{k_{f1} + k_{c1}}{m_1} \\ \frac{c_1}{m_1} = \frac{\omega_1}{Q_1} \end{array} \right\} \& \left\{ \begin{array}{l} \omega_2^2 = \frac{C_h + k_{c1}L^2 + k_{c2}l^2}{L^2 m_2} \\ \frac{c_2}{m_2 L^2} = \frac{\omega_2}{Q_2} \end{array} \right\} \& \left\{ \begin{array}{l} \omega_3^2 = \frac{k_{f3} + k_{c3} + k_{c2}}{m_3} \\ \frac{c_3}{m_3} = \frac{\omega_2}{Q_3} \end{array} \right\} \quad 6-32$$

The equivalent stiffness of the accelerometer $K_{eq} = x_2/F_1$ consists in k_{c3} in parallel with k_{f3} , all in series with k_{c2} . This equivalent stiffness integrated in the lever arm in series with k_{f1} and k_{c1}

$$K_{eq} = k_{f1} + \frac{k_{c1} \times \frac{C_h^* + l^2 \left(\frac{k_{c2}(k_{c3} + k_{f3})}{k_{c2} + k_{c3} + k_{f3}} \right)}{L^2}}{k_{c1} + \frac{C_h^* + l^2 \left(\frac{k_{c2}(k_{c3} + k_{f3})}{k_{c2} + k_{c3} + k_{f3}} \right)}{L^2}} \quad 6-33$$

Considering $m_1 \gg m_2 \gg m_3$ the accelerometer resonance can be estimated

$$\omega_{0m} = \sqrt{\frac{K_{eq}}{m_1}} \quad 6-34$$

The dynamics of the mechanical decoupling structure can be estimated by

$$\left\{ \begin{array}{l} \omega_3 = \sqrt{\frac{k_{f3} + k_{c2} + k_{c3}}{m_3}} \\ \omega_{f3} = \sqrt{\frac{k_{f,f3}}{m_{f3}}} \\ \omega_{c2} = \sqrt{\frac{k_{f,c2}}{m_{c2}}} \end{array} \right. \quad 6-35$$

where ω_3 is the cut-off frequency of the mechanical decoupling structure. ω_{f3} is the bending mode of the beam represented by the stiffness k_{f3} , with $k_{f,f3}$ and m_{f3} , which are respectively its flexural stiffness and effective mass. ω_{c2} is the bending mode of the beam represented by the stiffness k_{c2} , with $k_{f,c2}$ and m_{c2} , which are respectively its flexural stiffness and effective mass.

Here the analytical modelling is compared to FEM simulation for this lever arm accelerometer geometry:

Geometries	Values
L_g	$2\ \mu m$
L_t	$0.5\ \mu m$
L_r	$10\ \mu m$
w_r	$250\ nm$
L_{m11}	$1250\ \mu m$
L_{m12}	$800\ \mu m$
l_{f1}	$70\ \mu m$
L_{m2}	$60\ \mu m$
l_{f2}	$20\ \mu m$
l_{c1}	$50\ \mu m$

Table 61 Geometry of the translation accelerometer

Parameters	Analytics modelling	COMSOL
$S_{\sigma a} = m_1 E / K_{eq} L_r$	$58.3\ MPa/g$	$56\ MPa/g$
ω_{0m}	$867\ Hz$	$755\ Hz$

Table 62 Comparison between analytical modeling and FEM simulation of accelerometer parameters

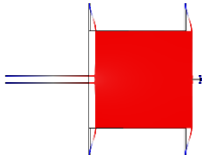
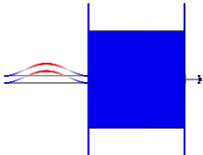
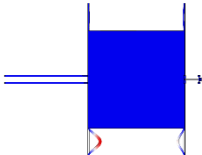
	ω_2	ω_{c2}	ω_{f2}
Analytic	3.57 MHz	2.44 MHz	22 MHz
Simulation	3.48 MHz	2.48 MHz	21.4 MHz
Mode shape			

Table 63 Comparison between analytical modeling and FEM simulation of mechanical decoupling structure

The next part is based only on the FEM simulation and allows quantify the cross-axis sensitivities, the thermal effect and the protection of the nanoresonator by stoppers.

acceleration	$\sigma_{R1}[MPa]$	$\sigma_{R1}[MPa]$	$\Delta\sigma[MPa]$	$\delta\sigma[\%]$
$a_X = 1g$	56.85	-56.78	113.63	100
$a_Y = 1g$	$8.5E - 4$	$-8.1E - 4$	$1.6E - 3$	0.0014
$a_Z = 1g$	-0.3	-0.3	$5E - 4$	$4.4E - 4$

Table 64 Differential sensitivities as a function 1g-acceleration applied on each directions.

displacement	$\sigma_{R1}[MPa]$	$\sigma_{R1}[MPa]$	$\sigma_{mean}[MPa]$
$x = 1\mu m$	112.09	-111.96	$FS = 112.025$
$y = 1\mu m$	$4.42E - 4$	$5.42E - 4$	$4.9E - 4$
$z = 0.8\mu m$	1.53	1.523	1.526

Table 65 Maximum stress applied on the nanoresonator when proof mass contacts stoppers.

effect	$\sigma_{R1}[MPa]$	$\sigma_{R1}[MPa]$	$\Delta\sigma[MPa]$	%FS
$\epsilon_{XX} = 100ppm$	2.26	2.37	0.12	0.1
$\epsilon_{YY} = 100ppm$	316.01	315.63	0.38	0.33
$\epsilon_{XY} = 100ppm$	-0.03	-0.04	0.01	0.01
$\Delta T = 100^\circ C$	-827.5	-826.81	0.69	0.61

Table 66 Differential sensitivities as a function of substrate deformation (ϵ_{XX} , ϵ_{YY} , ϵ_{XY}) and thermal expansion (ΔT).

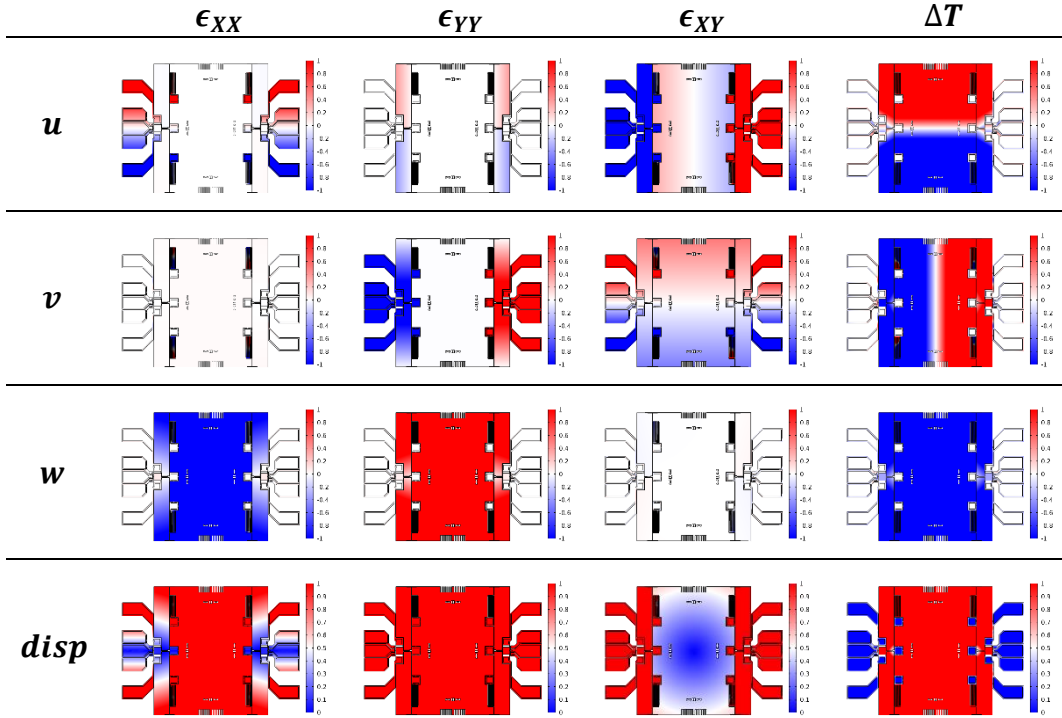


Table 67 Differential sensitivities as a function of substrate deformation (ϵ_{XX} , ϵ_{YY} , ϵ_{XY}) and thermal expansion (ΔT).

Bibliography

- [1] ‘A new electric telemeter’, *Journal of the A.I.E.E.*, vol. 43, no. 3, pp. 196–196, Mar. 1924, doi: 10.1109/JAIEE.1924.6534032.
- [2] P. K. Stein, ‘1936—A banner year for strain gages and experimental stress analysis—An historical perspective’, *Experimental Techniques*, vol. 30, no. 1, pp. 23–41, Jan. 2006, doi: 10.1111/j.1747-1567.2006.00009.x.
- [3] L. M. Roylance and J. B. Angell, ‘A batch-fabricated silicon accelerometer’, *IEEE Transactions on Electron Devices*, vol. 26, no. 12, pp. 1911–1917, Dec. 1979, doi: 10.1109/T-ED.1979.19795.
- [4] Yole Developpement, ‘Status of the MEMS Industry 2021’, *i-Micronews*.
- [5] S. Jean-Michel, ‘Market opportunities for advanced MEMS accelerometers and overview of actual capabilities vs. required specifications’, in *PLANS 2004. Position Location and Navigation Symposium (IEEE Cat. No.04CH37556)*, Monterey, CA, USA, 2004, pp. 78–82. doi: 10.1109/PLANS.2004.1308977.
- [6] P. Zwahlen, A.-M. Nguyen, Y. Dong, F. Rudolf, M. Pastre, and H. Schmid, ‘Navigation grade MEMS accelerometer’, in *2010 IEEE 23rd International Conference on Micro Electro Mechanical Systems (MEMS)*, Wanchai, Hong Kong, China, Jan. 2010, pp. 631–634. doi: 10.1109/MEMSYS.2010.5442327.
- [7] R. Zhu, H. Ding, Y. Su, and Z. Zhou, ‘Micromachined gas inertial sensor based on convection heat transfer’, *Sensors and Actuators A: Physical*, vol. 130–131, pp. 68–74, Aug. 2006, doi: 10.1016/j.sna.2005.11.022.
- [8] ‘Colibrys Capacitive Accelerometers MS1000 / MS9000 / HS8030 / VS1000 / SI1000’.
- [9] J. He, W. Zhou, H. Yu, X. He, and P. Peng, ‘Structural Designing of a MEMS Capacitive Accelerometer for Low Temperature Coefficient and High Linearity’, *Sensors*, vol. 18, no. 2, p. 643, Feb. 2018, doi: 10.3390/s18020643.
- [10] R. Abdolvand, B. V. Amini, and F. Ayazi, ‘Sub-Micro-Gravity In-Plane Accelerometers With Reduced Capacitive Gaps and Extra Seismic Mass’, *J. Microelectromech. Syst.*, vol. 16, no. 5, pp. 1036–1043, Oct. 2007, doi: 10.1109/JMEMS.2007.900879.
- [11] W. T. Pike, I. M. Standley, S. B. Calcutt, and A. G. Mukherjee, ‘A broad-band silicon microseismometer with 0.25 NG/rtHz performance’, in *2018 IEEE Micro Electro Mechanical Systems (MEMS)*, Belfast, Jan. 2018, pp. 113–116. doi: 10.1109/MEMSYS.2018.8346496.
- [12] B. Vakili Amini, R. Abdolvand, and F. Ayazi, ‘A 4.5-mW Closed-Loop $\Delta\Sigma$ Micro-Gravity CMOS SOI Accelerometer’, *IEEE J. Solid-State Circuits*, vol. 41, no. 12, pp. 2983–2991, Dec. 2006, doi: 10.1109/JSSC.2006.884864.
- [13] M. Yucetas, J. Salomaa, A. Kalanti, L. Aaltonen, and K. Halonen, ‘A closed-loop SC interface for a 1.4g accelerometer with 0.33% nonlinearity and 2.5g/vHz input noise density’, in *2010 IEEE International Solid-State Circuits Conference - (ISSCC)*, San Francisco, CA, USA, Feb. 2010, pp. 320–321. doi: 10.1109/ISSCC.2010.5433899.
- [14] A. Utz, C. Walk, A. Stanitzki, M. Mokhtari, M. Kraft, and R. Kokozinski, ‘A High-Precision and High-Bandwidth MEMS-Based Capacitive

-
- Accelerometer’, *IEEE Sensors J.*, vol. 18, no. 16, pp. 6533–6539, Aug. 2018, doi: 10.1109/JSEN.2018.2849873.
- [15] A. G. Krause, M. Winger, T. D. Blasius, Q. Lin, and O. Painter, ‘A high-resolution microchip optomechanical accelerometer’, *Nature Photonics*, vol. 6, no. 11, pp. 768–772, Nov. 2012, doi: 10.1038/nphoton.2012.245.
- [16] ‘Louise Banniard. Inertial sensors with optomechanical transduction. Micro and nanotechnologies/Microelectronics. Université Grenoble Alpes [2020-..], 2020. English. ffNNT : 2020GRALT059ff. fftel-03163570’.
- [17] M. Sansa *et al.*, ‘Optomechanical mass spectrometry’, *Nature Communications*, vol. 11, no. 1, Dec. 2020, doi: 10.1038/s41467-020-17592-9.
- [18] R. Toda, N. Takeda, T. Murakoshi, S. Nakamura, and M. Esashi, ‘Electrostatically levitated spherical 3-axis accelerometer’, in *Technical Digest. MEMS 2002 IEEE International Conference. Fifteenth IEEE International Conference on Micro Electro Mechanical Systems (Cat. No.02CH37266)*, 2002, pp. 710–713. doi: 10.1109/MEMSYS.2002.984369.
- [19] M. Haub, M. Bogner, T. Guenther, A. Zimmermann, and H. Sandmaier, ‘Development and Proof of Concept of a Miniaturized MEMS Quantum Tunneling Accelerometer Based on PtC Tips by Focused Ion Beam 3D Nano-Patterning’, *Sensors*, vol. 21, no. 11, p. 3795, May 2021, doi: 10.3390/s21113795.
- [20] J. Han, Z. Zhao, W. Niu, R. Huang, and L. Dong, ‘A low cross-axis sensitivity piezoresistive accelerometer fabricated by masked-maskless wet etching’, *Sensors and Actuators A: Physical*, vol. 283, pp. 17–25, Nov. 2018, doi: 10.1016/j.sna.2018.09.040.
- [21] A. L. Roy and T. K. Bhattacharyya, ‘Design, fabrication and characterization of high performance SOI MEMS piezoresistive accelerometers’, *Microsyst Technol*, vol. 21, no. 1, pp. 55–63, Jan. 2015, doi: 10.1007/s00542-013-1904-y.
- [22] Ph. Robert *et al.*, ‘M&NEMS: A new approach for ultra-low cost 3D inertial sensor’, in *SENSORS, 2009 IEEE*, Oct. 2009, pp. 963–966. doi: 10.1109/ICSENS.2009.5398195.
- [23] ‘7270A-20K ENDEVCO PIEZORESISTIVE ACCELEROMETER’.
- [24] Y. Nemirovsky, A. Nemirovsky, P. Muralt, and N. Setter, ‘Design of novel thin-film piezoelectric accelerometer’, *Sensors and Actuators A: Physical*, vol. 56, no. 3, pp. 239–249, Sep. 1996, doi: 10.1016/S0924-4247(96)01324-6.
- [25] B. Tian, H. Liu, N. Yang, Y. Zhao, and Z. Jiang, ‘Design of a Piezoelectric Accelerometer with High Sensitivity and Low Transverse Effect’, *Sensors*, vol. 16, no. 10, p. 1587, Sep. 2016, doi: 10.3390/s16101587.
- [26] S. Tadigadapa and K. Mateti, ‘Piezoelectric MEMS sensors: state-of-the-art and perspectives’, *Measurement Science and Technology*, vol. 20, no. 9, p. 092001, Sep. 2009, doi: 10.1088/0957-0233/20/9/092001.
- [27] B. L. Norling, ‘Superflex: A Synergistic Combination of Vibrating Beam and Quartz Flexure Accelerometer Technology’, *Navigation*, vol. 34, no. 4, pp. 337–353, Dec. 1987, doi: 10.1002/j.2161-4296.1987.tb01511.x.
- [28] A. A. Seshia *et al.*, ‘A vacuum packaged surface micromachined resonant accelerometer’, *J. Microelectromech. Syst.*, vol. 11, no. 6, pp. 784–793, Dec. 2002, doi: 10.1109/JMEMS.2002.805207.
-

-
- [29] S. Hentz, L. Duraffourg, and E. Colinet, ‘Comparison of capacitive and frequential readout when scaling accelerometers down from Micro- to Nano-Electro Mechanical Systems’, 2012, doi: 10.48550/ARXIV.1205.4860.
 - [30] A. Caspani, C. Comi, A. Corigliano, G. Langfelder, V. Zega, and S. Zerbini, ‘A Differential Resonant Micro Accelerometer for Out-of-plane Measurements’, *Procedia Engineering*, vol. 87, pp. 640–643, 2014, doi: 10.1016/j.proeng.2014.11.569.
 - [31] S. A. Zotov, B. R. Simon, A. A. Trusov, and A. M. Shkel, ‘High Quality Factor Resonant MEMS Accelerometer With Continuous Thermal Compensation’, *IEEE Sensors J.*, vol. 15, no. 9, pp. 5045–5052, Sep. 2015, doi: 10.1109/JSEN.2015.2432021.
 - [32] C. R. Marra, A. Tocchio, F. Rizzini, and G. Langfelder, ‘Solving FSR Versus Offset-Drift Trade-Offs With Three-Axis Time-Switched FM MEMS Accelerometer’, *J. Microelectromech. Syst.*, vol. 27, no. 5, pp. 790–799, Oct. 2018, doi: 10.1109/JMEMS.2018.2851143.
 - [33] S. Shin, H. Wen, H.-K. Kwon, G. D. Vukasin, T. W. Kenny, and F. Ayazi, ‘A Dual-Axis Resonant Accelerometer Based on Electrostatic Stiffness Modulation in Epi-Seal Process’, in *2019 IEEE SENSORS*, Montreal, QC, Canada, Oct. 2019, pp. 1–4. doi: 10.1109/SENSORS43011.2019.8956601.
 - [34] S. Beeby, G. Ensel, M. Kraft, and N. White, “MEMS mechanical sensors”, *Artech House*, vol. 1, 2004.
 - [35] F. Chen, W. Tian, and Y. Wei, ‘Highly sensitive resonant sensor using quartz resonator cluster for inclination measurement’, *Review of Scientific Instruments*, vol. 91, no. 5, p. 055005, May 2020, doi: 10.1063/5.0001406.
 - [36] T. Zhang, X. Wei, Z. Jiang, and T. Cui, ‘Sensitivity enhancement of a resonant mass sensor based on internal resonance’, *Applied Physics Letters*, vol. 113, no. 22, p. 223505, Nov. 2018, doi: 10.1063/1.5057439.
 - [37] D. Thuau, P.-H. Ducrot, P. Poulin, I. Dufour, and C. Ayela, ‘Integrated Electromechanical Transduction Schemes for Polymer MEMS Sensors’, *Micromachines*, vol. 9, no. 5, p. 197, Apr. 2018, doi: 10.3390/mi9050197.
 - [38] B. Yang, X. Guo, Q. H. Wang, C. F. Lu, and D. Hu, ‘A novel flow sensor based on resonant sensing with two-stage microleverage mechanism’, *Review of Scientific Instruments*, vol. 89, no. 4, p. 045002, Apr. 2018, doi: 10.1063/1.5000506.
 - [39] C. Chen *et al.*, ‘Performance of monolayer graphene nanomechanical resonators with electrical readout’, *Nature Nanotechnology*, vol. 4, no. 12, pp. 861–867, Dec. 2009, doi: 10.1038/nnano.2009.267.
 - [40] N. Anzar, R. Hasan, M. Tyagi, N. Yadav, and J. Narang, ‘Carbon nanotube - A review on Synthesis, Properties and plethora of applications in the field of biomedical science’, *Sensors International*, vol. 1, p. 100003, 2020, doi: 10.1016/j.sintl.2020.100003.
 - [41] T. Kim *et al.*, ‘A New Simple Fabrication Method for Silicon Nanowire-Based Accelerometers’, in *2019 20th International Conference on Solid-State Sensors, Actuators and Microsystems & Eurosensors XXXIII (TRANSDUCERS & EUROSENSORS XXXIII)*, Jun. 2019, pp. 1949–1952. doi: 10.1109/TRANSDUCERS.2019.8808764.
 - [42] S. C. Masmanidis, R. B. Karabalin, I. De Vlaminck, G. Borghs, M. R. Freeman, and M. L. Roukes, ‘Multifunctional Nanomechanical Systems via
-

-
- Tunably Coupled Piezoelectric Actuation', *Science*, vol. 317, no. 5839, pp. 780–783, Aug. 2007, doi: 10.1126/science.1144793.
- [43] 'Luca Leoncino. Optomechanical transduction applied to M/NEMS devices. Optics [physics.optics]. Université Grenoble Alpes, 2017. English. ffNNT : 2017GREAY067ff. fftel-01757058f'.
- [44] E. Mile *et al.*, 'In-plane nanoelectromechanical resonators based on silicon nanowire piezoresistive detection', *Nanotechnology*, vol. 21, no. 16, p. 165504, Apr. 2010, doi: 10.1088/0957-4484/21/16/165504.
- [45] J. Chaste, A. Eichler, J. Moser, G. Ceballos, R. Rurali, and A. Bachtold, 'A nanomechanical mass sensor with yoctogram resolution', *Nature Nanotechnology*, vol. 7, no. 5, pp. 301–304, May 2012, doi: 10.1038/nnano.2012.42.
- [46] P. Weber, J. Güttinger, A. Noury, J. Vergara-Cruz, and A. Bachtold, 'Force sensitivity of multilayer graphene optomechanical devices', *Nature Communications*, vol. 7, no. 1, Nov. 2016, doi: 10.1038/ncomms12496.
- [47] O. Le Traon, D. Janiaud, S. Muller, and P. Bouniol, 'The VIA vibrating beam accelerometer: concept and performance', in *IEEE 1998 Position Location and Navigation Symposium (Cat. No.98CH36153)*, 1998, pp. 25–29. doi: 10.1109/PLANS.1998.669865.
- [48] T. V. Roszhart, H. Jerman, J. Drake, and C. de Cotiis, 'An Inertial-Grade, Micromachined Vibrating Beam Accelerometer', in *Proceedings of the International Solid-State Sensors and Actuators Conference - TRANSDUCERS '95*, 1995, vol. 2, pp. 656–658. doi: 10.1109/SENSOR.1995.721917.
- [49] G. Sobreviela-Falces *et al.*, 'A Mems Vibrating Beam Accelerometer for High Resolution Seismometry and Gravimetry', in *2021 IEEE 34th International Conference on Micro Electro Mechanical Systems (MEMS)*, Jan. 2021, pp. 196–199. doi: 10.1109/MEMS51782.2021.9375431.
- [50] J. Zhao *et al.*, 'A 0.23- μg Bias Instability and 1 $\mu\text{g}/\text{rtHz}$ Acceleration Noise Density Silicon Oscillating Accelerometer With Embedded Frequency-to-Digital Converter in PLL', *IEEE J. Solid-State Circuits*, vol. 52, no. 4, pp. 1053–1065, Apr. 2017, doi: 10.1109/JSSC.2016.2645613.
- [51] D. D. Shin, Y. Chen, I. B. Flader, and T. W. Kenny, 'Temperature compensation of resonant accelerometer via nonlinear operation', in *2018 IEEE Micro Electro Mechanical Systems (MEMS)*, Jan. 2018, pp. 1012–1015. doi: 10.1109/MEMSYS.2018.8346730.
- [52] Y. Yin, Z. Fang, Y. Liu, and F. Han, 'Temperature-Insensitive Structure Design of Micromachined Resonant Accelerometers', *Sensors*, vol. 19, no. 7, p. 1544, Mar. 2019, doi: 10.3390/s19071544.
- [53] J. Cui, H. Yang, D. Li, Z. Song, and Q. Zhao, 'A Silicon Resonant Accelerometer Embedded in An Isolation Frame with Stress Relief Anchor', *Micromachines*, vol. 10, no. 9, p. 571, Aug. 2019, doi: 10.3390/mi10090571.
- [54] D. D. Shin, C. H. Ahn, Y. Chen, D. L. Christensen, I. B. Flader, and T. W. Kenny, 'Environmentally robust differential resonant accelerometer in a wafer-scale encapsulation process', in *2017 IEEE 30th International Conference on Micro Electro Mechanical Systems (MEMS)*, Jan. 2017, pp. 17–20. doi: 10.1109/MEMSYS.2017.7863328.
-

-
- [55] C. Zhao *et al.*, ‘A Resonant MEMS Accelerometer With 56ng Bias Stability and 98ng/Hz^{1/2} Noise Floor’, *Journal of Microelectromechanical Systems*, vol. 28, no. 3, pp. 324–326, Jun. 2019, doi: 10.1109/JMEMS.2019.2908931.
- [56] C. Comi, A. Corigliano, G. Langfelder, A. Longoni, A. Tocchio, and B. Simoni, ‘A Resonant Microaccelerometer With High Sensitivity Operating in an Oscillating Circuit’, *Journal of Microelectromechanical Systems*, vol. 19, no. 5, pp. 1140–1152, Oct. 2010, doi: 10.1109/JMEMS.2010.2067437.
- [57] E. Esteves Moreira *et al.*, ‘Highly sensitive MEMS frequency modulated accelerometer with small footprint’, *Sensors and Actuators A: Physical*, vol. 307, p. 112005, Jun. 2020, doi: 10.1016/j.sna.2020.112005.
- [58] Y. Wang, ‘A MEMS piezoelectric in-plane resonant accelerometer based on aluminum nitride with two-stage microleverage mechanism’, p. 8, 2017.
- [59] C. Wang *et al.*, ‘Micromachined Accelerometers with Sub- $\mu\text{g}/\sqrt{\text{Hz}}$ Noise Floor: A Review’, *Sensors*, vol. 20, no. 14, p. 4054, Jul. 2020, doi: 10.3390/s20144054.
- [60] ‘SiliconMicrogravity Inertial Navigation Gen2 <https://silicong.com/inertial-navigation.html>’.
- [61] Xudong Zou, P. Thiruvengathan, and A. A. Seshia, ‘A Seismic-Grade Resonant MEMS Accelerometer’, *Journal of Microelectromechanical Systems*, vol. 23, no. 4, pp. 768–770, Aug. 2014, doi: 10.1109/JMEMS.2014.2319196.
- [62] A. Mustafazade *et al.*, ‘A vibrating beam MEMS accelerometer for gravity and seismic measurements’, *Sci Rep*, vol. 10, no. 1, p. 10415, Dec. 2020, doi: 10.1038/s41598-020-67046-x.
- [63] F. Maspero, S. Delachanal, A. Berthelot, L. Joet, G. Langfelder, and S. Hentz, ‘Quarter-mm² High Dynamic Range Silicon Capacitive Accelerometer With a 3D Process’, *IEEE Sensors J.*, vol. 20, no. 2, pp. 689–699, Jan. 2020, doi: 10.1109/JSEN.2019.2942797.
- [64] F. Souchon, L. Joet, C. Ladner, P. Rey, and S. Louwers, ‘High-Performance MEMS Pressure Sensor Fully-Integrated with a 3-Axis Accelerometer’, in *2019 IEEE SENSORS*, Montreal, QC, Canada, Oct. 2019, pp. 1–4. doi: 10.1109/SENSORS43011.2019.8956512.
- [65] M. Gadola, A. Buffoli, M. Sansa, A. Berthelot, P. Robert, and G. Langfelder, ‘1.3 mm² Nav-Grade NEMS-Based Gyroscope’, *J. Microelectromech. Syst.*, vol. 30, no. 4, pp. 513–520, Aug. 2021, doi: 10.1109/JMEMS.2021.3088940.
- [66] ‘Cassinelli, V. Modeling and experimental characterization of an innovative piezoresistive M&NEMS magnetometer. School of Industrial and Information Engineering, Master Thesis of Electronics Engineering, 15–22 (The Polytechnic University of Milan, Milan, Italy, 2016).’
- [67] B. Fain *et al.*, ‘High-damped accelerometer based on squeeze-film damping and piezoresistive nanogauge detection for vibrating environments’, in *2017 19th International Conference on Solid-State Sensors, Actuators and Microsystems (TRANSDUCERS)*, Kaohsiung, Jun. 2017, pp. 603–606. doi: 10.1109/TRANSDUCERS.2017.7994121.
- [68] M. Geradin, *Mechanical Vibrations theory and application to structural dynamics*, Third.
- [69] E. Sage, ‘New concept of mass spectrometer based on arrays of resonating nanostructures’, p. 210.
-

-
- [70] I. H. Shames and C. L. Dym, *Energy and finite element methods in structural mechanics*. New York: Taylor & Francis [u.a.], 1985.
- [71] H. A. C. Tilmans, M. Elwenspoek, and J. H. J. Fluitman, ‘Micro resonant force gauges.pdf’, *Sensors and Actuators A: Physical*, pp. 35–53, 1992.
- [72] H. W. Ch. Postma, I. Kozinsky, A. Husain, and M. L. Roukes, ‘Dynamic range of nanotube- and nanowire-based electromechanical systems’, *Appl. Phys. Lett.*, vol. 86, no. 22, p. 223105, May 2005, doi: 10.1063/1.1929098.
- [73] V. Kaajakari, T. Mattila, A. Oja, and H. Seppa, ‘Nonlinear Limits for Single-Crystal Silicon Microresonators’, *J. Microelectromech. Syst.*, vol. 13, no. 5, pp. 715–724, Oct. 2004, doi: 10.1109/JMEMS.2004.835771.
- [74] S. Chowdhury, M. Ahmadi, and W. C. Miller, ‘Pull-In Voltage Study of Electrostatically Actuated Fixed-Fixed Beams Using a VLSI On-Chip Interconnect Capacitance Model’, *Journal of Microelectromechanical Systems*, vol. 15, no. 3, pp. 639–651, Jun. 2006, doi: 10.1109/JMEMS.2005.863784.
- [75] ‘Harrie A. C. Tilmanst and Siebe Bouwstra, "Excitation and Detection of Silicon-Based Micromechanical Resonators ",’ *Sensors and Materials, Vol. 9, No. 8 (1997) 521-540*.
- [76] A. Lacaita, S. Levantino, and C. Samori, ‘Integrated Frequency Synthesizers for Wireless Systems’, p. 249.
- [77] N. El-Sheimy, H. Hou, and X. Niu, ‘Analysis and Modeling of Inertial Sensors Using Allan Variance’, *IEEE Trans. Instrum. Meas.*, vol. 57, no. 1, pp. 140–149, Jan. 2008, doi: 10.1109/TIM.2007.908635.
- [78] K. L. Ekinci, Y. T. Yang, and M. L. Roukes, ‘Ultimate limits to inertial mass sensing based upon nanoelectromechanical systems’, *Journal of Applied Physics*, vol. 95, no. 5, pp. 2682–2689, Mar. 2004, doi: 10.1063/1.1642738.
- [79] *ROBINS, William P. Phase noise in signal sources: theory and applications. IET, 1984.*
- [80] P. Monajemi and F. Ayazi, ‘Design optimization and implementation of a microgravity capacitive HARPSS accelerometer’, *IEEE Sensors J.*, vol. 6, no. 1, pp. 39–46, Feb. 2006, doi: 10.1109/JSEN.2005.854134.
- [81] M. Sansa *et al.*, ‘Frequency fluctuations in silicon nanoresonators’, *Nature Nanotech*, vol. 11, no. 6, pp. 552–558, Jun. 2016, doi: 10.1038/nnano.2016.19.
- [82] Y. Deimerly, P. Rey, P. Robert, T. Bourouina, and G. Jourdan, ‘Electromechanical damping in MEMS accelerometers: A way towards single chip gyrometer accelerometer co-integration’, in *2014 IEEE 27th International Conference on Micro Electro Mechanical Systems (MEMS)*, San Francisco, CA, USA, Jan. 2014, pp. 725–728. doi: 10.1109/MEMSYS.2014.6765743.
- [83] B. Fain, F. Souchon, A. Berthelot, R. Anciant, P. Robert, and G. Jourdan, ‘Dynamic control of an accelerometer bandwidth through tunable damping factor and effective moment of inertia’, in *2018 IEEE Micro Electro Mechanical Systems (MEMS)*, Belfast, Jan. 2018, pp. 948–951. doi: 10.1109/MEMSYS.2018.8346714.
- [84] D. Pinto *et al.*, ‘A Small and High Sensitivity Resonant Accelerometer’, *Procedia Chemistry*, vol. 1, no. 1, pp. 536–539, Sep. 2009, doi: 10.1016/j.proche.2009.07.134.
- [85] D. Van Hieu, L. Van Tam, K. Hane, and C. M. Hoang, ‘Models for analyzing squeeze film air damping depending on oscillation modes of micro/nano beam
-

-
- resonators', *Arch Appl Mech*, vol. 91, no. 1, pp. 363–373, Jan. 2021, doi: 10.1007/s00419-020-01775-3.
- [86] G. Lehee, F. Parrain, J.-C. Riou, and A. Bosseboeuf, 'Thermoelastic damping modeling of a Si resonant beam with nanowire strain gauges', in *2014 Symposium on Design, Test, Integration and Packaging of MEMS/MOEMS (DTIP)*, Cannes, France, Apr. 2014, pp. 1–6. doi: 10.1109/DTIP.2014.7056653.
- [87] J.-P. Polizzi, L. Duraffourg, E. Ollier, J. Arcamone, and P. Robert, 'Nano Electro Mechanical Devices for Physical and Chemical Sensing', *ECS Trans.*, vol. 44, no. 1, pp. 1367–1373, Mar. 2012, doi: 10.1149/1.3694473.
- [88] J. Arcamone *et al.*, 'Nanomechanical Mass Sensor for Spatially Resolved Ultrasensitive Monitoring of Deposition Rates in Stencil Lithography', *Small*, vol. 5, no. 2, pp. 176–180, Dec. 2008, doi: 10.1002/sml.200800699.
- [89] G. Jourdan, E. Colinet, J. Arcamone, A. Niel, C. Marcoux, and L. Duraffourg, 'NEMS-based heterodyne self-oscillator', *Sensors and Actuators A: Physical*, vol. 189, pp. 512–518, Jan. 2013, doi: 10.1016/j.sna.2012.10.038.
- [90] F. Han, B. Sun, L. Li, and G. Ma, 'A sensitive three-axis micromachined accelerometer based on an electrostatically suspended proof mass', in *2013 IEEE SENSORS*, Baltimore, MD, USA, Nov. 2013, pp. 1–4. doi: 10.1109/ICSENS.2013.6688167.
- [91] P. Touboul, B. Foulon, and E. Willemenot, 'Electrostatic space accelerometers for present and future missions', *Acta Astronautica*, vol. 45, no. 10, pp. 605–617, Nov. 1999, doi: 10.1016/S0094-5765(99)00132-0.
- [92] Fengtian Han, Boqian Sun, Linlin Li, and Qiuping Wu, 'Performance of a Sensitive Micromachined Accelerometer With an Electrostatically Suspended Proof Mass', *IEEE Sensors J.*, vol. 15, no. 1, pp. 209–217, Jan. 2015, doi: 10.1109/JSEN.2014.2340862.
- [93] L. Huang, H. Yang, Y. Gao, L. Zhao, and J. Liang, 'Design and Implementation of a Micromechanical Silicon Resonant Accelerometer', *Sensors*, vol. 13, no. 11, pp. 15785–15804, Nov. 2013, doi: 10.3390/s131115785.
- [94] 'Lesson, D. B. (1966). A simple model of feedback oscillator noise spectrum. *proc. IEEE*, 54(2), 329-330.'
- [95] A. Demir, 'Understanding fundamental trade-offs in nanomechanical resonant sensors', *Journal of Applied Physics*, vol. 129, no. 4, p. 044503, Jan. 2021, doi: 10.1063/5.0035254.
- [96] 'ALLAN, David W., et al. Time and frequency(time-domain) characterization, estimation, and prediction of precision clocks and oscillators.', *IEEE transactions on ultrasonics, ferroelectrics, and frequency control*, 1987, vol. 34, no 6, p. 647-654..
- [97] E. Rubiola, 'On the measurement of frequency and of its sample variance with high-resolution counters', *Review of Scientific Instruments*, vol. 76, no. 5, p. 054703, May 2005, doi: 10.1063/1.1898203.
- [98] J. E. An, U. Park, D. G. Jung, C. Park, and S. H. Kong, 'Die-Attach Structure of Silicon-on-Glass MEMS Devices Considering Asymmetric Packaging Stress and Thermal Stress', *Sensors*, vol. 19, no. 18, p. 3979, Sep. 2019, doi: 10.3390/s19183979.
- [99] P. Peng, X. P. He, L. M. Du, W. Zhou, H. J. Yu, and B. Peng, 'The Influence of Die-Attach Adhesives on the Packaging of MEMS Accelerometer', *KEM*,
-

-
- vol. 645–646, pp. 533–537, May 2015, doi: 10.4028/www.scientific.net/KEM.645-646.533.
- [100] J. Song, Q.-A. Huang, M. Li, and J.-Y. Tang, ‘Influence of environmental temperature on the dynamic properties of a die attached MEMS device’, *Microsyst Technol*, vol. 15, no. 6, pp. 925–932, Jun. 2009, doi: 10.1007/s00542-009-0818-1.
- [101] X. Zhang, S. Park, and M. W. Judy, ‘Accurate Assessment of Packaging Stress Effects on MEMS Sensors by Measurement and Sensor–Package Interaction Simulations’, *J. Microelectromech. Syst.*, vol. 16, no. 3, pp. 639–649, Jun. 2007, doi: 10.1109/JMEMS.2007.897088.
- [102] U. Park, J. Rhim, J. U. Jeon, and J. Kim, ‘A micromachined differential resonant accelerometer based on robust structural design’, *Microelectronic Engineering*, vol. 129, pp. 5–11, Nov. 2014, doi: 10.1016/j.mee.2014.06.008.
- [103] SHIN, Dongsuk. *High-Stability and Temperature-Compensated MEMS Resonant Beam Accelerometer*. Stanford University, 2019.
- [104] M. Spletzer, A. Raman, A. Q. Wu, X. Xu, and R. Reifenberger, ‘Ultrasensitive mass sensing using mode localization in coupled microcantilevers’, *Appl. Phys. Lett.*, vol. 88, no. 25, p. 254102, Jun. 2006, doi: 10.1063/1.2216889.
- [105] M. Pandit, C. Zhao, G. Sobreviela, and A. Seshia, ‘Practical Limits to Common Mode Rejection in Mode Localized Weakly Coupled Resonators’, *IEEE Sensors J.*, vol. 20, no. 13, pp. 6818–6825, Jul. 2020, doi: 10.1109/JSEN.2019.2930117.
- [106] M. Pandit, C. Zhao, G. Sobreviela, A. Mustafazade, X. Zou, and A. A. Seshia, ‘A mode-localized MEMS accelerometer with 7 μ g bias stability’, in *2018 IEEE Micro Electro Mechanical Systems (MEMS)*, Belfast, Jan. 2018, pp. 968–971. doi: 10.1109/MEMSYS.2018.8346719.
- [107] M. Pandit, C. Zhao, G. Sobreviela, X. Zou, and A. Seshia, ‘A High Resolution Differential Mode-Localized MEMS Accelerometer’, *J. Microelectromech. Syst.*, vol. 28, no. 5, pp. 782–789, Oct. 2019, doi: 10.1109/JMEMS.2019.2926651.
- [108] H. Zhang *et al.*, ‘A Low-Noise High-Order Mode-Localized MEMS Accelerometer’, *J. Microelectromech. Syst.*, vol. 30, no. 2, pp. 178–180, Apr. 2021, doi: 10.1109/JMEMS.2021.3057260.
- [109] ‘HF2LI amplifier Zurich Instrument
<https://www.zhinst.com/europe/fr/products/hf2li-lock-in-amplifier#introduction>’.
- [110] T. Miani *et al.*, ‘Resonant Accelerometers Based on Nanomechanical Piezoresistive Transduction’, in *2021 IEEE 34th International Conference on Micro Electro Mechanical Systems (MEMS)*, Gainesville, FL, USA, Jan. 2021, pp. 192–195. doi: 10.1109/MEMSYS51782.2021.9375287.
- [111] K. Clement *et al.*, ‘Requirements and attributes of nano-resonator mass spectrometry for the analysis of intact viral particles’, *Anal Bioanal Chem*, vol. 413, no. 29, pp. 7147–7156, Dec. 2021, doi: 10.1007/s00216-021-03511-4.
- [112] E. Sage *et al.*, ‘Single-particle mass spectrometry with arrays of frequency-addressed nanomechanical resonators’, *Nat Commun*, vol. 9, no. 1, p. 3283, Dec. 2018, doi: 10.1038/s41467-018-05783-4.
-

-
- [113] V. T. K. Sauer, Z. Diao, M. R. Freeman, and W. K. Hiebert, ‘Wavelength-division multiplexing of nano-optomechanical doubly clamped beam systems’, *Opt. Lett.*, vol. 40, no. 9, p. 1948, May 2015, doi: 10.1364/OL.40.001948.
 - [114] A. H. Safavi-Naeini, D. Van Thourhout, R. Baets, and R. Van Laer, ‘Controlling phonons and photons at the wavelength scale: integrated photonics meets integrated phononics’, *Optica*, vol. 6, no. 2, p. 213, Feb. 2019, doi: 10.1364/OPTICA.6.000213.
 - [115] M. Metcalfe, ‘Applications of cavity optomechanics’, *Applied Physics Reviews*, vol. 1, no. 3, p. 031105, Sep. 2014, doi: 10.1063/1.4896029.
 - [116] *PREUMONT, André. Vibration control of active structures: an introduction. Springer, 2018.*

Additional work

This work has been communicated in two international conferences and has led to the development of three patents. In addition, a journal article is in progress:

- At the 34th IEEE International Conference on Microelectromechanical Systems (MEMS) in 2021, the proof-of-concept of the first generation of sensors was presented [110] and awarded the "Outstanding student paper" prize. The main result is the highest scaling factor in the state of the art, made possible by the bilayer fabrication process.
- The advanced results of the first generation of sensors will be presented at the 9th IEEE International Symposium on Inertial Sensors and Systems (2022). Noise analysis highlights improved wafer-level conditioning that overcomes the thermomechanical noise of the proof mass, the previous limitation of the inertial sensor.
- An accelerometer architecture based on an electrostatic decoupling structure was developed and patented during this work. A prototype has been designed with the latest generation of accelerometer.
- An accelerometer architecture allowing two different pressure environments has been patented. Its objective is to provide a vacuum environment for the nanoresonator and an atmospheric environment for the proof of concept.
- The mechanical decoupling structure proposed on the latest generation of accelerometers has been patented.

The experimental method to characterize the coupling, the tool to identify the coupled modes (FEM simulation) as well as the solution of the mechanical decoupling structure and its validation by the identification tool are being written for a journal article.

Abstract:

Resonant beam accelerometers have demonstrated their ability to achieve sub- μg resolutions previously reserved for macroscopic accelerometers. These microelectromechanical systems (MEMS) are promising candidates for high-precision commercial applications due to their low cost, small size, and batch manufacturability. In the vast majority of commercial MEMS inertial sensors, the proof mass and sensing elements are defined in the same silicon layer. When the sensing element is a resonant beam, the use of a single layer of silicon imposes a trade-off between the sensitivity and the bandwidth of the accelerometer. In order to circumvent this trade-off, we propose here to use a bi-layer technology, so-called M&NEMS, which results in sensors that are more sensitive and would open the field to new applications requiring high-performance integrated sensors. The proposed accelerometer combines a micrometric proof mass with the high detection sensitivity of a nanoresonator. In addition, we propose to employ a piezoresistive detection that provides a performance transduction at high frequency, unlike capacitive detection.

This work represents the first proof of concept of a resonant accelerometer based on a piezoresistive nanoresonator detection. First, the modelling, design and fabrication of the first generation of sensors is presented. Because the designed nanoresonator operates at several MHz, a dedicated readout electronics was designed in partnership with the group of Prof. Langfelder from the Politecnico di Milano. The second part of this work focuses on the characterization of the accelerometers. The use of the M&NEMS multi-layer process allows reaching the highest sensitivity of the state of the art for a 0.18 mm^2 mass footprint, i.e. $100,000\text{ ppm/g}$ with $<1\%$ nonlinearity over the $\pm 1\text{g}$ range. The noise analysis shows a noise floor of $1.75\mu\text{g}/\sqrt{\text{Hz}}$ over a 1-kHz bandwidth. The last part deals with the improvement of the accelerometer and nanoresonator architecture in order to overcome the operating limitations highlighted by the first experimental results. Because the manufacturing process is compatible with gyros and out-of-plane accelerometers, the proposed nanoresonator-based detection represents a high-sensitivity alternative for 6-axis inertial measurement units (IMU), as well as other devices such as pressure sensors or magnetometers.